Universidad del País Vasco
Euskal Herriko Unibertsitatea

Theoretical approach to atomic-scale nanoplasmonics as probed by light and swift electrons

PhD thesis by

Mattin Urbieta Galarraga

Supervised by

Prof. Nerea Zabala

and

Prof. Javier Aizpurua

Department of Electricity and Electronics
University of the Basque Country (UPV/EHU)

February 2021

This report is a PhD thesis developed during the period from October 2015 to February 2021 at the Theory of Nanophotonics Group, led by Prof. J. Aizpurua (CSIC - UPV/EHU, DIPC and Department of Electricity and Electronics in UPV/EHU). This thesis was funded by the University of the Basque Country UPV/EHU Grant PIF15/237 with a PhD fellowship and project GIU18/202, Donostia International Physics Center (DIPC) (Reference 2015/11) and Materials Physics Center (MPC) for financial support at the initial steps of the PhD, the Basque Government for projects IT756-13 and IT1164-19, and and by Spanish Ministry of Economy and Competitiveness MINECO for projects FIS2013-41184-P, FIS2016-80174-P and PID2019-107432GB-I00. The author thanks DIPC for the computing facilities and CFM for its support.

An electronic version of this thesis can be found at https://addi.ehu.es/
This document was generated with the 2018 LaTeX distribution.
The LaTeX template is adapted from a template of Iagoba Apellaniz, including some modifications by Iraultza Unzueta.
The bibliographic style was created by Sofía Martinez Garaot.

eman ta zabal zazu

Universidad del País Vasco

Euskal Herriko Unibertsitatea

Theoretical approach to atomic-scale nanoplasmonics as probed by light and swift electrons

Thesis by

Mattin Urbieta Galarraga

for the degree of
Doctor of Philosophy in Physics

Supervised by

Prof. Nerea Zabala

and

Prof. Javier Aizpurua

Department of Electricity and Electronics
University of the Basque Country (UPV/EHU)

February 2021

Bizipozez betetzen nauzuenei

Contents

Acknowledgments

"And now leave me in peace for a bit! I don't want to answer a string of questions while I am eating. I want to think!"
"Good Heavens!" said Pippin. "At breakfast?"

- J. R. R. Tolkien, The Fellowship of the Ring

During these five years, six if I count the period during the Master in Nanoscience at the CFM in Donostia, which would be the true starting point of this journey, I had the opportunity to meet a great deal of extraordinary individuals, to whom I owe most, if not all, what I have learned and achieved during these years.

First and foremost, I want acknowledge my supervisors Prof. Nerea Zabala and Prof. Javier Aizpurua, as this thesis would not come to existence without them. Nerea and Javi, you both have guided and advised me along my first steps in the scientific world, and I am deeply grateful for the time spent with you and the patience you had with me. If there is something of a researcher within myself, it is thanks to your dedication and effort during these years. Mila esker bihotzez emandako guztiagatik.

Luca, you have been an irreplaceable support and companion during this journey. I am specially grateful for your guidance and support, specially during my first steps on the PhD, and for all discussions, work and life related, both in the office and on numerous trips to Donostia. Grazie per tutto, amico!

During my PhD, I have been lucky to collaborate with several brilliant scientists. In this regard, I want to show my deepest gratitude to Dr. Marc Barbry for his readiness and disposition to lend a hand anytime I requested, and of course, for all these years of fruitful collaboration, for which I also want to thank his PhD supervisors Dr. Peter Koval and Prof. Daniel Sánchez-Portal. Without them half of this thesis would be orphaned of key TDDFT data.

I want to acknowledge Prof. Jeremy J. Baumberg, Dr. Cloudy Carnegie, and the rest of the members of his group in Cambridge, for the privilege to collaborate with such bright and passionate researchers. A big part of this thesis is possible thanks to you. In fact, thanks to the knowledge that I presume to have acquired from the innumerable discussions held these past years, I believe that you managed to make a theoretician like me able to grasp some of the experimental details. Moreover, I am grateful for the opportunity to join you in Ericeira where I had the pleasure to meet the members of your wonderful research group. I will always remember with joy those exciting days.

Another considerable piece of this work would not have been possible without Alberto, who guided me with patience through my numerous missteps with the Hydrodynamic Model. It took a while, but we finally made it to shore. In this sense, I want to acknowledge Edu for the insightful discussions and fine ideas, and for that last push that I needed in the right direction.

I would also like to thank Prof. Peter Nordlander, and his group, for hosting me at Rice University in Houston, Texas, and for an enriching stay that boosted my scientific curiosity and served as fertile ground for novel ideas, with special mention to Dr. Alessandro Alabastri and Dr. Luca Bursi, who made the stay even more enjoyable along with their friends.

Moreover, I would like to acknowledge Prof. Ulrich Hohenester for his disposition as the developer of the MNPBEM Toolbox that I used any time that I asked for his help or queried an issue.

I cannot leave without mentioning the members of the increasing scientific *family* comprising the Theory of Nanophotonics Group in Donostia, with whom I had the pleasure to share many ideas and experiences: Ameen, Mikolaj, Gari, Aitzol, Tomas, Andrea, Christos, Mario, Alvaro, Antton, Jon, Carlos, Unai, Bruno, Yuan, Roberto, Fernando, Luis, Jonathan and Adrián, with special mention to Yao and Ruben, for their help during the thesis and the writing of the manuscript.

Along with UPV/EHU, I would also like to thank the Donostia International Physics Center (DIPC) for financial support at the initial of my PhD, and for the computational resources. Apart from the people in Donostia, I have been lucky to share this years with many wonderful people that made the daily basis more enjoyable.

Tesian zehar Leioan denbora gehien igaro dudan lekua nirekin elkarbanatu dutenekin ezin ahaztu. Leihorik izan ez arren zuei eskerrak argi-printza batzuk behintzat ikusi ditut bertan. Besarkada bat denoi: Eneko eta Eneko, Maite, Anabel, Irati, Jorge, Nerea, Bea, Luis... Horrez gain, Elektrizitatea eta Elektronika Departamentuan beste jende asko ezagutzeko aukera izan dut, eta hauek ere agurtu nahi nituzke, tartean,

Lulu, Popi, Libe, Inari, Oscar, Javi, Esti, Aitziber, Andoni, Katarina, Edu, Dani, Iván, Mireia, Raúl, Andrés, Juan Mari Collantes, Amparo Varona, Josu Jugo, Fernando Plazaola, Jose Angel García (Fisika Aplikatua)... eta aipatu gabe gelditzen direnak ere. Bide batez, nire esker ona adierazi nahi nieke irakaskuntzaren munduan lehen ezagutzeko aukera eta laguntza eskaini didatenei: Ruth Lazcoz, David Brizuela, Raül Vera eta Iñaki Garay.

Bestalde, urte hauek Gose Naiz Taldea (GNT) osatzen duten lagunik gabe ezingo lirateke ulertu. Bazkalorduaren bueltan bildutako taldea zena bizi-osorako lagun taldea bihurtu da: Joanes, Asier, Iraultza, Iagoba, Julen S., Iñigo, Peio, Lafu, Haritz, Xabi, Telmo, Oscar eta Julen. Ez dadila haria eten!

Horrez gain, mila esker lagunei, hasieratik bukaera arte hor izatearren, onean eta txarrean. Ezin aipatu gabe utzi Turri eta Vela, gure Talka! Urte hauetan musika aitzakiatzat hartuta une batzuez behintzat deskonektatzen laguntzearren.

Familia. Ama, aita, Jule. Zuek gabe ez tesia, ez beste ezer ez zatekeen posible izango. Zuei zor dizuet naizena eta honaino iritsi izana. Hemen esan dezakedan oro motz geldituko litzateke zuekin dudan zortea adierazteko, eta bizitzan lehen egunetik emandako maitasun eta babesa eskertzeko. Izarretaraino joan eta etorri, maite zaituztet.

Bidean hautsi ez banaiz, zuri esker izan da, Eider. Eta noizbait hautsi banaiz, zeuk osatu nauzulako iritsi naiz helmugara. Zure bizitzeko grinarekin urte hauetako egunik ilunenak ere argitu dizkidazu. Bihotzez, mila esker zure babesagatik eta pazientziagatik, eta bizitzako plazer txikiak, eta ez horren txikiak, nirekin elkarbanatzeagatik.

Ia ezeren zergatia jakitera heldu gabe
bizitzaren barnean bizitzen lehiatu
eta horrela itsumustuka, gau bakoitzean
ilunari galdegiten dioten hitzekin
irudien zorabio desorekatuan barneratu.

Ai balego gizakumearen barnerik barnekoenean
argiaren zehaztasun hori ordu urdinetan
osotasunez blaitutako ikusmen gardena
antzinako zorionaren lur zabal haietan...!
baina irautea iluntzen joatea da
ortzilerro eta ikusmen distiratsuak galtzea,
oinaze tematuaren bitartez bizitzari galdezka aritzea,
kolpeka hor eta deman
materiarekin, izpirituarekin, hurkoarekin...

Horrela egunsentia dator, goizalba harrigarria
eta adigalkor bilutsik harrapatzen gaitu.

- X. Lete, Egunsentiaren esku izoztuak, Vulnerant omnes, XXXI

List of Abbreviations

BC Boundary Condition

BEM Boundary Element Method

BDP Bonding Dimer Plasmon

BPT Biphenyl-4-thiol

BQP Bonding Quadrupolar Plasmon

CPIM Capacitance-Polarizability Interaction Model

CTP Charge Transfer Plasmon

CTP' Higher-Order Charge Transfer Plasmon

CBP Confined Bulk Plasmon

DDA Discrete Dipole Approximation

DFT Density Functional Theory

DIM Discrete Interaction Model

DP Dipolar Plasmon

EEL Electron Energy Loss

EELS Electron Energy Loss Spectroscopy

EM Electromagnetic

ERS Electronic Raman Scattering

GGA Generalized Gradient Approximation

HDM Hydrodynamic Model

HK Hohenberg-Kohn

HOP Higher Order Plasmon

ILS Inelastic Light Scattering

KS Kohn and Sham

LCAO Linear Combination of Atomic Orbitals

LDA Local-Density Approximation

LSP Localized Surface Plasmon

LRE Lightning Rod Effect

MIM Metal-insulator-metal

MNP Metallic Nanoparticle

MNPBEM Metallic nanoparticles using a boundary element method (MNPBEM)

NP Nanoparticle

NPoM NanoParticle-on-Mirror

PB Product Basis

PDI Point-Dipole Interaction

QM Quantum Mechanics

QNM Quasinormal Modes

QP Quadrupolar Plasmon

SERS Surface Enhanced Raman Scattering

SIESTA Spanish Initiative for Electronic Simulations with Thousands of Atoms

SNOM Scanning Near-field Optical Microscopy

s-SNOM scattering-type Scanning Near-field Optical Microscopy

SPP Surface Plasmon Polariton

SRM Specular Reflection Model

STEM Scanning Transmission Electron Microscope

TDDFT Time-Dependent Density Functional Theory

TEM Transmission Electron Microscopy

Introduction

The story tells that a day between 214-212 BC, during the Second Punic War between romans and carthaginians, Archimedes burnt the roman ships that were attacking Syracuse by using mirrors as reflectors to focus sunlight on the ships and set them on fire. Little information has reached the present days about Archimedes and his life, and the veracity of this incident has been contested many times [1]. Be it a fictitious tale, or part of the Ancient History, the idea of focusing light has inspired the creation of many artifacts and tools that have proven to be beneficial during History, albeit for less dramatic applications, such as to gain sight of distant or small objects, undistinguishable otherwise. Indeed, enhancing our visual capability is the cornerstone of many technological improvements and scientific discoveries. For instance, magnifying glasses and in particular the appearance of the first optical microscopes in the 16^{th} and 17^{th} centuries boosted advances in biology and medicine, improving the quality of live of human beings to this day.

Visible and infrared light are widely used for imaging and in other optical microscopy techniques, although only features similar in dimension, or larger, than the wavelength of the illuminating light, can be distinguished this way, i.e., traditional optical systems are limited by the *diffraction limit* [2]. To be observable, objects of sub-wavelength sizes require techniques that overcome the diffraction limit by confining light into sub-wavelength dimensions. Such extreme localization of light is

possible due to the interaction between light and matter at the nanoscale, which is addressed by the field of Nanophotonics [3].

Sub-wavelength confinement of light can be achieved, for instance, using Surface Plasmon Polaritons (SPPs), i.e., resonant electron density waves that are excited at metal/dielectric interfaces as an hybridization of collective oscillations of conduction electrons in the metal (surface plasmons) and incident electromagnetic (EM) fields at visible and near-infrared frequencies [2,4]. Electrons in the metal and their behavior under an external electromagnetic field have been addressed with different levels of complexity within *nanoplasmonics*. For instance, within the so-called Drude model, the optical response of the conduction electrons of a metal are described as a non-interacting free electron gas. Despite its simplicity, this approach is widely used in nanophotonics, as it provides good accuracy to describe the response at energies below d-band excitations and allows for understanding the main trends in optical spectroscopy of metals.

Drude model

In the frequency-domain, ω, the relative dielectric permittivity of a metal, $\varepsilon_{\mathrm{m}}(\omega)$, within the Drude model can be expressed as:

$$\varepsilon_{\mathrm{m}}(\omega) = \varepsilon_{\infty} - \frac{\omega_p^2}{\omega(\omega + i\gamma_p)}, \tag{1}$$

where γ_p is the damping coefficient that accounts for the losses in the metal, ε_{∞} is the background screening that accounts phenomenologically for the polarizability of bounded electrons (the damping related to these contributions is not included in the Drude model) and ω_p is the plasma frequency of the metal, which is related to the electron density of the metal, n, as:

$$\omega_p = \sqrt{\frac{ne^2}{\varepsilon_0 m^*}}, \tag{2}$$

with ε_0 the vacuum permittivity, e the electron charge, and m^* the effective electron mass.

Propagating SPPs confine optical fields in the region near a flat metal/dielectric interface extending a few tens of nanometers in the direction normal to the interface, as sketched in Fig. 1. Although SPPs in a perfectly planar geometry cannot couple to incoming light due to the mismatch in the momentum associated to light and SPPs [5,6], different strategies have been proposed to overcome this problem. For instance, in scanning near-field optical microscopy (SNOM) a sharp metallic tip is placed on top of the metallic interface [7]. Another technique consists in placing fluorescent molecules near the metallic interface [8,9]. Another common solution to overcome such momentum mismatch and excite SPPs is creating grated patterns in a region of the metallic surface [10,11]. These strategies have been used to overcome

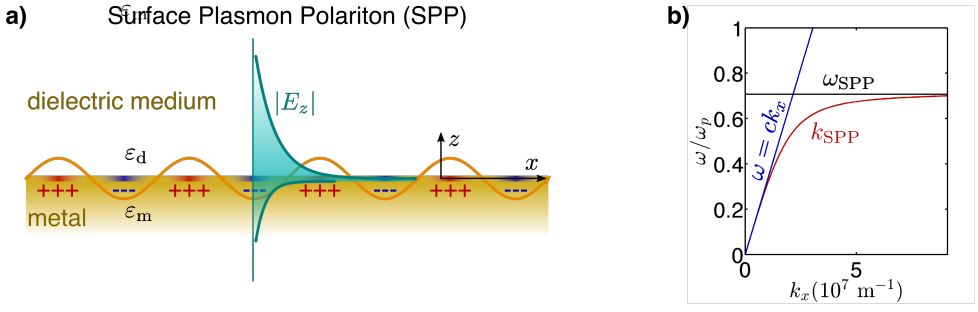

Figure 1: a) Sketch of a Surface Plasmon Polariton (SPP) propagating at the metal-dielectric interface, where the z-component of the electric field decays exponentially. b) Dispersion relation for a SPP (solid red line) in comparison to the light cone dispersion (blue) for photons in free space. The horizontal black line marks the SPP frequency, which satisfies $\varepsilon_m(\omega_{SPP}) = -\varepsilon_d$ [see Eq. (3)].

such momentum mismatch and excite SPPs.

Surface Plasmon Polaritons (SPPs)

For a planar metal/dielectric interface illuminated by a monochromatic plane wave, the boundary conditions for the EM field at the interface lead to parallel component of the wavevector of the propagating SPP at the metal/dielectric interface $k_x = k_{SPP}$ [2, 4] (see Fig. 1):

$$k_{SPP} = \sqrt{\frac{\varepsilon_m(\omega)\varepsilon_d}{\varepsilon_m(\omega) + \varepsilon_d}}\frac{\omega}{c}, \tag{3}$$

where ε_d is the relative permittivity of the dielectric, c is the speed of light in vacuum and $k_0 = \omega/c$ is the electromagnetic plasmon wavevector in vacuum. Complete theoretical definitions can be found in Ref. [2].

While propagating SPPs travel along a metal/dielectric interface, Localized Surface Plasmons (LSPs) are confined at small nanoparticles (NPs) and can be excited by direct illumination. The extra momentum needed to overcome the mismatch between the SPP dispersion relation and light is given by the finite geometry of the NP. Under illumination, small spherical metallic NPs, such as the one depicted in Fig. 2(a), show a plasmonic resonance that corresponds to the Dipolar Plasmon (DP) mode of the spherical NP [see Fig. 2(b)], clearly apparent in the charge distribution of Fig. 2(a). The dipolar pattern oscillates in time resonantly at the frequency of the illumination, with a $\pi/2$ phase offset with respect to the excitation EM field, producing a large enhancement (total field amplitude at each point normalized to the amplitude of the incident field, $|E/E_0|$) and localization of the near fields around the nanoparticle [see Fig. 2(c)]. Interestingly, the field is localized in a region with dimensions much smaller than the wavelength of the incoming light. The plasmon

resonance frequency strongly depends on the size, shape, material and surroundings of the NPs [12–15], which make them useful for designing sensitive nanodevices that require optical responses with specific properties. Moreover, the strongly localized fields by the SPPs and LSPs can be used to enhance light-matter interactions of matter deposited nearby [16, 17] inaccessible by other means.

Localized Surface Plasmons (LSPs)

For a small spherical NP with radius R much smaller than the wavelength of light ($R \ll \lambda$) the optical response can be calculated analytically within the quasistatic approximation. For a metallic spherical NP with permittivity $\varepsilon_{\mathrm{m}}(\omega)$, embedded in a dielectric medium ε_{d}, the dipole moment induced at the nanoparticle by an electric field $\mathbf{E}_0$ is obtained from the NP's polarizability [2], α, as:

$$\mathbf{p}(\omega) = \varepsilon_{\mathrm{d}} \alpha(\omega) \mathbf{E}_0(\omega), \tag{4}$$

where

$$\alpha(\omega) = 4\pi\varepsilon_0 R^3 \frac{\varepsilon_{\mathrm{m}}(\omega) - \varepsilon_{\mathrm{d}}}{\varepsilon_{\mathrm{m}}(\omega) + 2\varepsilon_{\mathrm{d}}}. \tag{5}$$

The DP resonance is excited for a frequency ω_{DP} that satisfies the condition $\varepsilon_{\mathrm{m}}(\omega_{\mathrm{DP}}) = -2\varepsilon_d$. If the metal is modeled as a lossless Drude metal without background screening, $\gamma_p = 0$ and $\varepsilon_\infty = 1$, in Eq. (1), we obtain:

$$\omega_{\mathrm{DP}} = \frac{\omega_p}{\sqrt{1 + 2\varepsilon_{\mathrm{d}}}}. \tag{6}$$

Therefore, if the surrounding medium is vacuum ($\varepsilon_{\mathrm{d}} = 1$), the energy of the DP in Eq. (6), ω_{DP}, becomes $\omega_{\mathrm{DP}} = \omega_p/\sqrt{3}$, which is accurate for perfect Drude-like metals. The *scattering* and *absorption* cross sections are given by,

$$\sigma_{\mathrm{sca}}(\omega) = \frac{k^4}{6\pi} |\alpha(\omega)|^2, \tag{7}$$

$$\sigma_{\mathrm{abs}}(\omega) = k\, \mathrm{Im}[\alpha(\omega)], \tag{8}$$

with $k = \omega/c\sqrt{\varepsilon_d}$ the wavenumber of the incident EM wave. The scattering and absorption cross sections can be found by comparing the powers dissipated into absorption and scattering with the intensity of the incident illumination. Their sum provides the *extinction* cross section, $\sigma_{\mathrm{ext}}(\omega) = \sigma_{\mathrm{sca}}(\omega) + \sigma_{\mathrm{abs}}(\omega)$.

In the case of noble metals such as gold (Au) and silver (Ag) there is a discrepancy between the theoretical value predicted by Eq. (6) and the experimental value mainly due to the contribution to the response of these materials of the background polarizability of bound d-electrons. The optical properties of noble-metal NPs are

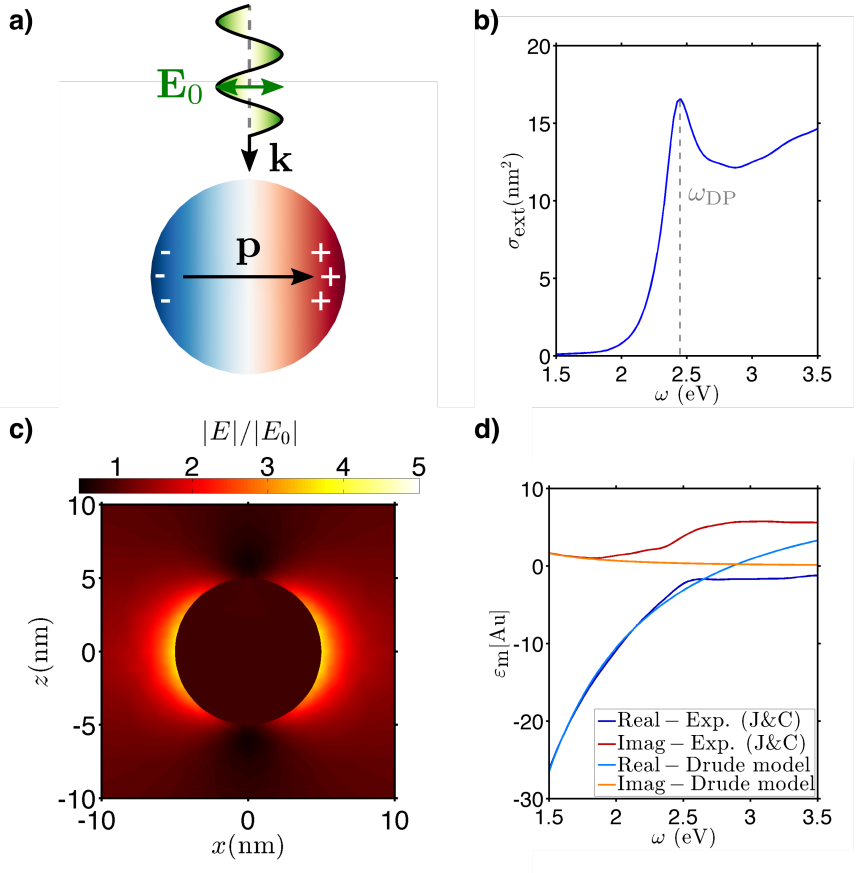

Figure 2: a) Sketch of the charge density corresponding to a Localized Surface Plasmon (LSP) excited by an incoming plane wave with amplitude E_0 and momentum **k** and the corresponding induced dipole moment **p**. b) Extinction cross section σ_{ext} of such a spherical Au particle as a function of the illumination frequency ω. c) Near-field enhancement ($|E/E_0|$) at the wavelength of the DP resonance. d) Dielectric function of gold from experimental data [18] and Drude model.

well reproduced when the contribution of these bound electrons and the damping of the material is included in the response[see Fig. 2(d) for the contribution of such bound electrons onto the metal dielectric function $\varepsilon_m(\omega)$].

Plasmonic nanoparticles are referred to as optical nanoantennas due to their capability not only to localize light but to also scatter it effectively into the far field. These nanoantennas have sizes that are in the range of a few nanometers to hundreds of nanometers. One of the many challenges in plasmonics has been the fabrication of NPs with high control of their shape, composition and positioning on a substrate. Indeed, the improvement and exploration of new fabrication techniques has received

much effort and attention over the last decades, allowing remarkable precision in top-down fabrication approaches [19–21], and large versatility in bottom-up ones [22–24].

Such control in the properties of plasmonic nanostructures is at the core of nanophotonics, mainly due to the high dependence of the near-field localization on the geometry of the metal/dielectric interface. Indeed, even if the incoming light is out of resonance with respect to the plasmon, a nanostructure can exhibit non-resonant field enhancement at sharp metal tips or NP vertices. This phenomenon, known as the "lightning rod" effect (LRE) in electrostatics, occurs due to an accumulation of charge at sharp metallic endings, i.e., the equipotential lines get closer from each other near sharp geometries, which implies larger EM fields in such regions [2]. The LRE, along with the field confinement due to plasmon resonances, is exploited for instance in scattering-type scanning near-field optical microscopy (s-SNOM) [25].

Further field enhancement and localization of the EM field can be reached by coupling of plasmons in adjacent metallic nanostructures due to Coulomb interaction. Indeed, nanostructures separated by gaps of ~ 1 nm or smaller show so-called electromagnetic "hot-spots", provide increased field enhancement at the gap due to the coupling between the plasmons of adjacent nanostructures. The optical response of such coupled nanostructures, i.e., a *dimer* in the case of two nanoparticles, strongly depends on the gap length and morphology, offering a platform for high spectral sensitivity. In this sense, the great field intensities confined into such nanogaps, also named *nanocavities*, can enhance optically-driven processes.

Nanocavities are formed by two NPs in close proximity, in which the Coulomb interaction between the charges associated to the individual LSP modes of each particle produce a hybridization of the modes forming a Bonding Dimer Plasmon (BDP), hybridized modes produced in a similar way as atomic orbitals hybridize when forming molecules [26–28]. Charge is accumulated at facing metallic surfaces across the gap, as shown in Fig. 3(a), leading to significant increases of the localization and enhancements of the near field at the gap, as compared to the single particle case [29, 30], as observed in Fig. 3(b). Moreover, due to the strong Coulomb interaction between these charges the spectral position of the BDP resonances is very sensitive to the gap separation distance [30,31], turning the gap nanoantennas into very sensitive plasmonic rulers.

When the particles are at physical contact electric charge can be transferred between two NPs and Charge Transfer Plasmon (CTP) modes can be excited. Moreover, CTPs can also be excited without direct contact if electrons can still flow from one NP to another by other mechanisms, such as electron tunneling [32, 33].

An alternative to dimers for obtaining nanometer-scale confinement of light can be found in structures such as the *NanoParticle-on-Mirror* (NPoM), which consists of a metallic nanoparticle placed on top of a metallic substrate and separated by a thin spacer-film in-between to prevent conductive contact, creating a nanogap between the NP and the substrate [see Fig. 3(c)]. NPoM structures show great stability and offer a suitable platform to perform molecular spectroscopy experiments onto molecules deposited in the cavity.

One of the most used molecular spectroscopic techniques is Raman scattering,

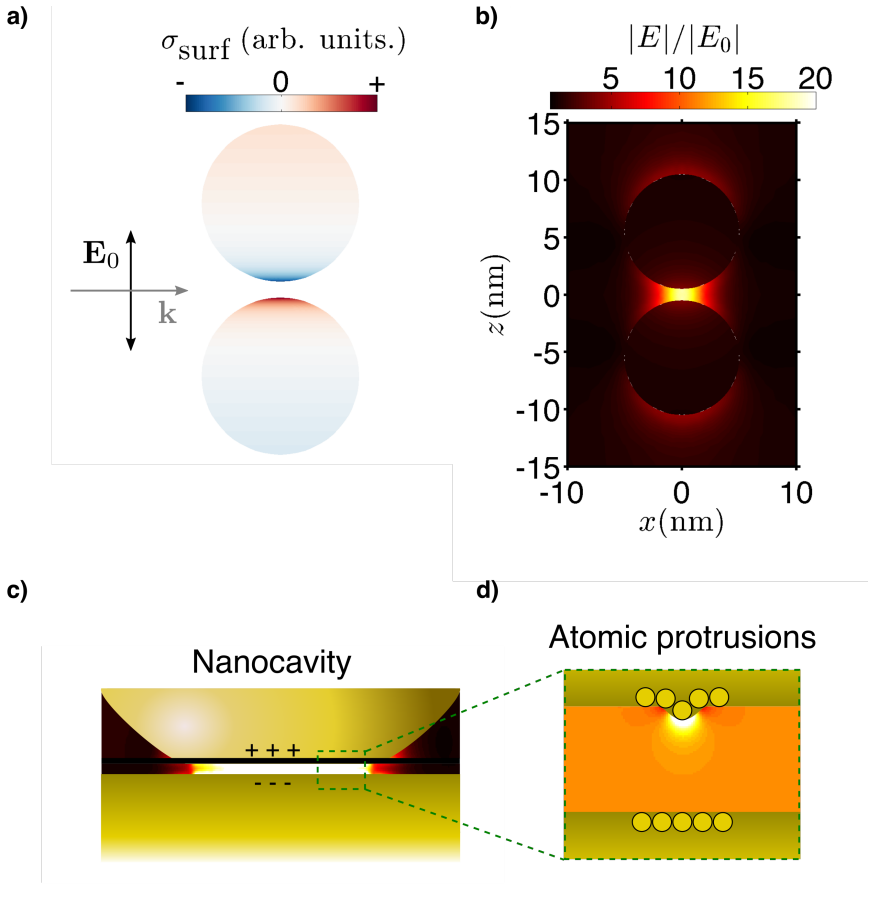

Figure 3: a) Dimer formed by two spherical nanoparticles showing charge accumulation, σ_{surf}, at the regions close to the gap. b) Charge accumulation at the gap produces large localization and enhancement of the near field $|E|/|E_0|$. c) Nanocavities can also be formed by placing a nanoparticle on top of a metallic substrate, separated by a thin spacer to prevent conductive contact and create a nanogap. d) Atomic protrusions at the nanogap can further increase the localization and enhancement of the near field at the nanogap due to a lightning rod effect.

with applications in archaeology [34], medicine [35], drug detection [36] and chemical sensing [37]. Raman scattering was discovered by C. V. Raman in the 1920s [38] and describes an inelastic light-scattering process in which an incident photon (light) excites a molecule to a virtual state, which can relax back to a different state emitting a photon of smaller energy with the production of a vibration (Stokes process), or alternatively it can relax to a state emitting a photon of larger energy, while absorbing a vibration (anti-Stokes process), Raman scattering complements Lord Rayleigh's scattering theory, which describes an elastic process of light.

Raman Scattering

An incident photon of energy $h\nu_0$ can excite a molecule from the vibrational ground state E_0 to a virtual state[a], which can relax back to the ground state emitting a photon of the same energy $h\nu_0$ (elastic process), or to another state of different energy (inelastic process) [see Fig. 4(a)]. The former case is known as Rayleigh scattering, being the dominant process.
Raman scattering is an inelastic process in which the molecule relaxes to a different state and therefore emits a photon with different energy to that of the incident photon. The most common situation is a relaxation to an excited state of energy $E_0 + h\nu_m$ where $h\nu_m$ is the energy of a vibration, which, following energy conservation, is accompanied by the emission a photon of energy $h\nu_0 - h\nu_m$, i.e., the emitted photon if of lower energy than the incident photon, and is known as *Stokes* scattering.
An inverse situation can also happen, i.e., a molecule can initially be in an excited state of energy $E_0 + h\nu_m$, and after excited to a virtual state, the molecule can relax to a state of lower energy, such as the ground state E_0. This process, known as *anti-Stokes* scattering, is accompanied by the emission a photon of higher energy than the incident photon ($h\nu_0 + h\nu_m$).

[a] A very short-lived, unobservable quantum state, which is an intermediate state in a multi-step process that mediates otherwise forbidden transitions, as in Raman scattering.

In Raman scattering, the difference in energy of the scattered light from the incident light corresponds to the difference in energy of the vibrational states of the probed molecule. As a molecule can have multiple vibrational modes, the scattered light can have different wavelengths, each corresponding to a Raman scattering process of a different vibrational mode. Thus, the resulting spectrum is very useful to identify vibrational modes and functional groups within a molecule, offering a tool to reconstruct the chemical structure of the molecule under study. The Raman scattering spectrum of a molecule is therefore considered as the *vibrational fingerprint* of such molecule.[1]

Anti-Stokes scattering requires the molecule to be in an excited state. Indeed, for zero temperature $T = 0$ K all molecules are considered to be in the ground state, so no anti-Stokes scattering can be observed in those circumstances. Experiments performed at room temperature typically show a dominance of Stokes scattering as molecules are mainly at the ground state [see Fig. 4(b)]. Moreover, the Stokes/anti-Stokes ratio is used to measure the temperature of the molecule if one assumes a Bose-Einstein distribution of vibrational states.

Nevertheless, Raman scattering has a big drawback, which is its small cross section, with typical Raman cross section having values often $\ll 10^{-28}$ m^2. The viability of Raman scattering as a spectroscopy technique is greatly improved by exploiting

[1] Raman spectra are typically plotted with an x-axis of Raman shift (cm^{-1}) calculated as $1/\lambda_0 - 1/\lambda_{\text{Raman}}$ where λ_0 is the wavelength of the incident light and λ_{Raman} the wavelength of the emitted Raman light.

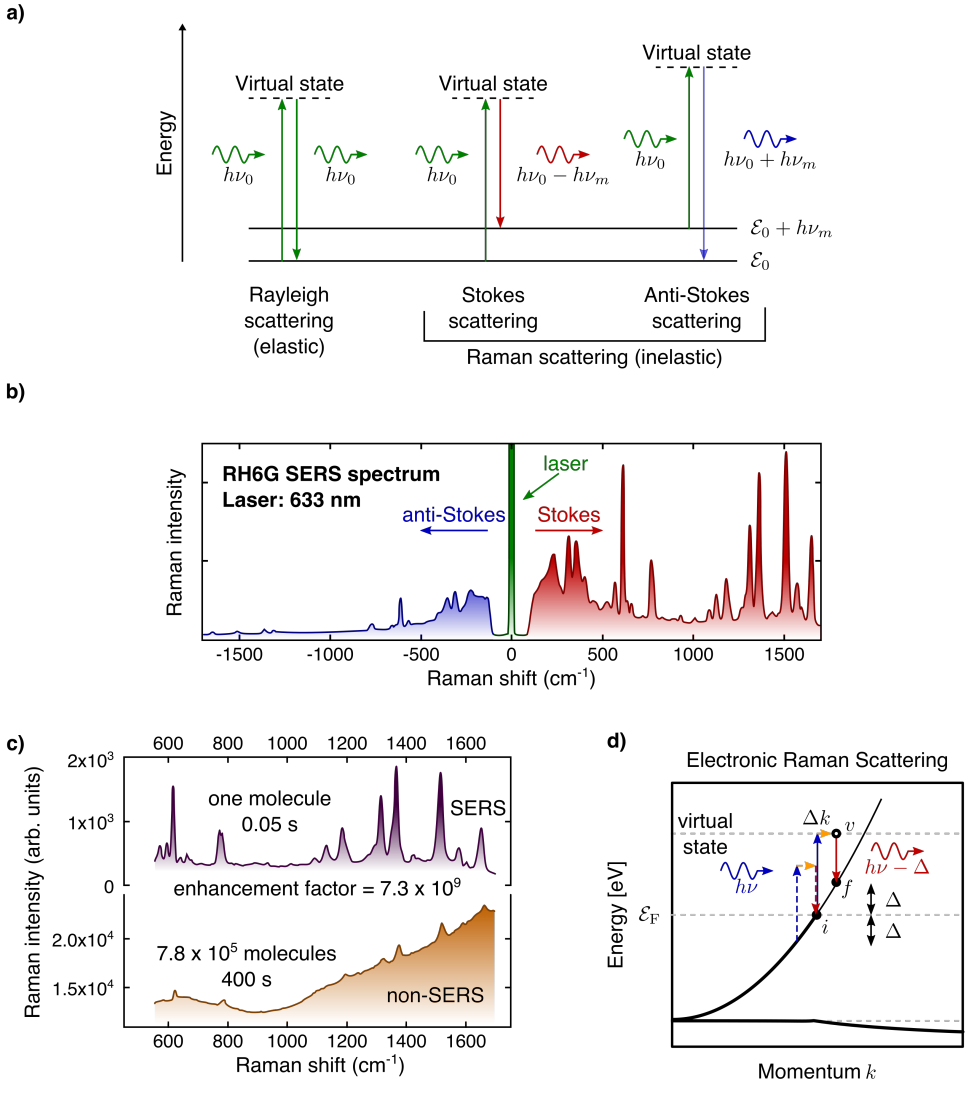

Figure 4: a) Energy-level diagrams in Rayleigh scattering (left), Stokes Raman scattering (center), and anti-Stokes Raman scattering (right), for a molecule with ground state energy with $\mathcal{E}_0$ and excited state with energy $\mathcal{E}_0 + h\nu_m$. b) A typical SERS spectrum (Raman intensity vs Raman shift) at 633 nm laser excitation is shown for rhodamine 6G molecules (RH6G) with several Raman peaks on the Stokes side and their (weaker) anti-Stokes counterparts. Figure adapted from [39]. c) Raman (non-SERS) and SERS spectra at 633 nm laser excitation for RH6G. The vertical intensity axis is in arbitrary units but its is the same for both spectra. Bottom spectrum corresponds to the signal of $\sim 7.8 \times 10^5$ RH6G molecules with 400 s integration time, while top spectrum corresponds to the signal from a single RH6G molecule under the same experimental conditions but with 0.05 s integration time, implying an amplification of the Raman signal by an enhancement factor of $\sim 7.3 \times 10^9$. Figure adapted from [39]. d) Sketch showing the electronic Raman scattering process in metals. Figure adapted from [40].

the enhancing effect of a plasmonic nanoantenna, which improves the performance of Raman scattering from molecules deposited at the near field of antenna resonances. This happens, for instance, when molecules are located in the near field of a nanocavity, which enhances light emission from the molecules, a technique known as Surface Enhanced Raman Scattering (SERS) [41]. Indeed, as the Raman scattering process scales with the 4^{th} power of the local EM field, the plasmonic field can lead to SERS enhancement factors of $\sim 10^{10}$ [see Fig. 4(c)].

The near field in nanocavities can be further enhanced and localized by the presence of atomic protrusions, giving rise to an atomic-scale lightning rod effect and reaching subnanometric light localization in the so-called *picocavities*, which we introduce in Chapter 2. Picocavities can boost the coupling of photons with electronic transitions of single emitters [42] or with vibrations of a molecule in optomechanical interactions [43]. Moreover, the large field gradients around picocavities break the symmetry rules of vibrations in molecules, opening the path to probe forbidden molecular transitions in SERS, appearing as additional sharp peaks in the SERS spectra [43].

Apart from the additional sharp peaks when a picocavity is formed in a nanocavity, there are additional spectral features that are often observed in the SERS spectra. In particular, broad background signal increases occurring on a timescale of ms have been observed in the literature [44–48]. The background signal of SERS spectra has been addressed as inelastic light scattering due to an electronic Raman scattering (ERS) process in the hosting metal, similar to molecular Raman scattering, but for electrons undergoing transitions within the Fermi sea of the metal [see Fig. 4(d)]. We give further details about this processes in Chapter 3.

Another possibility to see at the nanoscale, or to even to resolve atoms, is to produce matter excitations using swift electrons as probes. Since the first prototype in Transmission Electron Microscopy (TEM) was demonstrated by Ernst Ruska and Max Knoll in 1931 [49, 50], TEMs have become one of the most important tools in modern science and have been crucial in many discoveries made in physics, chemistry and biology during the 20th century [51, 52].

Improvements in electronics have allowed the generation of tightly focused, atom-sized electron beams that scan the sample at high rates, obtaining images with atomic resolution. Sub-Ångstrom resolution imaging is possible with the current state-of-the-art aberration-corrected scanning transmission electron microscopes (STEM) [53, 54], which can capture the diverse signals emerging from the interaction of the fast electron with matter (e.g., electromagnetic radiation, secondary and Auger electron emission) correlated with the well-controlled position of the electron beam at the various detectors attached to the microscope. Therefore, STEM represents a versatile technique for spatially-resolved analysis of materials at the atomic scale.

Electron probes transmitted through or near a sample lose a small fraction of their initial energy (and momentum) as a results of the interaction with the sample. The probability to lose such energy is directly related to the excitations produced by the probe in the sample [see Fig. 5(a)]. An spectral analysis of the electron energy loss (EEL) probability serves to identify matter excitations in a broad energy

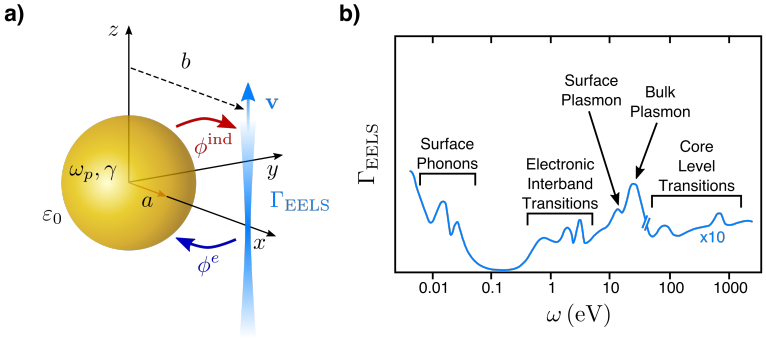

Figure 5: a) Schematics of an electron beam interacting with a sample (a nanoparticle) in aloof geometry, where we show the main terms describing the interaction between the electron beam and the sample. b) Qualitative overview of the major excitations that contribute to an electron energy loss probability, Γ_{EELS}, spectrum over a wide loss energy, ω (eV) range. Plasmons are excited in the range of a few eV. Figure adapted from [60].

range, which makes electron energy loss spectroscopy (EELS) an important analytical technique in STEM. For instance, EELS can be used to detect core losses at high energies (from approximately 50 eV up to keVs) coming from excitations of electrons in inner atomic shells [55, 56], which provide chemical information correlated with atomic-scale imaging [57–59]. On the other hand, at low energies (typically below 50 eV) valence electronic excitations, interband electronic transitions and lattice or molecular vibrations can appear in EEL spectra [see Fig. 5(b)].

Within the framework of classical electrodynamics a fast electron beam can be described as a point-like charge at position $\mathbf{r}_e(t) = \mathbf{r}_0 + \mathbf{v}t$ with $\mathbf{r}_0$ the initial position, $\mathbf{v}$ its velocity and evolution in time t. The field created by the fast traveling electron acting on a nanostructure gives rise to an induced EM field, $[\mathbf{E}^{\text{ind}}(\mathbf{r},t), \mathbf{B}^{\text{ind}}(\mathbf{r},t)]$, that acts back on the probing electron. Within the classical description, these EM fields exert an EM (Lorentz) force $\mathbf{F}(\mathbf{r},t) = -e[\mathbf{E}^{\text{ind}}(\mathbf{r},t) + \mathbf{v} \times \mathbf{B}^{\text{ind}}(\mathbf{r},t)]$ on the probing electron of charge e; which is responsible for the energy loss of this probing electron. The energy loss can be evaluated by integrating the the force along the electron trajectory [61,62]. For highly energetic probing electrons, it is assumed that the recoil due to the perpendicular force is negligible [63], and therefore the electron energy loss W can be expressed as:

$$W = e \int dt\, \mathbf{v} \cdot \mathbf{E}^{\text{ind}}[\mathbf{r}_e(t), t] \tag{9}$$

where $\mathbf{r}_e(t)$ is the position of the probing electron.

Within the quasistatic approximation, which we use in Chapters 4 and 5 of this thesis dedicated to EELS, the electron energy loss W can be expressed as (atomic

units are used $e = \hbar = m_e = 1$):

$$W = \frac{1}{2\pi}\int_{-\infty}^{\infty} d\omega \int_{-\infty}^{\infty} dz' \frac{\partial \phi(\mathbf{r},\omega)}{\partial z}\bigg|_{z=z'} e^{-i\omega z'/v}. \tag{10}$$

where the potential in frequency domain ω, $\phi(\mathbf{r},\omega)$, satisfies $\mathbf{E}^{\mathrm{ind}}(\mathbf{r},\omega) = -\nabla\phi(\mathbf{r},\omega)$. Integrating this expression by parts and taking into account that the induced potential created by a nanoparticle vanishes at infinity, $\phi(x,y,\pm\infty) \to 0$, and the condition $\rho(\mathbf{r},\omega) = \rho^*(\mathbf{r},-\omega)$, and therefore, $\phi(\mathbf{r},\omega) = \phi^*(\mathbf{r},-\omega)$, we finally obtain

$$W = \frac{1}{\pi v}\int_{0}^{\infty} d\omega\, \omega \int_{-\infty}^{\infty} dz' \mathrm{Im}\Big\{ -\phi(\mathbf{r}',\omega) e^{-i\omega z'/v}\Big\}. \tag{11}$$

Electron energy loss probability

The probability for an electron to lose energy $\hbar\omega$, $\Gamma_{\mathrm{EELS}}(\omega)$, the so-called electron energy loss probability, is defined according to [61]:

$$W = \int_{0}^{\infty} d\omega\, \omega\, \Gamma_{\mathrm{EELS}}(\omega), \tag{12}$$

Thus, the electron energy loss probability is given by,

$$\Gamma_{\mathrm{EELS}}(\omega) = \frac{1}{\pi v}\int_{-\infty}^{\infty} dz' \mathrm{Im}\Big\{ -\phi(\mathbf{r}',\omega) e^{-i\omega z'/v}\Big\}. \tag{13}$$

The evanescent field created by the fast electrons can efficiently couple to plasmons in the energy range of a few eV. Interestingly, this evanescent nature of the broadband electromagnetic field associated to the fast probing electrons in STEM-EELS brings the possibility of exciting "dark" plasmons that are not possible to access with conventional light-spectroscopy techniques. Characterization of the near field, which is naturally accessible by the fast electron probes [64], is often crucial for understanding the behavior and functionality of plasmonic nanostructures.

The use of EELS to investigate plasmonic excitations and nanoplasmonic structures is widespread nowadays. It is worth mentioning that the identification of bulk plasmons [65, 66] and the discovery of SPPs in the 1950s and 1960s [61] are directly linked to EELS experiments with broad electron beams interacting with metallic foils and interfaces [67, 68]. Studies at that time were typically performed with a broad (unfocused) beam and devoted to momentum-resolved EELS, as such measurements can be related to the dispersion of the excited modes.

In the last two decades STEM-EELS has witnessed several technical improvements [69–71] that have enabled sub-nanometer resolution [53, 72], and sub-eV energy sensitivity [73]. Such progress has opened the possibility for characterization of novel materials and nanostructures [54, 74], vibrational spectroscopy with nanometer resolution of phonons [56, 75–78] or characterization of biomaterials with low energy

beams and radiation damage reduction [56, 79, 80]. The aforementioned improvements have allowed to perform single-NP EELS experiments with NP sizes below 10 nm [81–86] with sub-Ångstrom resolution.

In recent years the size-dependent shifts observed in the resonance energy of the LSPs in such small metallic NPs have received considerable attention in the literature [82–84, 87–89]. Moreover, the increased resolution obtained for the experimental setups has motivated the development of a wide variety of theoretical models to account for specific quantum effects in the properties of LSP resonances, such as electron confinement [90], electron spill-out at the interfaces [31, 91–93], non-local effects [94, 95] in the dielectric response, modification of local environments [86], or activation of quantum tunneling across subnanometer interparticle gaps [33, 87, 96]. Nevertheless, the faceted shape of such small NPs and the influence of atomic-scale features on EEL spectra, has been usually neglected by considering the NPs to have spherical shape.

Apart from the excitation of LSPs confined to the surface of metallic NPs, electron beams can excite longitudinal pressure waves of the electron density within their volume, i.e., confined bulk plasmons (CBPs) [94]. CBPs were first observed experimentally in thin-films in 1971 in Ag [97] and in K [98] using optical spectroscopy. Moreover, they have been also observed more recently in Mg films down to three atomic monolayers using core-level photoemission [99]. Within EELS, CBPs have been observed experimentally for a wide range of structures and materials, including Ge nanorods [100], Bi nanowires [101], Bi NPs [90, 102], and Al nanodisks [85]. Theoretically, CBPs arise naturally within hydrodynamic models of the response of the electron density at the target sample, which accounts for the dynamical screening of the electrons in the target sample, as opposed to the local dielectric response approximation. Nanostructures with at least one finite dimension can confine the volume oscillations of the charge density in such dimension producing standing waves. For instance, theoretical studies for cylinders [103–105] show excitation of CBPs for penetrating probing electron trajectories. In this thesis, we explore the interaction between noanometer-scale matter and electromagnetic sources, such as light and electron beams, with a special focus on the influence of atomic-scale features present in small metallic nanoparticles and nanocavities.

In Chapter 1 we introduce the numerical methods used for the description of the optical response of plasmonic nanostructures and the excitations: (i) the Boundary Element Method (BEM), a local response method that assumes the media to be continuous and homogeneous, as well as bounded by sharp interfaces, (ii) a modified Discrete Dipole Approximation (DDA) in which the atoms composing the nanostructures are described as dipoles, and (iii) *ab initio* atomistic Time-Dependent Density Functional Theory (TDDFT) which includes the atomistic structure and quantum effects in the response of the plasmonic nanostructure.

Using the aforementioned methods, in Chapter 2 we explore the optical response and near-field localization at Na nanometer-size NPs (clusters of 380 atoms) that present atomistic features such as vertices, edges and facets. The presence of such atomistic features allows for localizing and confining the near field down to subnano-

metric dimensions [106], well below the underlying plasmonic background, pushing the spatial features of the induced near fields below the limit imposed by nanocavities, and thus reaching the realm of *picocavities*. By adopting a sharp boundary interface which resembles the electronic density profile of the corresponding atomistic distribution within a plasmonic structure, we show that classical approaches can faithfully reproduce the properties of the near field induced at the surface of these NPs, including the subnanometric confinement of the field. We identify the extra localization of the field as a non-resonant atomic-scale lightning rod effect that enhances the plasmon-driven near field, and propose a simplified local model to address it. Moreover, we extend this concept to cover the influence of picocavities in nanogaps, obtaining a good agreement between quantum and classical models of the response in these extreme situations. The quantum description of these optical picocavities at the full atomistic level reveals the importance of atomic-scale features, although such a detailed description is limited by computational demands, which make them unfeasible in large nanostructures. The simplified local classical approach proposed in this thesis allows for addressing the presence of such picocavities in larger nanostructures, thus allowing standard methods of electrodynamics to tackle the optical response in this challenging regime [107].

In Chapter 3 we discuss the emission of transient broadband spectral features in SERS spectra obtained for NPoM structures hosting molecules at the nanogap. We term these events of inelastic light scattering "flares", and provide a conceptual framework to effectively address their optical properties. We analyze flares observed in experimental SERS spectra obtained within the group of Prof. Jeremy J. Baumberg at the University of Cambridge. We propose a model of flares based on the dynamic restructuring of atoms at transient defects, such as twin planes and grain boundaries, which leads to localized changes of the plasma frequency of the metal, inducing a stronger electric field within the metallic NP and thus an increase in the background ERS signal.

As in optical spectroscopy, discussed in Chapter 2, *ab initio* atomistic TDDFT also provides an appropriate framework to consider quantum effects in a complete manner including the role of the atomistic structure in EELS. In Chapter 4 we study the influence of atomic-scale features on the EEL spectra in small Na nanoparticles using TDDFT and compare the results with those obtained within classical descriptions which reproduce the atomic faceting of the NP by introducing sharp surface boundaries, as a way to address the influence of subnanometric features in EELS. We prove that these atomistic features reveal their footprints in EEL spectra, showing great sensitivity to the relative orientation of the NP with respect to the electron trajectory and departing from the spectra of a typical spherical nanoparticle. Moreover, we identify the excitation of LSPs and CBPs in the EEL spectra, the latter only occurring in the case of penetrating electron beam trajectories, and study their dependence on the impact parameter of the incident electron beam.

The footprints of the CBPs observed in the TDDFT spectra presented in Chapter 4 are further explored in Chapter 5, using a linear Hydrodynamic Model of the response that takes into account non-locality. We obtain an impact parameter depen-

dent semi-analytical expression for the EEL probability of a spherical NP, including penetrating trajectories. Such model allows for a clearer analysis of the dependence of CBPs on parameters such as the NP size, electron beam velocity and impact parameter, which we exploit to analyze the EEL spectra in spherical Na NPs. We show that the energy shifts in the main peaks corresponding to bulk plasmons observed experimentally for Al disks [85] are ruled by similar symmetry arguments to those applied to LSP modes.

The contribution of quantum and classical models to the optical response in plasmonic nanoantennas and nanocavities showing atomic-scale features is proven to be an adequate strategy to unveil novel optical fingerprints in such structures. This thesis thus offers an initial step to address picophotonics in the framework of optical and electron spectroscopies.

1 Numerical Methods

Classical electrodynamics describes the optical response of matter using the macroscopic formulation of Maxwell's equations and corresponding boundary conditions at the interfaces of an inhomogeneous system. It is commonly assumed that the materials' response to external electromagnetic excitation sources is local in nature but at the nanoscale this description shows limitations. Quantum effects emerge at the nanometer scale as the atomistic structure and wave nature of the constituent electrons play a major role in the response.

In this chapter we present the numerical methods used to obtain the results presented in this thesis. First, in Sec. 1.1, we provide the main ingredients of the Boundary Element Method (BEM), a local response method that assumes the media to be continuous and homogeneous, as well as bounded by sharp interfaces. These surfaces are discretized and boundary conditions are solved numerically to obtain the response of the nanostructures to external electromagnetic stimuli, including light and electron beams. Layered structures require a special treatment within BEM, which is also described in this chapter. This approach is used to describe nanoparticles on top of surfaces as considered in Chapter 3. BEM is the main tool in this thesis and was used to obtain the results presented in Chapters 2 to 4.

Furthermore, in Sec. 1.2, we summarize the Discrete-Dipole Approximation (DDA), a local response method in which matter is considered to be composed of polarizable

units which respond as discrete dipoles to an external electromagnetic field. This method was used to obtain some of the results presented in Chapter 2.

Last, in Sec. 1.3, we briefly introduce the Time-Dependent Density Functional Theory (TDDFT) used to calculate the plasmonic response of Na clusters to light and electron beam excitations, as used in Chapters 3 and 5. This theory allows us to compare predictions of modified local and non-local response models with those of a quantum model which accounts for many-body dynamical screening and general quantum effects.

Analytical methods developed in this thesis to account for nonlocal effects in the plasmonic response of spherical nanoparticles are treated separately and included in Chapter 5.

1.1 Boundary Element Method (BEM)

The classical electromagnetic interaction of external sources with matter can be described by Maxwell's equations, and in the presence of arbitrarily shaped abrupt dielectric interfaces, their solution can be expressed in terms of surface integrals that involve surface charges and currents acting as sources of the induced electromagnetic field. The boundary element method (BEM) [108] introduced in this section is based on finding self-consistently those interface charge and current distributions for a given external field. We use the Matlab implementation of this method to simulate the plasmonic response of metallic nanoparticles (MNP), using a boundary element method (BEM) approach (MNPBEM) developed by Hohenester *et al.* [109]. Macroscopic Maxwell's equations in frequency-domain can be expressed as[2],

$$\nabla \cdot \mathbf{D} = 4\pi\varrho, \qquad (1.1)$$

$$\nabla \times \mathbf{H} + ik\mathbf{D} = \frac{4\pi}{c}\mathbf{j}, \qquad (1.2)$$

$$\nabla \cdot \mathbf{B} = 0, \qquad (1.3)$$

$$\nabla \times \mathbf{E} - ik\mathbf{B} = 0, \qquad (1.4)$$

where $k = \omega/c$, ω being the angular frequency and c the speed of light, $\mathbf{D} = \varepsilon\mathbf{E}$ is the electric displacement field, $\mathbf{B} = \mu\mathbf{H}$ is the magnetic induction, ϱ is the charge density and $\mathbf{j}$ is the electric current density. The dielectric function $\varepsilon(\mathbf{r}, \omega)$ and the magnetic permeability $\mu(\mathbf{r}, \omega)$ might depend on space $\mathbf{r}$ and frequency ω in the local response approximation. The last two equations [Eqs. (1.3) and (1.4)] allow us to write the electric and magnetic fields $\mathbf{E}$ and $\mathbf{H}$ in terms of scalar ϕ and vector $\mathbf{A}$ potentials as,

[2] We use Gaussian units.

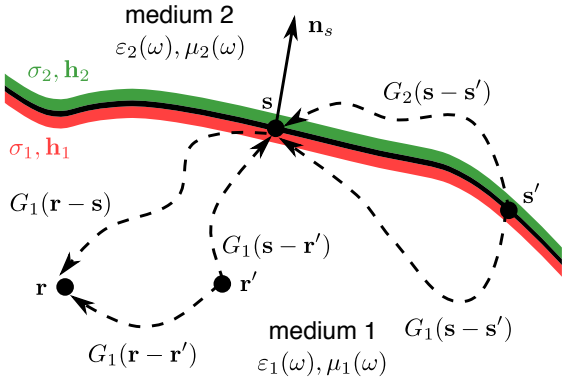

Figure 1.1: Schematic representation of the elements involved in the boundary element method (BEM). The interface (black solid line) separates medium 1 from medium 2. We chose the interface normal $\mathbf{n}_s$ (black solid arrow) at point $\mathbf{s}$ to be directed towards medium 2. The interaction between two points in a given medium j is described by the Green's function G_j (dashed arrows), and the field at position $\mathbf{r}$ is expressed by the sum of the external sources (located at $\mathbf{r}'$) plus a contribution from the boundary charges and currents, $\sigma_j(\mathbf{s})$ and $\mathbf{h}_j(\mathbf{s})$, respectively, that account for the influence of any external and induced sources beyond the boundary surface.

$$\mathbf{E} = ik\mathbf{A} - \nabla\phi, \qquad (1.5) \qquad\qquad \mathbf{H} = \frac{1}{\mu}\nabla \times \mathbf{A}. \qquad (1.6)$$

Adopting the Lorenz gauge,

$$\nabla \cdot \mathbf{A} = ik\varepsilon\mu\phi, \qquad (1.7)$$

the first two equations [Eqs. (1.1) and (1.2)] can be recast as two decoupled wave equations for ϕ and $\mathbf{A}$,

$$(\nabla^2 + k^2\varepsilon\mu)\phi = -4\pi\left(\frac{\varrho}{\varepsilon} + \sigma_s\right), \qquad (1.8)$$

$$(\nabla^2 + k^2\varepsilon\mu)\mathbf{A} = -\frac{4\pi}{c}(\mu\mathbf{j} + \mathbf{m}), \qquad (1.9)$$

where,

$$\sigma_s = \frac{1}{4\pi}\mathbf{D}\cdot\nabla\frac{1}{\varepsilon}, \qquad (1.10)$$

$$\mathbf{m} = -\frac{1}{4\pi}[i\omega\phi\nabla(\varepsilon\mu) + c\,\mathbf{H}\times\nabla\mu], \qquad (1.11)$$

are the charge density and current density respectively. These expressions are valid for inhomogeneous media where dielectric functions $\varepsilon(\mathbf{r},\omega)$ and magnetic permeabilities $\mu(\mathbf{r},\omega)$ change in space. For abrupt interfaces separating two homogeneous media

with frequency dependent response functions $[\varepsilon_1(\omega),\, \mu_1(\omega)]$ and $[\varepsilon_2(\omega),\, \mu_2(\omega)]$, the charge densities σ_s and current densities $\mathbf{m}$ only contribute at the interface, and they can be understood as extra charges and currents localized at the surface, which originate from the discontinuity of ε and μ at the boundary. While $\mathbf{m}$ cannot be considered as a physical current in a general basis (it is not parallel to the interface, and in particular for nonmagnetic materials it is perpendicular to the interface[3]), σ_s is related to the surface polarization charges. Instead of using σ_s and $\mathbf{m}$, the interfaces are separated into two parts (inside and outside the boundary, defined by the normal vector $\mathbf{n}_s$) and effective surface charges σ_j and currents $\mathbf{h}_j$ are introduced in order to satisfy self-consistently the appropriate boundary conditions at the interface (see Fig. 1.1).

The general solution of Eqs. (1.8) and (1.9) that vanishes at infinity for $\mathbf{r}$ inside medium j is written as,

$$\phi_j(\mathbf{r}) = \frac{1}{\varepsilon_j(\omega)} \int d\mathbf{r}' G_j(|\mathbf{r}-\mathbf{r}'|)\varrho(\mathbf{r}') + \int_{S_j} d\mathbf{s}\, G_j(|\mathbf{r}-\mathbf{s}|)\sigma_j(\mathbf{s}) \tag{1.12}$$

$$\mathbf{A}_j(\mathbf{r}) = \frac{\mu_j(\omega)}{c} \int d\mathbf{r}' G_j(|\mathbf{r}-\mathbf{r}'|)\mathbf{j}(\mathbf{r}') + \int_{S_j} d\mathbf{s}\, G_j(|\mathbf{r}-\mathbf{s}|)\mathbf{h}_j(\mathbf{s}). \tag{1.13}$$

Here S_j refers to the boundary of media $j = 1, 2$. Moreover,

$$G_j(|\mathbf{r}-\mathbf{r}'|) = \frac{e^{ik_j|\mathbf{r}-\mathbf{r}'|}}{|\mathbf{r}-\mathbf{r}'|} \tag{1.14}$$

is the Green's function that satisfies the wave equation,

$$(\nabla^2 + k_j^2) G_j(|\mathbf{r}-\mathbf{r}'|) = -4\pi\delta(|\mathbf{r}-\mathbf{r}'|) \tag{1.15}$$

in medium j, and $k_j = k\sqrt{\varepsilon_j \mu_j}$, with $\mathrm{Im}\{k_j\} > 0$. The first integrals on the right hand side of Eqs. (1.12) and (1.13) satisfy Eqs. (1.8) and (1.9) outside the interface where $\sigma_s = 0$ and $\mathbf{m} = 0$. The additional integrals are relevant at the interface, as they include the effects of σ_s and $\mathbf{m}$ and compensate the discontinuity of the Green's function at the interface. Thus Eqs. (1.12) and (1.13) are solutions of Eqs. (1.8) and (1.9) if the boundary charges and currents σ_j and $\mathbf{h}_j$ are chosen to satisfy the customary boundary conditions. Moreover, there is some freedom when choosing σ_j and $\mathbf{h}_j$, i.e., one can choose them in such a way that the field induced in medium j is just produced by charges lying in the side of the boundary S_j facing medium j (which is in general the implementation used in the MNPBEM Toolbox [109–111] used throughout this thesis), or by the whole set of interface charges at both sides.

[3] For an abrupt interface where the interface normal $\mathbf{n}_s$ points towards medium 2 (see Fig. 1.1, we have $4\pi\sigma_s = \left(\frac{1}{\varepsilon_2} - \frac{1}{\varepsilon_1}\right)\mathbf{n}_s \cdot \mathbf{D}\,\delta_s$, and $4\pi\mathbf{m} = [i\omega(\varepsilon_1\mu_1 - \varepsilon_2\mu_2)\phi\mathbf{n}_s + (\mu_1 - \mu_2)c\mathbf{H} \times \mathbf{n}_s]\delta_s$, where δ_s is a surface Dirac delta δ function placed at the interface. It is straightforward to see that in general, $\mathbf{m}$ is not parallel to the surface, and in particular for nonmagnetic materials it is perpendicular to the surface.

The numerical implementation to calculate the charge densities σ_j and current densities $\mathbf{h}_j$ which meets the boundary conditions of Maxwell's equations relies on the discretization of the interface integrals into contributions evaluated at a finite number (N) of discrete points at the interface. The external sources and the charge and current distributions (σ_j, $\mathbf{h}_j$) are assumed to have very small variations within contiguous discretization elements, so that they are considered constant within each finite element. This reduces the problem to a system of equations where the operators can be approximated by matrices of dimension $N \times N$. In particular, the surface integrals become sums of boundary elements, $\Delta S_{l'}$, as:

$$\int_{S_j} G_j(\mathbf{s}_l - \mathbf{s}')\sigma_j(\mathbf{s}')d\mathbf{s}' = \sum_{l'} G_{j,ll'}\sigma_{j,l'}\Delta S_{l'} \tag{1.16}$$

where indices l and l' refer to the lth and l'th discrete elements, respectively.

Matrix notation will be adopted from now on, which implies a summation over the surface elements for matrix-vector products such as $G_{ll'}\sigma_{l'}$. The potentials inside and outside the boundaries are therefore given by,

$$\phi_1 = G_{11}\sigma_1 + G_{12}\sigma_2 + \phi_1^{\text{ext}} \tag{1.17}$$

$$\phi_2 = G_{22}\sigma_2 + G_{21}\sigma_1 + \phi_2^{\text{ext}} \tag{1.18}$$

$$\mathbf{A}_1 = G_{11}\mathbf{h}_1 + G_{12}\mathbf{h}_2 + \mathbf{A}_1^{\text{ext}} \tag{1.19}$$

$$\mathbf{A}_2 = G_{22}\mathbf{h}_2 + G_{21}\mathbf{h}_1 + \mathbf{A}_2^{\text{ext}}, \tag{1.20}$$

where ϕ_j^{ext} and $\mathbf{A}_j^{\text{ext}}$ are the potentials of the external excitation. Here G_{11} connects elements of the inner boundary, G_{22} connects elements of the outer boundary, and G_{12} and G_{21} connect elements from the inner to the outer boundary and vice versa. In Figure 1.2(a) the case of a sphere formed out of two hemispheres of distinct materials, labelled II and III surrounded by medium I, is shown to illustrate the connectivity of the Green's functions. Surfaces S_{A}, S_{B} and S_{C} define the interfaces separating the media, with normal vectors $\mathbf{n}_{\text{A}}$, $\mathbf{n}_{\text{B}}$ and $\mathbf{n}_{\text{C}}$ defining the inside and outside of each interface, respectively. We also show the scheme representing the Green's functions as matrices in Figure 1.2(b). Each matrix can be subdivided into blocks that connect the elements of different interfaces, e.g., the only nonzero elements in G_{21} are those connecting the inner elements of interface S_{B} with the outer elements of interface S_{C}, i.e., G_{21}^{CB}.

The boundary conditions of the electromagnetic fields, i.e., the continuity of the tangential component of the electric field and the normal component of the magnetic induction, along with the Lorenz gauge condition given in Eq. (1.7), imply the continuity of ϕ and $\mathbf{A}$. Thus, the scalar potential and vector potential need to have the same value at each side of the interface separating medium 1 and medium 2, yielding,

$$G_1\sigma_1 - G_2\sigma_2 = \phi_2^{\text{ext}} - \phi_1^{\text{ext}} = \phi^{\text{ext}} \tag{1.21}$$

$$G_1\mathbf{h}_1 - G_2\mathbf{h}_2 = \mathbf{A}_2^{\text{ext}} - \mathbf{A}_1^{\text{ext}} = \mathbf{A}^{\text{ext}}, \tag{1.22}$$

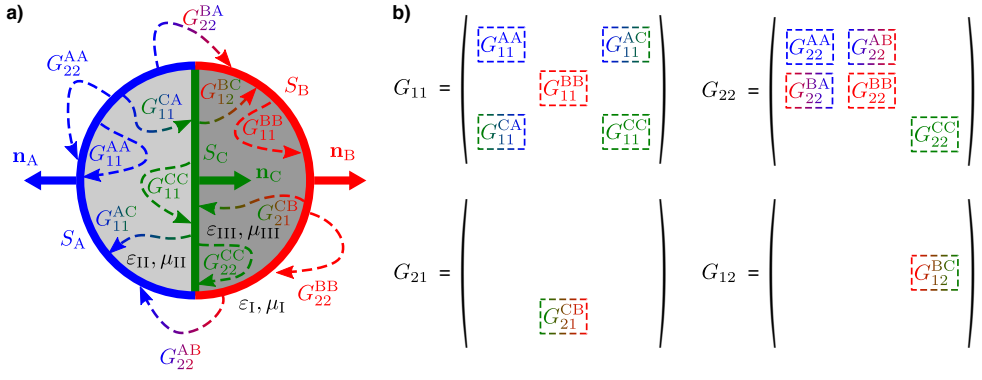

Figure 1.2: (a) Sketch of a sphere surrounded by a medium with electric permitivitty ε_I and magnetic permeability $\mu_I$and formed out of two hemispheres of materials with optical properties (ε_{II}, μ_{II}, and ε_{III}, μ_{III}). The left hemisphere is bounded by surfaces S_A and S_C, and the right hemisphere by surfaces S_B and S_C. Solid arrows represent the outward normal vectors of each surface ($\mathbf{n}_A$, $\mathbf{n}_B$, and $\mathbf{n}_C$), and the dashed arrows show the connectivity of the Green's functions. (b) Sketch of the matrices defining the Green's functions G_{11}, G_{22}, G_{21} and G_{12}, blank spaces mean regions filled with Green's functions that equal zero (as they do not connect boundary elements within the same medium).

where, we have used,

$$G_1 = G_{11} - G_{21}; \qquad \phi^{\text{ext}} = \phi_2^{\text{ext}} - \phi_1^{\text{ext}} \tag{1.23}$$

$$G_2 = G_{22} - G_{12}; \qquad \mathbf{A}^{\text{ext}} = \mathbf{A}_2^{\text{ext}} - \mathbf{A}_1^{\text{ext}} \tag{1.24}$$

From here on we will assume that the media are nonmagnetic, i.e., $\mu_j = 1$. Indeed, for this case it holds that both the tangential derivatives of all components of the vector potential and the normal derivative of the tangential vector potential must be continuous (enforced by the continuity of the tangential component of the magnetic field and the vector potential). Using the continuity relationships and the Lorenz condition given by Eq. (1.7), one obtains that $(\mathbf{n}_s \cdot \nabla)\mathbf{A} - i\mathbf{n}_s k\varepsilon\mu\phi$ is also continuous. Thus, the following equation yields[4]:

$$H_1\mathbf{h}_1 - H_2\mathbf{h}_2 - ik\mathbf{n}_s(G_1\varepsilon_1\sigma_1 - G_2\varepsilon_2\sigma_2) = \boldsymbol{\alpha}, \tag{1.25}$$

where

$$\boldsymbol{\alpha} = (\mathbf{n}_s \cdot \nabla_s)\mathbf{A}^{\text{ext}} + ik\mathbf{n}_s(\varepsilon_1\phi_1^{\text{ext}} - \varepsilon_2\phi_2^{\text{ext}}). \tag{1.26}$$

and $H_{1,2} = F_{1,2} \pm 2\pi$ is the normal derivative of the Green's function G_j (not to be confused with the magnetic field), which must be taken from both sides of the

[4]Following Ref. [108] here we use $\varepsilon_2 G_2 = G_2\varepsilon_2$ which later results in Eq. (1.38) for the generalization to an arbitrary number of media. This exchange is possible because G_2 connects points within the same medium. This will not hold when introducing infinite layers in Sec. 1.1.2, as the reflected Green's functions can connect points in different layers and different media [111].

interface, and F_j is the surface derivative of the Green's function, given by,

$$F_j = (\mathbf{n}_s \cdot \nabla_{\mathbf{s}}) G_j(\mathbf{s}-\mathbf{s}') = \frac{\mathbf{n}_s \cdot (\mathbf{s}-\mathbf{s}')}{|\mathbf{s}-\mathbf{s}'|^3}(ik_j|\mathbf{s}-\mathbf{s}'|-1)e^{ik_j|\mathbf{s}-\mathbf{s}'|} \tag{1.27}$$

The singular contribution originating from the limit $\mathbf{r} \to \mathbf{s}$ gives rise to the 2π term and has to be dealt with care [108, 112].

On the other hand, the continuity of the normal component of the electric displacement vector $\varepsilon\, \mathbf{n}_s \cdot (ik\mathbf{A} - \nabla\phi)$, leads to,

$$H_1\varepsilon_1\sigma_1 - H_2\varepsilon_2\sigma_2 - ik\mathbf{n}_s \cdot (G_1\varepsilon_1\mathbf{h}_1 - G_2\varepsilon_2\mathbf{h}_2) = D^{\text{ext}}, \tag{1.28}$$

where

$$D^{\text{ext}} = \mathbf{n}_s \cdot [\varepsilon_1(ik\mathbf{A}_1^{\text{ext}} - \nabla_s\phi_1^{\text{ext}}) - \varepsilon_2(ik\mathbf{A}_2^{\text{ext}} - \nabla_s\phi_2^{\text{ext}})]. \tag{1.29}$$

Considering the vectorial character of some of the quantities in Eqs. (1.21), (1.22), (1.25) and (1.28), these equations constitute a system of eight linear surface integral equations with eight unknown complex functions of the interface coordinates (σ_j and $\mathbf{h}_j$ for $j = 1, 2$).

After some algebra [108, 112], the solutions for the charge and current distributions, can be obtained:

$$\sigma_2 = G_2^{-1}\Sigma^{-1}\Big[D^{\text{ext}\prime} + ik\mathbf{n}_s(L_1 - L_2)\Delta^{-1}\boldsymbol{\alpha}'\Big], \tag{1.30}$$

$$\sigma_1 = G_1^{-1}(G_2\sigma_2 + \phi^{\text{ext}}), \tag{1.31}$$

$$\mathbf{h}_2 = G_2^{-1}\Delta^{-1}\Big[ik\mathbf{n}_s(L_1 - L_2)G_2\sigma_2 + \boldsymbol{\alpha}'\Big], \tag{1.32}$$

$$\mathbf{h}_1 = G_1^{-1}(G_2\mathbf{h}_2 + \mathbf{A}^{\text{ext}}), \tag{1.33}$$

where,

$$D^{\text{ext}\prime} = D^{\text{ext}} - \Sigma^{-1}L_1\phi^{\text{ext}} + ik\mathbf{n}_s \cdot L_1\mathbf{A}^{\text{ext}}, \tag{1.34}$$

$$\boldsymbol{\alpha}' = \boldsymbol{\alpha} - \Sigma_1 A^{\text{ext}} + ik\mathbf{n}_s L_1\phi^{\text{ext}}, \tag{1.35}$$

$$\Sigma = \Sigma_1 L_1 - \Sigma_2 L_2 + k^2\mathbf{n}_s \cdot (L_1 - L_2)\Delta^{-1}\mathbf{n}_s(L_1 - L_2), \tag{1.36}$$

$$\Delta = \Sigma_1 - \Sigma_2, \tag{1.37}$$

$$L_{1,2} = G_{1,2}\varepsilon_{1,2}G_{1,2}^{-1}. \tag{1.38}$$

The discretized problem of $8N$ linear equations requires a computation time proportional to $(8N)^3$ if direct inversion is to be used to find the solution. Nevertheless, by separately manipulating the $N \times N$ matrices such as G_j, the calculation time can be reduced to times proportional to $6N^3$ [108].

Quasistatic approximation

The electromagnetic interaction between two points can be considered instantaneous if their distance is much smaller than the wavelength of the interaction λ. This holds

for small particles of size $R \ll \lambda$, where one can assume $k \to 0$, reducing Helmholtz equation [Eq. (1.8)] to Poisson's equation,

$$\nabla^2 \phi(\mathbf{r}) = -\frac{4\pi \varrho(\mathbf{r})}{\varepsilon}. \tag{1.39}$$

This equation can be solved with the quasistatic Green's function that describes the Coulomb interaction,

$$G(\mathbf{r} - \mathbf{r}') = \frac{1}{|\mathbf{r} - \mathbf{r}'|} \equiv G(\mathbf{r}, \mathbf{r}') \tag{1.40}$$

and is the solution of the equation,

$$\nabla^2 G(\mathbf{r} - \mathbf{r}') = -4\pi \delta(\mathbf{r} - \mathbf{r}'), \tag{1.41}$$

in an unbounded, homogeneous medium. For inhomogenous dielectric environments, with sharp boundaries S_j separating regions V_j of homogeneous dielectric medium inside a given region, the solution takes the form

$$\phi(\mathbf{r}) = \int_{\partial S_j} G(\mathbf{r}, \mathbf{s}') \sigma(\mathbf{s}') d\mathbf{s}' + \phi^{\text{ext}}(\mathbf{r}), \tag{1.42}$$

where $\phi^{\text{ext}}(\mathbf{r})$ is the scalar potential of the external excitation source and $\sigma(\mathbf{s})$ is a surface charge distribution located at the boundaries S_j. In analogy to the retarded case, the solution is constructed in such a way that Poisson's equation is automatically satisfied, and the surface charge distribution $\sigma(\mathbf{s})$ has to be chosen such that it satisfies the boundary conditions of the electromagnetic field at the boundaries. The continuity of the tangential electric field at the boundary is satisfied when the potential is continuous along the boundary, which is fulfilled if $\sigma(\mathbf{s})$ is the same at both inner and outer sides of the boundary. On the other hand, the continuity of the normal component (with respect to the boundary) of the electric displacement implies the boundary integral equation

$$\lim_{\mathbf{r} \to \mathbf{s}} \mathbf{n}_s \cdot \nabla \phi(\mathbf{r}) = \lim_{\mathbf{r} \to \mathbf{s}} \frac{\partial \phi(\mathbf{r})}{\partial n} = \lim_{\mathbf{r} \to \mathbf{s}} \int_{S_j} \frac{\partial G(\mathbf{r}, \mathbf{s}')}{\partial n} \sigma(\mathbf{s}') d\mathbf{s}' + \frac{\partial \phi^{\text{ext}}(\mathbf{r})}{\partial n}. \tag{1.43}$$

Special caution has to be taken to deal with the integral on the RHS for $r \to s$. By considering a coordinate system with normal vector $\mathbf{n}_s$ pointing in the z direction, i.e., $\mathbf{n}_s = \hat{\mathbf{z}}$, we can write, $\mathbf{r} = (0, 0, z)$ and $\mathbf{s} = \rho(\cos\varphi, \sin\varphi, 0)$ in polar coordinates. By assuming the charge distribution $\sigma(\mathbf{s})$ constant in a small circle of radius R, the boundary integral becomes,

$$\lim_{z \to \pm 0} \mathbf{n}_s \cdot \int \frac{\mathbf{r} - \mathbf{s}'}{|\mathbf{r} - \mathbf{s}'|^3} d\mathbf{s}' \to \lim_{z \to \pm 0} 2\pi z \int_0^R \frac{\rho \, d\rho}{(\rho^2 + z^2)^{3/2}} = \pm 2\pi \tag{1.44}$$

The sign depends on whether the direction of approximation is from the inside or outside the boundary (i.e. positive for the inside case, negative for the outside case). We finally obtain,

$$\lim_{\mathbf{r}\to\mathbf{s}} \mathbf{n}_s \cdot \nabla\phi(\mathbf{r}) = \frac{\partial\phi(\mathbf{r})}{\partial n} = \int_{S_j} F(\mathbf{s},\mathbf{s}')\sigma(\mathbf{s}')ds' \pm 2\pi\sigma(\mathbf{s}) + \frac{\phi^{\text{ext}}(\mathbf{s})}{\partial n} \tag{1.45}$$

where,

$$F(\mathbf{s},\mathbf{s}') = \frac{\partial G(\mathbf{s},\mathbf{s}')}{\partial n}. \tag{1.46}$$

Now, we discretize the boundary into small surface elements and assume that the charges are located at the centroids of each ith surface element. Then, Eq. (1.45) becomes,

$$\left(\frac{\partial\phi}{\partial n}\right)_i = \sum_j F_{ij}\sigma_j \pm 2\pi\sigma_i + \left(\frac{\partial\phi^{\text{ext}}}{\partial n}\right)_i, \tag{1.47}$$

which can be written in compact matrix notation as:

$$\frac{\partial\phi}{\partial n} = \boldsymbol{F}\sigma \pm 2\pi\sigma + \frac{\partial\phi^{\text{ext}}}{\partial n}. \tag{1.48}$$

The continuity of the normal component of the electric displacement field sets:

$$\varepsilon_2\left(\boldsymbol{F}\sigma + 2\pi\sigma + \frac{\partial\phi^{\text{ext}}}{\partial n}\right) = \varepsilon_1\left(\boldsymbol{F}\sigma - 2\pi\sigma + \frac{\partial\phi^{\text{ext}}}{\partial n}\right). \tag{1.49}$$

From this expression we obtain for the surface charge distribution:

$$\sigma = -(\Lambda + \boldsymbol{F})^{-1}\frac{\partial\phi^{\text{ext}}}{\partial n}. \tag{1.50}$$

where,

$$\Lambda = 2\pi\frac{\varepsilon_2 + \varepsilon_1}{\varepsilon_2 - \varepsilon_1}\mathbb{1}. \tag{1.51}$$

This implies that the material parameters (included in Λ) and geometrical properties (included in $\boldsymbol{F}$) are fully decoupled. This is the central equation of the quasistatic BEM approach. Once the charge distribution is calculated, one can all the sought quantities, e.g., electric fields, optical spectra or electron energy loss spectra.

1.1.1 Electron energy loss spectroscopy within the BEM

In principle, the BEM can address for any external source by establishing the external scalar and vector potentials [110]. This includes the case of swift electrons of electron microscopes which lose energy exciting plasmons by passing close to or penetrating

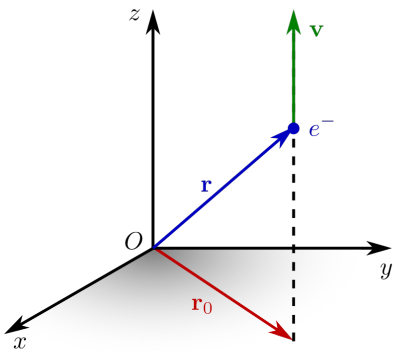

Figure 1.3: Sketch showing the electron (blue dot) with a trajectory along the z-axis defined by $\mathbf{r}(t) = \mathbf{r}_0 + \mathbf{v}t$ (blue arrow), with velocity $\mathbf{v} = v\hat{\mathbf{z}}$ (green arrow) and constant position in the xy-plane $\mathbf{r}_0$ (red arrow), setting the impact parameter.

metallic nanoparticles, . Here we briefly introduce the basics of the calculation of the quantities analyzed within electron energy loss spectroscopy (EELS). In particular in MNPBEM the kinetic energy of the exciting electron is assumed to be much higher than the plasmon energies (typical electron microscopes operate with electron energies of several hundreds of keV). Thus, the change in the velocity of the electron due to plasmon excitations can be considered negligible, and therefore the loss process can be described in the lowest order perturbation theory. As emphasized in Ref. [110], this approach is not suited for low electron energies or thick samples.

Without any loss of generality, let us consider an electron trajectory along the z-axis, with the position of the electron given by $\mathbf{r}(t) = \mathbf{r}_0 + \mathbf{v}t$, with $\mathbf{v} = v\hat{\mathbf{z}}$ the velocity of the electron, as sketched in Fig. 1.3. The electron charge distribution is thus,

$$\varrho(\mathbf{r},\omega) = -e\int dt e^{i\omega t}\delta(\mathbf{r}-\mathbf{r}_0-\mathbf{v}t) = -\frac{e}{v}\delta(\rho-b)e^{i\frac{\omega}{v}(z-z_0)}, \tag{1.52}$$

where $-e$ is the charge of the electron, and b is the impact parameter in the xy-plane. In the quasistatic approximation, the external potential is given by the solution of Poisson's equation

$$\phi_{\text{ext}} = \int \frac{\varrho(\mathbf{r}',\omega)}{\varepsilon(\mathbf{r}',\omega)|\mathbf{r}-\mathbf{r}'|}dz'. \tag{1.53}$$

In unbounded space the potentials associated with the charge distribution of Eq. (1.52) are given analytically by the Liénard-Wiechert potentials [113], leading to

[64, 108, 110]:

$$\phi_{\rm ext}(\mathbf{r}) = -\frac{2}{v\varepsilon_j} K_0\left(\frac{\omega}{v}\frac{|\rho - b|}{\gamma_j}\right) e^{i\frac{\omega}{v}(z-z_0)} \tag{1.54}$$

$$\mathbf{A}_{\rm ext}(\mathbf{r}) = \varepsilon_j \frac{\mathbf{v}}{c}\phi_{\rm ext}(\mathbf{r}), \tag{1.55}$$

where $K_0(x)$ is the modified Bessel function of order zero, and $\gamma_j = (1 - \varepsilon_j v^2/c^2)^{-\frac{1}{2}}$ the Lorentz factor. Within MNPBEM these expressions for the unbounded medium can be directly introduced into Eqs. (1.12) and (1.13), as the charge and current distributions σ_j and $\mathbf{h}_j$ will automatically guarantee that the boundary conditions are satisfied at the interfaces.

We have already introduced in the Introduction the electron energy loss, W, in Eq. (9), which can be calculated from the work performed by the electron against the induced field, $\mathbf{E}_{\rm ind}$, as:

$$W = e\int dt\, \mathbf{v}\cdot\mathbf{E}_{\rm ind}[\mathbf{r}(t), t] = \int_0^\infty d\omega\, \omega\, \Gamma_{\rm EELS}(\omega) \tag{1.56}$$

where $\Gamma_{\rm EELS}(\omega)$ is the electron energy loss probability, given per unit of transferred energy,

$$\Gamma_{\rm EELS}(\omega) = \frac{e}{\pi\omega}\int dt\, {\rm Re}\big\{e^{-i\omega t}\mathbf{v}\cdot\mathbf{E}_{\rm ind}[\mathbf{r}(t), \omega]\big\}, \tag{1.57}$$

and $\mathbf{E}_{\rm ind}[\mathbf{r}(t), \omega]$ is the induced electric field evaluated at the electron's trajectory. Within the local response approximation, the electron energy loss probability can be separated into two contributions,

$$\Gamma_{\rm EELS} = \Gamma_{\rm boundary} + \Gamma_{\rm bulk}, \tag{1.58}$$

where $\Gamma_{\rm boundary}$ is the energy loss probability due to localized surface plasmons, which can be calculated from the surface charge and current distributions σ_j and $\mathbf{h}_j$; and $\Gamma_{\rm bulk}$ is the bulk loss probability for electron propagation inside a lossy medium:

$$\Gamma_{\rm bulk}(\omega) = \frac{e^2 L}{\pi v^2}{\rm Im}\left\{\left(\frac{v^2}{c^2} - \frac{1}{\varepsilon(\omega)}\right)\ln\left(\frac{q_c^2 - k^2\varepsilon(\omega)}{(\omega/v)^2 - k^2\varepsilon(\omega)}\right)\right\}, \tag{1.59}$$

where L is the propagation length inside the medium, $k = \omega/c$ is the wavenumber of light with frequency ω in vacuum, ε is assumed to be local (independent of wave vector q) and q_c is a cutoff for collected momentum transfer [64].

In most cases, $\Gamma_{\rm boundary}$ can be calculated by obtaining an expression for the induced electric field along the electron trajectory and evaluating the expression given in Eq. (1.57). By introducing the induced potentials of Eqs. (1.12) and (1.13) into the energy loss probability of Eq. (1.57) one obtains a more efficient scheme for

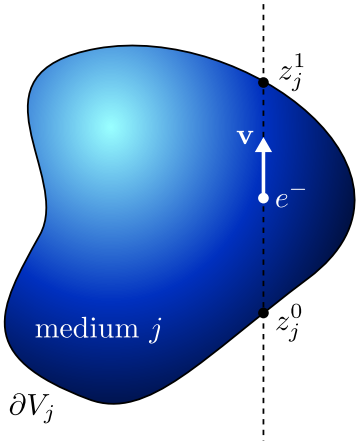

Figure 1.4: Sketch of an electron with velocity $\mathbf{v} = v\hat{\mathbf{z}}$ (white arrow) along a trajectory following the $z - axis$ (dashed lines) that crosses the boundary with medium j (blue region) at the entrance and exit points, z_j^0 and z_j^1 respectively.

calculating Γ_{boundary}:

$$\Gamma_{\text{boundary}}(\omega) = \frac{e}{\pi\omega}\int_{z_j^0}^{z_j^1} dz\,\text{Re}\Big[e^{-i\omega z/v}\oint_{\partial V_j} da\,\mathbf{v}\cdot\Big\{ikG_j(\mathbf{r}-\mathbf{s})\mathbf{h}_j(\mathbf{s}) - \nabla G_j(\mathbf{r}-\mathbf{s})\sigma_j(\mathbf{s})\Big\}\Big] \tag{1.60}$$

where z_j^0 and z_j^1 are the entrance and exit points of the electron beam in a given medium, $\mathbf{r} = \mathbf{r}_0 + z\hat{\mathbf{z}}$ gives the electron trajectory, and ∂V_j is the boundary separating each medium, as sketched in Fig. 1.4. Integration by parts allows to write the second term in the parentheses of Eq. (1.60) as:

$$\int_{z_j^0}^{z_j^1} dz e^{-i\omega z/v}\frac{\partial G_j(\mathbf{r}-\mathbf{s})}{\partial z} = e^{-i\omega z/v}G_j(\mathbf{r}-\mathbf{s})|_{z_j^0}^{z_j^1} + i\frac{\omega}{v}e^{-i\omega z/v}\varphi_j(\mathbf{s}),$$

where the potential-like term $\varphi_j(\mathbf{s}) = \int_{z_j^0}^{z_j^1} dz e^{-i\omega z/v}G_j(\mathbf{r}-\mathbf{s})$ associated with the electron propagation inside medium j is introduced. The first right-hand side (RHS) term, once introduced in Eq. (1.60), gives $e^{-i\omega z/v}\oint G_j(\mathbf{r}-\mathbf{s})\sigma_j(\mathbf{s})da|_{z_j^0}^{z_j^1}$, where the integral expression corresponds to the scalar potential at the crossing points of the trajectory with the particle boundary. Moreover, as the potential is continuous across the boundaries, this term needs to be zero for all crossing points. Finally we end up

with:

$$\Gamma_{\text{boundary}}(\omega) = -\frac{e}{\pi\omega}\sum_j \text{Im}\Big[\oint_{\partial V_j} da\varphi_j(\mathbf{s})\big\{k\,\mathbf{v}\cdot\mathbf{h}_j(\mathbf{s}) - \omega\sigma_j(\mathbf{s})\big\}\Big], \tag{1.61}$$

where the integration, instead of along the electron trajectory, is only performed over the boundary, where the surface charge and current distributions σ_j and $\mathbf{h}_j$ have been already calculated. It must be noticed that the points where the trajectory crosses the boundary have to be treated with care in Eqs. (1.54), (1.55) and (1.61) [110].

Quasistatic approximation in EELS

As already mentioned, in the quasistatic approximation Laplace or Poisson's equation needs to be solved instead of Helmholtz equation.

Details about the calculation of EELS probabilities within the BEM can be found in Refs. [64, 108, 110, 114], and here only the basics are outlined. First one can calculate the external potential from the solution of Poisson's equation given by Eq. (1.53), and then one calculates the surface charge distribution $\sigma(\mathbf{s},\omega)$ by solving the boundary integral equation, given by Eq. (1.50). Once the charge distribution is calculated, it is straightforward to obtain the induced potential along the electron beam path [see Eq. (1.12)] and therefore the electron energy loss probability, as given by Eq. 13 in the Introduction,

$$\Gamma_{\text{EELS}}(\omega) = \frac{e}{\pi\hbar}\int dt\,\text{Im}\{-\phi_{ind}[\mathbf{r}(t),\omega]e^{-i\omega t}\} \tag{1.62}$$

in the quasistatic approximation, and can be written in terms of the surface charge distribution as,

$$\Gamma_{\text{EELS}}(\omega) = -\frac{2e}{\pi v}\oint K_0(\omega|\mathbf{R}-\mathbf{R}_0|/v)\,\text{Im}\big\{\sigma(\mathbf{s},\omega)e^{i\omega z/v}\big\}da + \Gamma_{\text{bulk}}(\omega). \tag{1.63}$$

In the quasistatic approximation, considering the limit $c\to\infty$, the bulk loss probability Γ_{bulk} given by Eq. (1.59) reduces to,

$$\Gamma_{\text{bulk}}(\omega) = \frac{2e^2L}{\pi\hbar v^2}\text{Im}\Big\{-\frac{1}{\varepsilon(\omega)}\Big\}\ln(q_c v/\omega), \tag{1.64}$$

where L is the propagation length inside the medium and q_c is a cutoff for collected momentum transfer in the detector [64].

1.1.2 Infinite layers in the Boundary Element Method

Many experiments are performed with nanoparticles placed on top of substrates or embedded within layered structures, with the corresponding influence on the plasmonic response of the nanostructure. This effect of infinite substrates has been included in the plasmonic response of metallic nanostructures within the BEM, and

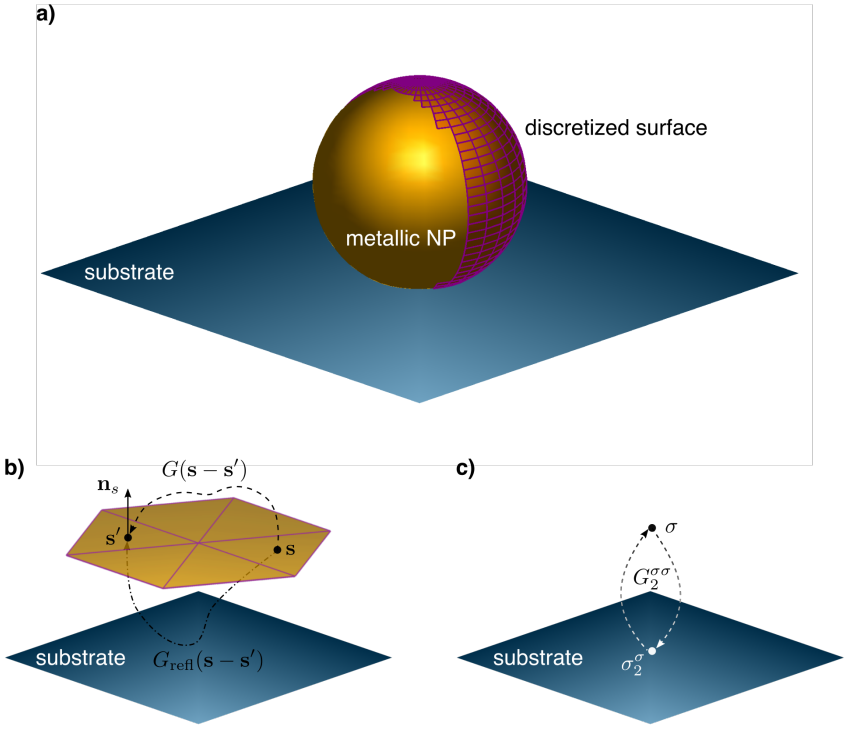

Figure 1.5: a) A metallic nanoparticle placed on top of an infinite substrate, showing the discretization of the NP's boundary. b) Infinite layers are incorporated in the MNPBEM by taking into account the reflected Green's function due to the substrate [111]. c) The reflected Green's functions $G_2^{\sigma\sigma}, G_2^{hh}, G_2^{h\sigma}, G_2^{\sigma h}$ and $G_2^{\parallel}$) are obtained in a three step process: (i) first, the scalar and vector potentials originating from the source points (e.g., σ in the sketch) are expanded in cylindrical waves; (ii) second, the reflection and transmission coefficients, i.e., charge and current densities induced at the layer (e.g., σ_2^{σ}) are calculated using the boundary conditions of Maxwell's equations;(iii) last, the potentials (e.g. $G_2^{\sigma\sigma}$) at the observation points are computed by integrating over all cylindrical waves.

implemented in the MNPBEM Toolbox [111]. In this section we give the details of such implementation, as used in this thesis to obtain the theoretical results presented in Chapter 3.

For substrates with the outer surface normal pointing in the z-direction, i.e., substrates extending in the xy-plane, the current distribution can be decomposed into parallel $\mathbf{h}^{\parallel}$ (lying in the xy-plane) and perpendicular components $h^{\perp}$ (pointing in the z-direction). Equation (1.25) shows that the parallel component $\mathbf{h}^{\parallel}$ is decoupled from the perpendicular component $h^{\perp}$ and the charge distribution σ, and that $h^{\perp}$ and σ are coupled through layer interactions. The first step is to rewrite Eqs. (1.21), (1.22), (1.25) and (1.28) for a layered structure, followed by expressing $\mathbf{h}^{\parallel}$ in terms of $h^{\perp}$ and σ, the one needs to set up the coupled equations for $h^{\perp}$ and σ and solve them within the BEM through matrix inversion. This approach deals with matrices

of order $2N$ instead of matrices of order N, which is the case of the BEM approach without layers.

We will first consider an isolated nanoparticle located in a dielectric environment of a layered structure as in Fig. 1.5(a), and assume that all boundary elements connected to the layered structure are *outer* elements (labelled with 2). The potentials *inside* the nanoparticle are still expressed as $\phi_1 = G_1\sigma_1 + \phi_1^{\rm ext}$. For the boundary elements *outside* the nanoparticle, one needs to replace G by the Green's function for the layered structure and to account for the fact that $h_2^\perp$ and σ_2 become coupled,

$$\phi_2 = \phi_2^{\rm ext} + G_2^{\sigma\sigma}\sigma_2 + G_2^{\sigma h}h_2^\perp, \tag{1.65}$$

$$A_2^\perp = A_2^{\rm ext\perp} + G_2^{hh}h_2^\perp + G_2^{h\sigma}\sigma_2. \tag{1.66}$$

The continuity of potentials becomes,

$$G_1\sigma_1 = G_2^{\sigma\sigma}\sigma_2 + G_2^{\sigma h}h_2^\perp + \phi^{\rm ext} \tag{1.67}$$

$$G_1h_1^\perp = G_2^{hh}h_2^\perp + G_2^{h\sigma}\sigma_2 + A^{\rm ext\perp} \tag{1.68}$$

$$G_1\mathbf{h}_1^\parallel = G_2^\parallel\mathbf{h}_2^\parallel + \mathbf{A}^{\rm ext\parallel}. \tag{1.69}$$

On the other hand, the continuity of Lorentz's condition becomes,

$$H_1\mathbf{h}_1^\parallel - H_2^\parallel\mathbf{h}_2^\parallel - ik\hat{\mathbf{n}}^\parallel\big(\varepsilon_1G_1\sigma_1 - \varepsilon_2G_2^{\sigma\sigma}\sigma_2 - \varepsilon_2G_2^{\sigma h}h_2^\perp\big) = \boldsymbol{\alpha}^\parallel \tag{1.70}$$

$$H_1h_1^\perp - H_2^{hh}h_2^\perp - H_2^{h\sigma}\sigma_2 - ik\hat{n}^\perp\big(\varepsilon_1G_1\sigma_1 - \varepsilon_2G_2^{\sigma\sigma}\sigma_2 - \varepsilon_2G_2^{\sigma h}h_2^\perp\big) = \alpha^\perp, \tag{1.71}$$

where $\boldsymbol{\alpha}^\parallel$ and $\alpha^\perp$ are the parallel and perpendicular components of $\boldsymbol{alpha}$ [see Eq. (1.26)], respectively. The continuity of electric displacement vector reads as,

$$\begin{aligned}\varepsilon_1H_1\sigma_1 - \varepsilon_2H_2^{\sigma\sigma}\sigma_2 - \varepsilon_2H_2^{\sigma h}h_2^\perp - ik\hat{\mathbf{n}}^\parallel\cdot\big(\varepsilon_1G_1\mathbf{h}_1^\parallel - \varepsilon_2G_2^\parallel\mathbf{h}_2^\parallel\big)\\ -ik\hat{n}^\perp\big(\varepsilon_1G_1h_1^\perp - \varepsilon_2G_2^{hh}h_2^\perp - \varepsilon_2G_2^{h\sigma}\sigma_2\big) = D^{\rm ext}.\end{aligned} \tag{1.72}$$

The surface charges and currents for this situation are then obtained from Eqs. (1.67)-(1.72) after some rearrangements (outlined in Appendix A of Ref. [111]):

$$\begin{aligned}&\big(\varepsilon_1\Sigma_1G_2^{\sigma\sigma} - \varepsilon_2H_2^{\sigma\sigma}\big)\sigma_2 + \big(\varepsilon_1\Sigma_1G_2^{\sigma h} - \varepsilon_2H_2^{\sigma h}\big)h_2^\perp\\ &\quad - ik\hat{\mathbf{n}}^\parallel\cdot\Gamma\hat{\mathbf{n}}^\parallel(\varepsilon_1-\varepsilon_2)\big(G_2^{\sigma\sigma}\sigma_2 + G_2^{\sigma h}h_2^\perp\big) - ik\hat{n}^\perp(\varepsilon_1-\varepsilon_2)\big(G_2^{h\sigma}\sigma_2 + G_2^{hh}h_2^\perp\\ &\quad = D^{\rm ext} - \varepsilon_1\Sigma_1\phi^{\rm ext} + ik\hat{\mathbf{n}}\cdot\varepsilon_1\mathbf{A}^{\rm ext} + \hat{\mathbf{n}}^\parallel\cdot\Gamma\big(\boldsymbol{\alpha}^\parallel - \Sigma_1\mathbf{A}^{\rm ext\parallel} + ik\hat{\mathbf{n}}^\parallel\varepsilon_1\phi^{\rm ext}\big)\end{aligned} \tag{1.73}$$

$$\begin{aligned}&\big(\Sigma_1G_2^{h\sigma} - H_2^{h\sigma}\big)\sigma_2 + \big(\Sigma_1G_2^{hh} - H_2^{hh}\big)h_2^\perp - ik\hat{n}^\perp(\varepsilon_1-\varepsilon_2)\big(G_2^{\sigma\sigma}\sigma_2 + G_2^{\sigma h}h_2^\perp\big)\\ &\quad = \alpha_\perp - \Sigma_1A^{\rm ext\perp} + ik\hat{n}^\perp\varepsilon_1\phi^{\rm ext},\end{aligned} \tag{1.74}$$

with $\Sigma_1 = H_1G_1^{-1}$, $\Sigma_2^\parallel = H_2^\parallel G_2^{\parallel-1}$ and $\Gamma = ik(\varepsilon_1-\varepsilon_2)(\Sigma_1 - \Sigma_2^\parallel)^{-1}$. Equations (1.73) and (1.74) can be understood as a matrix equation for $(\sigma_2, h_2^\perp)$ to be solved through matrix inversion. Once both quantities are obtained, $\mathbf{h}_2^\parallel$ is calculated from the following equation:

$$\big(\Sigma_1 - \Sigma_2^\parallel\big)G_2^\parallel\mathbf{h}_2^\parallel = ik\hat{\mathbf{n}}^\parallel(\varepsilon_2-\varepsilon_1)\big(G_2^{\sigma\sigma}\sigma_2 + G_2^{\sigma h}h_2^\perp\big) + \boldsymbol{\alpha}^\parallel - \Sigma_1\mathbf{A}^{\rm ext\parallel} + ik\hat{\mathbf{n}}^\parallel\varepsilon_1\phi^{\rm ext}. \tag{1.75}$$

The rest of the quantities (σ_1, $h_1^{\perp}$ and $\mathbf{h}_1^{\parallel}$) can be obtained from Eqs. (1.67) - (1.69).

The generalization to structures made of an arbitrary number of media is not straightforward. In the absence of a layered structure, the Green's functions can be considered such that they connect only points within the same medium, as in [108], which makes it possible to use $G_2\varepsilon_2 = \varepsilon_2 G_2$. Nevertheless, with the presence of layers this is no longer valid, as the reflected Green's functions can connect points within different media, and thus ε_2 and G_2 cannot be exchanged. In particular, the potentials are given by,

$$\phi_1 = G_{11}\sigma_1 + G_{12}\sigma_2 + \phi_1^{\text{ext}} \tag{1.76}$$

$$\phi_2 = G_{22}^{\sigma\sigma}\sigma_2 + G_{22}^{\sigma h}h_2^{\perp} + G_{21}\sigma_1 + \phi_2^{\text{ext}} \tag{1.77}$$

$$A_1^{\perp} = G_{11}h_1^{\perp} + G_{12}h_2^{\perp} + A_1^{\text{ext}\perp} \tag{1.78}$$

$$A_2^{\perp} = G_{22}^{hh}h_2^{\perp} + G_{22}^{h\sigma}\sigma_2 + G_{21}h_1^{\perp} + A_2^{\text{ext}\perp} \tag{1.79}$$

$$\mathbf{A}_1^{\parallel} = G_{11}\mathbf{h}_1^{\parallel} + G_{12}\mathbf{h}_2^{\parallel} + \mathbf{A}_1^{\text{ext}\parallel} \tag{1.80}$$

$$\mathbf{A}_2^{\parallel} = G_{22}^{\parallel}\mathbf{h}_2^{\parallel} + G_{21}\mathbf{h}_1^{\parallel} + \mathbf{A}_2^{\text{ext}\parallel}. \tag{1.81}$$

The continuity of the potential can be expressed by Eqs. (1.67), (1.68) and (1.69), by redefining the Green's functions as

$$G_1 = G_{11} - G_{21} \tag{1.82}$$

$$G_2^{\sigma\sigma} = G_{22}^{\sigma\sigma} - G_{12} \tag{1.83}$$

$$G_2^{\sigma h} = G_{22}^{\sigma h} \tag{1.84}$$

$$G_2^{hh} = G_{22}^{hh} - G_{12} \tag{1.85}$$

$$G_2^{\parallel} = G_{22}^{\parallel} - G_{12} \tag{1.86}$$

$$G_2^{h\sigma} = G_{22}^{h\sigma}, \tag{1.87}$$

which also holds for the derivatives of the Green's functions H. In a similar fashion, the continuity of the Lorentz's condition and continuity of the electric displacement vector can be expressed by Eqs. (1.70), (1.71) and (1.72), by considering the following relations:

$$\varepsilon_1 G_1 = \varepsilon_1 G_{11} - \varepsilon_2 G_{21} \tag{1.88}$$

$$\varepsilon_2 G_2^{\sigma\sigma} = \varepsilon_2 G_{22}^{\sigma\sigma} - \varepsilon_1 G_{12} \tag{1.89}$$

$$\varepsilon_2 G_2^{\sigma h} = \varepsilon_2 G_{22}^{\sigma h} \tag{1.90}$$

$$\varepsilon_2 G_2^{hh} = \varepsilon_2 G_{22}^{hh} - \varepsilon_1 G_{12} \tag{1.91}$$

$$\varepsilon_2 G_2^{\parallel} = \varepsilon_2 G_{22}^{\parallel} - \varepsilon_1 G_{12} \tag{1.92}$$

$$\varepsilon_2 G_2^{h\sigma} = \varepsilon_2 G_{22}^{h\sigma}, \tag{1.93}$$

Let us refer to $\varepsilon_1 G_1 = \widetilde{G}_1$ and similarly for $\varepsilon_2 G_2 = \widetilde{G}_2$. Now, by proceeding as for two media, the following equations are obtained:

$$\begin{aligned}
&(\widetilde{\Sigma}_1 G_2^{\sigma\sigma} - \widetilde{H}_2^{\sigma\sigma})\sigma_2 + (\widetilde{\Sigma}_1 G_2^{\sigma h} - \widetilde{H}_2^{\sigma h})h_2^{\perp} - ik\hat{\mathbf{n}}^{\parallel} \cdot \Gamma\hat{\mathbf{n}}^{\parallel}[(L_1 G_2^{\sigma\sigma} - \widetilde{G}_2^{\sigma\sigma})\sigma_2 \\
&+ (L_1 G_2^{\sigma h} - \widetilde{G}_2^{\sigma h})H_2^{\perp}] - ik\widetilde{n}^{\perp}[(L_1 G_2^{h\sigma} - \widetilde{G}_2^{h\sigma})\sigma_2 + (L_1 G_2^{hh} - \widetilde{G}_2^{hh})h_2^{\perp}] \\
&= D^{\text{ext}} - \widetilde{\Sigma}_1\phi^{\text{ext}} + ik\hat{\mathbf{n}}L_1\mathbf{A}^{\text{ext}} + \hat{\mathbf{n}}^{\parallel} \cdot \Gamma(\boldsymbol{\alpha}^{\parallel} - \Sigma_1\mathbf{A}^{\text{ext}\parallel} + ik\hat{\mathbf{n}}^{\parallel}L_1\phi^{\text{ext}}),
\end{aligned} \tag{1.94}$$

and

$$(\Sigma_1 G_2^{h\sigma} - H_2^{h\sigma})\sigma_2 + (\Sigma_1 G_2^{hh} - H_2^{hh})h_2^{\perp} - ik\hat{n}^{\perp}[(L_1 G_2^{\sigma\sigma} - \widetilde{G}_2^{\sigma\sigma})\sigma_2 + (L_1 G_2^{\sigma h} - \widetilde{G}_2^{\sigma h})h_2^{\perp}] = \alpha^{\perp} - \Sigma_1 A^{\mathrm{ext}\perp} + ik\hat{n}^{\perp} L_1 \phi^{\mathrm{ext}}, \tag{1.95}$$

where, $\widetilde{\Sigma}_1 = \widetilde{H}_1 G_1^{-1}$, $\Gamma = ik(L_1 - L_2^{\parallel})(\Sigma_1 - \Sigma_2^{\parallel})^{-1}$, $L_1 = \widetilde{G}_1 G_1^{-1}$, and $L_2 = \widetilde{G}_2^{\parallel} G_2^{\parallel -1}$ have been used. As previously, this expression can be understood as a matrix equation for $(\sigma_2, h_2^{\perp})$ to be solved through matrix inversion. Once both quantities are obtained, $\mathbf{h}_2^{\parallel}$ is calculated from,

$$(\Sigma_1 - \Sigma_2^{\parallel}) G_2^{\parallel} \mathbf{h}_2^{\parallel} = ik\hat{\mathbf{n}}^{\parallel}[(L_1 G_2^{\sigma\sigma} - \widetilde{G}_2^{\sigma\sigma})\sigma_2 + (L_1 G_2^{\sigma h} - \widetilde{G}_2^{\sigma h})h_2^{\perp}] + \boldsymbol{\alpha}^{\parallel} - \Sigma_1 \mathbf{A}^{\mathrm{ext}\parallel} + ik\hat{\mathbf{n}}^{\parallel} L_1 \phi^{\mathrm{ext}}. \tag{1.96}$$

The Green's functions $G_2^{\parallel}$, $G_2^{\sigma\sigma}$, $G_2^{\sigma h}$, $G_2^{h\sigma}$, and G_2^{hh} are the essential ingredients of the BEM approach for layered structures, and are computed similarly to related field-based approaches [115, 116]. For instance, let us consider a boundary element with surface charges σ and currents $\mathbf{h}$ within a layered structure [see Figure 1.5(c)]. These sources lead to potentials $\phi^{\mathrm{ext}} = G\sigma$ and $\mathbf{A}^{\mathrm{ext}} = G\mathbf{h}$ evaluated at the interfaces of the layered structure. In accordance to field-based approaches, the induced potentials containing the interaction with the layers are calculated in three steps: (i) first the scalar and vector potentials originating from the source points, where the source surface charges σ and currents $\mathbf{h}$ are located, are expanded in cylindrical waves, (ii) second the surface charge densities, $\sigma_2^{\sigma}, \sigma_2^{h}$ and current densities $\mathbf{h}_2^{\sigma}, \mathbf{h}_2^{h}$ induced at the interfaces are computed by using the BEM equations, and (iii) finally the potentials at the observation points are computed by integrating over all cylindrical waves.

In step (i) the Sommerfeld identity

$$\frac{e^{ikr}}{r} = i \int_0^{\infty} \frac{k_\rho}{k_z} J_0(k_\rho \rho) e^{ik_z |z|} dk_\rho \tag{1.97}$$

is employed [115], with $J_0(x)$ the Bessel function of order zero and the wavevector k decomposed into the radial component k_ρ and the z-component $k_z = \sqrt{k^2 - k_\rho^2}$.

The wave impinging at the interface is reflected and transmitted, and therefore in step (iii) one needs to sum up over all reflected and transmitted waves to calculate the potentials at the observation points, i.e., one has to calculate integrals of the form,

$$I = i \int_0^{\infty} \frac{k_\rho}{k_z} J_0(k_\rho \rho) e^{ik_z z} A(k_\rho, k_z) dk_\rho, \tag{1.98}$$

where $A(k_\rho, k_z)$ is a generalized reflection or transmission coefficient to be discussed below. To evaluate the integral of Eq. (1.98) we directly follow reference [116] and deform the integration path in the complex plane using the recipes given in that work.

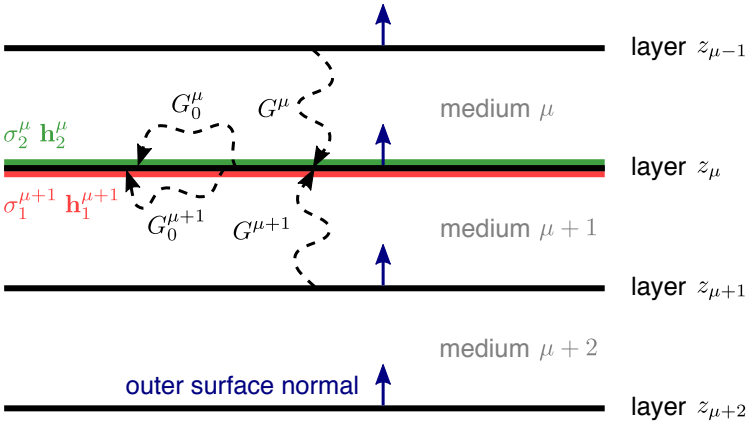

Figure 1.6: Scheme representing the layered structure. The intra-layer Green's function G_0^μ connects points at layer z_μ in medium μ and the inter-layer Green's function G_μ connects points between different layers (located at layers z_μ and $z_{\mu-1}$) in medium μ.

To compute the reflection and transmission coefficients in the BEM for the layered structure, we proceed as follows. Consider a layered structure with interfaces at z_μ. As shown in Fig. 1.6, we denote the medium *above* the layer with μ and the medium *below* the layer with $\mu+1$. Thus, $\mu = 1$ denotes the uppermost medium. We assume that the outer surface normal points into the positive z-direction, and denote the surface charges and currents at the upper side of z_μ with σ_2^μ and $\mathbf{h}_2^\mu$, and at the lower side of z_μ with $\sigma_1^{\mu+1}$ and $\mathbf{h}_1^{\mu+1}$. Additionally, we introduce the intra-layer Green's function G_0^μ that connects points in layer z_μ and in medium μ (on the same side of the interface), and inter-layer Green's function G^μ that connects points between different layers.

Let $\phi_{1,2}^\mu$ and $\mathbf{A}_{1,2}^\mu$ denote the external excitations described by scalar and vector potentials, respectively. As the BEM equations (1.21), (1.22), (1.25) and (1.28) decouple $\mathbf{h}^\parallel$ from $(\sigma,\, h^\perp)$, we can treat excitations $\mathbf{A}^\parallel$ and ϕ, $A^\perp$ separately. For parallel excitations, $\mathbf{A}_{1,2}^\mu$, we obtain the following set of equations for the parallel surface currents $\mathbf{h}_{1,2}^\mu$:

$$G_0^{\mu+1}\mathbf{h}_1^{\mu+1} - G_0^\mu \mathbf{h}_2^\mu - G^\mu \mathbf{h}_1^\mu + G^{\mu+1}\mathbf{h}_2^{\mu+1} = \mathbf{A}_2^\mu - \mathbf{A}_1^{\mu+1} \tag{1.99}$$

$$2\pi i(\mathbf{h}_1^{\mu+1} + \mathbf{h}_2^\mu) - k_z^\mu G^\mu \mathbf{h}_1^\mu - k_z^{\mu+1} G^{\mu+1}\mathbf{h}_2^{\mu+1} = k_z^\mu \mathbf{A}_2^\mu + k_z^{\mu+1}\mathbf{A}_1^{\mu+1}, \tag{1.100}$$

which can be solved for each wavevector through matrix inversion. For a perpendicular

vector potential $A^{\mu}_{1,2}$ or a scalar potential $\phi^{\mu}_{1,2}$ the BEM equations become:

$$G_0^{\mu+1}\sigma_1^{\mu+1} - G_0^{\mu}\sigma_2^{\mu} - G^{\mu}\sigma_1^{\mu} + G^{\mu+1}\sigma_2^{\mu+1} = \phi_2^{\mu} - \phi_1^{\mu+1} \tag{1.101}$$

$$G_0^{\mu+1}h_1^{\mu+1} - G_0^{\mu}h_2^{\mu} - G^{\mu}h_1^{\mu} + G^{\mu+1}h_2^{\mu+1} = \mathbf{A}_2^{\mu} - \mathbf{A}_1^{\mu+1} \tag{1.102}$$

$$\begin{aligned} &2\pi i\Big(\varepsilon_{\mu+1}\sigma_1^{\mu+1} + \varepsilon_{\mu}\sigma_2^{\mu}\Big) + k\Big(G_0^{\mu+1}\varepsilon_{\mu+1}h_1^{\mu+1} - G_0^{\mu}\varepsilon_{\mu}h_2^{\mu}\Big) \\ &- k_z^{\mu}\varepsilon_{\mu}G^{\mu}\sigma_1^{\mu} - k_z^{\mu+1}\varepsilon_{\mu+1}G^{\mu+1}\sigma_2^{\mu+1} - k\varepsilon_{\mu}G^{\mu}h_1^{\mu} + k\varepsilon_{\mu+1}G^{\mu+1}h_2^{\mu+1} \\ &= k_z^{\mu}\varepsilon_{\mu}\phi_2^{\mu} + k_z^{\mu+1}\varepsilon_{\mu+1}\phi_1^{\mu+1} + k\varepsilon_{\mu}A_2^{\mu} - k\varepsilon_{\mu+1}A_1^{\mu+1} \end{aligned} \tag{1.103}$$

$$\begin{aligned} &2\pi i\Big(h_1^{\mu+1} + h_2^{\mu}\Big) + k\Big(G_0^{\mu+1}\varepsilon_{\mu+1}\sigma_1^{\mu+1} - G_0^{\mu}\varepsilon_{\mu}\sigma_2^{\mu}\Big) \\ &- k_z^{\mu}G^{\mu}h_1^{\mu} - k_z^{\mu+1}G^{\mu+1}h_2^{\mu+1} - k\varepsilon_{\mu}G^{\mu}\sigma_1^{\mu} + k\varepsilon_{\mu+1}G^{\mu+1}\sigma_2^{\mu+1} \\ &= k_z^{\mu}A_2^{\mu} + k_z^{\mu+1}A_1^{\mu+1} + k\varepsilon_{\mu}\phi_2^{\mu} - k\varepsilon_{\mu+1}\phi_1^{\mu+1}. \end{aligned} \tag{1.104}$$

The reflected Green's functions for layered structures can be computed from these equations. For instance, one can calculate $G^{h\sigma}$ by considering an exciting scalar potential produced by a surface charge σ at the source point, and then computing the perpendicular component of the vector potential produced by the induced surface current density $h^{\mu}_{1,2}$ at the observation point.

In summary, the reflected Green's functions are calculated following a three-step process: (i) first, the positions of a set of sources in space (source points) need to be defined; (ii) for each source point the surface charges and currents induced at the interface of a layered structure are calculated; (iii) the scalar and vector potentials, generated by the source point and influenced by the layered structure, are obtained in another set of points in space (observation points).

The evaluation of the reflected Green's functions is rather time consuming, and it can be a bottleneck for BEM simulations. Waxenegger *et al.* implemented in the MNPBEM Toolbox [111] an approximate method to calculate the reflected Green's functions and therefore to speed up the calculation. The approach is based on setting up a table of reflected Green's functions, for which a suitable grid of different radii r and z-values is defined, followed by an interpolation. The reflected Green's functions $G(r, z_1, z_2)$ depend on the radial distance between the observation and source points r, and the z-values of the observation points z_1 and the source points z_2. For the uppermost or lowermost medium, the Green's functions only depend on the distance in the z-axis between the observation points, i.e., $z_1 + z_2$ [115], which allows for an additional calculation speed-up. In order to evaluate H_2, the derivatives $F_r = \partial G/\partial r$ and $F_z = \partial G/\partial z_1$ are also needed. Moreover, instead of directly interpolating, a further assumption is made, by assuming that G, F_r, and F_z follow a functional dependence of the form,

$$G(r, z_1, z_2) = \frac{g(r, z_2, z_2)}{\widetilde{r}}, \quad F_r - \frac{f_r(r, z_1, z_2)r}{\widetilde{r}^3}, \quad F_z(r, z_1, z_2) = -\frac{f_z(r, z_1, z_2)\widetilde{z}}{\widetilde{r}^3}, \tag{1.105}$$

where $\widetilde{z}$ is the sum of the z_1 and z_2 distances to the respective closest layer interfaces, $\widetilde{r} = \sqrt{r_2 + \widetilde{z}_2}$, and g, f_r, f_z are tabulated values. Equation (1.105) has the advantage

that for small r and z-values the functional shape is the same as for quasistatic Green's functions using image charges [113], and for layered structures g, f_r, and f_z are expected to have only a weak spatial dependence in general.

Once the reflected Green's functions have been computed, they can be used along with the direct Green's functions to obtain the solutions of the BEM equations (1.94) and (1.95). Nevertheless, there is a critical issue regarding the boundary elements that are directly located on an interface. Before pondering on such interface elements, we recall that in the normal BEM approach one has to be careful when computing the surface derivative of the Green's function for diagonal elements [108]

$$\lim_{\mathbf{r}\to\mathbf{s}}(\hat{\mathbf{n}}\cdot\nabla_{\mathbf{r}})G(\mathbf{r},\mathbf{s}') = (\hat{\mathbf{n}}\cdot\nabla_{\mathbf{s}})G(\mathbf{s},\mathbf{s}') \pm 2\pi\delta(\mathbf{s}-\mathbf{s}'), \tag{1.106}$$

where the sign of the singular term depends on whether $\mathbf{r}$ approaches $\mathbf{s}$ from the inside or outside. Inspection of Eq. (1.105) shows that a similar singular contribution is present in the reflected Green's function for elements belonging to a layer interface. The surface derivative F_z of the reflected Green's function is now split into two contributions (note that $\hat{\mathbf{n}}$ points into the z-direction):

$$F_z(r,z_1,z_2) = -f_0\frac{\widetilde{z}}{\widetilde{r}^3} - [f_z(r,z_1,z_2)-f_0]\frac{\widetilde{z}}{\widetilde{r}^3}, \tag{1.107}$$

where $f_0 = \lim_{r,\widetilde{z}\to 0} f_z(r,\widetilde{z})$. When approaching the boundary through $\lim_{\mathbf{r}\to\mathbf{s}} F_z(r,z_1,z_2)$, the first term gives a singular contribution $\pm 2\pi f_0\delta(\mathbf{s}-\mathbf{s}')$, similarly to Eq. (1.106), whereas the second term has a smooth r and z dependence and can be safely integrated over the boundary element.

In summary, infinite layered structures can be efficiently handled within BEM by setting a table of reflected Green's functions that can be used via interpolation to calculate the induced charge and current densities at the boundaries of a nanostructure with arbitrary shape. The consideration of infinite layers is useful in situations such as the one presented in Chapter 3 where we simulate the optical response of nanoparticle-on-mirror (NPoM) structure, which consists of a metallic nanoparticle placed on top of a metallic substrate and separated by a thin spacer-film in-between to prevent conductive contact, creating a nanogap between the NP and the substrate. We use the implementation of infinite layered structure for the MNPBEM Toolbox [111] with such purpose.

1.2 Discrete Dipole Approximation (DDA)

We explain in this section the discrete interaction model (DIM) as introduced in Ref. [117] which is used to calculate the optical response of small metallic clusters to compare with the results obtained within the BEM and TDDFT in Chapter 2.

In the DIM the nanoparticle is described as formed by a number of atoms, each characterized by its corresponding polarizability. One could consider the DIM as an atomistic variant of the discrete dipole approximation (DDA), which is commonly used to simulate the plasmonic response of large metallic nanoparticles. The DDA consists in discretizing the volume of the particle in an array of points, each acquiring a dipole moment in response to a local electric field, which is calculated iteratively. Indeed, the DIM is an extension of the point-dipole interaction (PDI) model used to calculate the optical response of molecules [118–121], by representing each atom with an atomic polarizability and calculating atomic induced dipoles self-consistently through their interactions with each other and with the external electric field according to classical electrostatics. The PDI model has been extended to include a damping term related to the internal electric fields at short distances [122–128], and also intramolecular charge-transfer using either atomic capacitances [121,129,130] or atomic electronegativity [131–133].

The molecular behavior of small metallic clusters has motivated the extension of the PDI model to metallic clusters as a capacitance-polarizability interaction model (CPIM) [134, 135]. The CPIM bridges the gap between quantum mechanical methods and the macroscopic electrodynamic description, although often relies in the parametrization of atomic polarizabilities and capacitances with data calculated within TDDFT, which limits its practical aspect. In the DIM this barrier is tackled by only taking into account the atomic polarizabilities, which are calculated from a Claussius-Mossotti relationship [117]. This is the scheme used to obtain the results presented in this thesis.

For a system with N interacting atoms such as the one shown in Fig 1.7, where each ith atom is characterized by a polarizability $\alpha_{i,\alpha\beta}$, the total energy of the system, V, can be written as:

$$V = \frac{1}{2}\sum_{i}^{N} \mu_{i,\alpha}^{\mathrm{ind}} \alpha_{i,\alpha\beta}^{-1} \mu_{i,\beta}^{\mathrm{ind}} - \frac{1}{2}\sum_{i}^{N}\sum_{j\neq i}^{N} \mu_{i,\alpha}^{\mathrm{ind}} T_{ij,\alpha\beta}^{(2)} \mu_{j,\beta}^{\mathrm{ind}} - \sum_{i}^{N} E_{\alpha}^{\mathrm{ext}} \mu_{i,\alpha}^{\mathrm{ind}}, \tag{1.108}$$

where Roman subscripts, i, j, denote ith and jth atoms, Greek subscripts, α, β, denote (x, y, z) components, and $\mu_{i,\alpha}^{\mathrm{ind}}$ is the induced dipole at the ith atom. Einstein summation convention is used for Greek subscripts. The first term is the self-energy required for creating an induced atomic dipole moment, where $\alpha_{i,\alpha\beta}$ represents a component of the atomic polarizability tensor of atom i. The second term is the dipole-dipole interaction, where $T_{ij,\alpha\beta}^{(2)} = \nabla_\alpha \nabla_\beta (1/R_{ij})$ is the interaction tensor of rank 2, with R_{ij} the interatomic distance. The last term in Eq. (1.108) is the interaction between the atomic dipoles and an external electric field $E_{\alpha}^{\mathrm{ext}}$. In the DIM a Gaussian charge distribution is used to describe the polarizable atom (considered to be a sphere) to ensure that there is no "polarizability catastrophe" [123], i.e., to make sure that the equations do not diverge as the interatomic distance tends to zero. The interaction tensor is therefore renormalized, which effectively introduces a

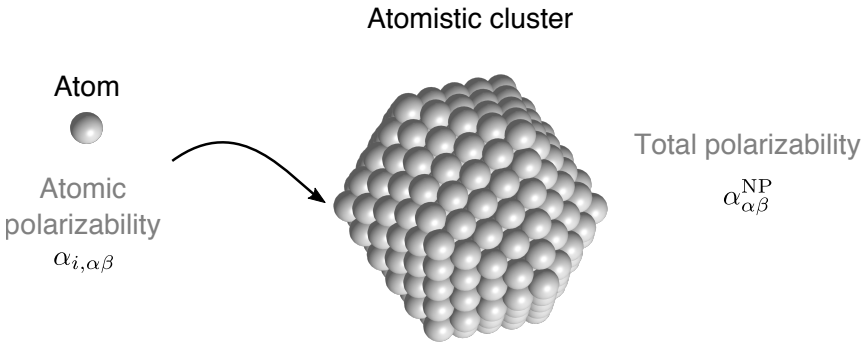

Figure 1.7: In the discrete interaction model (DIM) the atoms are represented by spheres with atomic polarizability $\alpha_{i,\alpha\beta}$, where the Roman subscript, i, denotes the ith atom, and Greek subscripts, α, β, denote x, y and z components. For an atomistic cluster of N interacting atoms the total polarizability of the atomistic cluster $\alpha^{\mathrm{NP}}_{\alpha\beta}$ can be found by minimizing the total energy of the system [Eq. (1.108)].

screening of the interaction at short distances [132, 135], given by,

$$T^{(2)}_{ij,\alpha\beta} = \frac{3r_{ij,\alpha}r_{ij,\beta} - \delta_{\alpha\beta}r^2_{ij}}{r^5_{ij}}\left[\mathrm{erf}\left(\frac{r_{ij}}{R_{ij}}\right) - \frac{2}{\sqrt{\pi}}\frac{r_{ij}}{R_{ij}}e^{-(r_{ij}/R_{ij})^2}\right] - \frac{4}{\sqrt{\pi}(R_{ij})^3}\frac{r_{ij,\alpha}r_{ij,\beta}}{r^2_{ij}}e^{-(r_{ij}/R_{ij})^2}, \tag{1.109}$$

where r_{ij} is the atomic distance between the ith and jth dipole, $R_{ij} = [(R_i)^2 + (R_j)^2]^{1/2}$, and R_i is the effective radius of the dipole i, which we consider to be the radius of the atom, and $\mathrm{erf}(x)$ is the error function. In contrast, the DDA model treats the atoms as point objects and thus the bare unscreened interaction tensor is used in that approach. Retardation effects are not included in our case because of the small size of the nanoparticles studied, however, this could be straightforwardly included using the fully retarded interactions tensor [136, 137].

The induced self-consistent dipole of an atom i, along direction β can then be found by minimizing the total energy given by Eq. (1.108) with respect to the induced atomic dipoles, which leads to the following set of linear response equations

$$\mu^{\mathrm{ind}}_{i,\beta} = \alpha_{i,\alpha\beta}\left(E^{\mathrm{ext}}_{\alpha} + \sum_{j\neq i}^{N} T^{(2)}_{ij,\alpha\beta}\mu^{\mathrm{ind}}_{j,\beta}\right) \tag{1.110}$$

which are solved self-consistently using an iterative solver. The total polarizability of the entire NP is then calculated by summing up on all atoms as:

$$\alpha^{\mathrm{NP}}_{\alpha\beta} = \sum_{i}^{N} \frac{\partial \mu^{\mathrm{ind}}_{i,\alpha}}{\partial E^{\mathrm{ext}}_{\beta}}, \tag{1.111}$$

from which the optical absorption cross section at frequency ω is obtained as

$$\sigma_{\text{abs}}(\omega) = \frac{4\pi\omega n}{c}\text{Im}\{\overline{\alpha}^{\text{NP}}(\omega)\}, \tag{1.112}$$

where n is the refractive index of the surrounding medium and $\overline{\alpha}^{\text{NP}}(\omega)$ is the isotropic polarizability of the nanoparticle,

$$\overline{\alpha}^{\text{NP}}(\omega) = \frac{1}{3}[\alpha_{xx}^{\text{NP}}(\omega) + \alpha_{yy}^{\text{NP}}(\omega) + \alpha_{zz}^{\text{NP}}(\omega)] \tag{1.113}$$

The electric field around the nanoparticle can be obtained directly from the atomic dipoles, using either the renormalized interaction tensor in the DIM or the bare interaction tensor in the DDA. In our calculations we consider the atomic polarizability to be isotropic and obtained from the Clausius-Mossotti relationship as [117]:

$$\alpha_i = \frac{6}{\pi}R_i^3\frac{\varepsilon - \varepsilon_0}{\varepsilon + 2\varepsilon_0} \tag{1.114}$$

where ε is the dielectric constant of the NP and ε_0 is the dielectric constant of vacuum.

1.3 Atomistic ab-initio quantum model: Time-Dependent Density Functional Theory

The study of the interaction of electromagnetic fields and matter has gathered much effort and interest throughout the history of modern physics. During the previous century, the description of this interaction surpassed the realm of classical macroscopic physics and reached down to the level of atoms and molecules with the aid of quantum mechanics (QM). In the approach presented here, the external fields are considered to be of low intensity, and therefore correctly described within perturbation theory. The optical perturbation is treated as a classical electric potential, while the perturbed system obeys the laws of QM. While our main interest is on the response of the system to the external perturbation, we first need to briefly summarize the theory behind the description of the unperturbed system, i.e. the ground-state of the system, and then formulate the time-dependent perturbation theory to follow the evolution of the excited states. The ground-state is obtained according to density functional theory (DFT), and the excited states are described by using linear-response time-dependent DFT (TDDFT). A priori, both DFT and TDDFT make it possible to model matter of arbitrary chemical composition with minimal empirical input, and are therefore considered to be *ab initio* frameworks.

The electrons and nuclei composing the atoms are fully described by the wave function $\psi(\mathbf{r}_1, \mathbf{r}_2, ..., \mathbf{R}_1, \mathbf{R}_2, ...; t)$ which depends on the electrons' coordinates $\mathbf{r}_i$, the

coordinates of the nuclei $\mathbf{R}_I$ and time t. The wave function represents a "probability amplitude". Although this amplitude is not directly measurable, its square in an infinitesimally small volume in the many-body configurational space gives the probability of finding the system at time t in a given configuration [138]. Moreover, the probability of finding particles at certain positions should not be time-dependent in the absence of a time-dependent perturbation, and so the wave function can be separated into a time-independent amplitude $\psi(\mathbf{r}_1, \mathbf{r}_2, ..., \mathbf{R}_1, \mathbf{R}_2, ...)$ and a time-dependent phase. The time-independent term obeys the eigenvalue equation

$$\hat{H}\psi = \mathcal{E}\psi, \tag{1.115}$$

where the eigenvalues $\mathcal{E}$ are the total energies that the system can have. In the non-relativistic approximation the Hamiltonian operator $\hat{H}$ can be constructed from the Schrödinger equation [139]

$$\hat{H} = -\sum_i \frac{\nabla_i^2}{2m_e} - \sum_I \frac{\nabla_I^2}{2M_I} + \frac{1}{2}\sum_{i\neq j} \frac{1}{|\mathbf{r}_i - \mathbf{r}_j|} - \sum_{iI} \frac{Z_I}{|\mathbf{r}_i - \mathbf{R}_I|} + \sum_{I\neq J} \frac{Z_I Z_J}{|\mathbf{R}_I - \mathbf{R}_J|}, \tag{1.116}$$

where m_e is the mass of the electron, $\mathbf{r}_i$ the position of the ith electron, and M_I, $\mathbf{R}_I$ and Z_I are the mass, position and atomic number of the Ith atomic nucleus, respectively. The small indices i, j run over electrons and the capital indices I, J run over nuclei. The first two terms of the Hamiltonian Eq. (1.116) correspond to the kinetic energy terms of electrons and nuclei, while the rest of the terms correspond to the Coulomb interaction between all pairs of bodies (electron-electron, electron-nucleus and nucleus-nucleus). Unfortunately, Eq. (1.116) does not allow for a simple separation of variables, neither for analytical solutions in almost all cases. Therefore, the diagonalization problem in Eq. (1.115) will require a discretization of the multi-dimensional wave function. Moreover, a direct diagonalization is generally impractical as the computational complexity will grow exponentially with the number of particles. Fortunately, it is possible to find accurate approximate solutions to Eq. (1.115) by using different methods, such as DFT. The first step, not exclusive to this method, consists in separating the electron and nuclei variables in the wave function, based on the three orders of magnitude difference between the mass of the electron m_e and the nuclei M_n, such that $\psi_{\text{total}}(\mathbf{r}_1, \mathbf{r}_2, ..., \mathbf{R}_1, \mathbf{R}_2) = \psi_{\text{elec}}(\mathbf{r}_1, \mathbf{r}_2, ..., \mathbf{r}_N) \times \psi_{\text{nuclei}}(\mathbf{R}_1, \mathbf{R}_2, ..., \mathbf{R}_M)$, also known as the Born-Oppenheimer approximation [138]. Moreover, in most cases the masses of nuclei can be safely assumed to behave as classical point particles and treated according to classical mechanics [139]. Therefore, the Hamiltonian in Eq. (1.116) can be further approximated by considering the interaction of the nuclei with the electrons as an external potential $V_{\text{ext}}(\mathbf{r})$, acting on the electrons. Thus, the Hamiltonian for a system with N electrons can be expressed under these approximations as,

$$\hat{H} = \sum_{i=1}^{N} \left\{ \frac{\mathbf{p}_i^2}{2m_e} + V_{\text{ext}}(\mathbf{r}_i) + \frac{1}{2}\sum_{j\neq i}^{N} \frac{e^2}{|\mathbf{r}_i - \mathbf{r}_j|} \right\}, \tag{1.117}$$

where $\mathbf{p}_i$ is the momentum of the ith electron, and $V_{\text{ext}}(\mathbf{r})$ the external potential at position $\mathbf{r}$. The Hamiltonian can also be expressed as,

$$\hat{H} = \hat{T} + \hat{V}_{\text{ext}} + \hat{W}_{\text{ee}}, \tag{1.118}$$

with $\hat{T}$ the kinetic-energy operator, $\hat{V}_{\text{ext}}$ the external potential operator and $\hat{W}_{\text{ee}}$ the electron-electron (Coulombian) interaction operator. Nevertheless, still further approximations are needed to treat this Hamiltonian, as the exact wave function $\psi_{\text{elec}}(\mathbf{r}_1, \mathbf{r}_2, ..., \mathbf{r}_N)$ cannot be so easily simplified. DFT is one of the theories allowing to effectively separate variables within the electronic wave function.

1.3.1 Density Functional Theory

As explained above, the main challenge to obtain quantities of interest in the many-body problem is the exponential growth of the computational complexity with the number of particles N. Among these quantities, one of great interest is the ground-state energy E_0. This quantity can be obtained from the variational principle with the following minimization [138]:

$$E_0 = \min_{\psi} \left\langle \psi \middle| \hat{H} \middle| \psi \right\rangle, \tag{1.119}$$

where the search is over all N-electron anti-symmetric wave functions $\psi(\mathbf{r}_1, \mathbf{r}_2, ..., \mathbf{r}_N)$, normalized to unity $< \psi | \psi >= 1$. DFT greatly reduces the complexity of the many-boy problem by reformulating the variational theorem in terms of the electron density $n(\mathbf{r})$, defined from the wave function $\psi_{\text{elec}}(\mathbf{r}_1, \mathbf{r}_2, ..., \mathbf{r}_N)$ as

$$n(\mathbf{r}) = N \int d^3 r_2 \int d^3 r_3 ... \int d^3 r_N \psi^*_{\text{elec}}(\mathbf{r}, \mathbf{r}_2, ..., \mathbf{r}_N) \psi_{\text{elec}}(\mathbf{r}, \mathbf{r}_2, ..., \mathbf{r}_N). \tag{1.120}$$

Moreover, the electron density $n(\mathbf{r})$ is normalized to the number N of electrons in the system, $\int n(\mathbf{r}) d^3 r = N$. In this section, we will highlight the main ingredients of DFT. Complete reviews and applications of DFT in atomic, molecular and solid-state physics can be found in Refs. [139, 140].

Hohenberg-Kohn theorems

In 1964 Hohenberg-Kohn (HK) demonstrated [141] that the ground-state electron density $n(\mathbf{r})$ determines the potential $V_{\text{ext}}(\mathbf{r})$ up to an arbitrary additive constant *cte*, thus there cannot exist two local potentials differing by more than a constant which have the same ground-state density.

The Hohenberg-Kohn theorem states that [141]: "*the ground-state density* $n(\mathbf{r})$ *determines the potential* $V_{\text{ext}}(\mathbf{r})$*, which in turn determines the Hamiltonian, and thus everything about the many-body problem. In other words, the potential* $V_{\text{ext}}(\mathbf{r})$ *is a unique functional of the ground-state density* $n(\mathbf{r})$*"*. Therefore, all the ground-state properties will be functionals of the electronic density $n(\mathbf{r})$. The ground-state wave

function ψ for potential $V(\mathbf{r})$ is itself a functional of n, denoted by $\psi[n]$, which was exploited by HK to define the universal (i.e., independent from the external potential) density functional

$$F[n] = \left\langle \psi[n] \middle| \hat{T} + \hat{W}_{ee} \middle| \psi[n] \right\rangle. \tag{1.121}$$

The universal density functional $F[n]$ can be used to define the total electronic energy function $E[n]$ for a specific external potential $V_{\text{ext}}(\mathbf{r})$,

$$E[n] = F[n] + \int V_{\text{ext}}(\mathbf{r}) n(\mathbf{r}) d^3 r. \tag{1.122}$$

Moreover, by minimizing the total electronic energy functional $E[n]$ with respect to N-electron densities with some local potential (referred to as $V(x)$-representable densities) we can obtain the ground-state energy E_0 of the system considered. This minimum energy is reached for a ground-state density $n_0(\mathbf{r})$ that corresponds to the potential $V_{\text{ext}}(\mathbf{r})$:

$$E_0 = \min_n E[n]. \tag{1.123}$$

Summarizing, the existence of the mapping from a ground-state density $n_0(\mathbf{r})$ to the external potential $V_{\text{ext}}(\mathbf{r})$, the existence of the universal density functional $F[n]$, and the variational property of the ground-state energy with respect to the density $n(\mathbf{r})$ constitute the set of *Hohenberg-Kohn theorems*.

Kohn-Sham method

In 1965 Kohn and Sham (KS) [142] proposed to decompose the universal functional $F[n]$ using a *single-determinant* wave function Φ, and a constrained search formulation for the kinetic energy

$$F[n] = \min_{\Phi \to n} \left\langle \Phi \middle| \hat{T} \middle| \Phi \right\rangle + E_{\text{Hxc}}[n], \tag{1.124}$$

with $E_{\text{Hxc}}[n]$ the Hartree-exchange-correlation functional and $\Phi \to n$ meaning that the minimization is done over the normalized *single-determinant* wave function Φ. We use $T_s[n]$ as the non-interacting kinetic energy functional, $T_s[n] = \min_{\Phi \to n} \left\langle \Phi \middle| \hat{T} \middle| \Phi \right\rangle = \left\langle \Phi[n] \middle| \hat{T} \middle| \Phi[n] \right\rangle$, with $\Phi[n]$ the minimizing *single-determinant* wave function for a given density (non necessarily unique), which is called the *KS wave function*. The idea of the KS method is then to use the exact expression of $T_s[n]$ by reformulating the variational property of $F[n]$ in terms of Φ,

$$\begin{aligned} E_0 &= \min_n \left\{ \min_{\Phi \to n} \left\langle \Phi \middle| \hat{T} \middle| \Phi \right\rangle + E_{\text{Hxc}}[n] + \int V_{\text{ext}}(\mathbf{r}) n(\mathbf{r}) d^3 r \right\} \\ &= \min_{\Phi} \left\{ \left\langle \Phi \middle| \hat{T} + \hat{V}_{\text{ext}} \middle| \Phi \right\rangle + E_{\text{Hxc}}[n_\Phi] \right\}. \end{aligned} \tag{1.125}$$

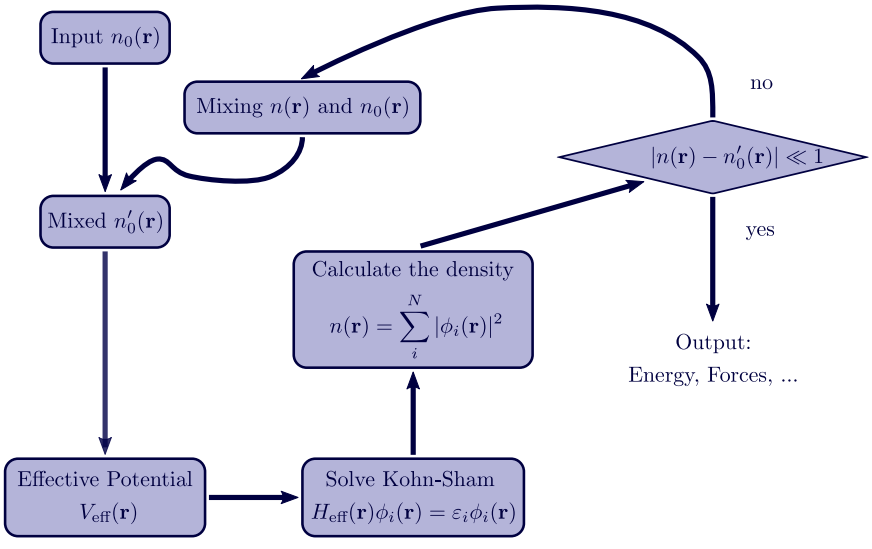

Figure 1.8: Schematic representation of the self-consistent loop used to solve the KS equations. One starts from an initial guess for the electron density corresponding to the ground state $n_0(\mathbf{r})$, which is used to calculate the effective potential $V_{\text{eff}}(\mathbf{r})$ to be introduced in the Kohn-Sham equation. The Kohn-Sham equation is solved and from the eigenfunctions $\phi_i(\mathbf{r})$ that are obtained one calculates the new charge density $n(\mathbf{r})$. The new charge density is mixed with the old charge density $n_0(\mathbf{r})$ to obtain the mixed $n_0'(\mathbf{r})$ to again begin the loop until the charge densities calculated between successive loops are converged.

Thus, the exact ground-state energy E_0 and density $n_0(\mathbf{r})$ can in principle be obtained by minimizing over single-determinant wave functions only. The advantage of the KS scheme is to use the single-determinant wave function Φ instead of the multi-determinant wave function ψ, which represents a tremendous simplification. With the single-determinant wave function, Φ, the kinetic energy can be treated explicitly, and only $E_{\text{Hxc}}[n]$ remains to be determined as a functional of the density.

Moreover, the minimization in Eq. (1.125) over the single-determinant wave function Φ can be reformulated to a minimization of the total electronic energy, as

$$E[\{\phi_i\}] = \sum_{i=1}^{N} \int \phi_i^* \Big(-\frac{1}{2}\nabla^2 + V_{\text{ext}}(\mathbf{r}) \Big) \phi_i(\mathbf{r}) d^3r + E_{\text{Hxc}}[n], \tag{1.126}$$

with respect to the spatial orbitals $\phi_i(\mathbf{r})$, which form a set of N orthonormal functions $\{\phi_i(\mathbf{r})\}_{i=1,\ldots,N}$. The density is then expressed in terms of the spatial orbitals $\phi_i(\mathbf{r})$ as,

$$n(\mathbf{r}) = \sum_{i}^{N} |\phi_i(\mathbf{r})|^2. \tag{1.127}$$

The method of the Lagrange multipliers can then be used to perform the mini-

mization with the Lagrangian

$$\mathcal{L}[\{\phi_i(\mathbf{r})\}] = E[\{\phi_i(\mathbf{r})\}] - \sum_{i=1}^{N} \varepsilon_i \Big(\int \phi_i^*(\mathbf{r})\phi_i(\mathbf{r}) d^3r - 1 \Big). \tag{1.128}$$

The Lagrange multiplier ε_i is associated to the normalization condition of $\phi_i(\mathbf{r})$. The functional derivative of the Lagrangian $\mathcal{L}$ with respect to $\phi_i^*(\mathbf{r})$ leads to the following equation,

$$\Big(-\frac{1}{2}\nabla^2 + V_{\text{ext}}(\mathbf{r}) \Big)\phi_i(\mathbf{r}) + \frac{\delta E_{\text{Hxc}}[n]}{\delta \phi_i^*(\mathbf{r})} = \varepsilon_i \phi_i(\mathbf{r}), \tag{1.129}$$

since the Lagrangian $\mathcal{L}$ should be stationary with respect to the variations of orbitals $\phi_i(\mathbf{r})$. The derivative of the functional Hartree-exchange-correlation energy $E_{\text{Hxc}}[n]$ with respect to $\phi_i^*(\mathbf{r})$ is given by,

$$\frac{\delta E_{\text{Hxc}}[n]}{\delta \phi_i^*(\mathbf{r})} = \int \frac{\delta E_{\text{Hxc}}[n]}{\delta n(\mathbf{r}')} \frac{\delta n(\mathbf{r}')}{\delta \phi_i^*(\mathbf{r})} d^3r'. \tag{1.130}$$

One can introduce the Hartree-exchange-correlation potential $V_{\text{Hxc}}(\mathbf{r})$, which is a functional of the density, as the function derivative of $E_{\text{Hxc}}[n]$ with respect to $n(\mathbf{r})$

$$V_{\text{Hxc}}(\mathbf{r}) = \frac{\delta E_{\text{Hxc}}[n]}{\delta n(\mathbf{r})}. \tag{1.131}$$

Using the decomposition $E_{\text{Hxc}}[n] = E_{\text{H}}[n] + E_{\text{xc}}[n]$, where $E_{\text{H}}[n]$ is the Hartree energy functional, and $E_{\text{xc}}[n]$ is the exchange-correlation energy functional, we get,

$$V_{\text{Hxc}}(\mathbf{r}) = \frac{\delta E_{\text{H}}[n]}{\delta n(\mathbf{r})} + \frac{\delta E_{\text{xc}}[n]}{\delta n(\mathbf{r})} = V_{\text{H}}(\mathbf{r}) + \frac{\delta E_{\text{xc}}[n]}{\delta n(\mathbf{r})}, \tag{1.132}$$

where the Hartree potential $V_{\text{H}}(\mathbf{r}) = \frac{\delta E_{\text{H}}[n]}{\delta n(\mathbf{r})}$ is defined as:

$$V_{\text{H}}(\mathbf{r}) = \int \frac{n(\mathbf{r}')}{|\mathbf{r} - \mathbf{r}'|} d^3r'. \tag{1.133}$$

Furthermore, from Eq. (1.127) one can obtain the derivative of $n(\mathbf{r})$ with respect to the orbitals $\phi_i(\mathbf{r})$

$$\frac{\delta n(\mathbf{r}')}{\delta \phi_i^*(\mathbf{r})} = \phi_i(\mathbf{r})\delta(\mathbf{r} - \mathbf{r}'). \tag{1.134}$$

Injecting Eq. (1.134) into Eq. (1.130) and using the definition given in Eq. (1.132) of the Hartree-exchange-correlation potential $V_{\text{Hxc}}(\mathbf{r})$, we finally obtain the Kohn-Sham equations

$$H_{\text{eff}}(\mathbf{r})\phi_i(\mathbf{r}) = \varepsilon_i \phi_i(\mathbf{r}), \tag{1.135}$$

where ε_i are the KS orbital energies with $H_{\text{eff}}(\mathbf{r}) = -\frac{1}{2}\nabla^2 + V_{\text{eff}}(\mathbf{r})$ the one-electron KS Hamiltonian and $V_{\text{eff}}(\mathbf{r}) = V_{\text{ext}}(\mathbf{r}) + V_{\text{Hxc}}[n](\mathbf{r})$ the so-called KS potential. The orbitals ϕ_i which satisfy the KS equation (1.135) are called KS orbitals. The KS equations constitute a set of coupled self-consistent equations since the potential $V_{\text{Hxc}}[n](\mathbf{r})$ depends on all the occupied orbitals $\{\phi_i(\mathbf{r})\}_{i=1,\ldots,N}$ through the density $n(\mathbf{r})$. The ground-state density $n(\mathbf{r})$ of the KS system of N non-interacting electrons, defined by the effective Hamiltonian H_{eff}, is the same that the exact ground-state density $n_0(\mathbf{r})$ of the physical system of N interacting electrons. The exact ground-state energy E_0 is then easily obtained by injecting the KS orbitals into Eq. (1.126).

Ideally, DFT is an exact theory and, with the Kohn-Sham method described previously, the approach is very appealing since the solution of a self-consistent one-body problem is much simpler than the original correlated many-body problem. Unfortunately, the exchange-correlation (xc) energy E_{xc} cannot be determined exactly and must be approximated. A number of approximations exist, such as the local-density approximation (LDA) [142, 143] or the generalized gradient approximation (GGA) [144, 145] which are the ones used in the results shown in this thesis.

1.3.2 Time-Dependent Density Functional Theory

The DFT can only be used to calculate physical quantities related to the ground-state of the system. To calculate the response of a system to an external perturbation one needs to implement the time-dependent DFT (TDDFT). A system under a time-dependent perturbation can be described by the time-dependent wave function, which satisfies the time-dependent Schrödinger equation [138]:

$$\hat{H}(t)\psi(t) = i\frac{d\psi(t)}{dt}, \tag{1.136}$$

with $\hat{H}(t)$ the time-dependent Hamiltonian similar to the time-independent Hamiltonian but with a time-dependent external potential V_{ext}. The initial (unperturbed at $t = 0$) wave function is typically obtained from the ground-state obtained within DFT. Moreover, as E. Runge and E. K. U. Gross demonstrated in 1984 [146], and in analogy to the HK theorems of DFT, in TDDFT there is a correspondence between the time-dependent density $n(\mathbf{r};t)$ and the external perturbation $V_{\text{ext}}(\mathbf{r};t)$, except for a constant. Following the idea of Kohn and Sham, one can define a fictitious system of non-interacting electrons that satisfy the time-dependent Kohn-Sham equations:

$$i\frac{\partial\phi_i(\mathbf{r};t)}{\partial t} = \left[-\frac{\nabla^2}{2} + V_{\text{eff}}[n](\mathbf{r};t)\right]\phi_i(\mathbf{r};t), \tag{1.137}$$

where $n(\mathbf{r};t)$ is the electron density computed from the time-dependent KS orbitals $\phi_i(\mathbf{r};t)$ similarly to Eq. (1.127) but now depending on time,

$$n(\mathbf{r};t) = \sum_{i=1}^{N} |\phi_i(\mathbf{r};t)|^2. \tag{1.138}$$

The KS density $n(\mathbf{r};t)$ is defined to be precisely that of the real system. By virtue of the one-to-one correspondence, the potential $V_{\text{eff}}(\mathbf{r};t)$ yielding this density is unique. We then define the xc potential, $V_{\text{xc}}(\mathbf{r};t)$, as part of the total effective potential, $V_{\text{eff}}(\mathbf{r};t)$, as:

$$V_{\text{eff}}(\mathbf{r};t) = V_{\text{ext}}(\mathbf{r};t) + V_{\text{H}}(\mathbf{r};t) + V_{\text{xc}}(\mathbf{r};t), \tag{1.139}$$

where the Hartree potential is given by

$$V_{\text{H}}(\mathbf{r};t) = \int d^3r' \frac{n(\mathbf{r}';t)}{|\mathbf{r}-\mathbf{r}'|}. \tag{1.140}$$

The xc potential $V_{\text{xc}}(\mathbf{r};t)$ is a functional of the entire history of the density, $n(\mathbf{r};t)$. This time-dependent functional $V_{\text{xc}}(\mathbf{r};t)$ is more complex than the similar functional for the ground-state case, and its knowledge implies the solution of all the time-dependent Coulomb interacting problems.

According to the KS theorem discussed previously, the ground-state of a quantum system is determined uniquely if the ground-state is non-degenerate. Therefore, the time-dependent xc potential is a functional of the time-dependent density alone only if the many-electron and KS wave functions are non-degenerate.

In ground-state DFT, the xc potential $V_{\text{xc}}(\mathbf{r};t=0)$ is the functional derivative of the xc energy functional $E_{\text{xc}}[n]$, i.e., $V_{\text{xc}}(\mathbf{r}) = \frac{\delta E_{\text{xc}}[n]}{\delta n(\mathbf{r})}$. It would be useful to find an xc functional $E_{\text{xc}}[n]$ whose functional derivative gives the xc potential $V_{\text{xc}}(\mathbf{r};t) = \frac{\delta E_{\text{xc}}[n](t)}{\delta n(\mathbf{r};t)}$. In this work, we are using adiabatic time-dependent xc functionals. In the adiabatic functionals, the xc action $A_{\text{xc}}[n](\mathbf{r};t)$ depends on the instantaneous density $n(\mathbf{r};t)$, i.e., there is no memory of previous times. This is a strong but very common approximation. Besides allowing us to use any standard approximation for the ground-state (as far as the xc kernel can be computed), this approximation solves the problem of the causality breaking, since all xc effects only depend on the instantaneous electron density. Moreover, in this thesis we mainly focus on spectroscopy properties of the system, therefore we will further assume a weak time-dependent perturbation $\delta V_{\text{ext}}(\mathbf{r};t)$ to the time-independent external potential $\widetilde{V}_{\text{ext}}(\mathbf{r})$,

$$V_{\text{ext}}(\mathbf{r};t) = \widetilde{V}_{\text{ext}}(\mathbf{r}) + \delta V_{\text{ext}}(\mathbf{r};t). \tag{1.141}$$

The perturbation theory for TDDFT can be formulated via so-called linear-response functions. In the following we discuss the linear-response theory within TDDFT.

1.3.3 Linear-Response Theory

Spectroscopic information about optical excitations within the time-dependent KS formalism can be extracted using the time-dependent KS Eqs. (1.137) - (1.139) with a simple adiabatic functional for the time-dependent xc potential $V_{\text{xc}}[n](\mathbf{r};t)$. The system is usually assumed to be in its ground-state before the perturbation is applied at $t = 0$, and therefore the KS ground-state (occupied KS orbitals) can be used

as the initial state. We can compute the time-dependent induced dipole moment $D_i(t) = \int \mathbf{r}_i \delta n(\mathbf{r};t) d^3r$ by adding a weak kick-like perturbation $\delta V_{\text{ext}} = \mathbf{E}_{\text{ext}} \cdot \mathbf{r}\, \delta(t)$ at instant $t = 0$, and solving the KS Eqs. (1.137) - (1.139). The Fourier transform of the induced dipole moment, $D_i(t)$ will give the spectrum of the dipole polarizability $\alpha(\omega)$, which is related to the optical absorption cross section given by Eq. (1.112). In fact, this procedure is found in many implementations of TDDFT [147, 148].

Compared to real-time TDDFT, linear-response TDDFT is restricted to small perturbations, and usually misses some information on the excitations (non-linear processes) and some other effects (charging/discharging) that are modeled within real-time TDDFT. Nevertheless, the computational cost of linear-response TDDFT is notably smaller than that of real-time TDDFT, as the frequency resolution of the latter is linked to the total propagation time, which also requires stable algorithms. Moreover, real-time TDDFT also requires sufficiently stable algorithms for the time propagation, which are not completely trivial [147, 148]. On the other hand, linear-response TDDFT is less general, although being formulated directly in frequency domain, it simplifies the interpretation of the results. Moreover, as described below, it can be formulated in an efficient way that allows for studying very large systems.

In the framework of linear-response TDDFT, the induced charge density $\delta n(\mathbf{r};t)$ is given by the convolution product in time of the external potential $\delta V_{\text{ext}}(\mathbf{r};t)$ with the so-called response function $\chi(\mathbf{r},\mathbf{r}';t)$:

$$\delta n(\mathbf{r};t) = \int dt' \int d^3r \chi(\mathbf{r},\mathbf{r}';t-t') \delta V_{\text{ext}}(\mathbf{r}';t'), \tag{1.142}$$

i.e., if the external potential is slightly changed at positione $\mathbf{r}$ and time t', χ encodes the information about how the density will be changed at point $\mathbf{r}$ and later time t. Moreover, we note that χ is a function only of $t - t'$, and not of (t, t'), as it does not depend on the time t_0 at which the perturbation is switched on. Since the present framework is in real-space, we can drop the spatial variables temporarily for the sake of clarity:

$$\delta n(t) = \int dt' \chi(t-t') \delta V_{\text{ext}}(t'). \tag{1.143}$$

Now, the Fourier transform of this expression is simply

$$\delta n(\omega) = \chi(\omega) \delta V_{\text{ext}}(\omega), \tag{1.144}$$

or

$$\delta n(\omega) = \chi_0(\omega) \delta V_{\text{eff}}(\omega), \tag{1.145}$$

where $\delta V_{\text{eff}} = \delta V_{\text{ext}} + V_{\text{Hxc}}$ is the KS potential which includes the small perturbation δV_{ext}, and $\chi_0(\omega)$ is the non-interacting response as defined in Eq. (1.145). In particular, $\chi_0(\omega)$ encodes how the non-interacting KS electrons would respond to changes in the effective potential $\delta V_{\text{eff}}(\omega)$. Thus, although χ and χ_0 are generally

different quantities, both must yield the same density response $\delta n(\omega)$. The reason behind using Eq. (1.145) over Eq. (1.144) is that $\chi_0(\omega)$ has a close expression in terms of KS orbitals and energies, which is not the case of $\chi(\omega)$:

$$\chi_0(\mathbf{r},\mathbf{r}';\omega) = \lim_{\varepsilon\to 0}\sum_{n,m}(f_n - f_m)\frac{\phi_n^*(\mathbf{r})\phi_m(\mathbf{r})\phi_m^*(\mathbf{r}')\phi_n(\mathbf{r}')}{\omega - (E_m - E_n) + i\varepsilon}, \tag{1.146}$$

where (n,m) are indices summing over the KS orbitals, and ϕ_n and E_n are the KS states and eigenfrequencies, respectively. Moreover, f_n are occupation terms: if n and m are both occupied or unoccupied states then $f_n - f_m = 0$, otherwise, $f_n - f_m \neq 0$. The constant ε is an infinitesimally small value to avoid divergency. Thus, χ_0 is obtained from the occupied and virtual ground-state KS orbitals ϕ_n obtained within DFT. In particular, if the Hartree-exchange-correlation potential V_{Hxc} is set not to change in response to the external perturbation $\delta V_{\text{ext}}(\omega)$, we end up with $\chi = \chi_0$. In such situation the excitations of the system can be exactly described as one-electron excitations in the KS potential obtained from the ground-state density. From Eqs. (1.145) and (1.144) we obtain:

$$\begin{cases} \chi(\omega) = \dfrac{\delta n(\omega)}{\delta V_{\text{ext}}(\omega)}, \\ \chi_0(\omega) = \dfrac{\delta n(\omega)}{\delta V_{\text{eff}}(\omega)}. \end{cases} \tag{1.147}$$

Since $\delta V_{\text{eff}}(\omega) = \delta V_{\text{ext}}(\omega) + \delta V_{\text{Hxc}}(\omega)$, taking the variational derivative with respect to $\delta n(\omega)$, we get:

$$\frac{\delta V_{\text{eff}}(\omega)}{\delta n(\omega)} = \frac{\delta V_{\text{ext}}(\omega)}{\delta n(\omega)} + \frac{\delta V_{\text{Hxc}}(\omega)}{\delta n(\omega)}. \tag{1.148}$$

Furthermore, taking into account that $\delta V_{\text{eff}}/\delta n = \chi_0^{-1}$ and $\delta V_{\text{ext}}/\delta n = \chi^{-1}$, and defining $\frac{\delta V_{\text{Hxc}}(\omega)}{\delta n(\omega)} = K_{\text{Hxc}}(\omega)$, usually referred to as xc kernel, we obtain:

$$\chi_0^{-1}(\omega) = K_{\text{Hxc}}(\omega) + \chi^{-1}(\omega), \tag{1.149}$$

or

$$\chi^{-1}(\omega) = [\chi_0^{-1}(\omega) - K_{\text{Hxc}}(\omega) + \chi^{-1}(\omega)]^{-1}. \tag{1.150}$$

Then, after some algebra, we can obtain:

$$\chi(\omega) = \chi_0(\omega) + \chi_0(\omega)K_{\text{Hxc}}(\omega)\chi(\omega). \tag{1.151}$$

This equation is the well known Petersilka-Gossman-Gross equation [149], which can be further simplified using Eqs. (1.147):

$$[1 - \chi_0(\omega)K_{\text{Hxc}}(\omega)]\delta n(\omega) = \chi_0(\omega)\delta V_{\text{ext}}(\omega). \tag{1.152}$$

Moreover, including Eq. (1.145) into Eq. (1.147), we obtain the following system of integral equations

$$[1 - \chi_0(\omega)K_{\mathrm{Hxc}}(\omega)]\chi_0(\omega)\delta V_{\mathrm{eff}}(\omega) = \chi_0(\omega)\delta V_{\mathrm{ext}}(\omega). \tag{1.153}$$

Acting from the left in the last equation with the inverse of the non-interacting response function $\chi_0^{-1}(\omega)$, we end up with:

$$[1 - K_{\mathrm{Hxc}}(\omega)\chi_0(\omega)]\delta V_{\mathrm{eff}}(\omega) = \delta V_{\mathrm{ext}}(\omega). \tag{1.154}$$

We note that Eq. (1.154) might be slightly more handy than Eq. (1.152) because, after determination of the effective potential $\delta V_{\mathrm{eff}}(\mathbf{r};\omega)$, one can easily apply several types of analysis of the induced density $\delta n(\mathbf{r};\omega)$ [150], which are difficult to achieve otherwise. The algorithm to discretize and solve the linear Eqs. (1.151) or (1.152), developed by D. Sánchez-Portal's group [151], is further detailed in the following lines.

1.3.4 Response Function within LCAO with Numerical Atomic Orbitals

The linear combination of atomic orbitals (LCAO) method was developed in the early days of quantum mechanics to expand molecular orbitals. Using the LCAO method one can expand the KS states $\phi_n(\mathbf{r})$ in Eqs. (1.135) and (1.146) as

$$\phi_n(\mathbf{r}) = X_a^n f^a(\mathbf{r} - \mathbf{R}_a). \tag{1.155}$$

where Einstein's summation convention is used over index a, which refers to the ath atomic nucleus. The expansion coefficients X_a^n are determined by self-consistently solving Eq. (1.127) and (1.135), while $f^a(\mathbf{r})$ is a set of atomic orbitals, i.e., a set of known functions centered at the atomic nuclei R_a. The atomic orbitals $f^a(\mathbf{r})$ possess a radial-angular decomposition (using Einstein's summation convention):

$$f^a(\mathbf{r}) = f^a(r)Y_{l_a,m_a}(\mathbf{r}), \tag{1.156}$$

where $f^a(r)$ is a radial function depending on the radial distance to the origin r, and $Y_{l,m}(\mathbf{r})$ are the spherical harmonics which will be chosen as real spherical harmonics. In order to assert in the notation the independence of the radial orbitals $f^a(\mathbf{r})$ on the magentic quantum number m_a, we use also a multiplet index μ:

$$f^{a_{\mu,m}}(\mathbf{r}) = f^{\mu,m}(\mathbf{r}) = f^{\mu}(r)Y_{l_\mu,m}(\mathbf{r}). \tag{1.157}$$

In this notation, the multiplet index μ and magnetic quantum number m determine the orbital index $a = a_{\mu,m}$.

When inserting the LCAO ansatz of Eq. (1.155) into Eq. (1.146) to describe the response function, one encounters products of localized functions $f^a(\mathbf{r})f^b(\mathbf{r})$, a set of quantities that are known to be linearly dependent. There is extensive literature [152–154] on the linear dependence of products of atomic orbitals.

The approach described here and initially devised by D. Foerster [155], constructs the basis for the products of orbitals $f^a(\mathbf{r})f^b(\mathbf{r})$ relying on the diagonalization of a Coulomb metric in the basis of original orbital products $< ab|cd >$. The diagonalization is done for each atomic pair individually in order to maintain the locality of the constructed product basis (PB). Moreover, in the process of constructing, we use the spatial symmetry of the orbitals' products in order to further reduce the dimension of the diagonalized metric [151, 155]. The resulting basis set of dominant products is of controlled quality and is locally-optimal by construction. However, the dominant functions belonging to different atom pairs could still overlap strongly and, thus, the problem of linear dependence is not fully solved. Therefore, the basis of dominant products was augmented by a re-expression procedure allowing to use only atom-centered product functions. Both product basis sets, the dominant products as well as the atom-centered PB set, allow to expand the atomic orbitals products $f^a(\mathbf{r})f^b(\mathbf{r})$ within the so-called product vertex ansatz [156]:

$$f^a(\mathbf{r})f^b(\mathbf{r}) = V_\mu^{ab} F^\mu(\mathbf{r}), \tag{1.158}$$

where V_μ^{ab} are the product vertex coefficients and $F^\mu(\mathbf{r})$ are the product functions of the orbitals of two atoms [μ stands as a shorthand for the ordered pair of atoms (a, b)]. Inserting the product vertex ansatz of Eq. (1.158) into the response function [Eq. (1.146)], the following is obtained:

$$\chi_0(\mathbf{r}, \mathbf{r}'; \omega) = \sum_{\mu,\nu} F^\mu(\mathbf{r}) \chi^0_{\mu\nu}(\omega) F^\nu(\mathbf{r}'), \tag{1.159}$$

where the matrix $\chi^0_{\mu\nu}(\omega)$ is given by:

$$\chi^0_{\mu\nu}(\omega) = (f_n - f_m) \frac{(X_a^n V_\mu^{ab} X_b^m)(X_c^m V_\nu^{cd} X_d^n)}{\omega - (E_m - E_n) + i\varepsilon}. \tag{1.160}$$

Furthermore, inserting the expansion of Eq. (1.159) into the Petersilka-Grossman-Gross equation for the interacting response given in Eq. (1.151), we obtain the matrix equation:

$$\chi_{\mu\nu}(\omega) = \chi^0_{\mu\nu}(\omega) + \chi^0_{\mu\mu'}(\omega) K_{\mathrm{Hxc}}^{\mu'\nu'} \chi_{\nu'\nu}(\omega), \tag{1.161}$$

for the interacting response matrix $\chi_{\mu\nu}(\omega)$. Inserting the PB in Eq. (1.154), one gets the linear equation for the induced effective potential $\delta V^\nu_{\mathrm{eff}}(\omega)$:

$$\left[\delta_{\mu\nu} - K_{\mathrm{Hxc}}^{\mu\mu'} \chi^0_{\mu'\nu'}(\omega)\right] \delta V^\nu_{\mathrm{eff}}(\omega) = \delta V^\mu_{\mathrm{ext}}(\omega), \tag{1.162}$$

to be solved iteratively. The interaction kernel $K_{\mathrm{Hxc}}^{\mu\nu}$ is defined by

$$K_{\mathrm{Hxc}}^{\mu\nu} = \int d^3r d^3r' F^\mu(\mathbf{r}) K_{\mathrm{Hxc}}(\mathbf{r}, \mathbf{r}') F^\nu(\mathbf{r}'), \tag{1.163}$$

while the external $\delta V^{\mu}_{\text{ext}}(\omega)$ and effective $\delta V^{\mu}_{\text{eff}}(\omega)$ potentials are defined by

$$\delta V^{\mu}_{\text{ext}}(\omega) = \int d^3 r F^{\mu}(\mathbf{r}) \delta V_{\text{ext}}(\mathbf{r};\omega), \tag{1.164}$$

$$\delta V^{\mu}_{\text{eff}}(\omega) = \int d^3 r F^{\mu}(\mathbf{r}) \delta V_{\text{eff}}(\mathbf{r};\omega). \tag{1.165}$$

In the following sections we apply this method to calculate the response of a cluster with two types of external excitations, of interest in this thesis: extended electromagnetic planewaves and electron beams.

1.3.5 Optical Polarizability Tensor

The external electric field of a monochromatic electromagnetic plane wave can be expressed as $\delta \mathbf{E}_{\text{ext}}(\mathbf{r};\omega) = \mathbf{E}_0 e^{i\mathbf{k}\cdot\mathbf{r}}$, where $\mathbf{E}_0$ is the amplitude of the electric field and $\mathbf{k}$ is the wavevector. If the characteristic size of the excited system $\widetilde{R}$ is much smaller than the wavelength of the incoming field $\lambda = \frac{2\pi}{k} = \frac{2\pi c}{\omega} \gg \widetilde{R}$, the optical perturbation of the system can be accurately described by the external potential $\delta V_{\text{ext}} = \mathbf{E}_0 \cdot \mathbf{r}$, as expressed within the quasistatic approximation. The optical response $\delta V^{\mu}_{\text{eff}}(\omega)$ [μ stands as a shorthand for the ordered pair of atoms (a,b)] for any direction of the external field $\mathbf{E}_0$ can be calculated by inserting the external potential δV_{ext} in Eq. (1.162):

$$\Big[\delta_{\mu\nu} - K^{\mu\mu'}_{\text{Hxc}} \chi^0_{\mu'\nu}(\omega)\Big] \delta V^{\nu}_{\text{eff}}(\omega) = d^{\mu}_i, \tag{1.166}$$

where the dipole moment d^{μ}_i is given by

$$d^{\mu}_i = \int d^3 r F^{\mu}(\mathbf{r}) r_i, \tag{1.167}$$

and the indices i enumerates the Cartesian space coordinates (x,y,z). Once the effective KS potential $\delta V^{\nu}_{\text{eff}}(\omega)$ is known, the induced density can be calculated as

$$\delta n^i_{\mu} = \chi^0_{\mu\nu}(\omega) \delta V^{\nu}_{\text{eff}}(\omega), \tag{1.168}$$

which can be transformed back into real space

$$\delta n_i(\mathbf{r};\omega) = F^{\mu}(\mathbf{r}) \delta n^i_{\mu}. \tag{1.169}$$

We will analyze the induced charge density $\delta n(\mathbf{r},\omega)$ in Na_{380} clusters in Chapter 2 under optical excitation and in Chapter 4 for excitation with electron beams. Moreover, the quasistatic approximation gives rise to the notion of the optical polarizability tensor

$$P_{ij}(\omega) = \int d^3 r d^3 r' r_i \chi(\mathbf{r},\mathbf{r}';\omega) r'_j. \tag{1.170}$$

The absorption cross section $\sigma(\omega)$ is proportional to the trace of the imaginary part of the polarizability $P_{ij}(\omega)$

$$\sigma(\omega) = -\frac{4\pi\omega}{3c}\mathrm{Im}[P_{xx}(\omega) + P_{yy}(\omega) + P_{zz}(\omega)] \tag{1.171}$$

which provides the optical response of the whole macroscopic object under study.

1.3.6 Electron Energy Loss Spectroscopy within TDDFT

In the previous section the iterative TDDFT method was applied to compute the optical polarizability tensor within the dipole approximation. The iterative method to calculate the induced density can be used to calculate the response of the system under other external perturbations, such as fast electrons as those used in Electron Energy Loss Spectroscopy (EELS). The observable measured in experiments within EELS, using TEM, is the electron energy loss probability $\Gamma_{\mathrm{EELS}}(\omega)$ (see Chapter). Typically the electron probes carry kinetic energy ranging from tens to hundreds of keVs. For such electrons their wavelength is rather short (from 0.5 to 4 Å), and therefore the interaction of the probe with the nanoparticle is too short to provoke any change in the trajectory with significant probability. The velocity of the probing electron is therefore considered to be constant. Moreover, the current density of the probe electrons can be kept small (i.e., the separation distance between consecutive electron probes is larger than the emission wavelength) and the interaction of the probe electrons with the target electrons remains in the linear-response regime [64]. Furthermore, in this thesis we focus on valence electron excitations. The later, together with the high speed of electrons, justifies the use of a linear-response formulation to obtain standard EEL spectra.

The general expression for the electron energy loss probability $\Gamma_{\mathrm{EELS}}(\omega)$ is given in Eq. (1.57) as a function of the induced field $\mathbf{E}_{\mathrm{ind}}(\mathbf{r};\omega)$ created by the induced density $\delta n(\mathbf{r};\omega)$. As in the classical approximation, retardation effects are not relevant due to the nanometer size of the particles considered here, and therefore the Coulomb potential can be used to calculate the induced field. After some algebra [157], the electron energy loss probability can be expressed in terms of the induced density $\delta n(\mathbf{r};\omega)$ and the external potential created by the moving charge $\delta V_{\mathrm{ext}}(\mathbf{r};\omega)$:

$$\Gamma_{\mathrm{EELS}}(\omega) = -\frac{1}{\pi}\mathrm{Im}\int d^3r \delta V^*_{\mathrm{ext}}(\mathbf{r};\omega)\delta n(\mathbf{r};\omega), \tag{1.172}$$

$$= -\frac{1}{\pi}\mathrm{Im}\int\int d^3r d^3r' \delta V^*_{\mathrm{ext}}(\mathbf{r};\omega)\chi_0(\mathbf{r},\mathbf{r}';\omega)\delta V_{\mathrm{eff}}(\mathbf{r}';\omega). \tag{1.173}$$

The induced charge density $\delta n(\mathbf{r};\omega)$ can be calculated within the linear-response theory by expansion in terms of $\{F^\mu(\mathbf{r})\}$, Eq. (1.168), and using linear Eqs. (1.145) and (1.154) to compute the expansion coefficients $\delta n_\mu(\omega)$. In this way, the components of the external potential $\delta V^\mu_{\mathrm{ext}}$ are expressed by

$$\delta V^\mu_{\mathrm{ext}}(\omega) = \frac{1}{2\pi}\int dt e^{i\omega t}\int \frac{F^\mu(\mathbf{r})}{|\mathbf{r} - \mathbf{R}^\mu_{\mathrm{elec}}(t)|}d^3r, \tag{1.174}$$

where $\mathbf{R}^{\mu}_{\text{elec}}(t) = \mathbf{R}_0 + \mathbf{v}_e t - \mathbf{R}^{\mu}$ and $\mathbf{R}^{\mu}$ are the positions of atomic nuclei at which the product functions $\{F^{\mu}(\mathbf{r})\}$ are centered, and $(\mathbf{R}_0, \mathbf{v}_e)$ are the electron probe position and velocity, respectively. In order to compute the components in Eq. (1.173), we will use the Laplace expansion [113] of the Coulomb interaction and Fourier transform of the components in time domain, as

$$\begin{aligned}\delta V^{\mu}_{\text{ext}}(t) &= \int \frac{F^{\mu}(\mathbf{r})}{|\mathbf{r} - \mathbf{R}^{\mu}_{\text{elec}}(t)|} d^3r \\ &= \sum_{lm} \frac{4\pi}{2l+1} \int d^3r \frac{r^l_<}{r^{l+1}_>} Y^*_{lm}(\hat{\mathbf{r}}) Y_{lm}(\hat{\mathbf{r}}^{\mu}_{\text{elec}}(t)) F^{\mu}(\mathbf{r}),\end{aligned} \tag{1.175}$$

where $r_< = \min(r, r')$, $r_> = \max(r, r')$ and $Y_{lm}(\hat{\mathbf{r}})$ are real spherical harmonics. Since $F^{\mu}(\mathbf{r}) = F^{\mu}(r) Y_{l_\mu m_\mu}(\hat{\mathbf{r}})$ and $\int Y^*_{lm}(\hat{\mathbf{r}}) Y_{l'm'}(\hat{\mathbf{r}}) d\Omega = \delta_{ll'}\delta_{mm'}$, we can then remove the sum over l and m, obtaining,

$$\delta V^{\mu}_{\text{ext}}(t) = \frac{4\pi}{2l_\mu + 1} Y_{l_\mu m_\mu}(\hat{\mathbf{r}}^{\mu}_{\text{elec}}(t)) \int r^2 \frac{r^l_<}{r^{l+1}_>} F^{\mu}(r) dr. \tag{1.176}$$

The final step consists in separating the radial integral into two integration intervals

$$\begin{aligned}\delta V^{\mu}_{\text{ext}}(t) = \frac{4\pi}{2l_\mu + 1} Y_{l_\mu m_\mu}(\hat{\mathbf{r}}^{\mu}_{\text{elec}}(t)) \Bigg[&\frac{1}{(R^{\mu}_{\text{elec}}(t))^{l_\mu + 1}} \int_0^{R^{\mu}_{\text{elec}}(t)} r^{l_\mu + 2} F^{\mu}(|\mathbf{r}|) dr \\ &+ (R^{\mu}_{\text{elec}}(t))^{l_\mu} \int_{R^{\mu}_{\text{elec}}}^{+\infty} \frac{F^{\mu}(|\mathbf{r}|)}{r^{l_\mu - 1}} dr \Bigg].\end{aligned} \tag{1.177}$$

Using the components computed in time domain, following Eq. (1.177), we apply Fourier transform (FFT is used) and get the components as in Eq. (1.174) in the frequency domain. Although it is possible to obtain a closed analytical expression for $\delta V^{\mu}_{\text{ext}}(\omega)$ for external trajectories, i.e., when the trajectory passes outside the support region of a given product basis functions $F^{\mu}(\mathbf{r})$, general trajectories do overlap with these function, and therefore $\delta V^{\mu}_{\text{ext}}(\omega)$ is computed numerically. In principle, following the work of Ferrel and Echenique [75] it is possible to find a close analytical expression for $\delta V^{\mu}_{\text{ext}}(\omega)$. Finally the electron energy loss probability can be expressed as a scalar product using the product basis set, as

$$\Gamma_{\text{EELS}}(\omega) = -\frac{1}{\pi} \text{Im}\big(\delta V^{\mu *}_{\text{ext}}(\omega) \delta n^{\mu}(\omega)\big), \tag{1.178}$$

which is the expression implemented in the calculation of spectra in Chapter 4.

2 Optical response of metallic picocavities

Most of the fascinating properties and applications of plasmonic nanoparticles are based on the tunability of their optical response, along with their ability to enhance electromagnetic fields, squeezing the electromagnetic energy down to nanometer scale volumes around sharp tips or at interparticle gaps, producing "hot spots", behaving as effective optical nanoantennas [29, 158–160]. This is possible through the excitation of localized surface plasmons that couple efficiently to light, allowing to overcome the diffraction limit [161]. The near-field patterns in nanostructures under light excitation strongly depend on the size, composition, and shape of the individual particles, along with plasmon hybridization in coupled nanostructures.

Light scattering of nanoparticles of arbitrary shape and size is usually well addressed within a classical electrodynamics framework (with the use of a suitable dielectric function), by solving Maxwell's equations for specific compositions, morphologies, and environments [17, 162–171]. When the size or the separation distance between plasmonic nanoparticles becomes on the order of a few nanometers or even smaller, the quantum nature of the electron dynamics emerges due, among others, to the particle-size effect in the electron confinement [82, 172–175], the inhomogeneous

dynamical screening of the electron response [176, 177], the electron spill-out at the metal interfaces [31], the presence of atomistic inhomogeneities [106, 178], or even the activation of quantum tunneling [179, 180] across subnanometer interparticle gaps. All of these effects are initially not included in typical local classical electrodynamical descriptions of the optical response, and different levels of approximation have been adopted to address their influence in the optical response in extended classical models [95, 96, 181, 182]. Among all these effects, the presence of atomic-scale features at the surfaces has not been deeply explored in the context of plasmonics up to recently, due to the intrinsic limitations of most of the phenomenological classical models, which do not address the quantum effects mentioned above. A proper description of the effect of atomic-scale edges, wedges, vertices, and protrusions at surfaces requires, in principle, a complete quantum theoretical framework, which includes the atomistic structure of the nanoparticles and the wave nature of electrons building up the plasmonic excitations.

Ab initio atomistic methods provide an appropriate quantum framework to consider the aforementioned effects including the atomistic structure in a straightforward and complete manner [162, 183–186], with the drawback of being computationally demanding. Recently, a few works [106, 178, 187, 188] have shown the impact of the atomistic structure on the optical response of metal clusters of a few nanometers and dimers within atomistic time-dependent density functional theory (TDDFT) [146,189], showing that the atomistic structure at the interfaces of a metallic nanostructure needs to be considered for an accurate description of the local field distribution around atomic-scale features. It has been shown [106], that the presence of single atoms or atomic edges in facets of the nanoparticles allows for localizing and confining the near field down to subnanometric dimensions, well below the underlying plasmonic background. This level of field confinement goes beyond that of nanocavities, where the field is localized to larger nanometric regions, thus reaching the realm of *picocavities*. This has enabled a possible route toward photonics at the picoscale, where the localization of EM fields in atomic-scale cavities leads to extremely small effective mode volumes, thus boosting the coupling of photons with the electronic transitions of single emitters [42] or with the vibrations of a molecule in optomechanical interactions [43].

The quantum description of these optical picocavities at the full atomistic level reveals the importance of atomic-scale features. However, such a detailed description is often limited by the computational requirements, even with the relatively efficient TDDFT methods. Here we propose the use of a simplified local classical approach to address the optical response and the EM field distribution around picocavities. By adopting a sharp boundary interface that coincides with the electronic density profile of the atomistic distribution within a plasmonic structure we show in Sec. 2.1 that a faithful reproduction of the near-field properties of the picocavity can be achieved for single metallic nanoparticles. The extra localization of the field around atomic-scale features is identified as a non-resonant atomic-scale lightning rod effect in Sec. 2.2. This concept is extended to cover the influence of picocavities in nanogaps in Sec. 2.3. The proposed methodology is capable of exposing the extreme nanophotonic

properties of these picocavities embedded in larger structures, thus allowing standard methods of electrodynamics to address this challenging regime [107].

The data corresponding to the results obtained within TDDFT were performed by Marc Barbry in the group of Prof. Daniel Sánchez-Portal, while the DDA data was calculated by Yao Zhang in the group of Prof. Javier Aizpurua, both at the CFM in Donostia. The analysis and visualization of such data were performed by myself.

2.1 Subnanometric features in single metallic nanoparticles

To understand the effects of subnanometric features in the plasmonic response of small metallic nanoparticles, we consider nanoparticles with icosahedral symmetry that present atomic-scale features such as facets, edges and vertices. We attempt to separate the influence of these morphological features from other effects such as electron confinement, inhomogeneous dynamical screening of the electron response, the electron spill-out at the metal interfaces, etc., and analyze to what extent classical approaches can reproduce the properties of the far- and near-field obtained within atomistic quantum approaches, with special interest in the field localization and enhancement around the vertices.

For such a purpose, we use three different approaches.

i) First, we consider a Na_{380} atomistic cluster within TDDFT framework described in Chapter 1, which is the largest cluster size for which the global minimum icosahedral symmetry (as described using an effective Murrell-Mottram potential [190]) is available [191]. This structure[5] is further relaxed using density functional theory (DFT), as implemented in the SIESTA code [192, 193], within the Generalized Gradient Approximation (GGA), with the use of the Perdew-Burke-Ernzerhof functional [144]. The geometry relaxation ensures the stability of the structure and that it corresponds at least to a local minimum of the DFT energy landscape of Na_{380}. Subsequently, we obtain the TDDFT linear optical response of the cluster within the so-called adiabatic local density approximation [142, 143]. Using an iterative scheme developed by Koval and co-workers [150] we calculate the optical response at the TDDFT level for large systems at moderate computational cost [106, 150, 188, 194].

ii) Secondly, we consider the same atomistic structure within a classical approach, i.e., the dipoles within DDA [117, 121, 134, 135] are placed at the very same positions as the atoms in TDDFT. Each atom i is characterized by an atomic

[5]The initial structure of the Na380 cluster was downloaded from the Cambridge Cluster Database. Wales, D. J.; Doye, J. P. K.; Dullweber, A.; Hodges, M.; Naumkin, F.; Calvo, F.; Hernández-Rojas, J.; Middleton, T. F. http://www-wales.ch.cam.ac.uk/CCD.html.

polarizability α_i, obtained from the bulk dielectric function $\varepsilon(\omega)$ through the Clausius-Mosotti relationship, $\alpha_i \propto (\varepsilon - 1)/(\varepsilon + 2)$. Each atom is treated as a sphere with polarizability α_i, and radius $r_{at} = 2.08$ Å. The interaction between atoms is described as a point dipole-dipole one and the distance between dipoles is determined from the relaxed atomistic structures. The optical response is obtained from the total polarizability of the system, α_{tot}, given by the coherent sum of the self-consistent atomic polarizabilities $\alpha_{tot} = \sum_i \alpha_i$, i.e., the optical absorption cross section of the structure is calculated as $\sigma_{abs} = 4\pi\omega \ \mathrm{Im}(\alpha_{tot})$.

iii) Last, we consider a continuous classical approach within the Boundary Element Method (BEM), which assumes the medium within the nanoparticle (metal) to be homogeneous and isotropic and to be separated from the surrounding medium (vacuum) by an abrupt boundary interface resembling the electronic density profile of the atomistic distribution. The optical response of the metal is characterized by a local dielectric function, $\varepsilon(\omega)$. The calculations are carried out with the MNPBEM Toolbox [109, 110]. BEM requires the discretization of the boundary surfaces, instead of the whole volume of the different dielectric media, speeding up the solution of Maxwell's equations in inhomogeneous media. For the size of the nanoparticles studied in this work, below the intrinsic mean free path of conduction electrons in bulk metals, surface scattering effects become important. In order to account for this effect in the classical approach, we include a correction to the free-electron model (Drude model) of the dielectric response following the prescriptions in the literature [195], with the assumption that surface scattering effects lead to a reduced effective mean free path L_{eff}, which adds a damping factor in the Drude dielectric function of the bulk metal. When specular reflection of electrons at the boundaries is assumed, as in the so-called Billiard model [196], the effective mean free path is given by $L_{\mathrm{eff}} = 4V/A$, where V and A are the volume and area of the nanoparticle, respectively [197]. Therefore, we adopted the modified Drude model of the dielectric function given by

$$\varepsilon(\omega) = \varepsilon_\infty - \frac{\omega_p^2}{\omega^2 + i\omega\left(\frac{v_{\mathrm{F}}}{L_{\mathrm{eff}}} + \gamma_d\right)} \tag{2.1}$$

where $\omega_p = 6.05$ eV [198] is the Na plasma frequency, v_{F} is the Fermi velocity ($v_{\mathrm{F}} = 1.07 \times 10^6$ m/s for Na [198]) and the intrinsic damping term is $\gamma_d = 27.6$ meV [199].

More details about the three approaches used to perform the numerical calculations are included in Chapter 1.

2.1.1 Influence of smoothening nanoparticle tips and edges

While the atomistic structure of nanoclusters is constrained by the crystallography and relaxation of the structure, continuous approaches such as that developed within

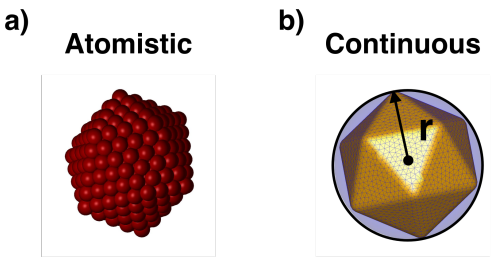

Figure 2.1: (a) Atomistic cluster composed by 380 atoms (dipoles) used in TDDFT (DDA) calculations. (b) Sketch of the continuous icosahedral cluster used in BEM calculations. The sphere of radius $r = 18.5$ Å surrounding the icosahedron has been drawn for reference. The tips and edges have been rounded to have a minimum cap radius of $r_{\mathrm{Na}} = 2.08$ Å.

BEM have the "freedom" to model any shape, a versatile aspect which can be exploited with care, and adapted to the context. For instance, an infinitely sharp apex is unphysical, even more for Ångstrom scales, and thus it usually requires some smoothening or rounding of the surface. We choose the endings of tips and edges in our structures to be rounded by means of a spherical cap of radius $r_{\mathrm{Na}} \sim 2.08$ Å (Wigner-Seitz radius of sodium) as shown in Fig. 2.2, i.e., we consider these ending-features to have the curvature of an atom approximated by a sphere.

Figure 2.3 shows the absorption cross section of single icosahedral particles of radii $r = 1$ nm, 1.6 nm, 1.8 nm and 2 nm with non-smoothened and with smoothened tips and edges in their surface morphology following the approach iii) described above. The radius r is defined as the minimum radius of the sphere surrounding the non-smoothened icosahedrons thus, the smoothened nanoparticles after the rounding are slightly smaller. The smoothening radius r_{Na} has been kept fixed for all particle sizes, while the damping term in the dielectric function due to surface scattering effects depends on the size of the nanoparticle following Eq. 2.1. Overall, the spectra show a dominance of the dipolar plasmonic (DP) mode, but the relative weight of higher-order modes with respect to the DP is larger in particles with sharp geometries (dashed lines) than in smoothened geometries (continuous lines). Also the plasmonic resonances of the smoothened geometries are slightly blue-shifted and spectrally more dispersed, as compared to the non-smoothened ones.

Regarding the influence of size in the absorption cross section, as the smoothening radius is kept constant for different particles sizes, the smaller the particle, the smoother its overall shape is, i.e., more similar to a sphere. Thus, the particle size affects both the relative weight and position of the plasmon peaks for smoothened NPs. On the other hand, for decreasing particle sizes, the damping due to surface-scattering effects increases, broadening the signal and smearing out the effects of the particle smoothening on the spectrum, which is observed for example in the response of the particle with $r = 1$ nm in Fig. 2.3, where only a broad peak can be distinguished.

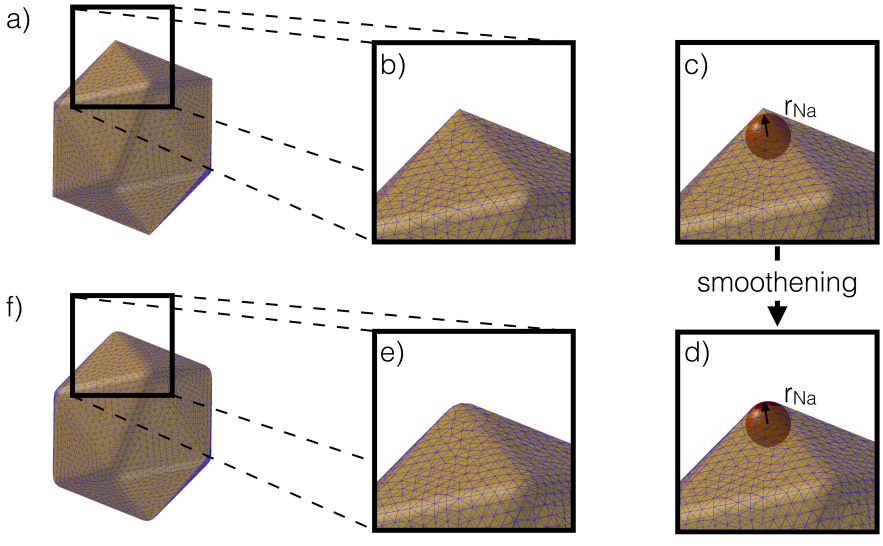

Figure 2.2: (a) Surface mesh used to model the initial regular icosahedral particle (sharp tips and edges). (b) Detail of one of the tips to be smoothened. (c) Location of the sphere of radius r_{Na} used to smoothen the tip. (d) Smoothened tip with the spherical cap in place. The smoothened surface matches the contour of the sphere. (e) Detail of the tip of the final smoothened particle. (f) Complete view of the final smoothened icosahedral particle. The number of elements of the surface mesh is kept constant during the smoothening process.

2.1.2 Far-field and near-field optical response of single nanoparticles

Now that we have set the procedure of the rounding of a continuous cluster, we explore the optical response and field localization around atomic-scale features associated with the edges and vertices of nanoparticle morphologies in isolated particles within the three different approaches. To that end we perform calculations of the absorption cross section and near-field distribution in single Na icosahedral clusters using the numerical methods introduced in Chapter 1. As mentioned above, quantum atomistic calculations adopt the geometry shown in Fig. 2.1(a), whereas the classical local calculations adopt the smooth icosahedral shape displayed in Fig. 2.1(b) (with $r = 1.85$ nm). Additionally, the situation of a smooth spherical geometry with no atomic-scale features is also considered as a reference. The absorption cross sections obtained from the three approaches are compared in Fig. 2.4. In the TDDFT calculation (blue line) we observe a single peak at 3.15 eV, corresponding to the dipolar plasmon (DP) resonance, and a shoulder at around 3.8 eV. In the DDA calculation (green line) we observe a single peak at 3.25 eV corresponding to the DP and a broad shoulder. The BEM calculation (red line) shows two clear peaks emerging at 3.2 eV and 3.6 eV, and corresponding to the DP and a higher order plasmon (HOP) mode, respectively.

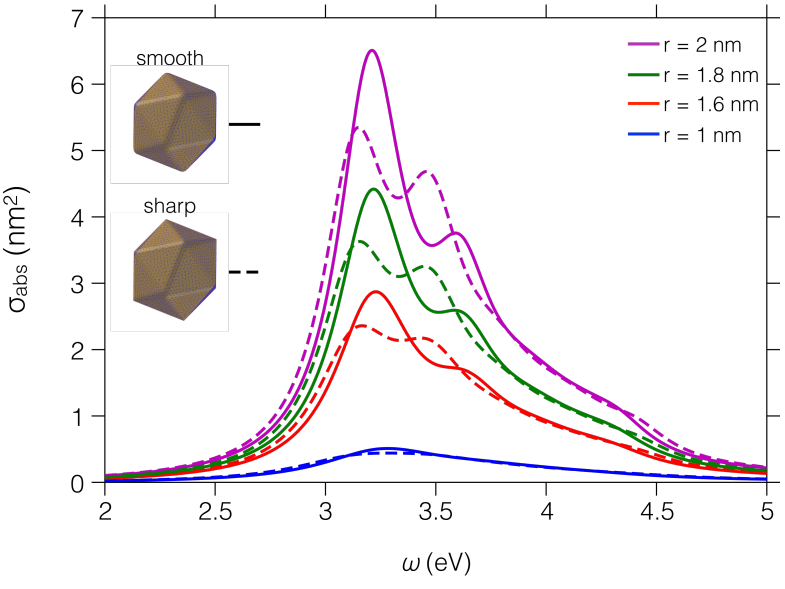

Figure 2.3: Absorption cross-section as a function of energy for icosahedral nanoparticles with smoothened (straight lines) and sharp (dashed lines) tips and edges in their morphology, as obtained using the BEM. The radii of the minimum sphere surrounding the nanoparticles are $r = 1$ nm, 1.6 nm, 1.8 nm and 2 nm. The smoothening radius has been set to $r_{\mathrm{Na}} = 2.08$ Å for all the nanoparticle sizes.

:

Moreover, due to the high symmetry of the system, the dependence of the far-field on the polarization of incident light is negligible.

The difference in the energies of the DP among the different models is minimal, but more pronounced differences can be found in their intensity, especially in the calculation with DDA. Moreover, when smoother geometries are considered in the classical BEM calculations, there is a predominance of the DP mode and a smearing out of the HOP mode, as shown in Fig. 2.3. This explains the presence of a clear second peak in the BEM cross section, as compared to the shoulder obtained in the full quantum calculation, effectively rounded by the effect of the electron cloud spilling at the interfaces. The spectrum corresponding to a classical spherical particle, of similar size ($r = 1.85$ nm) sketched in Fig. 2.1(b), is also shown (dashed black line) for reference. A single peak, corresponding to the DP, emerges at 3.45 eV for the smooth spherical particle. The difference in the intensity of the DP arises in part due to the activation of higher order modes in the case of the icosahedral particle.

One of the most important aspects of an optical resonator is its capacity to localize the optical mode to an effective volume as small as possible. In Fig. 2.5 the field distribution around the Na nanoparticle is mapped for two perpendicular incident polarizations. The energy considered in all the plots corresponds to the dipolar plasmonic resonance. Data are displayed in the (y, z) plane passing through the center of the particle. The polarization of the incident field is parallel to the y-axis for the plots

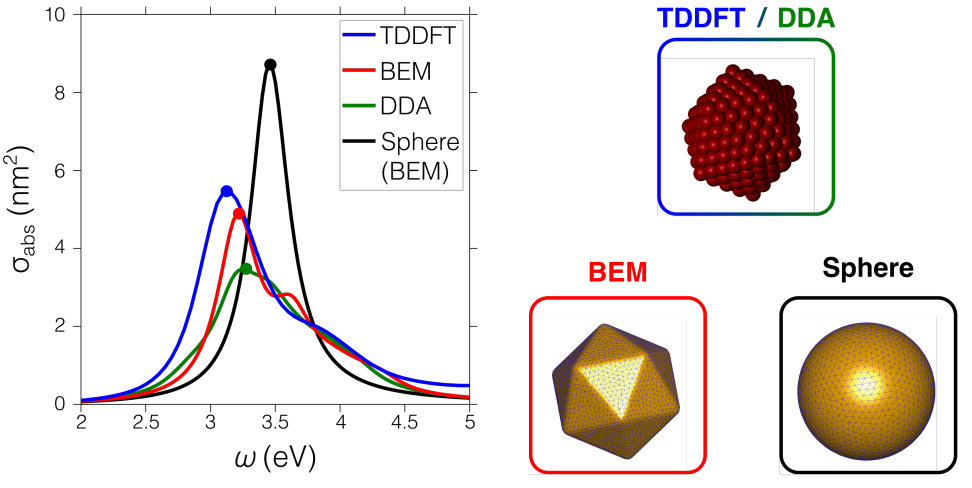

Figure 2.4: Absorption cross-section of a Na particle calculated using TDDFT (blue line), BEM (red line) and DDA (green line). The energies of the dipolar plasmons obtained for all three models are highlighted by round dots. The dashed black line corresponds to the absorption cross section of the sphere in Fig. 2.1 b), as calculated with BEM. A peak corresponding to a higher order plasmon (HOP) is observed for BEM at $\omega = 3.6$ eV, while a shoulder is appreciated for TDDFT and DDA around $\omega \sim 3.8$ eV. TDDFT data provided by Marc Barbry and DDA data provided by Yao Zhang, both in CFM.

on the top row, and along the z-axis for the plots on the bottom row. The atomistic structure of the nanoparticle clearly emerges in the TDDFT and DDA results (left and right columns), and as one might expect, there is no atomistic contrast in the classical near-field map (middle column), due to the continuous description of the media interfaces within this model. Remarkably, both model descriptions reproduce very similarly the effect of localization of the near field at the atomic protrusions within the particles interfaces (at their tips and edges), giving rise to pronounced atomic scale "hot spots". These subnanometric-scale hot spots are clearly identified in all the field distributions on top of the plasmonic nanometric background, and they are also correctly captured by the classical local description (middle column). One can thus conclude that it is possible to describe the main features of sub-nanometric localization of the fields if the atomistic structure of the particle is correctly approximated by a smooth and continuous surface. This extreme confinement of the field to subnanometric effective volumes goes beyond that of *nanocavities*, where the field is localized to nanometric regions, so these cavities showing subnanometric localization are referred to as *picocavities*.

These results set the validity of classical approaches to effectively address the actual local field distribution around atomistic features, even in the most extreme situations of localization. With this result at hand, it can be proposed that atomic-scale hot spots in large plasmonic configurations can be correctly tackled by a proper classical approach which accounts for the atomistic structure geometrical profile.

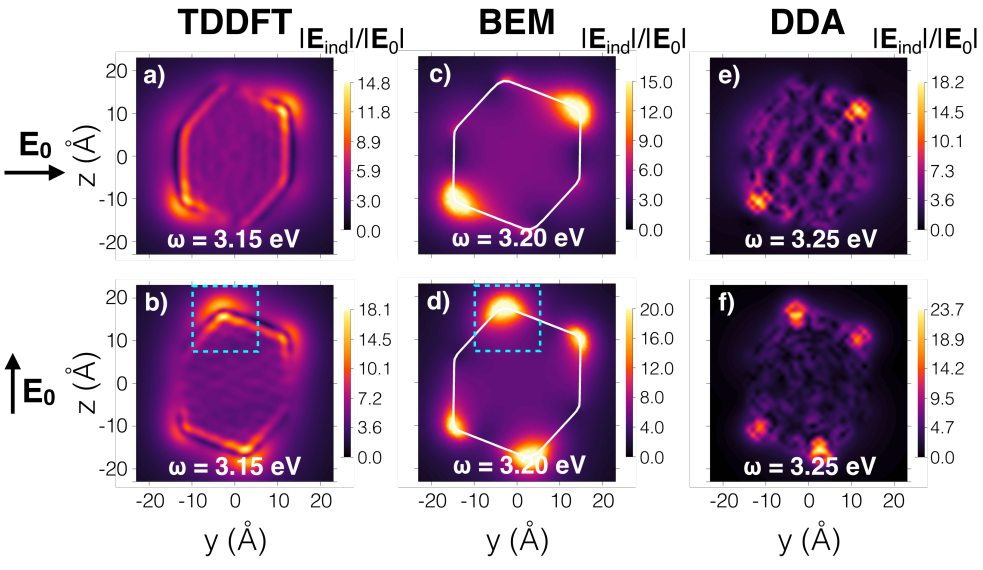

Figure 2.5: Induced near-field enhancement for a single icosahedral Na nanoparticle obtained using (a-b) TDDFT, (c-d) BEM, and (e-f) DDA. The external field E_0 is polarized along the y axis (top row) and along z axis (bottom row). TDDFT data provided by Marc Barbry and DDA data provided by Yao Zhang, both in CFM.

Next we analyze deeper the physical mechanism underlying this atomic-scale optical localization.

2.2 Atomic-scale lightning rod effect

In the previous section we have studied the influence of atomic-scale features in the optical response of single metallic nanoparticles, and observed that the electromagnetic field can be localized in subnanometric regions. In this section we will show that this extra-localization of the field around atomistic features is sustained by a non-resonant effect which cooperates with the overall plasmonic enhancement produced by the collective oscillation of the electronic surface charge density in the nanoparticle. At the macroscopic scale, it is well known that isopotential regions which expel the electric field and present a pronounced geometrical curvature produce an abrupt change of the electrical potential, $\phi(\mathbf{r})$, in their proximity (large potential gradient), and thus strong induced electric fields $\mathbf{E}_{\text{ind}}$, since, in the quasistatic limit, $\mathbf{E}_{\text{ind}} = -\nabla\phi(\mathbf{r})$. The field enhancement following a strong potential gradient due to the curvature of a perfectly metallic curved interface is commonly described as the

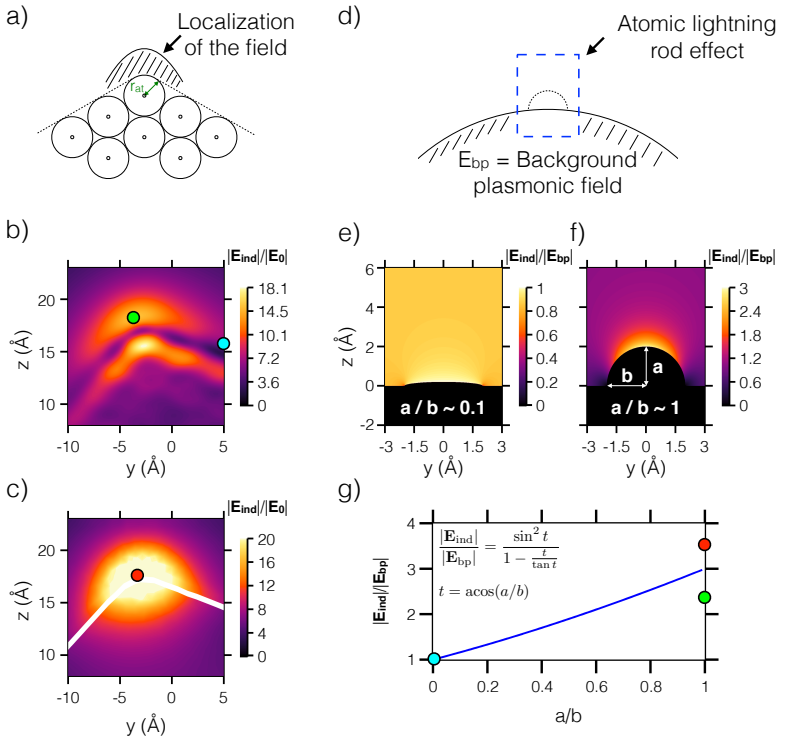

Figure 2.6: a) Sketch showing a tip on an icosahedral atomistic nanoparticle used in TDDFT (circles represent atoms). The dotted line along the nanoparticle interface shows the surface used in the BEM calculations. The zone where the field is localized has been highlighted with oblique lines. (b) Zoom-in of the region enclosed by the cyan dashed lines of the TDDFT near-field maps from Fig. 2.5(b); (c) zoom-in of the BEM near-field maps from Fig. 2.5(d). (d) Sketch of an atomic protrusion on a spherical nanoparticle that produces an atomic lightning rod effect enhancing the background plasmonic field given by the spherical nanoparticle. (e) Near-field enhancement map of the induced electric field $|\mathbf{E}_{\rm ind}|$ with respect to the background plasmonic field $|\mathbf{E}_{\rm bp}|$, corresponding to an almost flat protrusion ($a/b \approx 0.1$), with practically no enhancement of the field. (f) Near-field enhancement map as in (e), corresponding to a spherical protrusion ($a/b \approx 1$), giving a maximum field enhancement, $|\mathbf{E}_{\rm ind}|/|\mathbf{E}_{\rm bp}|$, of ≈ 3. (g) Field enhancement at the boundary ($x = 0$, $z = a$) of an oblate spheroidal protrusion as a function of the aspect ratio. The colored dots correspond to the field enhancements at the positions marked in panels (b) and (c). The enhancement of the induced fields has been calculated with respect to the plasmonic background field, $|\mathbf{E}_{\rm bp}|$, obtained at the boundary of a typical spherical surface, which is on the order of $|\mathbf{E}_{\rm bp}| \approx 6$ [blue dot as a reference in (g)]. TDDFT data provided by Marc Barbry in CFM.

"lightning rod effect". In analogy to the macroscopic situation, in the proximity of an atomic protrusion, an atomic-scale lightning rod effect is produced, which is responsible for the extra localization at the tips and edges of an interface [see schematics in Fig. 2.6(a)]. In spite of the strong quantum effects that govern the optical response of the electron gas at the subnanometric scale, including dynamical screening and spill-out, the main features of the field localization and enhancement in atomic protrusions

can be correctly addressed by the consideration of a sharp curvature that follows the atomistic profile, as demonstrated with the quantum and classical calculation of this effect in Fig. 2.5(a-d). A zoom-in of the near field around one of these protrusions [marked with blue dashed squares in Figs. 2.5(b,d)] is displayed in more detail in Figs. 2.6(b,c). The classical calculation faithfully reproduces the spatial extension and the intensity of the quantum atomic-scale localization, with a field distribution that corresponds to a protrusion of the size of the metal atomic radius.

From *nano*cavities to *pico*cavities

Photonic resonators or cavities withstand standing optical waves (modes) and thus can be used to store energy. Their main properties are given by the quality factor Q, which gives the rate of energy loss relative to the energy stored in the resonator in each optical cycle, and the effective mode volume V_{eff}, which describes the spatial extension of the mode (i.e., how much is light confined) within the cavity. Plasmonic nanoparticles and nanogaps present low Q values ($Q \sim 10$) due to their intrinsic losses, but are able to confine the electromagnetic field to nanometric dimensions ($V_{\text{eff}} > 1 - 100$ nm^3), and are therefore referred to as *nano*cavities. The presence of atomic protrusions or features on these nanostructures can produce an atomic-scale lightning rod effect that, when mounted on a plasmonic resonance, decreases the V_{eff} to subnanometric dimensions ($V_{\text{eff}} < 1$ nm^3), and are thus referred to as *pico*cavities. These picocavities define the ultimate limit of the confinement of light provided by condensed matter, which relies on the lightning rod effect associated with the potential profile driven by the electron density in the vicinity of a protruding atom.

A quantitative estimation of the atomic-scale lightning rod effect can be inferred from a quasistatic analysis of the field distribution around a semispheroidal feature on top of a metallic flat interface [see schematics in Fig. 2.6(d)]. The exemplary semispheroidal feature mimics an atomic protrusion and is characterized by a semiwidth b, and a semiheight a, as depicted in Fig. 2.6(f). We consider an incident background plasmonic field $\mathbf{E}_{\text{bp}}$, which would be the induced field in a spherical particle without corrugations, and calculate the induced field $\mathbf{E}_{\text{ind}}$ distribution and intensity around the semispheroidal protrusion for two distinctive situations: (i) a featureless protrusion of very small height ($a/b \approx 0.1$) in Fig. 2.6(e), and (ii) half an atom protruding from the flat surface ($a/b \approx 1$) in Fig. 2.6(f), mimicking the supporting particle surface (of much larger radius). Whereas the featureless protrusion hardly provides any field enhancement ($|\mathbf{E}_{\text{ind}}|/|\mathbf{E}_{\text{bp}}| \approx 1$), the atomic-sized protrusion produces a 3-fold extra enhancement over the incident background field. The full set of field enhancements obtained for all the different values of a/b are shown in Fig 2.6(g), which is given by:

$$\frac{E}{E_{\text{bp}}} = \frac{\sin^2 t}{1 - \frac{t}{\tan t}}, \tag{2.2}$$

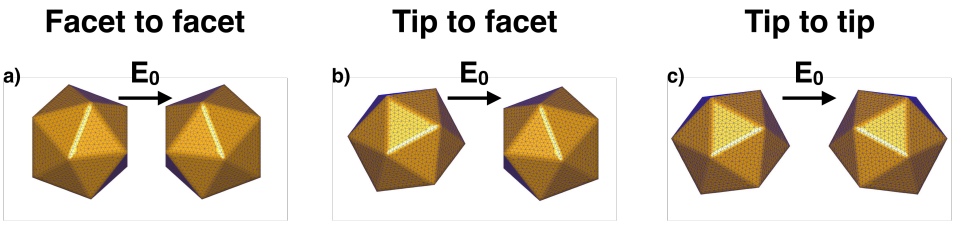

Figure 2.7: Sketch of the three inter-particle gap geometries considered, a) facet-to-facet , b) tip-to-facet and c) tip-to-tip, and the polarization of the incident electric field E_0, oriented along the dimer axis.

where $t = \text{acos}(a/b)$. This analytical estimation is in very good agreement with the actual values obtained from the classical and quantum calculations (red and green dots in Fig. 2.6(g), respectively), validating the interpretation of a non-resonant lighting rod effect at the atomic scale as responsible for the extra enhancement observed in atomistic protrusions.

The good agreement between the classical and quantum results paves the way to perform simple and general calculations, and make predictions of the field enhancement produced in much larger and complex structures in which these picocavities are present. Quantum approaches generally cannot deal with nanometric structures of large size due to the high computation demands of such systems. This atomic-scale lightning rod effect is commonly present in many situations in nanophotonics, as for instance in molecular spectroscopy, where the subnanometric localization of the field has been key to resolve single-molecule picoscopy [43].

2.3 Picocavities in plasmonic nanogaps

We have analyzed the optical response of picocavities present in single metallic nanoparticles, and characterized the subnanometric localization as an atomic-scale lightning rod effect. One of the best plasmonic resonators is given by the formation of a metal-insulator-metal (MIM) structure, connecting two metallic nanostructures at a nanometric separation distance, forming a plasmonic nanogap as the one sketched in Fig. 3(c) of the Introduction. In order to explore the properties of local field enhancements and effective mode volumes in plasmonic nanocavities with atomic-scale protrusions, we consider three different configurations of metallic dimers formed by the sodium clusters analyzed in the previous section, according to their mutual orientation. The icosahedral clusters present atomistic features and are aligned across the gap in configurations referred to as (a) *facet-to-facet*, (b) *tip-to-facet*, and (c) *tip-to-tip*, as sketched Fig. 2.7. Moreover, the separation distance also affects the properties of the system and will be considered as a parameter.

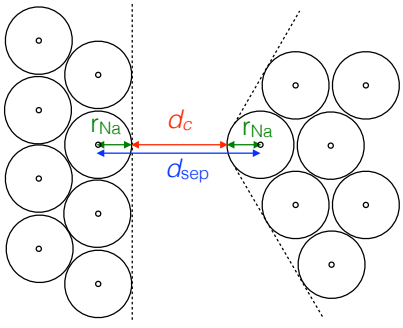

Figure 2.8: Sketch showing the parameters used to define the separation distance between particles in the three approaches. For the two atomistic models, TDDFT and DDA, the separation distance is defined as the smallest distance between the center of the atoms (circles) from opposite clusters, d_{sep}, and for the continuous approach, BEM, it is defined as the sum of the distance between the surfaces (dashed lines) that define the continuous metallic particles, d_{c}, corrected with the classical radius of a sodium atom, $r_{\mathrm{Na}} = 2.08$ Å, $d_{\mathrm{sep}} = d_{\mathrm{c}} + 2r_{\mathrm{Na}}$.

Due to the the distinct nature of the three approaches considered in this chapter, we need to define the separation distance of the gap d_{sep} differently for the atomistic approaches (TDDFT and DDA) and the continuous classical approach (BEM). For the atomistic framework, within both TDDFT and DDA, the separation distance is set as the distance between the centers of the closest gap atoms (or dipoles for DDA) from opposite clusters d_{sep}. In the case of the continuous classical description, BEM, the separation distance is considered as the distance between the closest points of the particles surfaces, d_{c}, with an additional correction term corresponding to the distance between the center of an outermost sodium atom and the surface of the particle (the Na atoms have been considered as spheres of radius $r_{\mathrm{Na}} = 2.08$ Å), $d_{\mathrm{sep}} = d_{\mathrm{c}} + 2 \cdot r_{\mathrm{Na}}$, as shown in Fig. 2.8.

2.3.1 Far-field optical response of picocavities

Before analyzing the local field and the effective mode volume, it is useful to address the far-field response of each gap configuration as a function of interparticle distance and compare the results obtained within TDDFT, BEM and DDA descriptions. We perform calculations of the absorption cross sections for the three different gap geometries corresponding to the three particle orientations, (a) facet-to-facet, (b) tip-to-facet, and (c) tip-to-tip, sketched in Fig. 2.7. We trace the optical modes of the cavities from a separation distance of $d_{\mathrm{sep}} = 20$ Å to a situation of touching and overlapping of the particles ($d_{\mathrm{sep}} \leq 4$ Å). The polarization of the incident light is oriented along the dimer axis.

The absorption cross section of all the plasmonic gaps is mainly characterized by the existence of a bonding dimer plasmon (BDP) that slightly redshifts when the two particles approach [26,30]. This effect is very clear in the classical calculations (middle

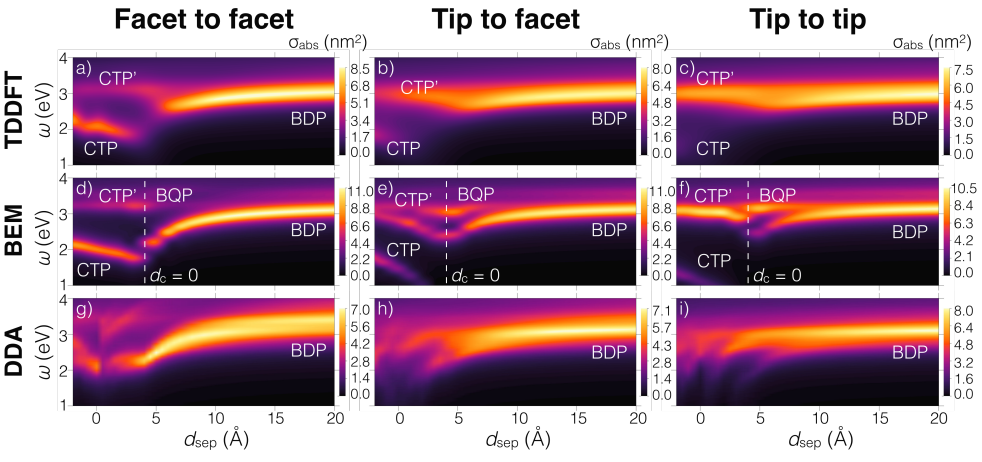

Figure 2.9: Absorption cross-section spectra of icosahedral dimers obtained using TDDFT in the first row a)-c), BEM in the second row d)-f), and DDA in the third row g)-i) as a function of the inter-particle separation distance d_{sep}. The hybridized bonding dimer plasmon (BDP) mode, bonding quadrupolar plasmon (BQP) mode, charge transfer plasmon (CTP) mode and higher-order charge transfer plasmon (CTP') mode are highlighted in the spectra for those cases where such identification is possible. The minimum distance ($d_{\mathrm{C}} = 0$ Å) for which the continuous (BEM) particles overlap is highlighted with dashed white lines. TDDFT data provided by Marc Barbry and DDA data provided by Yao Zhang, both in CFM.

and bottom rows in Fig. 2.9) and appears as less pronounced in the quantum results (top row in Fig. 2.9). For large separation distances ($d_{\mathrm{sep}} > 6$ Å) the gap modes appear at a similar energy for all the configurations considered.

In the TDDFT calculations [first row in Figs. 2.9(a-c)] the BDP slightly red-shifts as the interparticle distance decreases, and below $d_{\mathrm{sep}} = 6$ Å it eventually fades away, indicating that the quantum tunneling regime is being reached [106]. At those separation distances, the charge transfer plasmon (CTP) at lower energy (around 2 eV) emerges due to the current induced by the tunneling effect, even if the particles are not in physical contact ($d_{\mathrm{sep}} \sim 5$ Å, while the interatomic distance is ~ 4 Å). Notice the higher intensity of the CTP mode for the facet-to-facet geometry with respect to the other two configurations, due to a larger particle surface area exposed at the minimum gap distance, which includes a greater overlapping of the electron densities of the clusters gap interfaces. Furthermore, for these short distances the higher-order charge transfer plasmon (CTP') mode is also excited at higher energy (about 3 eV). Notice that for tip-to-facet and tip-to-tip geometries in Figs. 2.9(b,c), the CTP' modes have larger relative weight than the lowest order CTP mode, as the tunneling transport of the electrons through the gap is reduced when going through a tip, rather than in a situation of facet-to-facet tunneling [Fig. 2.9(a)].

Similarly to the situation of the isolated nanoparticle, we also mimic the configuration of the plasmonic gaps of different morphologies with the use of a classical approach based on the BEM. Overall, the optical response calculated within the classical framework is very similar to the quantum one for $d_{\mathrm{sep}} > 6$ Å. For this classical

separation range, a similar redshift of the BDP mode is observed in the classical description to that observed in the results of the TDDFT calculation. This behavior also appears for dimers composed by spheres [30], and it is enhanced here by the extreme geometrical features of our system. This can be clearly observed by comparing the facet-to-facet gap (d) which shows a slight excitation of the bonding quadrupolar plasmon (BQP) and intense BDP mode, and the tip-to-tip (f) with a much stronger excitation of BQP and lower BDP intensity.

Beyond this classical regime, major differences with respect to the TDDFT results are observed in the 4 Å $< d_{\mathrm{sep}} <$ 6 Å separation range, where electron spilling effects and a strong tunneling affect the optical spectra. A local classical electrodynamical approach cannot reproduce these effects due to their pure quantum nature, even though novel effective approaches have been developed to account for them with extended classical treatments [96].

Finally, for overlapping particles with $d_{\mathrm{sep}} <$ 4 Å, the pattern observed in the classical spectra, characterized by a distribution of charge transfer plasmons (CTPs and CTP's), perfectly reproduces that of the TDDFT results, although the relative intensity of CTP and CTP' are dramatically dependent on the geometry and width of the neck connecting the particles. As far as the optical spectrum is concerned, most of the spectral features are well reproduced by the classical approach, identifying clearly the bonding plasmon at the gap and the charge transfer when overlap is produced. The quantum situation for separations below 6 Å requires further elaboration as shown in the literature [96].

We complement our study on plasmonic gaps with the use of an atomistic classical approach based on DDA. The optical response obtained within this framework shares some spectral features as observed within both the quantum and continuous classical approaches for $d_{\mathrm{sep}} >$ 6 Å. The BDP mode shows a similar redshift compared to BEM (and thus slightly larger than in TDDFT) for decreasing separation distances. Moreover, the comparison among the different configurations reveals the same trend as in BEM: the facet-to-facet gap (g) shows an attenuated excitation of the BQP and intense BDP compared to the tip-to-facet (h) and tip-to-tip (i) configurations, although they are not as distinguishable as in BEM calculation.

As it happens for BEM calculations, the limitations of DDA are noticeable when entering the quantum regime in the $d_{\mathrm{sep}} <$ 6 Å separation range. Evenmore, difficulties arise to properly address the situation for overlapping particles with $d_{\mathrm{sep}} <$ 4 Å. In particular, this situation requires a different approach compared to TDDFT, as the direct removal of layers of dipoles from a cluster leads to a new nanogap with non-overlapping clusters. On the other hand, if the layers were kept in their position, the dipoles would overlap leading to unphysical results. Thus, in an attempt to avoid both situations, a smooth transition from non-overlapping to overlapping has been modeled, which yet does not recover the response observed for TDDFT and BEM.

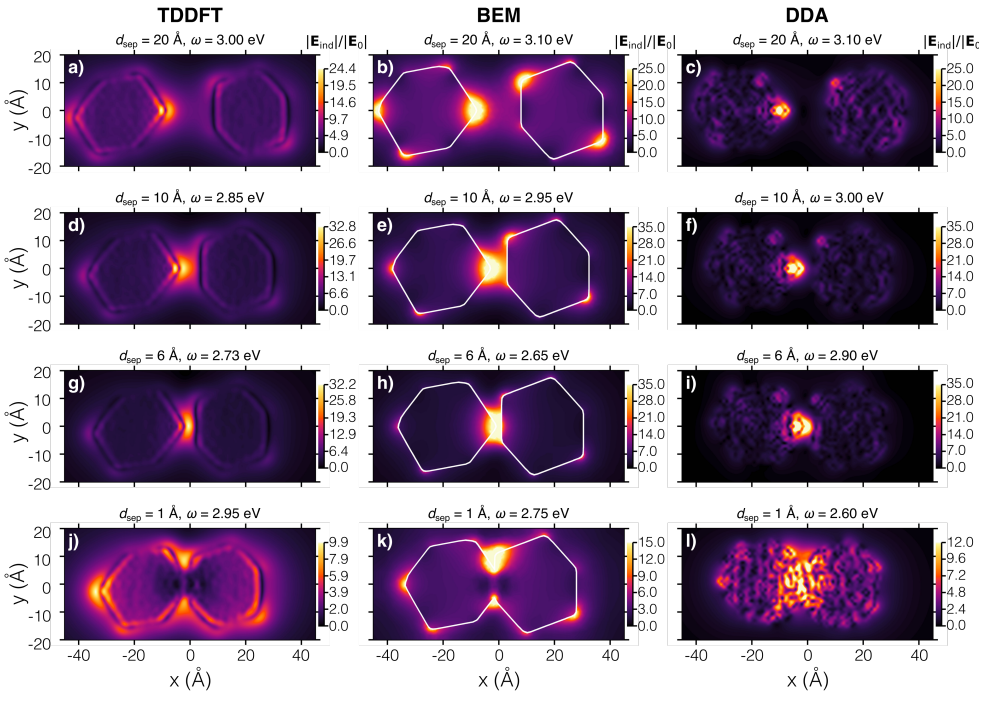

Figure 2.10: Induced near-field enhancement maps in the plane (x, y) for a metallic dimer characterised by a tip-to-facet gap configuration [sketch in Fig. 2.7(b)] calculated with quantum TDDFT (left column), with classical BEM (middle column), and with DDA (right column). Separation distances between particles are $d_{\mathrm{sep}} = 20$ Å panels (a-c), $d_{\mathrm{sep}} = 10$ Å panels (d-f), $d_{\mathrm{sep}} = 6$ Å panels (g-i) and $d_{\mathrm{sep}} = 1$ Å panels (j-l). The most intense resonances are selected for each separation distance. In most of the cases this resonance corresponds to the BDP, except those shown in panels (j-l), where the charge transfer CTP' is the most intense resonance. TDDFT data provided by Marc Barbry and DDA data provided by Yao Zhang, both in CFM.

2.3.2 Near-field optical response of picocavities

The gap plasmon identified for the three morphologies in Fig. 2.9 is a canonical mode in plasmonics widely exploited as a building block for molecular sensing and spectroscopy [200–203]. We now analyze the validity of the classical approaches to address the local field distribution and the effective mode volume of the gap mode. We focus on the tip-to-facet configuration and analyze the local field distribution for different separation distances within both quantum and classical approaches. We select this configuration because it gathers both tip and facet features and thus illustrates adequately the outcome for each morphology. In Fig. 2.10, we show the induced fields for four different particle separations, namely, $d_{\mathrm{sep}} = 20$ Å (first row, a-c), $d_{\mathrm{sep}} = 10$ Å (second row, d-f), $d_{\mathrm{sep}} = 6$ Å (third row, g-i) and $d_{\mathrm{sep}} = 1$ Å (fourth row, j-l), which have been chosen to illustrate the different interaction regimes: weak interaction, medium interaction, strong interaction and charge transfer regimes.

Quantum (TDDFT) results are displayed in the left column of Fig. 2.10, continuous classical (BEM) results in the middle column, and atomistic classical (DDA) results in the right column. In the weak interaction regime, ($d_{\mathrm{sep}} = 20$ Å, a-c) the near-field distribution resembles that in isolated single particles. Nevertheless, a larger enhancement of the field is observed in the gap, meaning that an hybridization of the dipolar modes of the particles into the BDP mode also emerges at this separation distance. Continuous classical (BEM), atomistic classical (DDA) and quantum (TDDFT) results equally reproduce the presence of the atomic-scale hot spots, not only in field distribution, but also in the intensity of the enhancement produced (of the order of 25-fold) with respect to the incoming field, although DDA lacks some of the field distribution around the nanoparticle and the field is mainly localized around the tip rather than in the gap. As the nanoparticles' gap is decreased, the BDP gets more localized at the gap [Figs. 2.10(d-h)]. All approaches predict the progressive localization of the field in the medium and strong interaction regimes, with values of the field enhancement at the gaps of around 35 fold. Finally, as the nanoparticles overlap [Figs. 2.10(j,l)], charge transfer across the particle is produced, expelling the field from the gap producing, an effect correctly captured by the quantum and continuous classical results, but not by the atomistic classical results. As observed in the comparison between quantum and classical results in Fig. 2.10, the continuous classical approach provides a very adequate framework to address the local-field distribution around atomic-scale features, even in the extreme situation of small clusters where quantum effects are more pronounced. We can thus conclude that this classical approach can be safely used to describe atomic-scale features in much larger plasmonic structures, which cannot be directly tackled by quantum methods.

The near-field maps in the charge transfer regime, plotted for the CTP' mode energies in Figs. 2.10(j,l) confirm that this regime can be also correctly captured by means of a continuous classical description. In the case of the TDDFT description (panel j) the charge is transferred through the "gap" due to the overlap of the electron wave functions, so that the field is expelled to the surrounding of the gap and thus the field confinement decreases. The same occurs in the classical BEM description (panel h), where the particles' profile follows the overlapping neck of the particles' electronic wave functions, and thus the field is also expelled to the outside with a very similar pattern when compared to the TDDFT result. Moreover, the main features of the near-field distribution around the tips are also preserved in both models. On the other hand, DDA fails to reproduce the field distribution pattern as there is always an effective gap among the nanoparticles where the field is localized instead of expelling it to the surrounding of the gap.

2.3.3 Effective mode volume of picocavities

One of the most important properties of an optical resonator is the effective mode volume V_{eff} associated to its resonance modes, i.e., the spatial confinement of the modes. Following the common (normal mode) prescription, the effective mode volume can be obtained as an integration of the energy of the induced local fields of

a mode, $|\mathbf{E}_{\rm ind}(x,y,z)|^2$, normalized to the maximum local energy, $|\mathbf{E}_{\rm ind}^{\rm max}|^2$, over the total volume, $V_{\rm tot}$:

$$V_{\rm eff} = \int_{V_{\rm tot}} \frac{|\mathbf{E}_{\rm ind}(x,y,z)|^2}{|\mathbf{E}_{\rm ind}^{\rm max}|^2} dx\, dy\, dz. \tag{2.3}$$

The definition of a general effective mode volume has been source of debate within the community of photonic cavities in the last decade [204, 205]. We note that the definition given above for $V_{\rm eff}$ is rigorous for cavities with infinite quality factor Q. A rigorous mathematical definition for leaky cavities (cavities that present losses, due to radiation and/or absorption, and therefore finite Q) has been given within the framework of Quasinormal Modes (QNM) [206]. Here we do not intend to explore the intricacies of QNMs [6] , but to analyze the field localization in the nanogap obtained within the full electromagnetic response of the plasmonic system using TDDFT, BEM and DDA. Thus, the above prescription for $V_{\rm eff}$ is adequate to evaluate the localization of the field in equal footing for the three models, taking into account that the plasmonic resonances are spectrally well separated.

When an atomic-scale lightning-rod effect is mounted on a plasmonic resonance, a slight modification of the field-enhancement and the effective mode volume is produced by this effect. As we have illustrated throughout this chapter, the classical description of the atomic-scale features turns to be a very adequate framework to address the properties of these picocavities. We thus compare now the maximal field enhancement and effective mode volume obtained in the different plasmonic cavities as a function of gap separation distance, $d_{\rm sep}$. Classical and quantum results for the effective mode volumes are displayed in Fig. 2.11, for three mutual orientations considered earlier in this chapter. Maximum near-field enhancement at the center of the gap $|\mathbf{E}_{\rm ind}^{\rm max}|/|\mathbf{E}_0|$ is shown in panels (a-c) of Fig. 2.11, and the corresponding effective mode volume $V_{\rm eff}$ in panels (d-f).

For separation distances larger than $d_{\rm sep} \sim 8-10$ Å, the maximum induced near fields show similar trends for all the configurations with excellent agreement between the quantum and the classical descriptions. For smaller separation distances, the quantum model properly accounts for the quenching of the local field enhancement produced by the quantum tunneling at optical frequencies [96], whereas the classical

[6] The fundamental difference between quasinormal modes and normal modes is that the former appear as solutions to a non-Hermitian differential equation problems, with complex eigenfrequencies, and consequently, many concepts derived for the normal modes of Hermitian problems do not apply. For instance, for a resonator embedded in an otherwise homogeneous permittivity distribution $\varepsilon_B = n_B^2$, quasinormal modes are obtained by solving the wave equation, $\nabla \times \nabla \times \mathbf{E}(\mathbf{r},\omega) - k^2 \varepsilon(\mathbf{r},\omega)\mathbf{E}(\mathbf{r},\omega) = 0$, with the Silver-Muller radiation condition (equivalent to Sommerfield radiation condition for scalar functions), $\hat{\mathbf{r}} \times \nabla \times \mathbf{E}(\mathbf{r},\omega) + i n_B k \mathbf{E}(\mathbf{r},\omega) \to 0$ (as $|\mathbf{r}| \to 0$), as the boundary condition, where $\varepsilon(\mathbf{r},\omega)$ is the position and frequency dependent relative permittivity, $k = \omega/c$ is the ratio of the angular frequency to the speed of light in vacuum and where $\hat{\mathbf{r}}$ is a unit vector in the direction of $\mathbf{r}$. The use of this radiation condition turns the wave equation into a non-Hermitian eigenvalue problem, even if $\varepsilon(\mathbf{r},\omega)$ is real, so that the eigenmodes are QNMs $\widetilde{\mathbf{f}}_\mu(\mathbf{r})$ with a discrete spectrum of complex resonance frequencies $\widetilde{\omega}_\mu = \omega_\mu - i\gamma_\mu$. The radiation condition ensures that the light propagates away from the cavity (for leaky resonators), although the QNMs diverge (exponentially) at large distances, which is rather challenging conceptually and numerically. Further details can be found in Ref. [204].

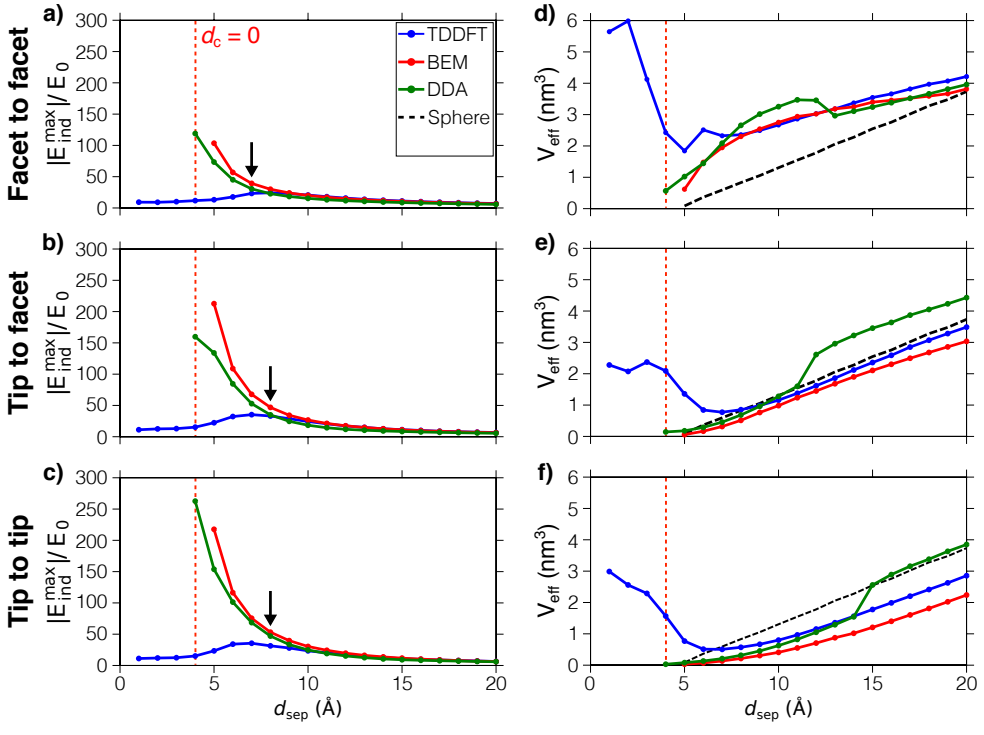

Figure 2.11: (a-c) Maximum local induced-field enhancement $|\mathbf{E}_{\mathrm{ind}}^{\mathrm{max}}|/|\mathbf{E}_0|$ at the central plane bisecting the gap between two nanoparticles forming a plasmonic gap in the three configurations shown on the top of Fig. 2.7: facet-to-facet, tip-to-facet, and tip-to-tip, as a function of the separation distance between the particles, d_{sep}. The blue line stands for the TDDFT quantum calculations, the red line shows the classical BEM results, and the green line the DDA results. The vertical dotted red line marks the touching situation, $d_{\mathrm{c}} = 0$. Small arrows indicate the threshold separation distance below which the effect of quantum tunneling becomes noticeable [96]. (d-f) Effective mode volume V_{eff} of the local field, as defined in the text (Eq. 2.3), for all three configurations. The data correspond to the energies for which the largest maximum of the induced near field for each configuration and distance is obtained. The dashed black line addresses the effective mode volume corresponding to the gap of spherical particles of radius $r = 1.85$ Å. TDDFT data provided by Marc Barbry and DDA data provided by Yao Zhang, both in CFM.

picture provides an unphysical increase of the local field. The quantum description (blue line, TDDFT) addresses the existence of a maximum of local field at $d_{\mathrm{sep}} = 8$ Å for the facet-to-facet configuration, which is slightly shifted to a smaller separation for the other configurations showing atomic-scale protrusions ($d_{\mathrm{sep}} = 7$ Å for tip-to-facet and tip-to-tip configurations), due to a reduced effect of the tunneling in those configurations. In the classical descriptions (red and green lines in Fig 2.11, the enhancement of the local fields increases exponentially as the gap is closed, with larger values for tip-to-tip and tip-to-facet configurations due to a more pronounced lightning rod effect. In light of these results one can conclude that the classical description of the atomic scale local fields is correct until separation distances of

about 8 Å.

Along with the maximum absolute value of the field enhancement, the corresponding effective mode volume, V_{eff} for each situation is shown in Fig. 2.11(d-f). As has been mentioned, V_{eff} provides the effective localization volume in which the field is localized in the middle of the gap. Figure 2.11(d-f) shows the results as a function of d_{sep} for the corresponding configurations and energies used in Fig. 2.11(a-c). For the quantum and continuous classical approaches, the dependence of V_{eff} shows similar trends for all the configurations with slight differences due to the details of each particular cavity. For $d_{\text{sep}} > 5$ Å, where the BDP mode dominates the response in all the gap configurations, there is a smooth increase of field confinement, i.e., decrease of V_{eff}, as the particles get closer, in both the quantum and classical descriptions. The classical approach agrees very well with the quantum one: for a facet-to-facet configuration [Fig. 2.11(d)] a confinement below 3 nm^3 is possible, only limited by the extension of the atomic facets. An extreme situation is achieved with the presence of atomic-scale tips (picocavities) [Figs. 2.11(e,f)]. In such a situation, the effective mode volumes reach subnanometric volumes, below 1 nm^3. This level of confinement of light is the ultimate limit provided by condensed matter and relies on the lightning rod effect associated with the potential profile driven by the electron density profile in the vicinity of a protruding atom, as described in Fig. 2.6.

It should be noted that the classical theory correctly describes this level of localization in spite of the presence of spill-out or dynamical screening effects, as demonstrated here. The atomistic quantum calculations are, for now, greatly limited in particle size, i.e., they cannot go beyond structures of a few nanometers (few thousands of atoms) due to computational cost. This barrier prevents direct comparison with experiments using medium-to-large sized nanostructures that are usually used in molecular spectroscopy. In particular, the large optical field gradient in these picocavities can change the Raman selection rules of molecules placed in their vicinity, exciting otherwise forbidden vibrational transitions in single molecules [43].

For gap separation distances $d_{\text{sep}} < 8$ Å, the BDP mode is quenched due to electron tunneling, and thus the effective mode volume increases as the local field spreads out from the plasmonic cavity. This sets a threshold separation distance below which the classical description is not appropriate. This behavior depends much on the geometrical details of each particular configuration, as observed from the difference in the blue line of Figs. 2.11(d-f).

2.4 Discussion and summary

The optical response of small metallic nanoparticles and nanogaps that contain atomic-scale features has been analyzed in this chapter, paying special attention to the extreme localization of light associated with them. In order to gain insight

into the influence of morphology on this localization, we have applied three different approaches to describe the atomic-scale boundaries, which account for different "complexity" levels: *i*) an atomistic *ab initio* quantum description based on TDDFT, *ii*) an atomistic classical approach based on the DDA, and *iii*) a continuous classical description based on the BEM.

We observe subnanometric localization of light around the tips of single metallic nanoparticles using all three approaches. Lightning rod effect at the atomic scale is identified as responsible for the extreme localization of light, induced by the electrical potential gradient produced by the electronic wave functions of the atomistic features. When superimposed on top of a nanometric plasmonic resonance, the lightning rod effect acts as a multiplier effect, producing an extra factor of field enhancement, which is characterized by a further spatial localization as compared to the supporting underlying resonance, with a similar spectral distribution. We show that the effective mode volumes of these atomistic features can reach subnanometric dimensions, taking the localization of light to the realm of the picoscale, with mode volumes below 1 nm^3. Based on these results we introduce the concept of picocavity.

Our calculations show that a classical model which solves Maxwell's equations, where the atomic-scale features are described by sharp boundaries following the profile of the electron density associated with the atoms, is able to reproduce very satisfactorily the field localization and the effective mode volume in relevant canonical plasmonic nanoresonators such as in single metallic nanoparticles and in nanometric gaps formed by nanoparticle dimers. The current work has focused on Na nanoparticles; however the classical description of the atomic-scale lightning rod effect can be extended to noble metals, such as Ag or Au, widely used in nanoplasmonics, with the appropriate description of the dielectric function to account for interband transitions in these materials. Moreover, the good agreement between the classical and quantum calculations supports the use of classical approaches in the calculation of the optical response of medium-to-large plasmonic nanostructures that can also show subnanometric localization of the field in the presence of atomic-scale features. In particular, picocavities are exploited in many situations in nanophotonics, such as molecular spectroscopy, where the the subnanometric localization of the field has been key to resolve single-molecule picoscopy [42, 43].

3 Addressing structural inhomogeneities in metallic nanocavities as probed by optical spectroscopy

The presence of atomic-scale features and protrusions localizes light down to sub-nanometric volumes forming picocavities, as discussed in Chapter 2. The large field enhancement and, specially, the large field gradients produced around these picocavities is of great interest in molecular spectroscopies, such as in *Surface-Enhanced Raman Scattering* (SERS). In particular, symmetries forbidding the excitation of specific molecular vibrational modes can be broken by these large field gradients, making these modes accessible to probes used in optical experiments [43, 207].

A suitable and robust structure to perform SERS experiments is the *nanoparticle-on-mirror* (NPoM) structure [208], which consists of a metallic nanoparticle placed on top of a metallic substrate and separated by a thin spacer-film in-between to prevent conductive contact, creating a nanogap between the NP and the substrate as sketched in Fig. 3.1(a). The charges induced in the NP under illumination produce a

mirror image charge distribution at the substrate, producing a confined plasmon at the nanogap similar to that produced in a NP dimer [209–211] (see Sec. 2.3 for dimers with small nanoparticles). The presence of picocavities at the nanogap of NPoM structures has been studied and successfully exploited to perform single-molecule SERS. Moreover, light-induced atomic restructuring at the surface of metallic nanostructures has been reported to be at the origin of the picocavities [43, 212].

In time-resolved SERS, the characteristic spectral signature of picocavities is revealed with the appearance and disappearance of light emission at specific wavelengths related to symmetry forbidden excitations/transitions. Along with these phenomena, other dynamical features have been observed in time-dependent SERS such as sudden broad-band Gaussian increases of the background signal [46–48], which we refer to as emission *flares*. Nevertheless, the origin of these flares has not been investigated systematically. In order to analyze these spectral events, experiments were performed by Cloudy Carnegie at Cambridge University under the supervision of Prof. Jeremy Baumberg to capture over a million time-dependent scattering spectra for more than 3000 NPoMs.

Great part of the background SERS signal in NPoM structures is known to come from *electronic Raman scattering* (ERS), which is proportional to the 4^{th} power of the electric field. In this chapter we study flares in SERS spectra and model them as a dynamic restructuring of atoms at transient defects, such as twin planes and grain boundaries, which lead to localized changes of the plasma frequency of the metal, and thus induce a stronger electric field within the metallic NP. In Section 3.1 we analyze the optical response of NPoM structures and characterize the modes present in such structures. We analyze flares observed in experimental SERS spectra obtained by the group of Prof. Jeremy Baumberg, which are included in this thesis for completeness, in Section 3.2. We follow up in Section 3.3 by providing a theoretical background of ERS. In Section 3.4 we theoretically study the influence of local changes in the plasma frequency on the optical response and on the field penetration in NPoM structures proposing a model to explain the appearance of flares in SERS spectra.

3.1 Nanoparticle-on-a-Mirror configuration

To understand the origin of the flares, we first need to gain insight into the optical response of the plasmonic structure, i.e., the *nanoparticle-on-mirror* (NPoM) configuration shown in Fig 3.1(a). As mentioned above, the NPoM structure consists of a metallic nanoparticle placed on top of a metallic substrate, separated by a thin spacer-film of thickness d in-between to prevent conductive contact. This creates a nanogap between the NP and the substrate as observed in Fig. 3.1(a).

Real nanoparticles typically show crystallographic faceting, and as such, they lay on one of the facets, creating a nanocavity of certain width w, which is similar to

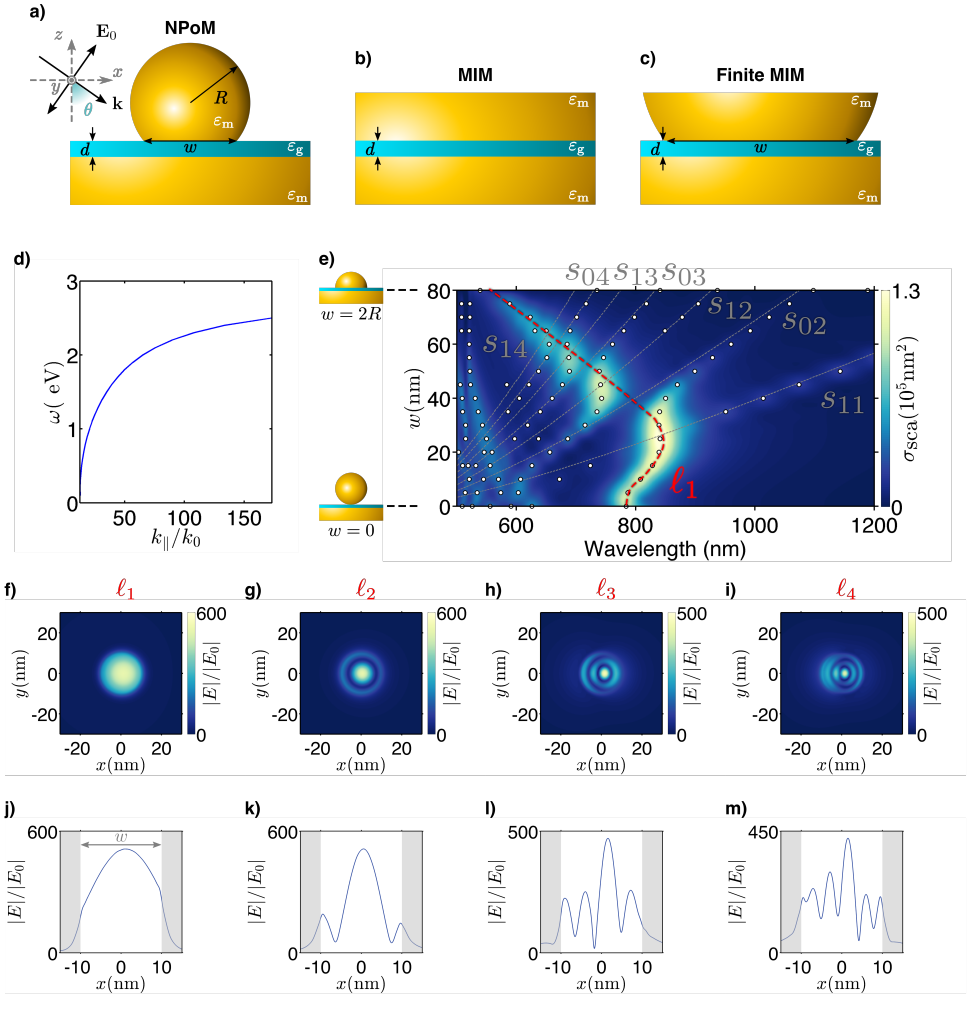

Figure 3.1: a) Sketch of a faceted spherical gold nanoparticle with radius $R = 40$ nm and facet width w separated from a gold substrate by a dielectric spacer of thickness $d = 0.9$ nm and permittivity $\varepsilon_g = 2.1$, under p-polarized illumination with angle of incidence $\theta = 55°$. b) Sketch of an infinite metal-insulator-metal (MIM) structure. c) Bottom facet of the NP in the NPoM structure showing the finite MIM structure. d) Dispersion relation of the infinite MIM structure, where $k_0 = 2\pi/\lambda$ is the wavevector of incident light in vacuum, $k_\parallel$ is the corresponding wavevector in the MIM waveguide. e) Extinction spectra map of the NPoM geometry described in (a) as a function of w (from perfectly spherical NP to hemispherical NP as in the schematics to the left). Open circles trace the resonance peaks of all excited modes, dashed grey lines track the dispersion relation of the cavity modes s_{mn} and the red dashed line is a guide to the eye of the bonding dimer antenna ℓ_1 mode. f-i) Near-field maps at the center of the gap corresponding to the modes excited for a facet width $w = 20$ nm (nominal facet width of the NPs often used in experiments). j-m) Corresponding near field along the x-axis at the center of the gap.

a finite *metal-insulator-metal* (MIM) waveguide. For small gaps ($d < 10$ nm) of dielectric permittivity $\varepsilon_\mathrm{g} = n_\mathrm{g}^2$ between infinite metallic walls (ε_m) the dispersion relation of the lowest MIM modes can be expressed by [213, 214]:

$$\left(\frac{k_\parallel}{k_0}\right)^2 = n_\mathrm{eff}^2 = \varepsilon_\mathrm{g} + 2\zeta\left[1 + \sqrt{1 + (\varepsilon_\mathrm{g} - \varepsilon_\mathrm{m})/\zeta}\right], \tag{3.1}$$

where $k_0 = 2\pi/\lambda$ is the wavevector of incident light in vacuum, $k_\parallel$ is the corresponding wavevector in the MIM waveguide, and $\zeta = (k_0 d\varepsilon_\mathrm{m}/\varepsilon_\mathrm{g})^{-2}$, where d is the gap distance. For very thin gaps and a Drude model with no damping for the metal this equation reduces to

$$k_\parallel = -\frac{2\varepsilon_\mathrm{g}}{d\varepsilon_m} = -\frac{2\varepsilon_\mathrm{g}}{d}\left[\varepsilon_\infty - \frac{\omega_p^2}{\omega^2}\right]^{-1}. \tag{3.2}$$

We can obtain the penetration depth of the electric field in the metal by taking into account that the wavevector satisfies $k_0^2 = k_\perp^2 + k_\parallel^2$, where $k_\perp$ is the perpendicular (respect to the nanoparticle and substrate interfaces) wavevector, and that for typical nanogap parameters such as $d = 0.9$ nm, $\varepsilon_\mathrm{g} = 2.1$, $\omega_p = 9$ eV, $\varepsilon_\infty = 10$, the nanogaps adopt large high wavevectors ($k_\parallel = 10 - 100k_0$ with $k_0 = 2\pi/\lambda$) and thus short effective wavelengths, as observed in Fig. 3.1(d). Thus, $k_\parallel \gg k_0$ and,

$$\delta_\perp = \frac{1}{\mathrm{Im}\{k_\perp\}} = \frac{d\varepsilon_\mathrm{m}}{2\varepsilon_\mathrm{g}}. \tag{3.3}$$

In the nanostructure considered, this continuum of MIM gap modes of the infinite MIM structure is broken into discrete states, as imposed by the finite size of the bottom facet of the NP, which localizes the modes in the gap due to partial reflection at the discontinuities of the MIM gap. Indeed, a two-dimensional Fabry-Pérot resonator model captures the nature and symmetry of the cavity modes sustained by the NPoM, whose associated electric field can be well described in cylindrical field coordinates (ρ, ϕ, z) (z perpendicular to the particle and substrate interface) [113, 215]:

$$E_z(r, \phi, z) = \sum_m A_m J_m(k_\parallel \rho) e^{im\phi} e^{-z/\delta_\perp}, \tag{3.4}$$

where J_m are the cylindrical Bessel functions of order m, A_m are the expansion coefficients, and $k_\parallel$ the component of the wavevector parallel to the top and bottom interfaces. For a finite-size cylindrical gap of width w, the discrete wavelengths are given by [113, 215, 216]:

$$\lambda_{mn} = \frac{\pi w n_\mathrm{eff}}{a_{mn} - \beta}. \tag{3.5}$$

Here a_{mn} is the n^th root of the m^th-order Bessel function J_m, with m the angular momentum number related to the azimuthal dependence of the modes in the cylindrical symmetry and β an appropriate phase accumulated due to the reflection of the

waves at the edges of the cavity [215–217]. Here we consider $\beta = \pi/2$ as the fields show a maximum near the edge of the cavity instead of a node. These cavity modes are confined to the nanogap and show strong near field-enhancements, although they are in general weakly radiative or nonradiative.

The structure of modes in a specific NPoM configuration is a result of a complex coupling of these cavity modes, which can be labeled as s_{mn} modes, and the modes of the nanoantenna deposited on the mirror, which one can label as "antenna" l modes [216]. Antenna modes with correct symmetry can couple to specific cavity modes s_{mn}, yielding strong anticrossings and mixed $s_{mn} + \ell = j_n$ modes. We show in Fig. 3.1(e) the scattering cross section, σ_{sca}, as a function of the facet width w for a NP with radius $R = 40$ nm, separated from an semi-infinite gold substrate by a dielectric spacer of thickness $d = 0.9$ nm and permitivitty $\varepsilon_{\text{g}} = 2.1$, as calculated within the MNPBEM [111] with the implementation for infinite layers. The spectral map shows that light is most efficiently coupled into the nanogaps around the anticrossings between the ℓ and modes s_{mn} [216]. The bonding dimer plasmon mode, here labeled as ℓ_1 [red dashed line in Fig. 3.1(e)], efficiently couples to the incoming light polarized along the NP-substrate axis, and thus dominates the far field. As it has been reported, for small separations higher-order antenna modes, ℓ_2, ℓ_3, ... can also be efficiently excited [30, 210].

These modes show large field enhancement at the nanogap, as shown in the near-field maps in Fig. 3.1(f-i) for the 4 lowest modes with a facet width $w = 20$ nm. The field is localized at the nanogap, showing a number of azimuthally symmetric nodes that increase in number with mode order. Moreover, as observed in Fig. 3.1(j-m) the field profiles are not perfectly concentric. This happens in part due to retardation effects, and, on the other hand, due to the slight mixing with the low wavelength branches of the cavity s_{mn} modes [grey dashed lines in Fig. 3.1(b)]. The latter specially happens for the low wavelength modes in small facet widths $w < 20$nm, where cavity modes are spectrally closer from each other.

3.2 Experimental observation of flares

In this section we will briefly introduce the flares observed in SERS experiments performed by Cloudy Carnegie in the University of Cambridge within the group of Jeremy Baumberg [218, 219], and summarize their main features. Further details about the experimental setup and observations can be found in Refs. [218,219]. In the study, nano-fabricated individual gold nanoparticles were spaced above an ultra-flat gold film by a self-assembled molecular monolayer (SAM) (initially biphenyl-4-thiol, BPT) forming a plasmonic hotspot in the gap between mirror and nanoparticle, and tracked using automated nanoparticle location to collect statistics on millions of events [212].

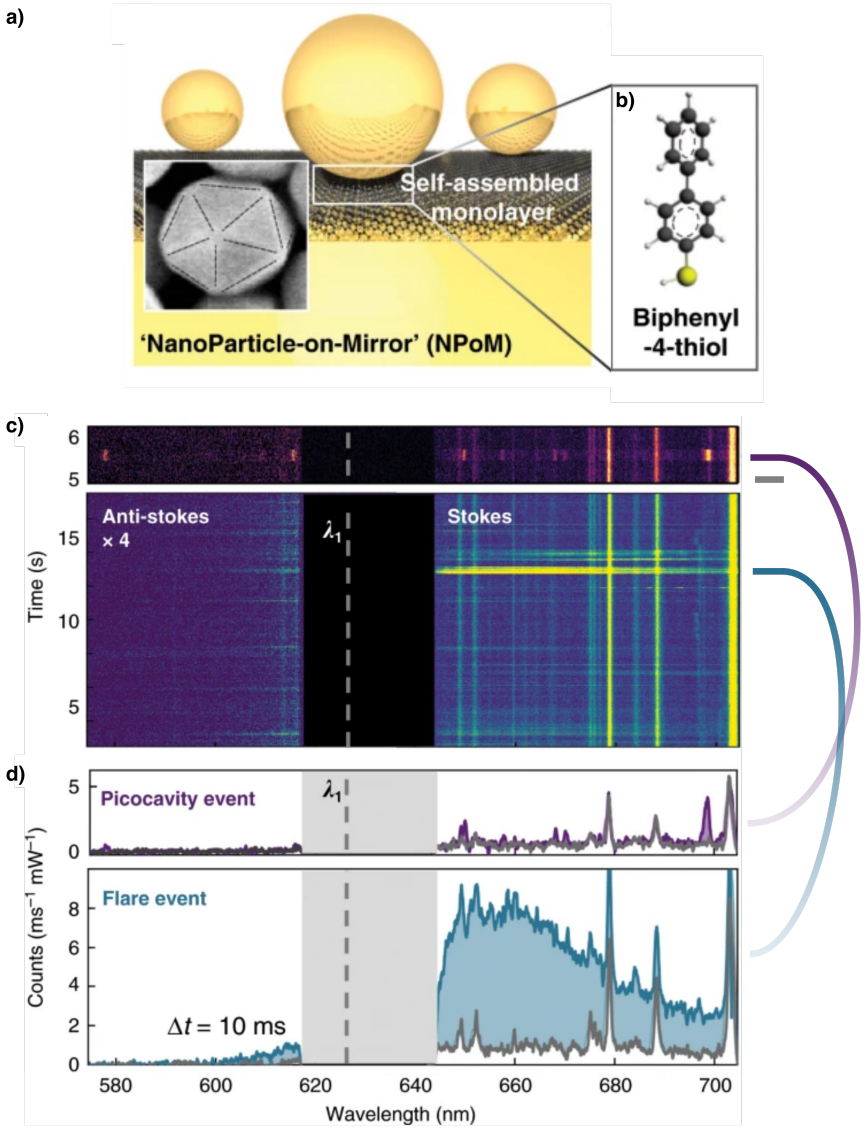

Figure 3.2: a) Nanoparticle-on-Mirror structure, sandwiching a molecular self-assembled monolayer. Inset shows typical icosahedral nanoparticle, with twin planes highlighted with dashed lines. b) Biphenyl-4-thiol (BPT) molecule making up monolayer. c) Time-dependent SERS spectra showing transient spectral features corresponding to picocavities (top panel, purple arrow) and multiple flares (bottom panel, blue arrow). d) Integrated snapshots ($\Delta t = 10$ ms) of a picocavity event (top panel, purple line) and a broad flare event (bottom panel, blue line) compared to stable BPT spectra for same nanoparticle (grey). Experimental measurements from Cloudy Carnegie at Cambridge University. Figure adapted from [218].

These NPoM structures of near-spherical 80 nm diameter colloidal noble-metal particles are however not quite uniform, most commonly appearing as icosahedrons and cuboctahedrons, as observed in the inset of Fig. 3.2(a). These nanoparticles contain multiple grain boundaries and crystal defects, as they are not monocrystalline [220], which alter the local electron density in the immediate vicinity [221]. Furthermore, it has been shown that the crystallinity of nanoparticles is open to movement and, therefore, not entirely fixed and constant [222–224], which is known as the "quasi-molten" model of nanoparticles.

The sample is illuminated by a 633 nm laser and scattered light is collected and filtered out to reveal inelastic scattering. The time-dependent SERS spectra, collected with 10 ms timescales, shows the sharp lines corresponding to the BPT vibrational modes on the Stokes side (see Introduction) in Fig. 3.2(c) (vertical persistent lines). The close-packing in the SAM ensures fixed-energy stable persistent SERS lines to be observed for the few hundred BPT molecules inside the nanogap. The molecular temperature is estimated as 341 ± 17K using the anti-Stokes-to-Stokes ratio, although the electronic Raman scattering (ERS) background contribution suggests the electrons in the metal might be up to 300K warmer in these pumped conditions.

Aside from the persistent lines, two other classes of spectral features are observed in Fig. 3.2(c). The first corresponds to the appearance and disappearance of new vibrational lines/peaks in both the Stokes and anti-Stokes spectra, evidencing "picocavity" formation. Picocavities, which have been studied in detail at cryogenic and room temperature [43, 212], arise from gold adatoms pulled out of the gap surface facets by trapped light. The extra optical confinement and large local field gradients around these picocavities lead to the breaking of Raman selection rules, giving single molecule SERS [43, 207]. Aside from picocavities, another spectral feature, rarer but more intense, can occasionally be observed in the spectra. These features, which we term as *flares*, are sudden Gaussian-shaped increases of the background of the SERS spectra. They last for only fractions of a second, as it is seen in Fig. 3.2(c). Individual events are plotted in Fig. 3.2(d) for a picocavity (top panel, purple line) and a flare (bottom panel, blue line) along with a stable BPT spectrum (grey). Picocavity lines are mirrored around the laser wavelength in the anti-Stokes, a behavior absent for the flares. In fact, the peak of the flare is on the Stokes side and its tail extends into the anti-Stokes, although no inversion symmetry is observed around the laser line.

To better identify the features of these events, the first SERS spectrum in each time series is subtracted from all the subsequent spectra, which leaves only the intensity increases for flare events (picocavity events are filtered out). Some cases can be seen in Fig. 3.3(a) from a single NPoM that have been fitted to a Gaussian profile. The transient peaks occurring briefly at different times vary in width and spectral position, demonstrating that the Gaussian lineshape can vary within the observation window (seconds) of a single nanostructure. Moreover, the lack of sharp features on these spectra imply that the SERS of the molecular vibrations does not change during flaring, which emphasizes their different origin to picocavities and their emergence from electronic Raman scattering inside the metal itself.

In addition to the collection of inelastic-scattering data via laser irradiation, dark-

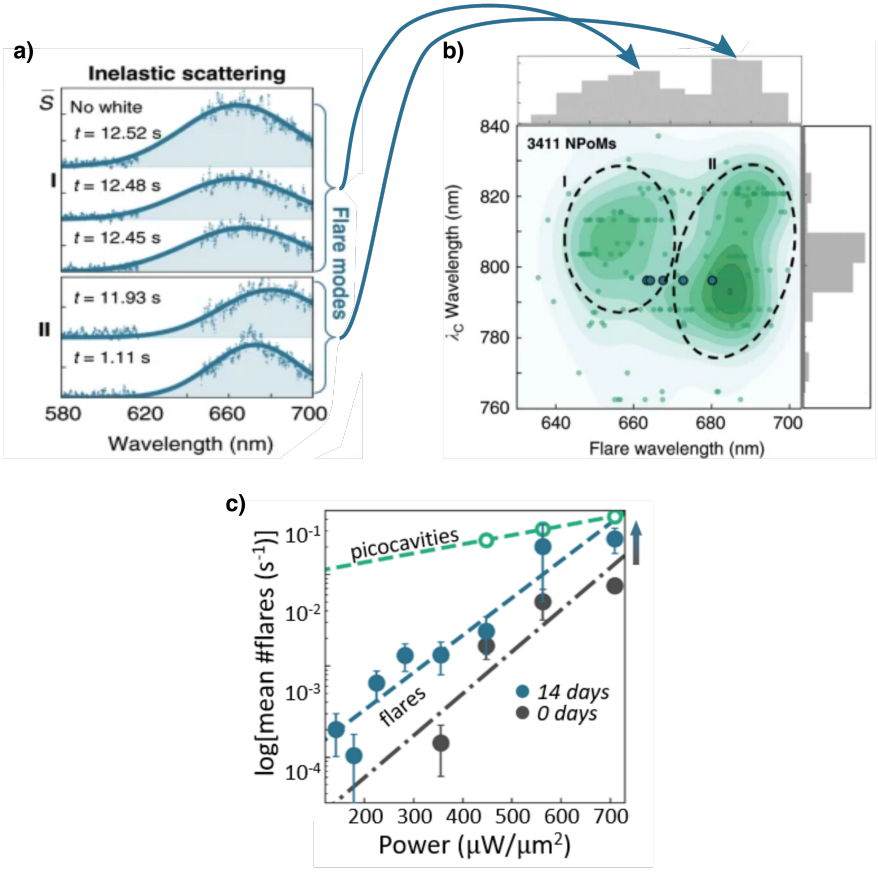

Figure 3.3: a) Different flare inelastic scattering spectra (with persistent stable SERS lines subtracted, $\bar{S}$) from a single NPoM, that have been collected at different times t. Spectra has been sorted into groups I, II by emission wavelength. b) Map of plasmon ℓ_1 mode wavelength λ_c against flare mode centre wavelength for flares from 3411 NPoMs. Grey histograms show distributions, from which two distinct groups are identified. Points corresponding to spectra in (a) highlighted with circles. c) Mean flares per second vs. power, for NPoM samples immediately after self-assembly (black) or after 14 days in air at 300 K (blue), picocavities (green). Here 500 NPoMs are surveyed for each power, lines show exponential fits, error bars indicate standard deviations. Experimental measurements from Cloudy Carnegie at Cambridge University. Figure adapted from [218].

field (elastic) measurements were also performed. The dark-field spectra were used to elucidate the plasmonic modes of the NPoM before and after laser irradiation, giving the range in nanoparticle size and geometry across the sample. To survey the range of flares, a map of the fitted flare wavelength vs. nanoparticle ℓ_1 mode wavelength (λ_c) is plotted in Fig. 3.3(b). Although the ℓ_1 mode positions lie at $\lambda_c \simeq 800$ nm, there is a bi-modal distribution in flare wavelengths which is not resolved in standard

elastic dark-field scattering experiments[7]. We label the two cluster groups I and II [Fig. 3.3(a-b)] and note that even a single NPoM nanostructure can show flare events of both types within the range of a few seconds, suggesting that flare events are not entirely nanoparticle-dependent.

Dark-field scattering can also reveal morphological changes to the NPoM nanostructures, in particular for the ℓ_1 mode spectral peak at λ_c, which red-shifts strongly with an increase in bottom facet width linked to nanoparticle damage from laser irradiation [216, 225]. Nevertheless, the laser irradiation required for the inelastic scattering measurements is not sufficient to cause significant damage to the nanostructure. The red-shift in the ℓ_1 mode has ben linked to a facet width increase which requires movement of surface atoms on the nanoparticle, which suggests that if the flare event is related to atomic displacements then the process that leads to a higher degree of damage could also create flares.

In the following lines we sum up the main features observed for flares:

- **Activation energy**. Experiments performed for different laser powers show an exponential power dependence, as can be observed in the average number of flare events per second of measurement as a function of laser power in Fig. 3.3(c) shows an exponential power dependence, suggesting that flare events require an activation energy, and indicating a structural process at play. Compared to picocavities, which have a known activation energy of ~ 0.8 eV [43], the flares show an activation energy of ~ 4 eV (calculated from the gradient of the flare power dependence), i.e., 5-fold that of the picocavity power. Samples left to "age" in air for two weeks show an increase in the number of flares, although it does not alter the activation energy as the gradient is unchanged. In fact, the aging process does not alter the morphology of NPoMs on the sample, as can be concluded from the near-identical distribution of the coupled-mode positions for both samples [218]. Moreover, flares seem to be metastable as long as energy continues to be injected.

- **Influence of Molecular Spacers**. Replacing the molecular spacer with other spacers showed variations in flare occurrence, although no relationship between the gap distance and number of flares was observed. Nevertheless, although the gap distance and gap refractive index varies between the molecules, and therefore the distribution in coupled-mode wavelengths is shifted [226, 227], the wavelength of the flares is observed to be centered around similar spectral ranges, suggesting that spacer molecules are not at the root of flares.

- **Reversibility**. With the aim of understanding what happens during flares, in addition to laser excitation, the system was simultaneously irradiated with broadband incoherent white-light, and the behavior of the coupled plasmon mode peak was tracked in real time from the elastic scattering (Fig. B.1 in

[7] In dark-field scattering experiments the sample is illuminated with light that is not collected back by the objective lens, and therefore is not part of the image, i.e., only the light scattered by the sample is collected, with reflected light blocked.

App. B). The ℓ_1 mode stays almost unperturbed before and after the flare, however when a flare happens there is a small but instantaneous red-shift of the ℓ_1 mode and an overall increase in the intensity, before returning to the initial position and intensity of the mode. Red-shifts to the ℓ_1 at the exact time of the flare event evidence structural changes in the NPoM that, nevertheless, are reversible (opposed to processes that cause permanent damage), which suggest metastable changes, or that they are ephemeral in the vicinity of the plasmonic hot-spot.

Further details about the experimental setup and experimental observations can be found in [218, 219].

3.3 Background signal in SERS: Electronic Raman Scattering in metals

In the previous section we described the flares observed in the background signal of SERS. The origin of the background signal of SERS has been assigned to an inelastic light scattering process, also described as electronic Raman scattering (ERS) [40,228]. In ERS, electrons within the Fermi sea inside the metal are excited into a virtual state by the incoming plasmon-coupled photon and then de-excited back down to an empty state within the Fermi sea. The difference in photon energy between ingoing and outgoing photons, Δ, requires a change in the momentum of the electron because of the quadratic free-electron s-band dispersion in noble metals. This extra momentum is supplied by the strongly localized field of the plasmon that couples photons into and out of the metal. Moreover, the d-bands can be ignored within this picture, as the incoming and outgoing photons are far detuned from any resonant transition between electronic states. We will assume a zero temperature for the Fermi distribution to retain analytic expressions, as in [40].

A sketch of the ERS process is depicted in Fig. 3.4(a). A pumping photon with energy $h\nu$ excites an electron from an initial state i at the Fermi energy, $\mathcal{E}_{\mathrm{F}}$, to a virtual state v with higher energy (solid blue arrow) together with a shift in the wavevector Δk (solid orange arrow) and a relaxation back to the final state f on the free electron dispersion band (solid red line), emitting a photon with energy $h\nu - \Delta$, where Δ is the energy difference between the initial i and final f states. Electrons that are below the Fermi level down to energies $\mathcal{E}_{\mathrm{F}} - \Delta$ are also able to undergo this process (dashed arrows), leaving the electron just above $\mathcal{E}_{\mathrm{F}}$.

The rate R_{if} for each step of this process can be considered using Fermi's golden rule (in atomic units),

$$R_{if} = 2\pi g_{if} |M_{if}|^2, \tag{3.6}$$

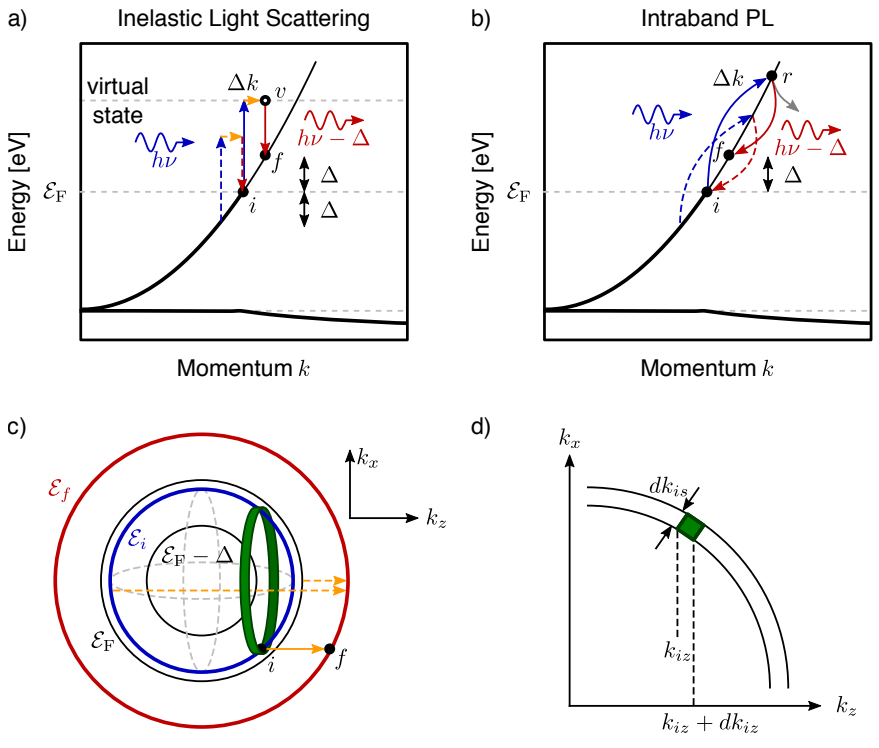

Figure 3.4: a) Intraband light scattering process of electronic Raman scattering (ERS), for pump (blue arrows) and emission (red arrows) photons that differ by energy Δ. The required change in momentum Δk is gained by the vertical transitions to a virtual state from the plasmon localization in space. Solid arrows show the transitions from the highest energy initial state i at the Fermi energy, while dashed lines show the lowest energy initial state i for which the only allowed transition is to a final state f just above the Fermi energy $\mathcal{E}_F$. b) Equivalent process of intraband scattering to real state r on the free particle dispersion. c) Scattering from energy $\mathcal{E}_i$ (blue solid line) to final energy $\mathcal{E}_f$ (red solid line) requires different wavevectors (orange arrows) along k_z. For the particular transition shown, a strip of states (blue) along the sphere of radius k_i hold the same Δk_z. d) Cross-section of k-volume that undergoes scattering of fixed Δk_z in (c). Figure adapted from [40].

where g_{if} is the density of states, and M_{if} is the matrix element for the transition from the initial state i to the final state f, and can be written as the overlap integral,

$$M_{if} = \langle f|H'|i\rangle = \int \psi_f^*(\mathbf{r})H'(\mathbf{r})\psi_i(\mathbf{r})d^2\mathbf{r} \tag{3.7}$$

where H' is the perturbation caused by electromagnetic field, $\mathbf{r}$ is the position of the electron, and $\psi_i(\mathbf{r})$ and $\psi_f(\mathbf{r})$ are the wave functions of the initial and final states. The perturbation due to the electromagnetic field can be expressed as [229],

$$H' = \mathbf{p} \cdot \mathbf{A} \tag{3.8}$$

where $\mathbf{p} = -i\nabla$ is the momentum operator and $\mathbf{A}$ is the vector potential describing the electromagnetic field.

To evaluate the matrix element for each process we need to know the wave functions of the states and the form of the perturbation due to the electromagnetic wave. In the case of MIM structures such as the NPoM, the electromagnetic field is mainly confined in one direction (here considered z), and it drops exponentially inside the metal $E(z) \propto e^{-qz}$ with a penetration depth $1/q = \delta_\perp = \frac{d\varepsilon_\mathrm{m}}{2\varepsilon_\mathrm{g}}$, as given by Eq. (3.3). Thus, here we exclude any dependence of the field on the xy-plane, therefore only the z component of the initial momentum, k_{iz}, of the electron is scattered, and the x and y components of the initial momentum, k_{ix}, k_{iy}, are conserved in the process. On the other hand, we consider the electron states to be described by the free particle wave function $\psi(\mathbf{r}) \propto e^{i\mathbf{k}\cdot\mathbf{r}}$.

One can calculate the rate R_{iv} for the $i \to v$ process shown in Fig. 3.4(a). The matrix element M_{iv} for this transition is given by,

$$M_{iv} = \langle v|\mathbf{p}\cdot\mathbf{A}|i\rangle = E\int dx\, e^{-ik_{fx}x}e^{ik_{ix}x}\int dy\, e^{-ik_{fy}y}e^{ik_{iy}y} \cdot \int dz\, e^{-ik_{fz}z}\frac{\partial}{\partial z}\big(e^{-qz}e^{ik_{iz}z}\big), \tag{3.9}$$

where E is the amplitude of the electric field within the metal, and k_{fx}, k_{fy} and k_{fz} are the x, y and z components of the momentum of the final state f (the momentum of the virtual state v, is the same as the final state f). For a specific initial state i, Eq. (3.9) yields

$$|M_{iv}|^2 = E^2\frac{k_{iz}^2+q^2}{\Delta k_z^2+q^2}, \tag{3.10}$$

with $\Delta k_z = k_{fz} - k_{iz}$. The conservation of wavevectors orthogonal to k_z implies that $k_f^2 - k_{fz}^2 = k_i^2 - k_{iz}^2$, and therefore,

$$\Delta k_z = \sqrt{k_f^2 - k_i^2 + k_{iz}^2} - k_{iz} = \sqrt{\kappa^2 + k_{iz}^2} - k_{iz}, \tag{3.11}$$

with $\kappa^2 = k_f^2 - k_i^2 = b(\mathcal{E}_f - \mathcal{E}_i) = b\Delta$, $b = 2m/\hbar^2$, $\mathcal{E}_i$ the energy of the initial state and $\mathcal{E}_f$ the energy of the final states.

To calculate the rate for this transition we have to integrate over all possible initial,

$$R_{iv} \propto \int_{\mathcal{E}_\mathrm{F}-\Delta}^{\mathcal{E}_\mathrm{F}} d\mathcal{E}_i\, g(\mathcal{E}_i)|M_{iv}|^2, \tag{3.12}$$

and therefore we need to know the density of electronic states $g(\mathcal{E}_i)$. For a specific initial energy $\mathcal{E}_i$ lying between $\mathcal{E}_\mathrm{F}-\Delta$ and $\mathcal{E}_\mathrm{F}$ (see Fig. 3.4(c)), the initial states lie on a sphere set by the free electron dispersion relation $\mathcal{E} = \hbar^2|\mathbf{k}|^2/2m = k^2/b$, shown as a blue circle in Fig. 3.4(c). Moreover, different initial states within the sphere defined

by $|k_i|$ (blue line) require different wavevector changes Δk_z (dashed orange arrows) to reach a final state within the sphere defined by $|k_f|$ (red line). Nevertheless, the wavevector change Δk_z required for states with the same k_{iz} and $|k_i|$ is the same, i.e., the rate is the same for a circular ribbon of k-space with constant k_{iz}, as shown by the green circular ribbon in Fig. 3.4(c-d) (green ribbon). The infinitesimal volume of the circular ribbon is given by $dV_k = 2\pi dk_{is} dk_{iz} = 2\pi dk_i dk_{iz}$, which can be applied to the integral over k-momentum space,

$$R_{iv} \propto E^2 \int_{k_F - k'}^{k_F} dk_i \int_{-k_i}^{k_i} dk_{zi} \frac{k_{iz}^2 + q^2}{\left(\sqrt{\kappa^2 + k_{iz}^2} - k_{iz}\right)^2 + q^2}, \tag{3.13}$$

with $k' = k_F - \sqrt{b(E_F - \Delta)}$, and $k_F = \sqrt{b\mathcal{E}_F}$ the Fermi wavevector.

On the other hand, the equivalent scattering rate from the virtual state back down to the free electron dispersion branch (but this time with no momentum change), R_{vf}, only provides another factor of E^2 as there is no change in momentum.

The total scattering rate is given by

$$R_{if} \propto R_{iv} R_{vf} V_m, \tag{3.14}$$

where V_m is the volume of the metal that is accessed by the plasmonic field. The lateral spatial width of the field in the gap is well approximated by a Gaussian intensity distribution with FWHM $= \sqrt{2Rd/\varepsilon_g}$, which gives an effective area of the plasmon mode $A_m \sim 2\pi Rd/\varepsilon_g$ [32, 208, 230]. By taking into account that the penetration depth is $1/q = \delta_\perp = \frac{d\varepsilon_m}{2\varepsilon_g}$ [Eq. (3.3)], we obtain $V_m \simeq A_m \delta_\perp = \left(\frac{2\pi Rd}{\varepsilon_g}\right)\left(\frac{1}{q}\right) = \frac{\pi Rd^2}{f\varepsilon_g}$, with $f = 2\varepsilon_g/\mathrm{Re}\{1/\varepsilon_m\}$, with Re the real part. As a result we obtain the full rate as:

$$R_{if} \propto \frac{E_c^4 R}{f\varepsilon_g}(1 - e^3)\mathcal{E}_F^2 \left(\frac{\ell}{d}\right)^2, \tag{3.15}$$

where, we have defined the critical length $\ell = \frac{2k_F}{b\Delta}$ and the energy difference $e = 1 - \Delta/\mathcal{E}_F$, and E_c is the field enhancement at the cavity. Details about this derivation can be found in Ref [40]. As in Raman scattering, this photon emission rate depends on the fourth power of the field enhancement, which is expectable as they are very similar processes. Both processes consist in exciting electrons up to a virtual state before returning to a state lying higher higher in than the initial state. In the case of anti-Stokes scattering, the final state would lay lower in energy than the initial state.

Instead of using the expression for the local field enhancement at the cavity, E_c, and to compare more accurately with experiments, one can use numerical simulations to obtain the intensity of the local field in the metal, $I(\mathbf{r}) = |E(\mathbf{r})|^2$, at the wavelength of the pumping light, λ_i, and light emission wavelength, λ_f, i.e., the local field intensities $I_{\lambda_i}(\mathbf{r})$ and $I_{\lambda_f}(\mathbf{r})$ respectively, allowing us to write:

$$R_{if} \propto k_F^4 \ell^2 (1 - e^3) \int I_{\lambda_i}(\mathbf{r}) \cdot I_{\lambda_f}(\mathbf{r}) dV \tag{3.16}$$

where the integral over volume is only evaluated within the metal (where the electrons can undergo ERS) and the prefactor depends on the material.

The inelastic light scattering (ILS) process shown here can be thought of as electronic Raman scattering (ERS, with no vibrational states involved). This process also produces background light in addition to the vibrational fingerprints from molecules nearby. For this reason, any change in the plasmonic structure (size, shape, etc.) invariably will modify both the SERS vibrational fingerprints as well as the SERS background [40, 228]. Nevertheless, a modification of the ratio between light just inside and just outside the metal will correspondingly alter the ratio of vibrational peaks to background.

3.4 SERS spectral flares from electron density inhomogeneities

In the previous section we have linked the background signal in SERS experiments with ERS emission from the metallic structures, and it has been shown that this effect depends on the fourth order of the electromagnetic field in the metal. Thus, a temporary situation which produced larger electromagnetic fields in the metal could explain the emergence of flares in the background SERS spectra shown at particular instants of time, as shown in Fig. 3.2(c) in Sec. 3.2.

In principle, one could consider some other mechanisms as a possible source for these spectral features. For instance, the broadband nature of flares could suggest black-body radiation. The spectral range of the flares (640-700 nm) also matches that of two-photon absorption and emission from some molecules. Hot electron emission in small nanoparticles is another possibility. Instead, the behavior observed for flares excludes some of these phenomena, based mainly on the following:

- Black-body radiation corresponding to the temperatures obtained from the anti-Stokes/Stokes ratio from molecules (300-400K) and electrons in the metal (600-1100K) does not match the measured flare wavelengths.

- The spectral range of the flares is not severely affected by the particular type of molecules, which discards two-photon emission as possible mechanism of the effect, which would depend on the concrete molecule.

- Experiments show millisecond time-scale dynamics for flares, which collides with the picosecond time-scale of hot electron emission, not to mention that both black-body radiation and two-photon emission should not depend on time.

Moreover, the broadband nature of the flares and the lack of new spectral lines exclude the molecules deposited at the nanocavity as the source of spectral flares. Thus here we consider that the spectral flares observed in the experiments could be

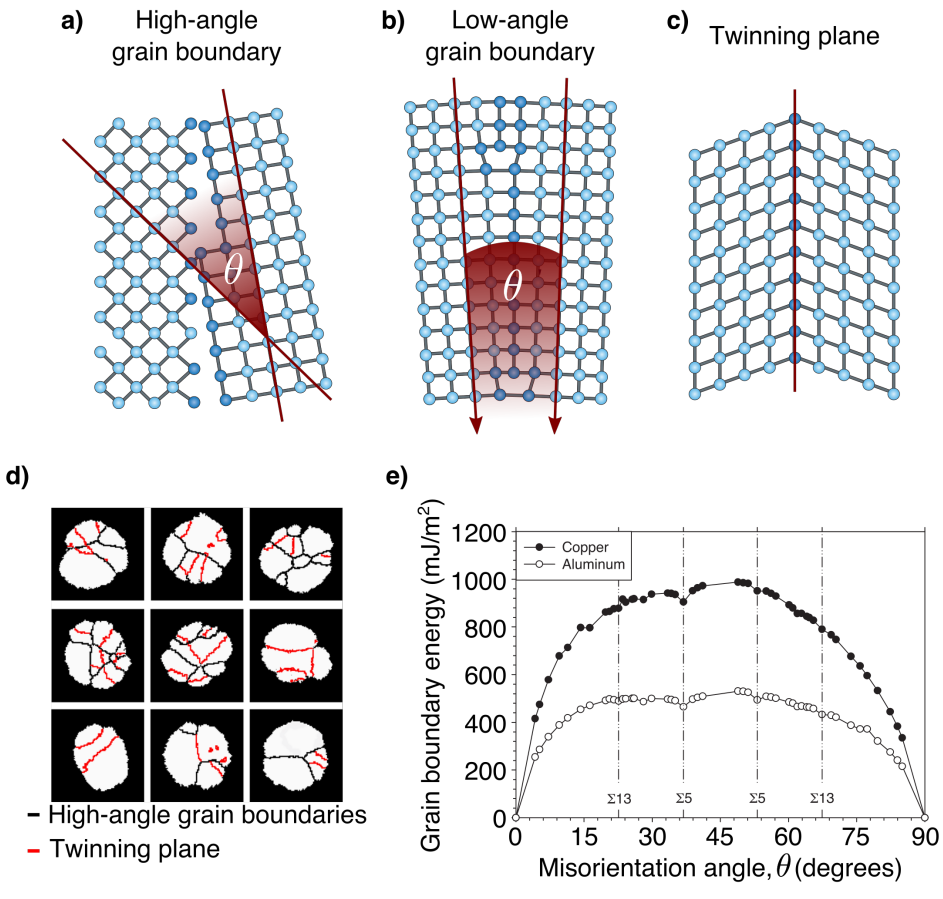

Figure 3.5: 2D sketches of a) high-angle, b) low-angle and c) twin-plane grain boundaries adapted from Ref. [231], where θ is the misorientation angle. d) Data from Alekseeva *et al.* [220] showing high-angle grain boundaries and twinning planes measured in 100 nm Pd nanoparticles. e) Simulations from Tschopp *et al.* [232] showing an example of the variation in grain-boundary energy with misorientation angle, θ. Figure composition adapted from [219].

due to dynamical local changes in the metallic structure that temporarily produce larger field enhancements within the metal, producing a larger field in it and therefore a temporary increase in ERS emission which would be observed as flares of the background signal in SERS.

We base our reasoning on the fact that, although we consider the nanoparticles to be spherical in our model calculations, as performed within the BEM [111], the actual nanoparticles used in the experiments have a crystallographic atomistic structure with faceting and polyhedral shapes, which can present defects and crystal mismatching. In order to account for the effects of these atomistic structure, we consider in a simple approach the crystalline defects in the metal nanoparticle and in the film,

made up of multiple crystal domains. The intersection between two crystallographic configurations can host 2D or 3D defect planes, also known as grain boundaries. Grain boundaries have been studied using electron microscopy methods [220, 233], which can reach atomic-precision resolution and allows the identification of crystal domains. Nevertheless, the effects of grain boundaries and crystallographic defects on the plasmonic resonance of such systems has not been properly addressed up to date. The simplest forms of grain boundaries are shown in Fig. 3.5(a-c) [231]. Here we consider only lattice planes in 2D, and particularly highlight the distinction between low-angle and high-angle grain boundaries. The lattice planes are offset to each other by certain angle, which defines the distinction between both categories: low-angle boundary if the angle is $\theta \lesssim 15°$, and high-angle boundary if the angle is $\theta \gtrsim 15°$. According to Alekseeva *et al.* [220], high angles outnumber low angles by $100:1$ in nanoparticles of diameter $D \sim 100$ nm, although the nanoparticles used in such study were made of palladium rather than gold, and were formed via hole-mask colloidal lithography.

The angle between lattice planes, known as misorientation angle, determines the amount of disorder and reduction in the density of metallic atoms in the grain boundaries. For instance, twinning plane defects such as those shown in Fig. 3.5(c), are a special case in which the adjoining planes are exactly mirrored, so the crystal pattern continues and there is no reduction in density. Figure 3.5(e) shows the angle-dependence of the grain boundary energy, for which a maximum at 45° is observed. The initial position with no misalignment is at 0° and for this particular lattice there is a 90° rotational symmetry, resulting in a twinning plane and subsequent energy minima at these points.

The consideration of exact lattices for complex geometries in the context of plasmonics is still beyond the scope/reach of full *ab initio* quantum methods, such as those based on TDDFT, due to their expensive computational requirements. To circumvent this challenge, we model the effect of the grain boundaries, and the corresponding local change in the lattice structure by considering the alteration of the average electron density at high- and low-angle boundaries as an effective change in the local plasma frequency, $\Delta\omega_p$, which yields an effective local plasma frequency $\omega_p^{\text{eff}} = \omega_p - \Delta\omega_p \propto \sqrt{n^{\text{eff}}/m^*}$ [see Eq. (2)]. In the case of a twinning plane, there is no change in the average electron density (by definition), but the band-structure of the material is locally altered, thus modifying the effective electron mass m^* [234], and therefore we could also consider the plasma frequency to be altered.

The number of possibilities regarding the position, size, shape and material-related properties of these localized regions with lower electron density is large and challenging to be fully explored. Here we will focus on three canonical situations which we deemed to be the most representative one among all considered and tested: vacuum cracks at the bottom facet. The effect of these structural modifications in the plasmonic response of the system is studied in the following sections.

3.4.1 Cracks

As mentioned above, the nanoparticles used in the experiments show polyhedral shapes, including pentagonal bipyramids which are known to have an angle mismatch in their structure that causes variable strain throughout the nanoparticle [235]. Furthermore, it has been shown that adatoms can form on the surface of nanoparticles, a process that can be further fed by the the strong fields induced at the gap and within the metal around the gap [43].

Although it is unclear to what extent optical fields localized at the gap can produce larger (nanometer-sized) changes in the crystal lattice, here we model the creation of a vacuum "crack" at the bottom of the nanoparticle with a geometry, as illustrated in Fig. 3.6(a), where we show two representative cracks, a vertical one in red, and an inclined one in purple. These cracks are assumed to be created due to the strain in the lattice. The actual simulated geometry corresponds to an hemiellipsoid of characteristic ellipsoid axis lengths of $a = 0.5$ nm, $b = 2.5$ nm and $c = 5$ nm. These cracks can show an inclination angle θ with respect to the xy-plane as shown in Fig. 3.6(a).

The scattering-cross section of a NPoM with such a crack, shown in Fig. 3.6(b), shows an almost identical spectrum for a vertical crack ($\theta > 90°$) compared to the situation without any crack (flat facet) for both the ℓ_1 and s_{20} modes. Moreover, for large inclination angles ($\theta > 60°$) a slight redshift of the scattering peaks is observed for wavelengths in the spectral flare region, although there is almost no dependence of the ℓ_1 mode on the inclination angle. On the other hand, small inclination angles of the crack ($\theta < 60°$) show a blueshift in the spectral flare region, which clashes with the experimental results shown in Sec.3.2. Moreover, small inclination angles (lightest blue line, $\theta = 30°$) also show the emergence of more scattering peaks and a redshift and decrease in intensity of the ℓ_1 mode due to the coupling of the lowest side of the crack with the bottom facet, while a blueshift is observed for the ℓ_2 mode.

Furthermore, the near-field map in the proximity of such cracks in Fig. 3.6(c) shows large field enhancements and gradients around the bottom edges of the cracks providing a lightning rod effect which would break the symmetry selection rules for molecular SERS similar to the case of picocavities, as in Chapter 2. Instead, the SERS spectra obtained in the experiments during the flare events do not show extra vibrational lines from the molecules, which suggests that the field around the molecules is not drastically affected. If disregarded that issue, inclined cracks would be a good candidate to explain the spectral flares in ERS as they show larger field enhancements inside the metal [Fig. 3.6(e)] when compared to the NPoM without a crack [Fig. 3.6(f)]. Nevertheless, along with mentioned pitfalls of the model, this geometry involves the creation of two new Au-air boundaries, which is energetically unfavorable [236], suggesting that this form of geometrical crstallographic defects might not be the most adequate candidate to explain the origin of the spectral flares.

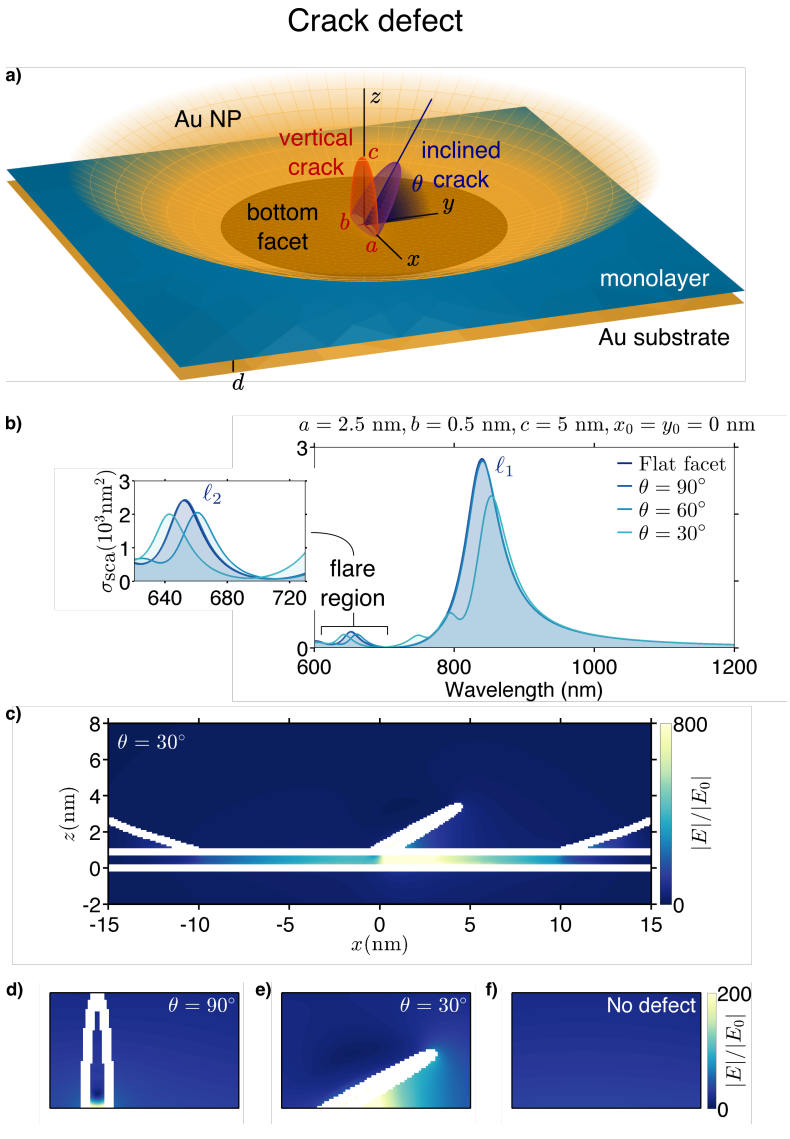

Figure 3.6: a) Detail of the nanoparticle cracks (red and purple regions) at the bottom of the nanoparticle in the NPoM configuration, simulated for vertical orientation and inclination of the crack θ. b) Inclination angle-dependence of the scattering cross-section for crack geometry with parameters $a = 0.5$ nm, $b = 2.5$ nm and $c = 5$ nm. c) Near-field maps for crack inclination angle 30°, showing field localization near the crack. Near-field maps showing the field inside the metal at the bottom facet of the nanoparticle around d) a vertical crack (90°), e) an inclined crack (30°), and f) no crack.

3.4.2 Grain boundaries at the NP facet edges

Instead of forming a crack, which is energetically unfavorable, it is more realistic to consider that grain boundaries host a reduced density of gold atoms. Electron-microscopy has confirmed that such grain boundaries appear at the facets of nanoparticles [220, 233], but alterations in their crystallographic structure have not been observed yet using optical methods. Considering the nanometric extension of the grain boundaries, we model the drop in the corresponding electron density as a reduction of the local plasma frequency in the vicinity of the defect. The reduction of the local plasma frequencies has been suggested to be of the order of 25% in the vicinity of a grain boundary [221].

This model accounts more realistically for grain boundaries and lattice defects than the crack described in Section 3.4.1 Grain boundaries could be placed at the facets or at the edges of these facets. We first consider the later, which we model as toroidal *patches* at the bottom facets with effective reduced plasma frequency, ω_p^{eff}, and size determined by parameters r_p and h, as illustrated with brown dark color in Fig. 3.7(a). This description effectively accounts for accounting for the existence of different types of defects, at the NP facet edges.

The scattering cross-section of a NPoM including such edge defect [Fig. 3.7(b)] shows a redshift and a decrease in intensity for increasing size (r_p value) of patches. The spectral region related to the flares (640 nm - 700 nm) shows variations with patch size in the position of the spectral peaks and intensities. Moreover, the near fields at the nanogap do not show any lightning rod effect around the NP edges that would produce increased field gradients, and therefore no extra SERS lines from the molecules deposited there would appear. This agrees well with the experimental observations. The field penetration within the patch is also increased when the plasma frequency at the edge is reduced, as shown in Figs. 3.7(d-e).

Changes at the edges of the bottom facet have been reported [225, 237], which are usually irreversible. For instance, light-induced damage is known to increase the facet width, which produces a redshift of the ℓ_1 mode [216, 225], as observed in Fig. 3.1(e). Nevertheless, the experimental results from Sec. 3.2 suggest a reversible mechanism to be behind the flares. In particular, the experiments in which white-light illumination was combined with inelastic laser light scattering described (in Fig. B.1 in App. B) show that the position and intensity of the ℓ_1 mode regain their initial position after a flare event.

3.4.3 Grain boundaries across the NP facet

So far we have considered the grain boundaries to be located at the edges of the facet of the NP, but grain boundaries and twinning planes are also present along the facets. The model considered for this situation is illustrated in Fig. 3.8(a), with the size of the patch (determined by the three semiaxes of the patch a, b and c) and the amount of effective ω_p^{eff} reduction accounting for the existence of different types of defects.

This structure accounts more realistically for grain boundaries and lattice defects

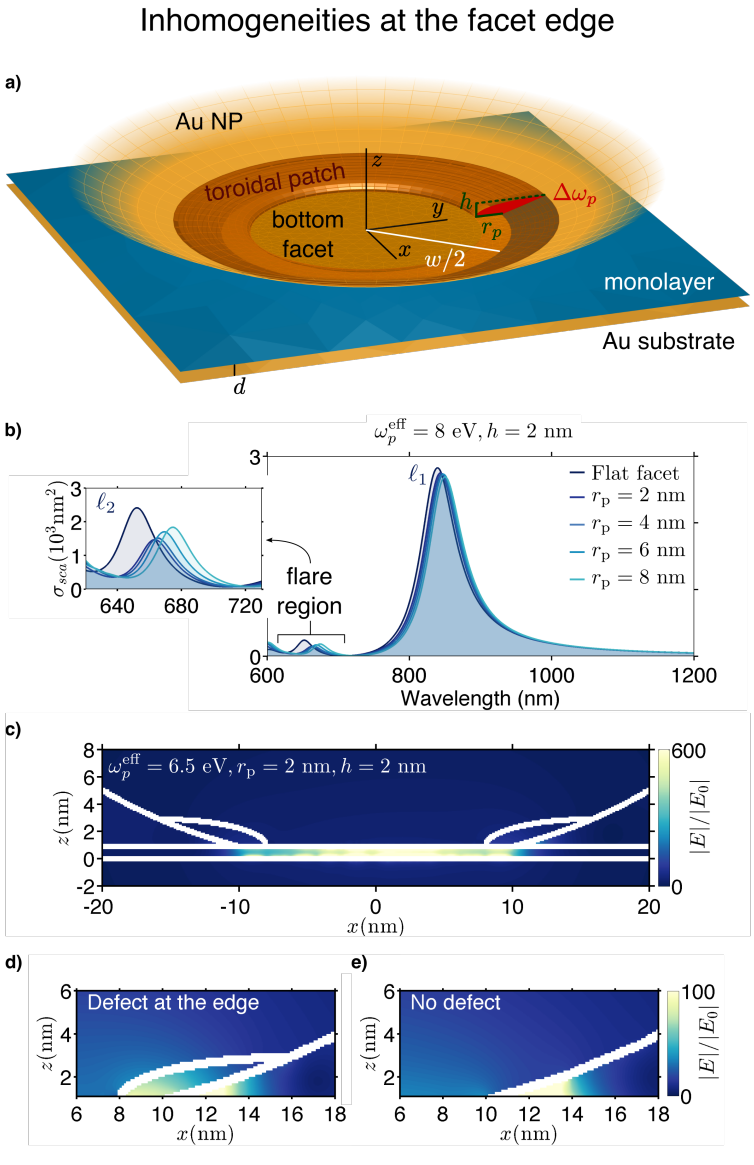

Figure 3.7: a) Detail of the grain-boundary at the NP facet edge (toroidal shape in dark brown) as used in model simulations. b) Scattering cross-section for such a geometry as a function of patch size r_{p}, with parameters $\omega_p^{\mathrm{eff}} = 8$ eV and height of the edge inhomogeneity $h = 2$ nm. c) Near-field maps of the grain boundaries at the edges of the facet with $r_{\mathrm{p}} = 2$ nm, $h = 2$ nm and $\omega_p^{\mathrm{eff}} = 6.5$ eV. Near-field maps showing a zoom-in of the field inside the metal in d) a defect at the edge and e) edge with no defect.

than the crack described in Section 3.4.1 We have calculated the dependence of the scattering cross-section for such configuration on several parameters, such as the reduction in effective plasma frequency in Fig. 3.8(b), patch size in Fig. 3.8(c) and patch position in Fig. 3.8(d). The main scattering-cross section plots in Figs. 3.8(b-d) show slight redshifts and decreases in intensity for the ℓ_1 mode, specially for large patches taking large areas of the bottom facet [Fig. 3.8(c)], as one would expect when considering that a reduction of one of the metallic facets (NP or substrate) would have a similar effect. Instead, the cavity modes across the 640-700 nm spectral region, which cover the region in which the flares are experimentally observed, show greater dependence on the inhomogeneity patch parameters, as the modes of the NPoM structure are specially sensitive to any changes happening at the nanogap.

Furthermore, this model does not show increased field gradients around the grain boundaries, as observed in Figs. 3.9(a), an issue that would cause additional Raman lines from the molecules nearby. Instead, the field penetration increases within the regions with reduced plasma frequency. According to Eq. (3.15) of the theory of ERS emission, the Raman signal scales with the 4^{th} power of the local field, and therefore, one could expect a larger local field within the metal to produce larger background ERS signal, i.e., flares.

With the aim of understanding these results, one can derive a simple expression to estimate the increase in the ERS emission as a function of the parameters of our model. First we will obtain the field penetration into the metal as a function of ω_p^{eff}. From the conservation of the perpendicular component of the displacement field $D_\perp$ at the metal-insulator interface, one gets:

$$\varepsilon_{\text{m}} E_{\perp,\text{m}} = \varepsilon_{\text{g}} E_{\perp,\text{g}}, \tag{3.17}$$

where ε_{g} and ε_{m} are the permittivities in the gap and metal respectively. The permittivity of the metal depends on the plasma frequency ω_p, and the penetration into the metal, η is then given by:

$$\eta(\omega_p) = \left| \frac{E_{\perp,\text{m}}}{E_{\perp,\text{g}}} \right| = \left| \frac{\varepsilon_{\text{g}}}{\varepsilon_{\text{m}}(\omega_p)} \right|, \tag{3.18}$$

which depends on the plasma frequency of the metal ω_p. In the grain boundary regions ω_p is reduced by $\Delta\omega_p$, which increases the field penetration into this region,

$$\eta(\omega_p - \Delta\omega_p) = \left| \frac{\varepsilon_{\text{g}}}{\varepsilon_{\text{m}}(\omega_p - \Delta\omega_p)} \right| \tag{3.19}$$

As mentioned in Sec. 3.1, the field within the metal decays exponentially at a rate which depends on the effective wavevector of the plasmon in the MIM waveguide [213, 214]. Moreover, the field is mainly polarized in the perpendicular direction, so from now on we will omit the explicit reference to the component $\perp$ of the field. For very thin MIM waveguides, the dispersion relation reduces to the one given by Eq. (3.2), $k_\parallel = -\frac{2\varepsilon_{\text{g}}}{d\varepsilon_{\text{m}}}$. Moreover, the skin depth $\delta_\perp = \frac{d\varepsilon_{\text{m}}}{2\varepsilon_{\text{g}}}$ given by Eq. (3.3) depends on

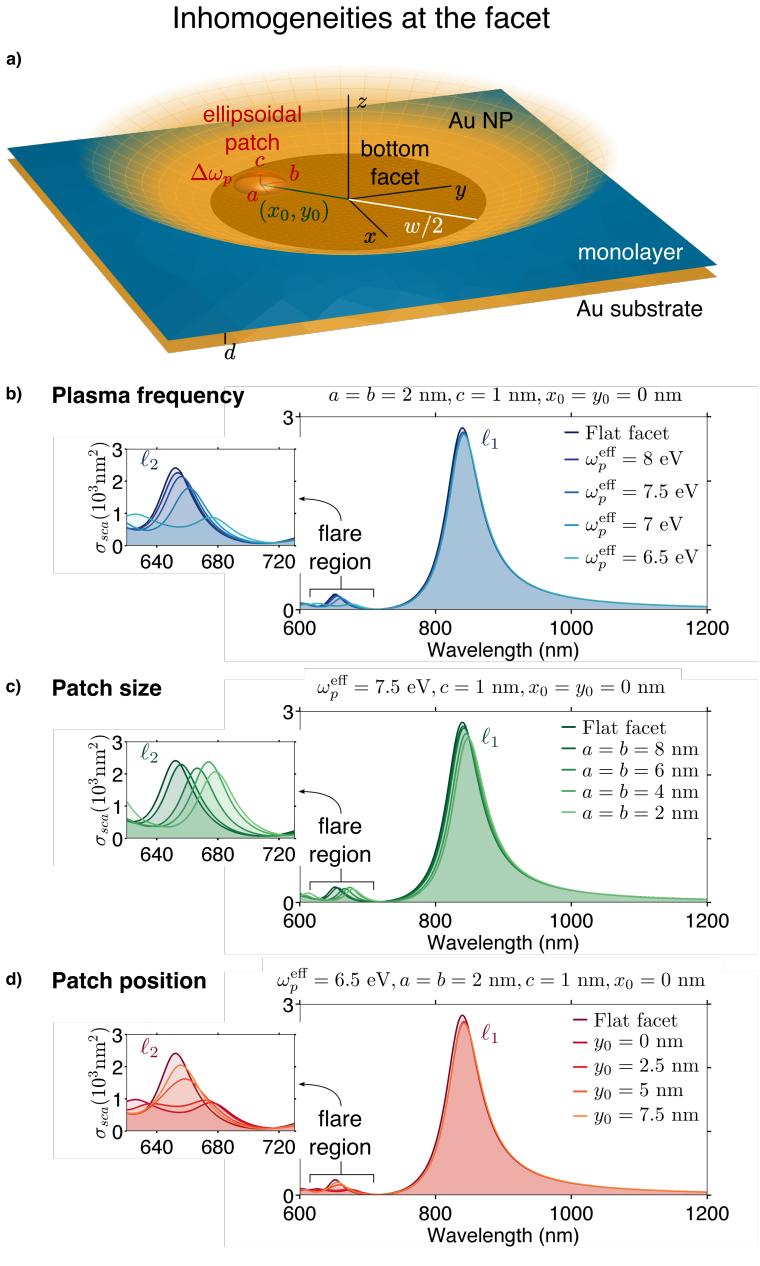

Figure 3.8: a) Detail of the grain-boundary at the NP facet (hemiellipsoidal shape) simulated. b) Local plasma frequency dependence of scattering cross-section for geometry with parameters $a = b = 2$ nm and $c = 1$ nm. c) Size dependence of scattering cross-section for geometry with parameters $\omega_p^{\text{eff}} = 6.5$ eV and $c = 1$ nm. d) Position dependence of scattering cross-section for geometry with parameters $\omega_p^{\text{eff}} = 6.5$ eV, $a = b = 2$ nm and $c = 1$ nm.

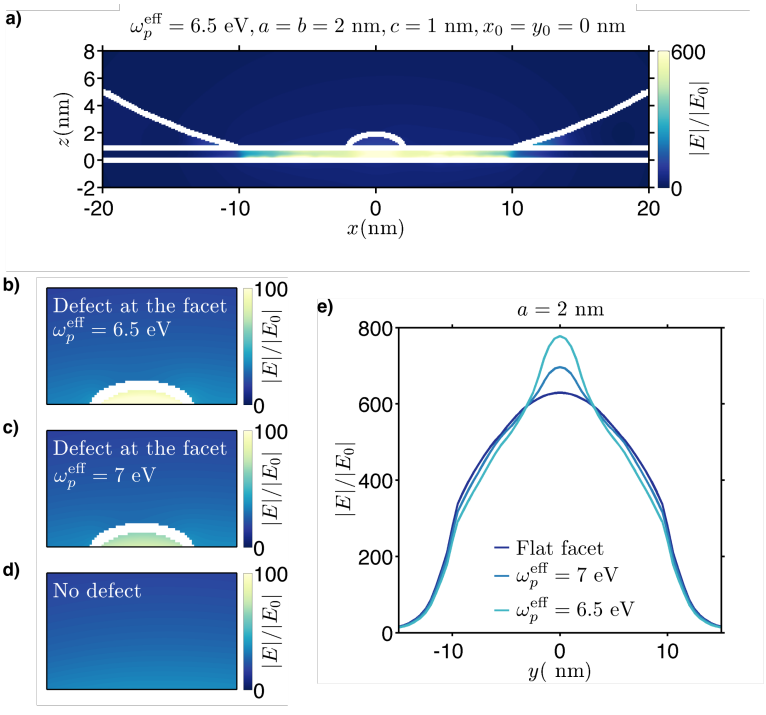

Figure 3.9: a) Near-field map for hemiellipsoidal patches with $a = b = 2$ nm and $c = 1$ nm and $\omega_p^{\text{eff}} = 6.5$ eV. Near-field maps showing the field inside the metal in a defect at the facet with b) $\omega_p^{\text{eff}} = 6.5$ eV, c) $\omega_p^{\text{eff}} = 7$ eV, and d) no defect. Near field at the center of the gap ($z = 0.45$ nm) for $a = 2$ showing an increase in the near field for decreasing ω_p^{eff}.

the metal permittivity and is therefore inversely proportional to the field penetration, $\delta_\perp \propto 1/\eta(\omega_p)$. Thus, the field in the metal is given by,

$$E_{\text{m}}(z) = \eta(\omega_p) E_{\text{g}} e^{-z/\delta_\perp}, \tag{3.20}$$

where E_{g} is the electric field at the nanogap. Furthermore, by assuming that the Poynting vector is conserved for MIM plasmons propagating in the gap, one gets that $|E_{\text{g}}|^2 k_{\|}$ is conserved, which leads to field enhancements within the dielectric material at the center of the facet of $E_{\text{g}} \propto \sqrt{\eta}$, further increasing the field inside the metal due to the reduction of ω_p. This is supported by simulations, as shown in Fig. 3.9(e). For instance, reducing $\omega_p = 9$ eV to 6.5 eV gives a +24 % increase in E_{g} as predicted.

Finally, as described in Sec. 3.3, the ERS in the metal giving rise to the flare is proportional to the 4^{th} power of the optical the field in the metal, integrated over the volume in which the field penetrates within the metal [see Eqs. (3.15) and (3.16)]. To calculate the contribution of metallic regions with different ω_p^{eff} to the background ERS intensity, $\mathcal{I}$, let us consider a small cylindrical region within one of the metallic sides in the MIM, with radius a, height $h \gg \delta_\perp$, and homogeneous plasma frequency

ω_p. The contribution of such cylindrical region to the background ERS intensity can be expressed as the volume integral of Eq. (3.20), which yields,

$$\mathcal{I} \propto \pi a^2 \delta_\perp [\eta(\omega_p) E_\mathrm{g}]^4, \tag{3.21}$$

where we assume the field to be invariant in the direction parallel to the MIM structure.

Proceeding in a similar fashion we calculate the increase in the background ERS intensity, $\mathcal{I}_\mathrm{fl}$, due to a cylindrical patch with a reduction to the plasma frequency $\Delta\omega_p$, radius a and height $c > \delta'_\perp/4 \sim 1$ nm, with $\delta'_\perp \propto 1/\eta(\omega_p - \Delta\omega_p)$, similar to the ones shown in Fig. 3.9, as,

$$\mathcal{I}_\mathrm{fl} \propto \pi a^2 \delta'_\perp [\eta(\omega_p - \Delta\omega_p) E'_\mathrm{g}]^4, \tag{3.22}$$

which neglects the background contribution from the rest of the facet (as it is much smaller), as detailed in Appendix C. Therefore the ratio of flares to background ERS intensity given by:

$$\frac{\mathcal{I}_\mathrm{fl}}{\mathcal{I}_\mathrm{bgd}} = \left(\frac{2a}{w}\right)^2 \left(\frac{\eta(\omega_p - \Delta\omega_p)}{\eta(\omega_p)}\right)^5, \tag{3.23}$$

where $\mathcal{I}_\mathrm{bgd}$ is the background ERS intensity from the whole facet of width w in the absence of the grain boundary.

Effective plasma model for antenna mode shift

Larger $\Delta\omega_p$ changes in the defect "patch" region at the centre of the nanoparticle facet and an increase in patch radius can affect the plasmonic modes and therefore the optical response of the whole NPoM plasmonic structure as observed in Fig. 3.8(b-c). In order to gain insight into these trends we will consider an analytical perturbation model to describe the system under consideration. We will focus on the redshift of the wavelength of the ℓ_1 mode, λ_c, produced by the patch of reduced effective ω_p^eff. As shown in Sec. 3.1, the MIM dispersion relation [Eq. 3.2] provides a good estimation of the modes within the NPoM cavity, which we can be recast as

$$\omega^2 = \frac{\omega_p^2}{\varepsilon_\infty + \frac{2\varepsilon_\mathrm{g}}{k_\parallel d}}. \tag{3.24}$$

When the facet width w is fixed, this also fixes $k_\parallel$ [see Eq. (3.5)], so that the MIM dispersion becomes proportional to ω_p.

We will assume that the main antenna mode, ℓ_1, follows a Gaussian intensity distribution $|E(r)|^2 = I(r) \propto e^{-4\ln 2 r^2/(\Delta x)^2}$ with FWHM $\Delta x = \sqrt{2Rd/\varepsilon_\mathrm{g}}$ as sketched in Fig. 3.10(a). The field is confined to the cavity due to a potential proportional to the *local* plasma frequency of the metal $V(r) \propto \omega_p(r)$. Thus, if the plasma frequency $\omega_p(r)$ is not uniform along the finite MIM waveguide, the potential $V(r)$ and frequency of the mode ω_c will also be affected.

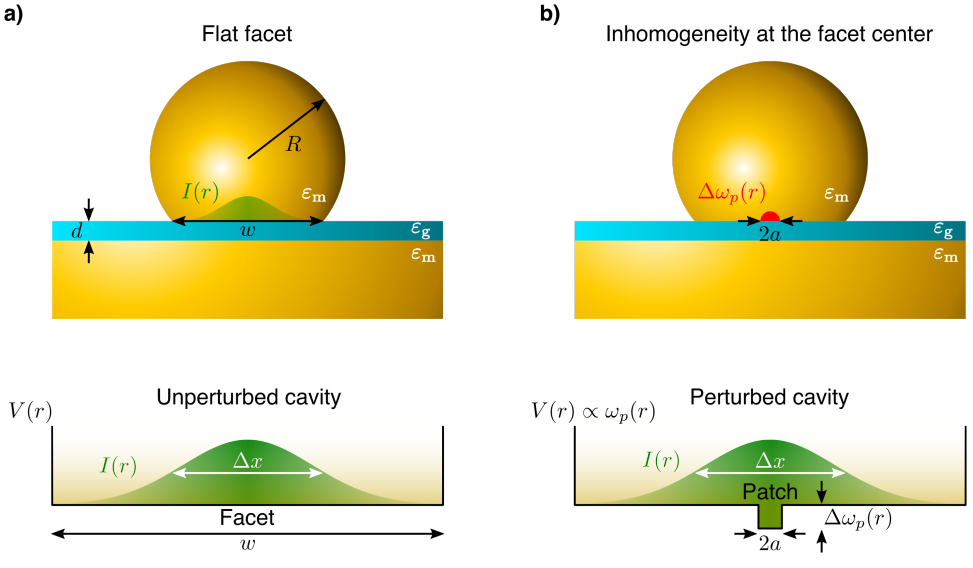

Figure 3.10: a) NPoM structure with flat facet (no inhomogeneity) showing a Gaussian intensity distribution, $I(r)$, with r the radial position at the unperturbed bottom facet with width w of the NP with radius R, separated from a metallic substrate by a dielectric spacer of thickness d. b) NPoM structure with a decrease plasma frequency, $\Delta\omega_p$, at the center of the facet perturbing the cavity in a patch with width $2a$. The panels at the low row show a zoom-in of the potential associated with each situation, with the Gaussian intensity distribution with FWHM Δx in green.

We can calculate the wavelength shift $\delta\lambda_c$ of the ℓ_1 mode due to a perturbation $\Delta\omega_p$ in a small region in the MIM [see Fig. 3.10(b)] using first order perturbation theory. Taking into account that Eq. (3.24) follows the dependence $\omega \propto \omega_p$, we will consider that the frequency shift $\delta\omega$ of the nanocavity mode is proportional to the plasma frequency change $\Delta\omega_p$. Therefore, considering ω_p^0, as the unperturbed plasma frequency, the relative shift of the nanocavity mode is given by,

$$-\frac{\delta\lambda}{\lambda_c} = \frac{\delta\omega}{\omega_c} = \frac{1}{2}\frac{\int_0^{w/2} r\,dr|E(r)|^2[-\Theta(a-r)\Delta\omega_p]}{\int_0^{w/2} r\,dr|E(r)|^2\omega_p^0} = -\frac{1}{2}\frac{\Delta\omega_p}{\omega_p^0}\frac{\int_0^a r\,drI(r)}{\int_0^{w/2} r\,drI(r)}, \tag{3.25}$$

where the prefactor of $1/2$ is included since the perturbation is assumed only on one side of the waveguide (the NP's facet side). Introducing the Gaussian dependence of

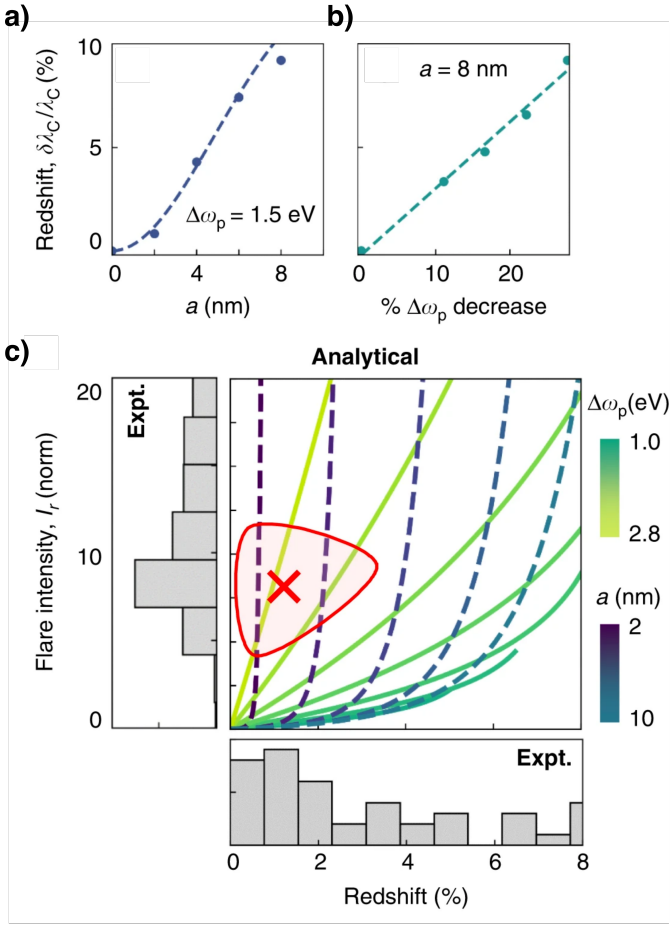

Figure 3.11: a-b) Simulated (points) and analytical (dashed lines) coupled NPoM mode redshifts vs a and $\Delta\omega_p$, showing their agreement. c) Analytical model for relative flare intensity vs mode redshift for (dashed) $a = 2, 4, 6, 8, 10$ nm over $\Delta\omega_p = 0 - 3.5$ eV and (solid) $\Delta\omega_p = 1, 1.3, 1.6, 1.9, 2.2, 2.5, 2.8$ eV over $a = 0 - 15$ nm. Grey histograms show experimental measurements of flare intensity (left) and ℓ_1 mode redshift (bottom) ocurrence. Red marker shows maximum likelihood realization. Experimental measurements from Cloudy Carnegie at Cambridge University. Figure adapted from [218].

the intensity,

$$\frac{\delta\lambda_c}{\lambda_c} = -\frac{\delta\omega}{\omega_c} = \frac{1}{2}\left(\frac{\Delta\omega_p}{\omega_{p0}}\right)\int_0^a r\,dr\exp\left(-4\ln 2\frac{r^2}{\Delta x^2}\right)$$
$$= \frac{1}{2}\left(\frac{\Delta\omega_p}{\omega_{p0}}\right)\left[1-\exp\left(\frac{2\ln 2\varepsilon_g a^2}{Rd}\right)\right], \tag{3.26}$$

which gives an analytical expression for ℓ_1 mode shifts on the introduction of a patch

of reduced ω_p.

In Figs. 3.11(a-b) we compare the values given by this equation (dashed lines) with those obtained within full electromagnetic calculations (BEM) (dots) and observe a good agreement for low values of a and $\Delta\omega_p$. Mapping the analytical flare intensity and redshift vs. (a, $\Delta\omega_p$), as indicated by the dashed and solid lines in Fig. 3.11(c), allows us to compare these results of the analytical model with the number of flare events in the experiments obtained in Cambridge (grey histograms), and so examine the most appropriate effective parameters (a, $\Delta\omega_p$) to reproduce the occurrence of events.

By inspection of the flares, we find that most of the data lies within $a = 2-3$ nm and $\Delta\omega_p = 2-3$ eV, which implies that such inhomogeneities are indeed small but strongly perturb the local electronic properties of Au. These parameters suggest single- or few-plane defects, such as those which have been observed via other methods such as TEM [220, 233]. The patch areas are indeed consistent with a line defect 1 nm wide stretching across the entire facet, typically found in electron microscope images.

This model matches many of the flares observed in the experiments. Moreover, the spectral range of flares is well matched to the higher order modes (short wavelengths) which are very sensitive to changes at the nanogap. Compared to the other two geometries considered in Section 3.4.1 and 3.4.2, this is the only effective configuration of ihomogeneities in which a change to the plasmonic modes is achieved without producing a lightning rod effect.

In order to match the time-scale of the spectral flares, the modifications of grain boundaries should happen on the millisecond time-scale, before reverting to an identical situation as before. Although this is unlikely, as this would imply a complete reorganization of the NP crystal structure, a plausible explanation would be that these defects move across and away from the plasmonic hot-spot on this time-scale, and therefore would only be observable directly in the vicinity of the facet centre.

It is worth mentioning that although nanoparticles have been shown to have a quasi-molten nature [222–224] and diffusive displacement [238, 239] via electron microscopy methods, this is the first time that these sort of effects have been observed optically. If the formation and restructuring of atomic-scale surface defects is indeed being observed via optical methods, this opportunities for non-destructive analysis of nanoparticle grain boundaries, which can be measured in situ and under ambient conditions. An inhomogeneous distribution of the plasma frequency serves as an effective model which captures the modification of the whole optical response of an entire NPoM, due to an underlying microscopic origin. Such simple effective models thus prove to be valid to obtain rough estimations of the size and extension of the inhomogeneity in the structure.

3.5 Discussion and Summary

In this chapter we have linked the apparition of flares in ms time-dependent SERS experiments of molecules in NPoM structures to dynamic changes of the atomic structure of the metallic NP. We have effectively modeled this structural changes as a drop in the local plasma frequency at small regions of the metallic nanostructure due to the decrease of the electronic density at the grain boundaries. The model explains the increase of the ERS due to a larger field penetration and the shifts observed for the NPoM modes.

Although this model is successful in explaining a number of the observed flare features, there are a number of issues not fully addressed. The increased likelihood of flares with age of nanoparticle is not understood, although it is possible that oxidative effects lead to a higher number of defects within the nanoparticle, leading to a higher number of flare modes observed. However, more research would be needed to ascertain whether defect numbers do in fact increase in this way, possibly through correlation with electron microscopy. Similarly, the model presented here accounting for grain changes in the grain boundaries at the bottom facet of the NP cannot explain why more flares are observed for different spacer molecules. It is likely that this difference is due to the effect of molecular binding to the gold (since purely molecular processes have been ruled out), but a deeper understanding of this effect is needed.

Additionally, although the red-shift in the ℓ_1 mode is predicted by simulations, the coupled-mode observations are not fully reproduced by the model based on a drop of the electronic density at the grain boundaries. In experimental observations, spectral flares are only observed in the 640-700 nm region, with broad-band white light required in order to observe the higher-wavelength ℓ_1 modes.

Finally it must be pointed out that this effective response model does not address why an increase in the $\ell_1$mode intensity is seen in the event of a flare. In fact, simulations predict that all ℓ_1 mode red-shifts should be seen alongside a decrease in intensity of the ℓ_1 mode. This could be explained by an stimulated electronic Raman scattering process, which depends on the 8^{th} power of the electromagnetic field, assuming that the confinement is sufficiently high to generate CW SRS [240–243] at the red- shifted coupled plasmon, even with incoherent illumination.

The effective local plasma frequency model presented in Sec. 3.4 explains with relative success the origin of the spectral flares observed in SERS experiments, and as an initial stepping stone, aims to address the need for a more fundamental framework for understanding such phenomena. In fact, this effective model fails to address some of the aspects observed for spectral flares, such as the increases in the scattered light intensity observed for laser+white light illumination. A complete description of the underlying physical mechanism would require for a quantum *ab initio* framework to capture the dynamics of the atomic structure and their influence on the local electron density, and therefore on ERS. Due the complexity of the system, the calculation

of its optical response is out of the scope of full *ab initio* frameworks, although they can be used, for instance, in simplified geometries (such as 2D infinite slabs) to understand the influence of grain boundaries and atomic-scale dynamics on the the local electron density at the surface of the metal, which can be useful for less sophisticated frameworks in more complex geometries. Thus, there is plenty of room to cover between the effective local plasma model and full *ab initio* frameworks in the way to gain a more precise understanding of the origin of the spectral flares.

4 Atomic-scale structural features as probed by swift electrons

Electron energy loss spectroscopy (EELS) [55–58] in scanning transmission electron microscopy (STEM) [53,54], together with optical spectroscopies [244,245], has played a crucial role in understanding the properties and dynamics of plasmons in nanoparticles (NPs). In particular, technical progress in the performance of STEM-EELS microscopy in the last two decades [69–71] has enabled sub-nanometer resolution [53,72] and sub-eV energy sensitivity [73] in EELS, opening new opportunities for characterization of novel materials and nanostructures [54,74]. Thanks to these advances it is possible to perform vibrational spectroscopy with nanometer resolution of phonons [56,75–78] or to characterize biomaterials with low energy beams reducing radiation damage [56,79,80]. Although this technique has been successfully used for decades in the characterization of localized plasmon resonances in metallic nanoparticles [246,247], only with the aforementioned improvements it is now possible to implement single-NP EELS experiments with sizes in the range below 10 nm [81–86] with extraordinary resolution, turning STEM into a suitable tool for the study of new and complex phenomena at the nanometer-scale.

In this context, much attention in the literature has been turned towards quantum

size effects of collective resonances localized at the surface of NPs (LSPs). Blue-shifts [82] of 0.5 eV were measured in the surface plasmon resonance energy of Ag nanoparticles when their radius was decreased from 20 nm to less than 2 nm [82–84, 88, 89]. The interaction between coupled gold nanoprisms has also been probed by EELS showing mode hybridization and large field localization at the nanogaps [248, 249]. Quantum plasmon resonances controlled by molecular tunnel junctions between two plasmonic Ag resonators have also been probed by EELS combined with atomic resolution imaging [250]. Moreover, a tomography scheme based on electron microscopy has allowed 3D-imaging of LSPRs in silver nanocubes [251], and more recently, 3D maps of local density of states of plasmonic nanoparticles with nm spatial resolution and sub-eV energy resolution have been obtained [252].

Classical electrodynamics, within local dielectric theory [64, 253–255], has successfully explained the plasmonic response of NPs, providing analytical expressions to account for EELS in targets of simple geometries. Solutions of Maxwell's equations have been implemented in numerical tools for EELS configurations such as the BEM [108,110] or FDTD methods [256] which allow for simulation of EELS in structures of complex geometrical shapes and different environments. Nevertheless, the increased resolution obtained in the last experimental setups has pushed the development of phenomenological and semiclassical theories to account for specific quantum effects in the properties of LSP resonances, such as electron confinement [90], electron spill-out at the interfaces [31, 91–93], non-local effects [94, 95] in the dielectric response, modification of local environments [86], or activation of quantum tunneling across subnanometer interparticle gaps [33, 96]. Most of the classical and semiclassical theories rely on spherical descriptions of the NP's geometry, characterized by a local $\varepsilon(\omega)$ or non-local $\varepsilon(\omega, k)$ dielectric functions with ω the frequency and k the wavevector of the excitations, but often these theoretical approaches do not consider the specific crystallographic faceting of the NP's sides, i.e., the atomic-scale surface features.

In analogy with optical spectroscopy, discussed in Chapter 2, *ab initio* atomistic methods such as TDDFT provide an appropriate quantum framework to consider the aforementioned effects in a straightforward and complete manner including the role of the atomistic structure in EELS. In the following we compare the results of electron energy losses obtained within atomistic TDDFT for an icosahedral Na_{380} cluster with those obtained within a classical BEM model that reproduces the atomic faceting of the NP by means of sharp surface boundaries, as a way to address the influence of subnanometric features in EELS. As a benchmark to understand the EEL probability in small nanoparticles, we first explore in Sec. 4.1 the canonical case of spherical nanoparticles within the local dielectric response approximation. We show the influence of subnanomatric features in EELS and identify the modes excited for axial electron trajectories in typical icosahedral NPs for different orientations in Sec. 4.2, which in general differ to those observed in a spherical nanoparticle. We extend this study to analyze the impact parameter dependence of EEL spectra in Sec. 4.3 and identify the excitation of key LSPs and CBPs. The nature of the latter is further explored in Chapter 5.

4.1 Electron energy loss in small nanoparticles

One of the most studied configurations in EELS is the spherical nanoparticle. The spherical symmetry simplifies the mathematical expressions of the electromagnetic fields induced by a probing electron and provides a direct way to analyze the system's response. Different models have been proposed to account for the response of the material constituting the NP, each accounting for certain effects, such as non-local effects, quantum confinement, spilling out of the electron density, or electron-beam-induced changes to the surrounding material. Nevertheless, all of these approaches have in common that the nanoparticle is considered to be spherical, whereas actual small nanoparticles ($a \sim 1-10$ nm), as studied within EELS, usually have polyhedral shapes [84,86], which include crystallographic features forming atomic-sale geometries such as facets, edges and vertices. Even so, the strength of a model that describes the NP's geometry as spherical relies on its simplicity, which allows for analytical or semi-analytical solutions of the EEL probability, and a benchmark that is useful to analyze the EEL spectra of nanoparticles with smaller degree of symmetry, such as icosahedral nanoparticles.

Regarding the description of the material's response, the local response approximation is the simplest description, yet relatively accurate, which could be used to describe the EEL probability in small nanoparticles. The expressions obtained for the EEL probability of a spherical particle can be further simplified if the nonretarded approximation is considered. For a spherical nanoparticle with radius a and whose material response is described by a local dielectric function $\varepsilon(\omega)$ [see Fig. 4.1(a)], the EEL probability of an electron, $\Gamma_{\rm EELS}(\omega)$, at an impact parameter b (which can be larger or smaller than the radius a) and velocity v, is given by the semi-analitycal expression [257]:

$$\Gamma_{\rm EELS}(\omega) = \Gamma_{\rm bulk}(\omega) + \frac{4a}{\pi v^2}\sum_{l=0}^{\infty}\sum_{m=0}^{m=l}(2-\delta_{m0})\frac{(l-m)!}{(l+m)!}\Big\{\mathrm{Im}[\gamma_l(\omega)](A^o_{lm})^2 + \mathrm{Im}\left[2\beta_l(\omega) - \frac{1}{\varepsilon(\omega)}\right]A^o_{lm}A^i_{lm} + \mathrm{Im}[\alpha_l(\omega)](A^i_{lm})^2\Big\}, \tag{4.1}$$

where,

$$\alpha_l(\omega) = \frac{(l+1)(\varepsilon(\omega)-1)}{\varepsilon(\omega)(l\varepsilon(\omega)+l+1)}, \quad \beta_l(\omega) = \frac{2l+1}{l\varepsilon(\omega)+l+1}, \quad \gamma_l(\omega) = \frac{l(1-\varepsilon(\omega))}{l\varepsilon(\omega)+l+1}, \tag{4.2}$$

and

$$A^o_{lm} = a^l\int_{\sqrt{a^2-b^2}}^{\infty}\frac{dz}{r^{l+1}}P_l^m\left(\frac{z}{r}\right)g_{lm}\left(\frac{\omega z}{v}\right) \tag{4.3}$$

$$A^i_{lm} = \frac{1}{a^{l+1}}\int_0^{\sqrt{a^2-b^2}}dz\, r^l P_l^m\left(\frac{z}{r}\right)g_{lm}\left(\frac{\omega z}{v}\right). \tag{4.4}$$

In these integrals, $z = \sqrt{r^2 - b^2}$, $P_l^m(x)$ is the associated Legendre polynomial of degree l and order m, and,

$$g_{lm}(x) = \begin{cases} \cos(x), & \text{if } l+m \text{ even} \\ \sin(x), & \text{if } l+m \text{ odd.} \end{cases} \tag{4.5}$$

The first term in Eq. (4.1), $\Gamma_{\text{bulk}}(\omega)$, gives the bulk losses due to the electron trajectory traveling a distance $L = \sqrt{a^2 - b^2}$ in a lossy medium. The other terms give the losses due to the presence of the surface. In particular, the second term [$\sim (A_{lm}^o)^2$] is related to the energy loss experienced by the electron when it is outside the sphere (before entering or after exiting the sphere); the third term [$\sim A_{lm}^o A_{lm}^i$] is related to losses experienced by the electron outside the sphere (after exiting) by plasmons excited when the electron is inside the sphere, and losses experienced by the electron when it is inside the sphere by plasmons excited when the electron was outside the sphere (before entering); the last term [$\sim (A_{lm}^i)^2$] gives the losses experienced the electron when it is inside the sphere by plasmons excited when the electron is still inside the sphere.

For external trajectories ($b > a$) equation 4.1 reduces to the following analytical expression [258, 259], which has been widely used in the literature:

$$\Gamma_{\text{EELS}}(\omega) = \frac{4a}{\pi v^2} \sum_{l=0}^{\infty} \sum_{m=0}^{m=l} \frac{2 - \delta_{m0}}{(l-m)!(l+m)!} \left(\frac{\omega a}{v}\right)^{2l} K_m^2\left(\frac{\omega b}{v}\right) \text{Im}\left[\frac{\varepsilon(\omega) - 1}{\varepsilon(\omega) + (l+1)/l}\right], \tag{4.6}$$

where $K_m(x)$ is the modified Bessel function of the second kind of order m.

This latter expression gives some insight about the dependence of the energy losses on the different parameters. For instance, when $\omega a/v \ll 1$, which is the case for small nanoparticles ($a \sim 1-10$ nm) and fast electrons ($E_{\text{k}} \sim 100$ keV, $v \sim 0.55\,c$), and the electron is far from the particle ($b \gg a$), the dipolar term ($l = 1$) dominates. For grazing trajectories, ($b \sim a$) the dominant contribution to each l comes from the $m = l$ term, and the dipolar mode does no longer dominate so strongly over the high-order modes. The dependence of the EEL probability on the impact parameter is illustrated in Fig. 4.1(b), where Γ_{EELS} is plotted as a function of the impact parameter for a Na nanoparticle of radius $a = 2$ nm, whose material is characterized as a Drude dielectric function with $\omega_p = 6.05$ eV and $\gamma = 0.3$ eV (including surface scattering effects as described in Chapter 1, Sec. 1.1). For external trajectories with large impact parameters ($b \gg a$), EELS provides similar plasmon excitation as those obtained in optical spectroscopy. Grazing trajectories imply that the field generated by the probing electron beam can no longer be considered to be similar to a plane wave, and together with the dipolar plasmon, higher-order modes also couple to the probing field as observed in Fig. 4.1(b) for $b \sim a$. The spectra in Fig. 4.1(b) also show that the main losses are cased by excitations produced when the probing electron trajectory crosses the NP.

For penetrating trajectories ($b < a$), we observe in Fig. 4.1(b) that the excitation of LSPs shows great dependence on the impact parameter, and the excitation of the

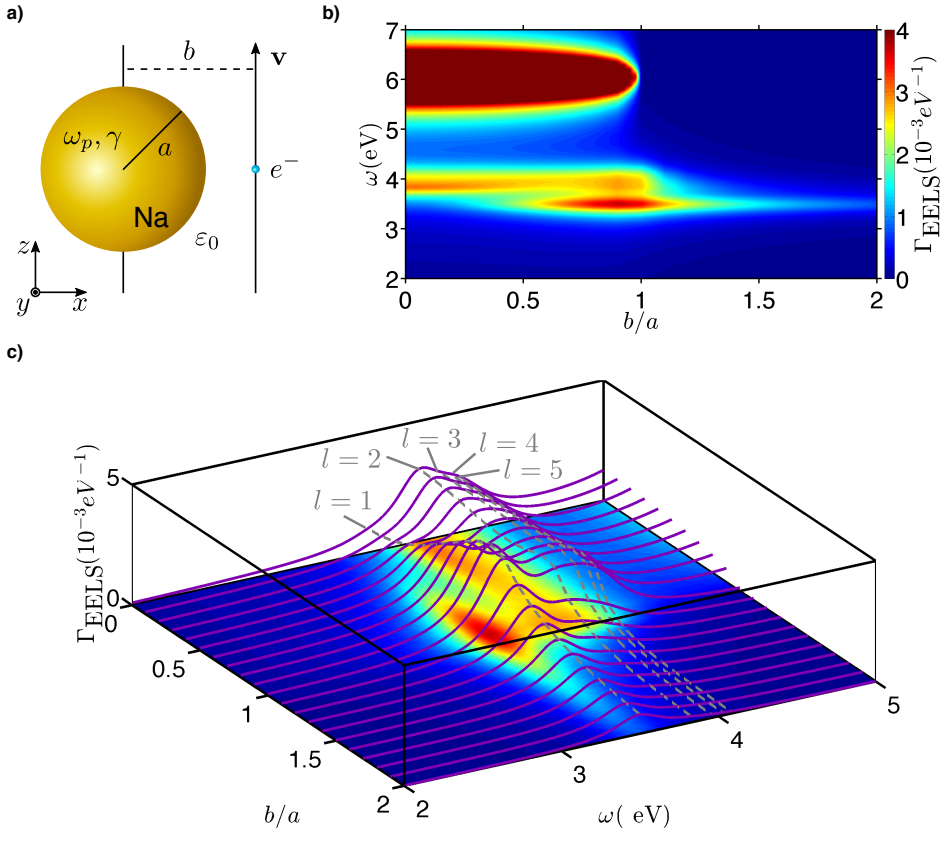

Figure 4.1: a) Spherical nanoparticle with radius a and frequency-dependent local dielectric function $\varepsilon(\omega)$ and a electron traveling nearby with impact parameter b and velocity v. b) EEL spectra colormap for a Na ($\omega_p \sim 6.05$ eV) spherical nanoparticle with radius $a = 2$ nm. c) Waterfall plots of the EEL probability spectra for the energy region corresponding to the LSPs for individual impact parameters (straight purple lines) with the energy corresponding to each l-mode highlighted (dashed grey lines).

bulk plasmon at ~ 6 eV with a much larger intensity than the LSPs (see saturation of Γ_{EELS} in Fig. 4.1(b). The excitation of the lowest five LSP modes ($l = 1 - 5$) in such situation is tracked in Fig. 4.1(c). Here we observe that the dipolar mode $l = 1$ fades away as the impact parameter tends to zero [left-hand side of Fig 4.1(b) at $\omega \simeq 3.45$ eV]. The reason for this behavior is explained by symmetry arguments: due to azimuthal symmetry, only $m = 0$ modes are excited by the electron beam, and as the external potential produced by the electron beam scales as $\phi_{\mathrm{ext}}(\mathbf{r}, \omega) \sim e^{i\omega z}/v$ [see equation 1.54], the change in the phase of the potential along a spherical NP for an axial trajectory is given by $\Delta\varphi = L\omega/v$, where L is the characteristic length of the nanostructure ($L \simeq 2a$ in this case). For small nanoparticles ($L = 2a \sim 4$ nm) and fast electrons ($E_k \sim 100$ keV), the change in the phase is almost negligible ($\Delta\varphi \sim$

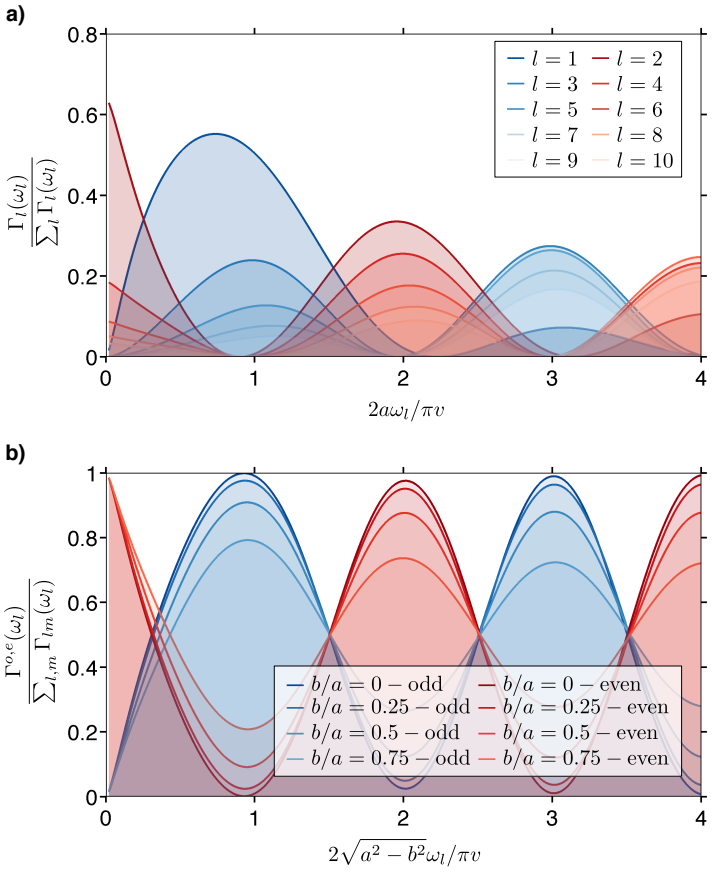

Figure 4.2: a) The contributions of the first $l = 10$ modes to the EEL probability, normalized with the sum of all contributions, is given for each l mode. Odd l modes (blue color palette) dominate for $2a\omega/\pi v \sim 2n+1$ $\forall n \in \mathbb{N}$, and even l modes (red color palette) dominate for $2a\omega/\pi v \sim 2n$ $\forall n \in \mathbb{N}$. b) The contribution of modes with $l + m$ odd (blue palette) and $l + m$ even (red palette) to the total EEL probability (normalized with the sum of all contributions) for impact parameters $b/a = 0, 0.25, 0.5, 0.75$.

$0.22 \ll \pi$, for $E \sim 6$ eV), which leaves the external potential almost unchanged along the electron path, and thus mainly even l modes are excited in the particle, as the phase of the induced charge density at the entry and exit points of the electron has to be almost equal. This happens for the excitation of the $l = 2$ modes at $E \simeq 3.8$eV and zero impact parameter $b = 0$ in Figs. 4.1(b) and (c). The activation of the modes ca be related to the properties of the terms in Eq. (4.1). The integrals A^i_{l0} in Eq. (4.1) are small for odd l modes compared to even l modes, as for odd l modes one gets $g_{l0}\left(\frac{\omega a}{v}\right) = \sin\left(\frac{\omega a}{v}\right) \sim \frac{\omega a}{v} \ll 1$, while for even l modes $g_{l0}\left(\frac{\omega a}{v}\right) = \cos\left(\frac{\omega a}{v}\right) \sim 1$

for axial trajectories ($b = 0$) [8].

In general, the contribution of even or odd l modes for axial trajectories ($b = 0$) depends on the reduced radius $\omega_l a/v$, where $\omega_l = \omega_p\sqrt{l/(2l+1)}$ is the energy of the l mode. In particular, the condition $\omega a/v \sim l\pi/2$ determines the dominance of either odd or even modes [255]. The dependence of odd and even modes on the reduced radius $a\omega_l/\pi v$ is illustrated in Fig. 4.2(a). Moreover, this symmetry argument not only holds for axial trajectories but for any penetrating trajectory (as long as the nanoparticles are small and the velocity of electrons large), i.e., in general, even $l+m$ modes dominate over odd $l+m$ modes. This behavior is clearly demonstrated in Fig. 4.2(b), where the contribution of modes with odd and even $l+m$ to the total EEL probability is shown for impact parameters $b/a = 0, 0.25, 0.5, 0.75$ as a function of the reduced length of the electron trajectory in the nanoparticle $L' = 2\sqrt{a^2 - b^2}\omega_l/\pi v$. One can observe that for small reduced lengths even $l+m$ modes dominate, almost independently of the impact parameter b, i.e., for small nanoparticles and fast electrons, even $l+m$ modes are mainly excited.

4.2 Influence of subnanometric features in nanoparticle EELS

In the previous subsection we have presented EEL spectra near a spherical NP as calculated within the local response approximation to describe the NP's material response. Most of the studies addressing EELS in this situations have focused on the effects produced by quantum confinement, non-locality, spill-out, and changes in the NP's environment. The influence of the atomic-scale features of the NPs in the plasmonic response is usually disregarded. Here we explore the sensitivity of EELS to the specific atomistic structure of a NP by addressing the energy loss spectrum in the valence region of a sodium nanocluster composed of 380 atoms, as shown in Fig. 4.3. We calculate the atomistic *ab initio* electron energy loss probability within TDDFT for different electron trajectories. This allows for including the crystallographic effects of the NP's facets naturally, within a quantum treatment of the electrons and atoms that form the NP. The probing electron energy is considered to be 100 keV in all the calculations. We select first three representative electron trajectories; crossing the center of the particle, and penetrating it through (i) a vertex, (ii) an edge, or (iii) a facet. In analogy to the previous chapter, and in order to ease the interpretation of the results and to evaluate the need for full quantum calculations, we implement three additional descriptions of the NP within a classical dielectric framework with abrupt interfaces, using the MNPBEM [110]: (i) a perfect icosahedron resembling the atomistic structure of the NP; (ii) a smoothed icosahedral NP which approaches

[8] For axial trajectories we have $P_l^m(z/r) = P_l^m(1) = \delta_{m0}$, which reduces the integrals to $A_{l0}^i = \frac{1}{a^{l+1}}\int_0^a dz\, z^l g_{l0}\left(\frac{\omega z}{v}\right)$ and $A_{l0}^o = a^l\int_0^a \frac{dz}{z^{l+1}} g_{l0}\left(\frac{\omega z}{v}\right)$.

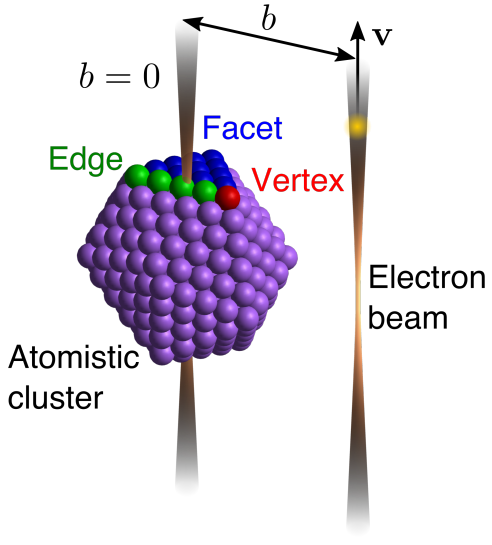

Figure 4.3: Scheme of an atomistic Na_{380} NP and electron beams, crossing through and passing by the NP, at impact parameter b, defined with respect to the trajectory crossing the center of the NP. Atoms forming atomistic features such as a vertex (red), edge (green) and facet (blue) are highlighted among generic Na atoms displayed in purple.

the shape of the electronic cloud in the atomistic cluster and would capture effects derived from the atomistic geometry; (iii) and a perfectly spherical nanoparticle (radius a=1.85 nm), as a benchmark of the NP shape commonly used in the literature.

As pointed out, the trajectories considered cross the center of the NP with the penetrating point at a vertex, a facet or an edge, as depicted in Fig. 4.4(a). Notice that for a structure with perfect icosahedral symmetry these trajectories correspond to the three symmetry axes of the icosahedron (5-fold, 3-fold and 2-fold, for vertices, facets and edges, respectively).

The EEL spectra calculated within the atomistic TDDFT framework are shown in Fig. 4.4(b). The sensitivity of the spectra to the particle orientation and the atomic-scale features is apparent in this figure. Depending on the trajectory, different peaks that correspond to the excitation of localized surface plasmons (LSPs) are activated: a peak at energy $\omega = 3.4$ eV emerges for the vertex trajectory (red line); the trajectory through the edge (green line) shows two peaks at $\omega = 3.45$ eV and $\omega = 4.1$ eV, the latter being more intense; and a single peak at $\omega = 4.05$ eV is observed for the facet trajectory (blue line). Moreover, a main peak at $\omega = 6.35$ eV and some shoulders at lower and higher energies are observed for all three trajectories (with some slight differences in intensity), which correspond to confined bulk plasmons (CBPs), as we will prove further on. Just notice that the intensities of the later are similar or even

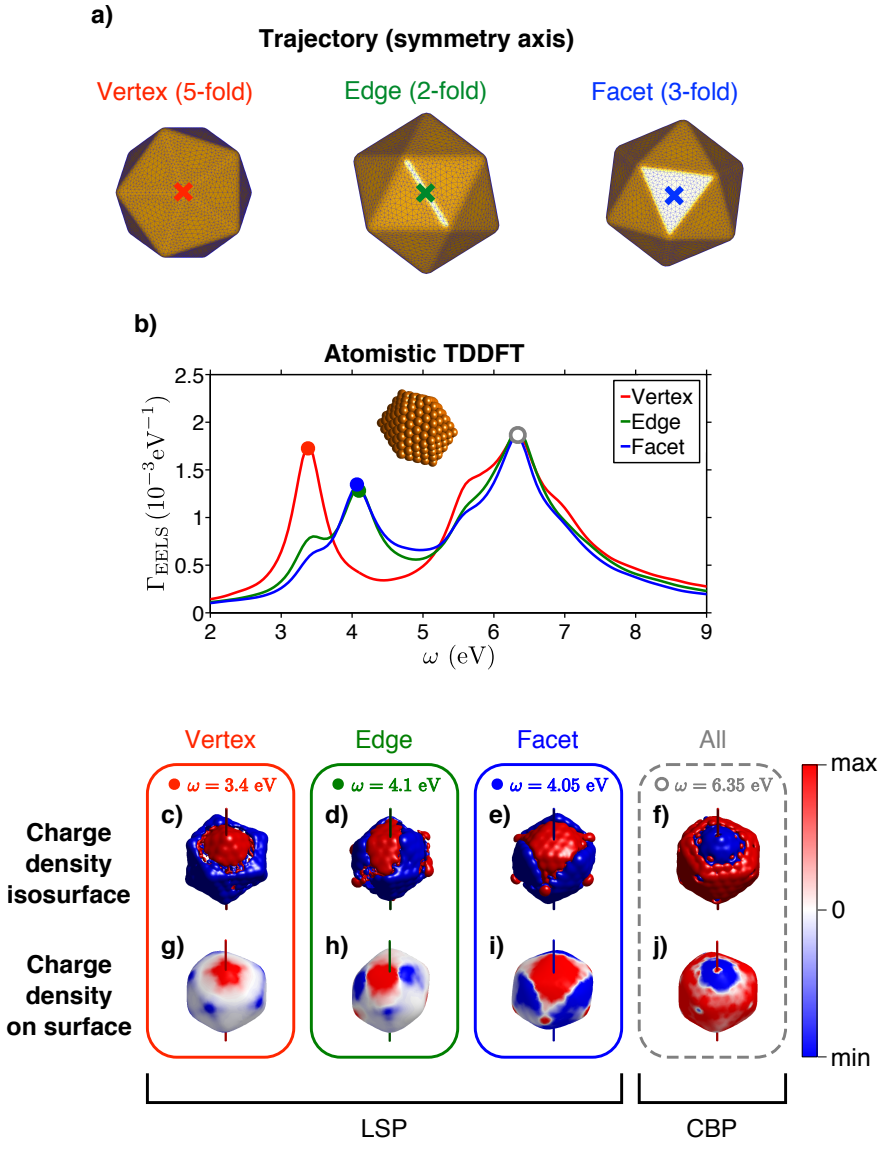

Figure 4.4: a) Three icosahedral nanoparticles oriented respect to the symmetry axes of a regular icosahedron: 5-fold, through two opposing vertices (red); 2-fold, through two opposing edges (green); and 3-fold, through two opposing facets (blue). The electron beam trajectories are set to penetrate the nanoparticle through/following these symmetry axes (marked by crosses). b) EEL spectra for the three trajectories shown in panel a) for a Na_{380} nanocluster as calculated within TDDFT. c-f) Isosurfaces of the charge density distribution for the main modes excited for each trajectory. g-j) Charge density distribution plotted at the NP surface (the NP surface is obtained from the isosurface calculated for the unperturbed charge density; more details in the main text). TDDFT data provided by Marc Barbry in CFM.

higher than those of the LSPs at lower energy. The characteristics of CBPs will be studied in detail in Chapter 5.

To get further insight into the impact of atomic-scale features in the EEL spectrum and into the properties of the corresponding plasmonic excitations, we explore in Figs. 4.4(c-j) the induced charge density distributions associated to the main plasmon modes identified in the EEL spectra of Fig. 4.4(b). On the one side, in Figs. 4.4(c-f) we plot the isosurfaces of the induced charge density, which show its phase (sign) at the NP's *surface* (and within the NP), allowing for an identification of the modes. Nevertheless, it is not straightforward to extract information about the charge localization at the surface from these isosurfaces, as one usually needs to calculate several isosurfaces for different isovalues of the charge density to that end. We intend to better visualize the charge localization in Figs. 4.4(g-j) by proceeding as follows: (i) we calculate an isosurface with an electron density threshold value $n_e = 0.00169\, e/\text{Å}^3$ [188] from the ground state charge density of the cluster in the absence of any external perturbation (this corresponds to the *surface* of the NP, which will be also used to create the smooth icosahedron geometry in the BEM calculations, presented below[9]), (ii) we plot the induced charge density data at the previously established NP *surface*, which makes easier to identify regions of greater charge localization at the surface.

The lowest energy LSP at $\omega = 3.4$ eV excited for the vertex electron trajectory [first column from the left, in Fig. 4.4(c,g)] shows a quadrupolar pattern [Fig. 4.4(c)]. Compared to the QP excited in spheres for axial trajectories ($l = 2$, $m = 0$), the charge density distribution observed in Fig. 4.4(g) shows strong charge localization around the vertices and a characteristic five-pointed star like charge distribution around the electron path, directly related to the five-fold symmetry of the NP respect to the electron trajectory. The LSPs excited for the edge ($\omega = 4.1$ eV, green) and facet ($\omega = 4.05$ eV, blue) electron trajectories, show lower symmetry of the charge distribution, with rhomboid, or triangle-like patterns around the electron path [Fig. 4.4(d-e)], but a stronger localization at vertices, edges and facets [Fig. 4.4(h-i)]. In contrast, the charge density distributions of the CBPs excited at $\omega = 6.35$ eV for the three trajectories do not show localization at vertices or patterns related to the shape of the nanoparticle, as observed in the charge density distributions [Fig. 4.5(f,j)]. In fact, due to the nature of the CBPs, i.e., electron collective oscillations localized in the volume of the NP, these oscillations mainly depend on the size of the nanoparticle, more than on the local atomistic morphology of the surface.

These results reveal the sensitivity of LSPs to the atomistic shape of a NP and to the crystallographic orientation probed by the electron. In this sense, shape effects in larger NPs have been studied extensively in the literature within the classical dielectric formalism [260], which accounts accurately for the response of large metallic

[9]The electron density threshold value to create the isosurface that we for BEM calculations is somewhat arbitrary [188]. Nevertheless, the volume of the resulting continuous NP used in the BEM calculations is equivalent to 380 Na atoms with atomic radius $r_s \sim 2.18$Å, which is close to the Wigner radius $r_s = 2.08$Å used to describe the plasmonic response, i.e., dielectric function, of Na in the BEM calculations. The larger size is due to certain spillage of electrons to the vacuum, making the NP effectively larger.

NPs. Nevertheless, as nanometric and subnanometric nanoparticle sizes are reached, the classical local dielectric formalism fails to reproduce quantum effects such as electron confinement into the NP, or electron spill-out effects, which need to be included in the material's response. Although some of these effects have been tackled for small spherical NPs [261], they oversight the influence of the NP's shape and the presence of crystallographic features, which greatly affect the EEL spectra, as we have shown in this section. With the aim of understanding the role of these atomic-scale features, we complete our atomistic study with classical calculations of the EEL spectra within the BEM where we reproduce the crystallographic shapes of the particles through classical sharp boundaries, mimicking the specific atomistic shape of each NP. The comparison of the results of the EEL spectra obtained from one and another method will reveal the accuracy and/or the limitations of classical local dielectric theories, as commonly used in EELS, to capture atomistic features in NPs.

4.2.1 Continuous description of atomic-scale features

The presence of atomic-scale features breaks the spherical symmetry of a NP, and can result in plasmon modes shifting and, even splitting [262], thus lifting the plasmon energy degeneracy with respect to the modes of a spherical particle, as shown in Fig. 4.4(b). This is very clear, in particular, for the vertex electron trajectory, but not so obvious for the edge and facet ones. The reason for this may be found in the electron density distribution induced by the beam at the surface, which does not vary much for an edge and the facet trajectories, but is quite different for the vertex trajectory.

This dependence of the EEL spectra on the NP's geometry is further explored in Fig. 4.5, where we show the results for two NPs using a continuous dielectric model to address the material's response within BEM. The geometries of the NPs, following the atomistic geometrical shape of the nanocluster, are shown together with the energy loss spectrum of a spherical NP of the same size ($a = 1.9$ nm). The numerical BEM and the dielectric approach used are detailed in Chapter 1. The spectra for the irregular smoothened icosahedron (sketch in the inset of Fig. 4.5(a), which captures the geometry of the unperturbed electron density of the nanocluster used in the atomistic TDDFT calculations, are plotted in Fig. 4.5(a). These spectra are very similar to those of Fig. 4.4 (TDDFT results): two modes appear at $\omega = 3.6$ eV, mainly excited for the vertex electron trajectory (red line), and $\omega = 4.0$ eV for the edge (green line) and facet (blue line) trajectories. In contrast, the spectra obtained for a regular icosahedron resembling the crystallographic/atomistic shape of the nanocluster [sketch in Fig. 4.5(b)] show three separate modes, each one corresponding to a specific trajectory; at $\omega = 3.3$ eV for the vertex trajectory (red line), at $\omega = 3.9$ eV for the edge trajectory (green line), and at $\omega = 4.2$ eV for the facet trajectory (blue line).

For reference, the spectrum of a spherical NP of the same size is shown with a black line in Figs. 4.5(a,b). The later clearly differs from the spectra of the icosahedral NPs used in TDDFT [Fig. 4.4(b)] and in the BEM simulations [Figs. 4.5(a,b)], highlighting the signature of the atomistic surface structure in the EEL spectra of

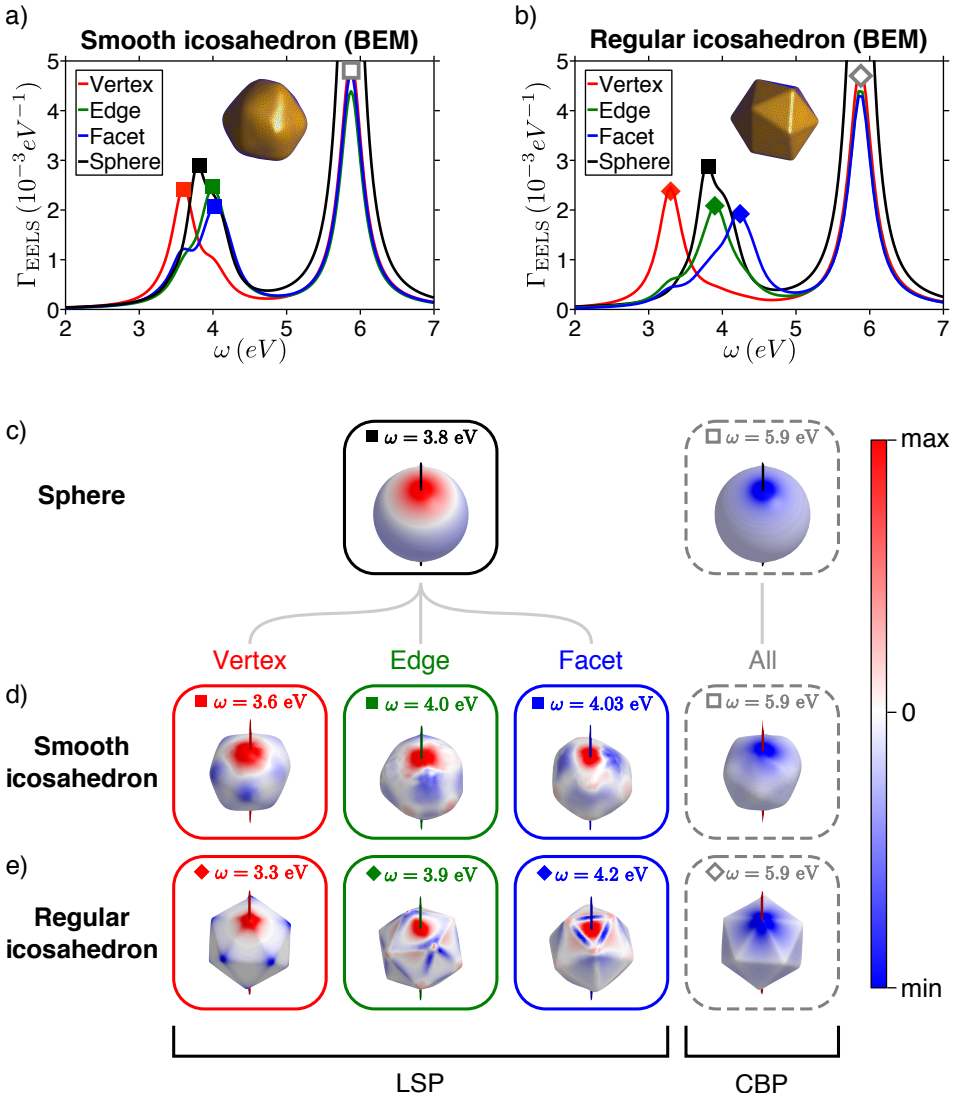

Figure 4.5: a) EEL spectra for a Na nanoparticle with smooth icosahedral shape and b) regular icosahedral shape calculated within BEM for three different trajectories crossing each NP through two opposing vertices (red), through two opposing edges (green), and through two opposing facets (blue). The EEL spectrum for a spherical NP is plotted in black in each figure, and the shape of each NP is plotted in the inset. Charge density plots representing the LSP modes highlighted with squares in Fig. 4.5 and with diamonds in Fig. 4.5(b) as calculated with BEM for c) a spherical Na NP of radius a =1.85 nm, d) for a smooth icosahedral Na NP and e) for a regular icosahedral Na NP.

nanoclusters. In particular, the main LSP peak observed for the spherical NP corresponds to the surface quadrupolar plasmon (QP, $l = 2$) at $E = 3.8$ eV, as depicted in Fig. 4.5(c), left box. Notice that this is the main surface mode excited for the electron trajectory crossing the center of the NP, as the dipolar mode $l = 1$ is inhibited, due to its azimuthal symmetry (only $m = 0$ modes are excited) as already explained in Sec. 3.1.

The induced charge densities in the smoothened irregular icosahedral and the regular icosahedron NP modelings are represented in Figs. 4.5(d) and 4.5(e), respectively. The patterns of the induced charge densities in the particles described with continuous boundaries are very similar to those obtained within the full TDDFT (Fig. 4.4). The patterns obtained for the icosahedral particles are qualitatively similar to those of Fig. 4.5(c) for the spherical NP. One can also observe the similarities between the charge density distributions of the smoothed continuous boundaries [Figs. 4.5(d,e)] and those of the atomistic TDDFT cluster [Fig. 4.4(c)] in spite of the energy difference.

Apart from the LSPs discussed above, the most intense EELS excitation appears at $\omega = \omega_p = 5.9$ eV, which is a bulk plasmon footprint, independent (in energy) of the nanoparticle's shape (sphere, smooth icosahedron or regular icosahedron) and trajectory. The lack of dependence on the NP shape and electron trajectory of the bulk plasmon appearing in BEM simulations is a direct consequence of the continuous dielectric framework, in which the contribution of the bulk plasmons to the energy loss probability is introduced *ad hoc* (see equation 1.64 in section 1).

On the other hand, Figs. 4.5(c-e) show a strong charge localization around the electron path, but no charge oscillations at the surface, in contrast to the TDDFT results [Fig. 4.4(f,j)]. We will address this issue in detail in Chapter 5. The comparison between the results obtained with the atomistic TDDFT and the three classical continuous approaches illustrates unambiguously the influence of atomic-scale features on the EEL spectrum, and the need for an accurate geometrical description of the atomistic cluster. Although LSP patters are reasonably well addressed with the use of classical description in smoothed surfaces, these approaches fail to describe the properties of CBPs due to the intrinsic constraints of the dielectric framework. The differences observed in bulk charge densities deserve a further analysis, which is presented at the end of Chapter 5.

4.3 Impact parameter dependence

So far we have focused on a particular set of electron trajectories, although typical EELS experiments usually scan the NPs, involving a wide variety of them, and particularly external trajectories. It is well known that for external trajectories with large impact parameters ($b \gg a$), EELS provides plasmon patterns similar to those

obtained in optical spectroscopy, i.e., the field generated by the electron beam at the surface of the NP is similar to that of a uniform and homogeneous external field. Under these conditions, the optical response of the icosahedral NPs does not differ much from that of a spherical one (the dipolar plasmon dominates the spectrum for small NPs, as observed in Fig. 2.4 of chapter 2), and does not show much dependence on its relative orientation [106, 260, 263]. Nevertheless, as the beam gets closer to the NP's surface, ($b \sim a$), the intensity of higher order modes increases, and thus the plasmonic response shows a dependence on the impact parameter [258, 259], which is no longer similar to that obtained with an optically homogeneous and uniform source. Moreover, in the previous section we showed that for axial penetrating electron trajectories the EEL spectra for icosahedral NPs depend on the relative orientation of the NP with respect to the electron beam. Thus, one could expect that in general, penetrating trajectories will show orientation dependent EEL spectra in atomistic NPs, which will be different to the EEL spectra for spherical NPs. Therefore, we explore now the influence of the atomistic features of the nanocluster on the excitation of different modes as a function of electron beam distance to the particle. To that end, we calculate EEL spectra for both penetrating and external electron trajectories for different impact parameters.

We show the dependence of the EEL spectra on impact parameter as calculated within the atomistic *ab initio* theory, for three different orientations of the NP as shown in the sketch of Figs. 4.6(a-c). Colormaps of such EEL spectra are shown in Figs. 4.6(d-f). The spectra shown in Fig. 4.6(d) correspond to the orientation labelled as "near-facet", which is chosen such that the external electron trajectories are parallel to the facet. The results shown in Fig. 4.6(e) and labelled as "near-edge" correspond to electron trajectories parallel to the closest edge. Last, the spectra presented in Fig. 4.6(f) labelled as "near-vertex" correspond to trajectories perpendicular to two opposing vertices and in plane with one of the edges formed by the closest vertex to the trajectory. Moreover, we have extracted five representative spectra from the results corresponding to impact parameters, $b = 0$, 0.5, 1, 1.5 and 3 nm [corresponding to the electron trajectories sketched in Figs. 4.6(a-c) and using the same colors] which are plotted in Fig. 4.6(g-i).

We first focus on the "near-facet" electron trajectories shown in Fig. 4.6(d,g). For external trajectories ($b \gtrsim 1.5$ nm) the spectra are dominated by the excitation of LSPs; there is no trace of CBPs (they are distinguishable only if a logarithmic scale is used). In particular, for trajectories far from the NP, such as $b = 3$ nm, the main excitation is the dipolar plasmon (S1) at $\omega = 3.2$ eV, in a similar fashion as when light is used as an excitation source [106, 263]. Decreasing the impact parameter increases the intensity of the energy loss, and specially the relative intensity of higher order plasmonic modes, which are more sensitive to the inhomogeneity of the coulombian field created by the electron beam, in contrast to the dipolar mode. For grazing trajectories, such as $b = 1.5$ nm, in addition to the dipolar mode (S1), a peak corresponding to higher order modes (S3) is observed at $\omega = 4.1$ eV, which perfectly matches the energy of the mode excited for edge and facet axial trajectories plotted in Fig. 4.4(a).

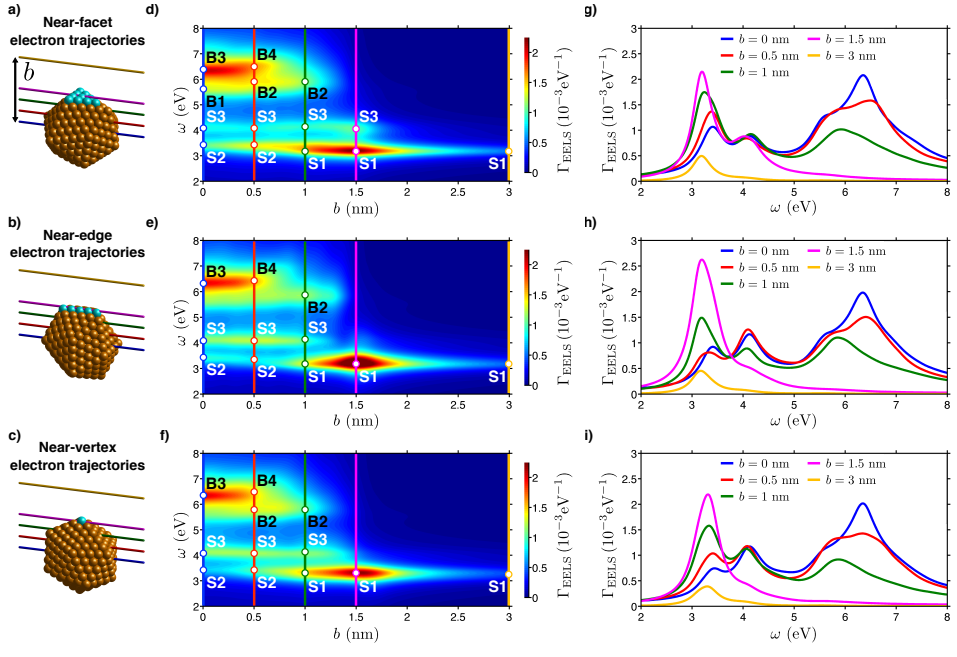

Figure 4.6: Trajectory sets are defined for specific orientations of the nanoparticle related to the trajectories passing near crystallographic features highlighted in cyan and labelled as a) near-facet, b) near-edge and c) near-vertex. Color maps of EEL spectra as a function of electron impact parameter b, for d) near-facet, f) near-edge, and g) near-vertex electron trajectories, calculated using atomistic TDDFT for a Na nanocluster. The peaks corresponding to different plasmon modes are highlighted by bullet points and labelled as surface (S) or bulk (B) modes. g-i) EEL spectra from a-c), respectively, for impact parameters $b = 0$ nm (blue line), $b = 0.5$ nm (red line), $b = 1$ nm (green line), $b = 1.5$ nm (magenta line), and $b = 3$ nm (amber line). TDDFT data provided by Marc Barbry in CFM.

For penetrating trajectories ($b < 1.5$ nm), together with the LSPs a band of CBPs is also present at higher energy in the spectra of Fig. 4.6(d), whose intensity is highly sensitive to the impact parameter of the electron beam. Regarding the LSPs, the dipolar mode (S1) dominates the spectrum only for trajectories close to the surface $b \gtrsim 2/3a$, but as the impact parameter decreases, the quadrupolar plasmon (S2) at $\omega = 3.4$ eV becomes the main excitation, consistent with the results of the excitation in the vertex trajectory, plotted in Fig. 4.4(a). This transition from the S1 to the S2 mode for small impact parameters clearly illustrates the deactivation of the dipolar mode due to its lack of azimuthal symmetry, as pointed out in the previous section for the spherical NP. When the electron probe approaches the NP axis, $b \to 0$, higher order modes (S3) are efficiently excited.

Similarly to the LSP in Figs. 4.6(d), the energy losses corresponding to CBPs show different behaviors as a function of the impact parameter. For $b = 1$ nm a single peak (B2) at $\omega = 5.9$ eV is observed. The spectrum for $b = 0.5$ nm has an additional CBP (B4) at $\omega = 6.5$ eV. The spectrum of the central trajectory $b = 0$ nm, on the

other hand, exhibits two different excitations at $\omega = 5.6$ eV (B1) and $\omega = 6.35$ eV (B3). Although bulk plasmon modes have received less attention than LSPs in the literature, shifts of bulk plasmon detected in experiments [82,85,90] can be explained by the existence of different CBPs whose excitation depends on the relative impact parameter, in a similar way as it occurs with the LSPs. As pointed out above for LSPs, by symmetry arguments, central trajectories inhibit certain CBPs, resulting in effective blue-shifts of the bulk plasmon in experiments. These results support the use of the properties of CBPs in EELS to characterize specific atomistic features in NPs.

Regarding the other two sets of trajectories, we observe that the spectra for the "near-edge" [Figs. 4.6(e,h)] and "near-vertex" [Figs. 4.6(f,i)] trajectories share some similarities with the results for the "near-facet" trajectories [Figs. 4.6(d,g)], such as the excitation of the dipolar plasmon (S1) for external trajectories, and the overall distribution of the peaks. Nevertheless, there are some differences regarding the excitation of higher order modes and the relative intensity of the peaks. For instance, for the trajectory labelled as "near-edge" almost no excitation of S3 modes is observed for grazing incidence and the relative intensities of modes S2 and S3 for penetrating trajectories are different as compared to the "near-facet" case. On the other hand, CBPs show seemingly to be independent to the NP's orientation.

To better illustrate the capability of EELS to characterize atomistic features in NPs and support our interpretation of the excitations within TDDFT, we compare now the atomistic results with those from a classical description in a smooth icosahedral NP with boundaries which reproduce the atomistic features. We show in Figs. 4.7(a-c) the EEL spectra corresponding to the "near-facet", "near-edge" and "near-vertex" electron trajectories, defined in the same way as for TDDFT calculations, and in Fig. 4.7(d) the EEL spectra corresponding to a spherical NP of radius $a = 1.5$ nm as a reference. Moreover, we have also selected five representative spectra from these results corresponding to impact parameters, $b = 0$, 0.5, 1, 1.5 and 3 nm, which are plotted in Figs. 4.7(e-h).

The general trends for the excitations of the LSPs observed for the classical calculations are similar to those observed within the TDDFT calculations: i) the spectra exhibit the excitation of the dipolar plasmon (S1) at $\omega = 3.35$ eV for external trajectories with large impact parameters ($b >> a$), ii) higher order modes (S3) at $\omega = 4.0$ eV are excited for grazing trajectories $b \sim a$ and penetrating trajectories $b < a$, and iii) the quadrupolar plasmon (S2) is excited at $\omega = 3.8$ eV for small impact parameters. Moreover, direct comparison between individual trajectory sets calculated within each model shows that the classical calculations qualitatively capture the spectral features observed in the TDDFT calculations. Nevertheless, there is an increased relative intensity of the LSPs in the classical model compared to the atomistic model, which may be attributed to non-local effects included in TDDFT but not accounted for in the classical description, producing more damped high-order plasmon modes [264]. Furthermore, the small discrepancies observed in the LSP energies can be attributed to quantum effects not considered within the BEM.

On the other hand, the classical approach fails to reproduce, as expected, the

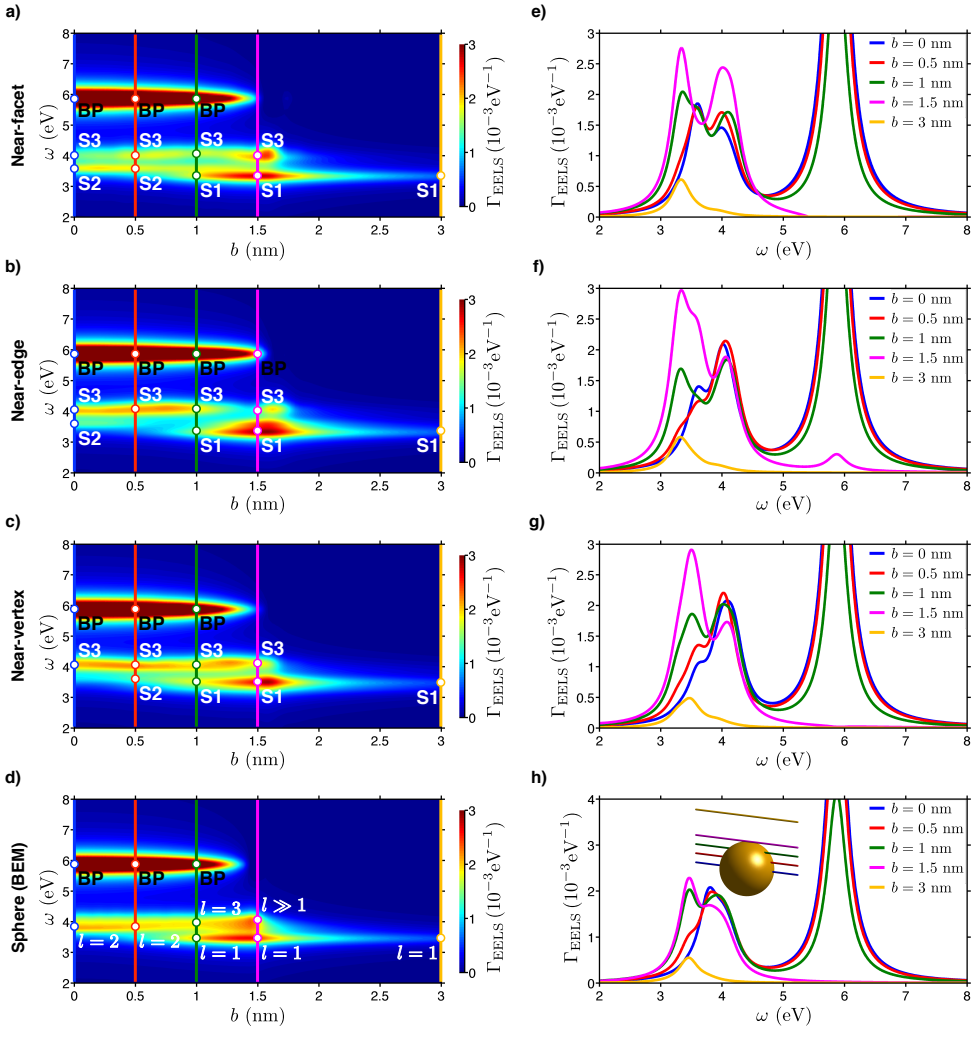

Figure 4.7: Color map of EEL spectra as a function of the impact parameter b, for a) near-facet, b) near-edge, and c) near-vertex electron trajectories, calculated for a smooth icosahedral shape using BEM. The peaks that correspond to different plasmon modes are highlighted by bullet points and labelled as surface (S) or bulk (B) modes. d) Color map of EEL spectra as a function of the impact parameter calculated using BEM for a spherical NP of radius $a = 1.5$ nm. The peaks are highlighted by bullet points and the LSPs are labelled according to their l order. EEL spectra for impact parameters $b = 0$ nm (blue line), $b = 0.5$ nm (red line), $b = 1$ nm (green line), $b = 1.5$ nm (magenta line), and $b = 3$ nm (amber line) for e) near-facet, f) near-edge, and g) near-vertex electron trajectories for a smooth icosahedral shape, and h) for a spherical NP.

spectral features observed in TDDFT for energies larger than the plasma energy. In particular, we observe that a sharp bulk plasmon is activated for penetrating trajectories, at the same energy $\omega = 5.9$ eV, independently of impact parameter, with identical value as that obtained for the axial trajectories of Figs. 4.5(a).

We also show for reference the EEL spectra for a spherical NP of radius $a = 1.5$ nm circumscribing the nanocluster Na_{380} in Figs. 4.7(d,h). The spectra exhibit the excitation of the dipolar plasmon $l = 1$ ($\omega = 3.45$ eV) for external trajectories with $b >> a$ and higher order modes $l > 1$ for grazing trajectories ($b \sim a$). Penetrating trajectories produce a fading of the dipolar plasmon and enhancement of the quadrupolar plasmon $l = 2$ ($\omega = 3.8$ eV) for small impact parameters. In particular, for the central trajectory with azimuthal symmetry ($b = 0$ nm), the dipolar peak disappears, and instead a broad peak appears, which gathers the contributions of high-order modes with even l number that are too close in energy from each other to be distinguishable. Additionally, a sharp bulk plasmon is activated for penetrating trajectories, at the same position $\omega = 5.9$ eV, independently of impact parameter, and of equal value as the one discussed for axial trajectories in icosahedral NPs shown in Figs. 4.5(a,b) (black lines).

When compared to the atomistic TDDFT results, the spherical approximation fails to reproduce even qualitatively the LSP spectra for penetrating and grazing trajectories (in particular the gap between modes S2 and S3). As we have shown, the differences observed in the spectra between the atomistic TDDFT (Fig. 4.6) and a spherical NP within a classical description [Fig. 4.7(d-h)], are mainly due to the different shapes considered in each model. The modes of a plasmonic NP greatly depend on its shape [265] both in energy and, in particular, symmetry. Their excitation depends on the relative symmetry of the mode with respect to the electron trajectory. The above argument are supported by corresponding induced charge density distributions plotted in Fig. 4.8(a). The charge density isosurfaces (red positive, blue negative) shown in this figure correspond to the modes highlighted and labelled in Fig. 4.6(d-f). In the low-energy LSP spectral band, mode S1 is clearly identified as a dipolar plasmon, mode S2 as a quadrupolar plasmon, and mode S3 as a higher order plasmon mode excited for the edge and facet trajectories, at least for $b \leq 0.5$ nm. The transition from the dipolar pattern S1 to the quadrupolar S2 one, from impact parameter $b = 1$ nm to 0.5 nm, explains the shift of the lowest energy excitation in the spectrum as the electron beam goes from the surface of the NP towards its center. Mode S3 has a more irregular charge distribution, as observed at the bottom panel of Fig. 4.8(a), with charge concentration on the vertex atoms. The presence of these hot-spots at the vertices and the high selectivity of the modes could be exploited in the recently developed techniques employing STEM to map molecular excitations using the subnanometric field localization produced atomic-scale features at the surface of metallic NPs, as implemented in SERS experiments, where even single-molecule detection has been achieved [43].

Notice also that the evolution of the charge pattern with impact parameter following the symmetry marked by the electron path with respect to the particle. Moreover, the charge density distributions corresponding to mode S3 for $b \geq 1$nm are slightly

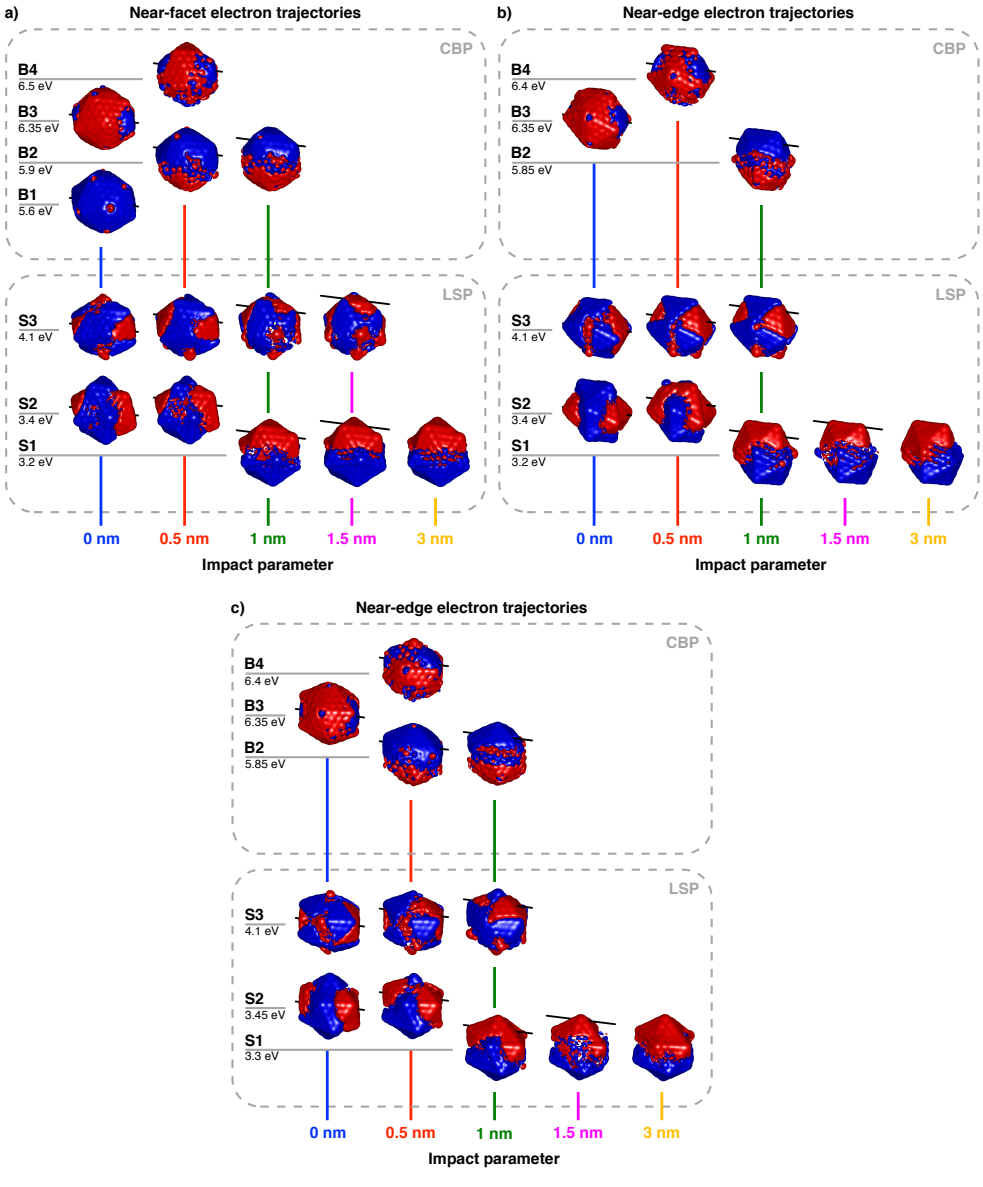

Figure 4.8: Isosurfaces of the imaginary part of the charge density corresponding to the a) near-facet, b) near-edge and c) near-vertex electro trajectories corresponding to the peaks highlighted, respectively, in Figs. 4.6(d-f), calculated using TDDFT for impact parameters $b = 0, 0.5, 1, 1.5, 3$ nm. TDDFT data provided by Marc Barbry in CFM.

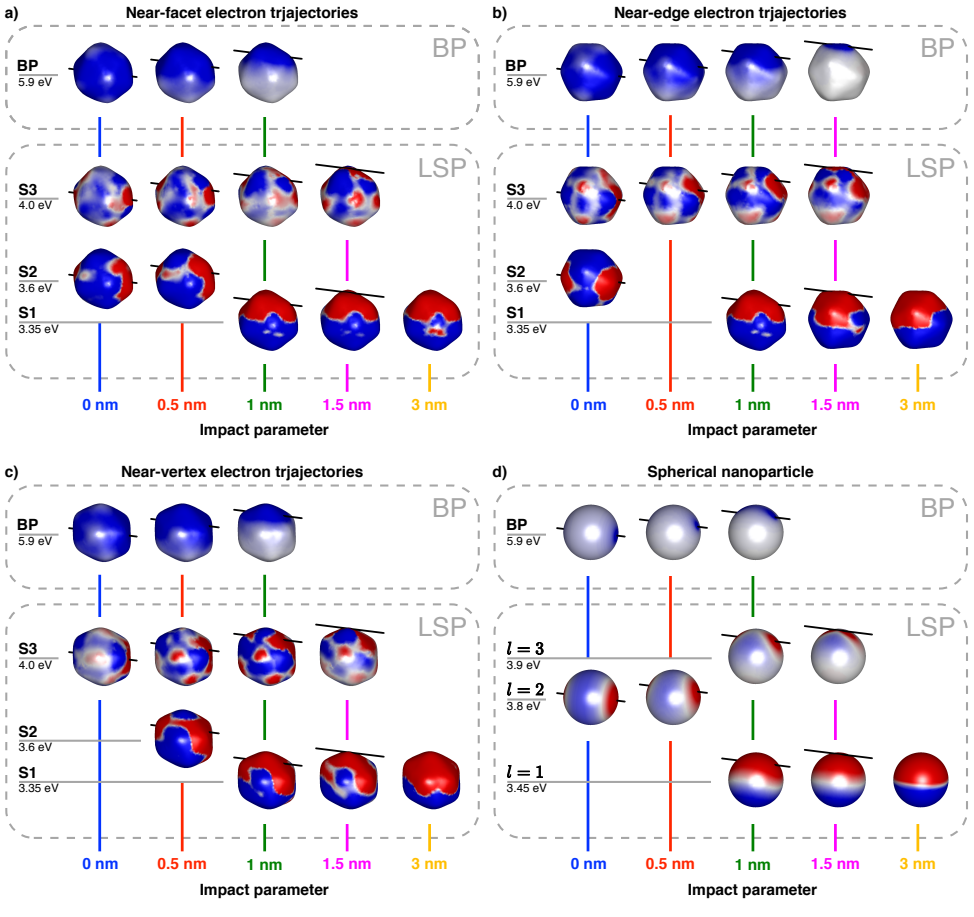

Figure 4.9: Induced surface charge density corresponding to the a) facet, b) edge and c) vertex trajectory sets, and d) to the sphere, corresponding to the peaks highlighted, respectively, in Figs. 4.7(a-c) for a smooth icosahedron and in Fig. 4.7(d) for a sphere, calculated using BEM for impact parameters $b = 0, 0.5, 1, 1.5, 3$ nm.

different to those observed for $b \leq 0.5$ nm, although they have similar energy, i.e., they are two *different* modes degenerated in energy. This is similar to the degeneracy in energy found in spherical NPs for modes with same l-number but different m-number.

It is also instructive to compare these charge distributions with those excited in the classical smooth icosahedral NPs and the reference spherical NP, plotted in Fig. 4.9. The icosahedral shapes [4.9(a-c)] capture the evolution of the charge distributions that correspond to the dipolar plasmon (S1), quadrupolar plasmon (S2) and higher-order modes (S3), including the atomic-scale features of the induced charge density.

The spherical nanoparticle [Fig. 4.9(d)] captures well the clean excitation of the

dipolar plasmon $l = 1$ and the quadrupolar plasmon $l = 2$ patterns, being the energy gap between both modes wider as compared to atomistic TDDFT results. The whole LSP band of the atomistic nanocluster spectrum is wider due to localization of the induced charge around the crystallographic features [265], as clearly observed in the charge densities of S3 in Fig. 4.8. Thus, these results illustrate the limitations of the spherical NP description (even if a jellium model is used) to address the spectral features arising from atomic-scale protrusions characteristic of such small NPs.

We analyze now the CBP band and its evolution with impact parameter. In the top panels of Fig. 4.8(a) the differences between the modes excited for $b = 0$ nm and $b = 0.5$ nm [Fig. 4.6] are evident from the corresponding charge density isosurfaces. As already mentioned, this evolution with impact parameter and the richness of the charge distributions of the CBPs obtained with the atomistic TDDFT framework cannot be reproduced within the classical framework calculations, neither within a spherical nor within a more accurate description of the particles shape (icosahedral models). In the energy range of 5.5-6 eV, mode B1 shows an almost homogeneous (angular monopolar) charge distribution with characteristic localization of the charge at the vertices, while mode B2 has a dipolar distribution (with flipped polarity as compared to S1). On the other hand, at 6.35 eV and 6.5 eV, modes B3 and B4 are so overlapped, that a qualitative characterization based on the surface charge density can be misleading. In fact, the charge oscillations of the CBPs occur inside the volume of the NP, as opposed to the LSPs which are localized at the surface. The characterization of the CBP modes will be elucidated in the next chapter, where the properties of the modes will be unveiled in terms of the non-local response of matter.

4.4 Discussion and Summary

The influence of atomic features of nanometer-scale metallic nanoparticles on the EEL spectra has been explored in this chapter. We have first considered the paradigmatic case of the nanosphere as a baseline to understand the underlying symmetry of the plasmonic response of small nanoparticles when excited by swift electron beams. Moreover, we have shown that atomic features of nanometer-scale metallic particles greatly influence their plasmonic response, as exposed through EEL spectra for axial trajectories and different NP orientations, and thus these features need to be accounted for in a full description of their plasmonic response. Besides the particular atomic morphology of the nanoparticle, the ab-initio TDDFT method used to calculate the EEL spectra includes naturally all the effects related to the quantum nature of electrons. Much of the discussion from previously published papers about EELS in NPs are focused on the shift, to the red or to the blue (mainly depending on the material), of the LSPs when their size is decreased, in particular the shift of the dipolar surface plasmon and the bulk plasmon. Different phenomenological descriptions

have been implemented in the literature to explain these shifts, including quantum effects as electron spill-out [31, 91, 92], dispersion in the dielectric response [94, 95] or dielectric functions which account for quantum confinement [90]. In general, these studies do not consider the non-spherical shape of the nanoparticle, not to say the atomic-scale structure which, as we have shown, dramatically affects the EEL spectra for grazing and penetrating trajectories (specially for excitation higher order modes), adding an additional aspect to be considered when interpreting the results in EELS experiments, where small NPs usually show icosahedral shapes [84, 86].

The shape effect on LSP and CBP bands has been explored by comparing the TDDFT spectra with those calculated with two classical dielectric models of the NP, adapted to the icosahedral shape of the atomistic distribution and the electronic landscape of the nanocluster. Concerning LSPs, the later model provides good agreement with sensitivity to the orientation of the electron beam trajectory with respect to the edge, facet or vertex crystallographic features.

Moreover, the excitation of collective electron oscillations inside the volume of the NPs, the so called CBPs, are inherently included in the TDDFT framework. Contrary to the LSPs, local dielectric models with boundaries resembling the atomistic shape of the NP are not able to account for the rich footprints of the CBP band of the spectrum, neither for the intensity nor for the width of the CBPs or their sensitivity to the impact parameter.

We have shown that ab-initio atomistic TDDFT offers a state-of-the-art framework to study the interaction of electron beams with small NPs. This method can be applied to a wide variety of materials, including Ag NPs, which are still object of much discussion and controversy in the literature [266]. The sensitivity to the atomic-scale features and diverse CBPs of the EEL spectra is at hand with the spatial and energy resolution of STEM microscopes, with a special mention to signal-to-noise ratio, as averaging over different sets of trajectories and statistic measurements can wash out the fine structure of spectra. Moreover, these atomic-scale features would further enhance the interaction between plasmons and molecules attached to the vertices, an aspect which can be exploited in plasmon-enhanced molecular spectroscopy with STEM, a technique with great potential to be developed in future [267].

5 Hydrodynamic model to address EELS of plasmonic nanoparticles

Confined Bulk Plasmons (CBPs) are volume oscillations of the electron density confined in finite regions, such as in nanostructures. They have been observed experimentally in EELS measurements for a wide range of structures and materials, including thin Mg films [99], Ge nanorods [100], Bi nanowires [101], Bi NPs [90, 102], and Al nanodisks [85]. On the other hand, bulk plasmon modes confined in nanostructures have been studied theoretically with different non-local dielectric approaches to account for dispersion and dynamical screening effects [103–105]. Non-local effects emerge in nanoplasmonics at the few-nanometer scale due to the spatial correlation of the induced charge density, an effect which prevents the pilling up of electrons at short distances.This pressure (known as Fermi-Dirac pressure) exerted by the electron density, and its effects (including CBPs), are parametrically included within hydrodynamic models, and have been used to study CBPs in spherical NPs excited with light or electron beams. Nevertheless, for external electron beam trajectories [94] the intensity of CBP excitation is several orders of magnitude smaller than that of LSPs.

However, as described in the previous chapter, the energy losses in small Na nanoclusters for penetrating electron trajectories show comparable intensities for CBPs and LSPs. Within the *ab initio* method presented in the previous chapter, CBP modes emerge naturally, in contrast to continuous local classical approaches of the response, where bulk modes are introduced through the loss function, $\mathrm{Im}[-1/\varepsilon(\omega)]$ [Eqs. (1.58) and (1.64) in Sec. 1].

Although electron energy losses have been theoretically studied since long ago, the expressions of the energy loss probability given in the literature for spherical nanoparticles and penetrating trajectories within a non-local approach consist of averages over impact parameters [268], momentum-dependent solutions for the EEL probability [269], formal solutions without explicit expressions for the EEL probability [270] or are directly limited to local descriptions [257, 271, 272]. Moreover, models accounting for confinement effects in a local dielectric framework [82] do not incorporate the impact-parameter dependence shown in the previous chapter as calculated with *ab initio* methods. To the best of our knowledge, we have not found in the literature any expression for the EEL probability showing an explicit impact parameter dependence that considers penetrating trajectories within a hydrodynamic model, which would be of high interest to study CBPs and their excitation by electron beams.

In this chapter we obtain such expression starting from a linear Hydrodynamic Model (HDM) that takes into account nonlocality. We first introduce the main aspects of this model and then apply it to a spherical nanoparticle with hard boundaries, to obtain the properties of surface and bulk plasmons with nanoparticle size in Section 5.1. In Section 5.2 an analysis of the non-local expression of the different term of the EEL probability is provided for internal/penetrating electron trajectories as well as for external ones. Once the EEL semi-analytical formula is obtained, the impact parameter dependence of the plasmon excitation is studied in Section 5.3. In Section 5.4 we focus on the influence of the electron beam energy, i.e., the velocity of the electron, to elucidate the symmetry dependence of the excitation of CBPs. Last, in Section 5.5 we compare the results obtained within *ab initio* atomistic TDDFT for penetrating trajectories presented in Chapter 4 with the results of the CBP excitations obtained in this chapter.

5.1 Hydrodynamic Model applied to a spherical nanoparticle

The excitation of small particles by a fast electron has been widely studied in the literature. Most works were developed in the framework of the classical local dielectric theory, where the target response is given by the bulk local dielectric function. Simple expressions for the EEL probability with the use of a local dielectric function of the material, $\varepsilon(\omega)$, have been obtained, both in the non-retarded limit (quasistatic approximation) [258] and in the fully relativistic approach [64]. In the non-retarded case, the excitations of the particle can be labeled by the angular momentum l, whose energy do do not depend on the size of the target. Retardation introduces a red shift of the energy of the modes as the size of the particle increases, which is significant for particle sizes which meet $\omega a c^{-1} \geq 1$, where a is the radius of the particle and c is the velocity of light. In the case of plasmon excitations in metallic particles, relativistic corrections are relevant for particles larger than ~ 10 nm. When considering the dispersion of the material's response, this introduces a dependence of the plasmon energies with the size of the nanoparticle target, due to the inability of the electrons in the NP to respond to fields of wave length of atomic range. This effect is thus expected to be more relevant for small particles. One way of addressing this situation consists in describing the target response by means of a momentum-dependent non-local dielectric function $\varepsilon(\mathbf{k}, \omega)$. For targets bounded by abrupt planar interfaces, Ritchie and Marusak [273] proposed the so-called *Specular Reflection Model (SRM)*, where some extra boundary conditions need to be imposed.

Nevertheless, the *SRM* presents two drawbacks. On the one hand it is suitable only for abrupt interfaces, so it does not account for effects related to the electron density variation along the interface, which is relevant at grazing or for penetrating electron trajectories. On the other hand the non-local dielectric function $\varepsilon(\mathbf{k}, \omega)$ describes the target's response in term of excitations with quantum numbers given by the energy $\hbar\omega$ and momentum $\hbar\mathbf{k}$. This description is appropriate in the case of planar surfaces, where the elemental excitations can be properly labeled by these magnitudes, but it fails to describe the excitations of a nanoparticle, by means of the *natural* momentum integer numbers l, m. In this chapter we will also consider the boundaries to be abrupt, but we will derive an expression for the EEL probability by a probing electron in spherical NPs with a derivation of the expressions in real-space.

In this section we introduce the basis of the non-retarded hydrodynamic approach [93] to study the interaction between a fast electron and a spherical metal nanoparticle. Although originally the general model is formulated for diffuse interfaces, we restrict our study to abrupt interfaces. The description of the bulk response of the corresponding infinite medium is equivalent to that of the *Hydrodynamic Dielectric Function*,

$$\varepsilon(\mathbf{k}, \omega) = 1 - \frac{\omega_p^2}{\omega(\omega + i\gamma) - \beta^2 \mathbf{k}^2}, \tag{5.1}$$

where ω_p is the frequency of the undispersed bulk plasmon, γ is the damping constant, which represents the inverse of the plasmon lifetime, and β a constant that accounts for the finite compressibility of the electron gas.

Following Ref. [93], we consider the excitation of an inhomogeneous electron gas under the influence of an external field perturbation, $\mathbf{E}^{\text{ext}}(\mathbf{r},\omega)$, which follows the dynamics equation:

$$\widetilde{\beta}^2(\mathbf{r})\nabla^2\rho(\mathbf{r},\omega) + [(\omega+i\gamma)\omega - \widetilde{\omega}_p^2(\mathbf{r})]\rho(\mathbf{r},\omega) + \nabla\widetilde{\beta}^2(\mathbf{r})\nabla\rho(\mathbf{r},\omega) + \frac{1}{4\pi}\nabla\widetilde{\omega}_p^2\nabla\int d\mathbf{r}'\frac{\rho(\mathbf{r},\omega)}{|\mathbf{r}-\mathbf{r}'|} = \widetilde{\omega}_p^2(\mathbf{r})\rho^{\text{ext}}(\mathbf{r},\omega) - \frac{1}{4\pi}\nabla\widetilde{\omega}_p^2\nabla\int d\mathbf{r}'\frac{\rho^{\text{ext}}(\mathbf{r},\omega)}{|\mathbf{r}-\mathbf{r}'|}, \tag{5.2}$$

where $\rho(\mathbf{r},\omega)$ is the induced charge density, $\rho^{\text{ext}}(\mathbf{r},\omega) = \frac{1}{4\pi}\nabla\cdot\mathbf{E}^{\text{ext}}$ is the probe charge density, the function $\widetilde{\omega}_p^2(\mathbf{r}) = 4\pi n(\mathbf{r})$[10] stands for the frequency of the local plasmon at $\mathbf{r}$, with $n(\mathbf{r})$ the unperturbed charge density, and $\widetilde{\beta}^2(\mathbf{r})$ is the *local* dispersion parameter that accounts for the finite compressibility of the electron gas. This equation is an integro-differential equation, and in the general case it is as cumbersome to solve as its counterpart in $\mathbf{k}$ space. Nevertheless, the complexity of this equation can be seriously reduced for sharp interfaces. Although both functions $\widetilde{\omega}_p^2(\mathbf{r})$ and $\widetilde{\beta}^2(\mathbf{r})$ are not continuous at the interface, they can be considered as the limiting case of an extremely thin interface. This way, inside the medium, Eq. (5.2) turns out to be the Helmholtz equation, which admits an analytical solution for simple shaped NP targets in terms of the natural coordinates associated to the geometry of the surface. In this situation, the interface terms in $\nabla\widetilde{\omega}_p^2(\mathbf{r})$ and $\nabla\widetilde{\beta}^2(\mathbf{r})$ just provide the boundary condition at the interface.

In the following lines we apply this formalism to small spherical metallic nanoparticles with abrupt boundaries. Thus, if we consider that the inner and outer media are separated by abrupt interfaces, and the plasma frequency and the compressibility parameter are constant within the nanoparticle, then $\tilde{\omega}_p^2(\mathbf{r}) = \omega_p^2\theta(a-r)$, $\tilde{\beta}^2(\mathbf{r}) = \beta^2\theta(a-r)$, with $\theta(x)$ the Heaviside function, $\omega_p = \sqrt{4\pi n}$, $\beta = \sqrt{3/5}v_{\text{F}}$, where $v_{\text{F}} = (3\pi^2 n)^{1/2}$ is the Fermi velocity of the electron gas, with $n = 3/4\pi r_s^3$ the unperturbed electron density, and r_s the free electron gas parameter, including a constant damping term γ. Equation (5.2) reduces to Helmholtz equation inside the metal (outside $\rho(\mathbf{r},\omega) = 0$),

$$[\nabla^2 + \mu(\omega)^2]\rho(\mathbf{r},\omega) = \frac{\omega_p^2}{\beta^2}\rho^{\text{ext}}(\mathbf{r},\omega), \tag{5.3}$$

where μ is a ω-dependent parameter defined as

$$\mu^2(\omega) = \frac{1}{\beta^2}\Big[\omega(\omega+i\gamma) - \omega_p^2\Big]. \tag{5.4}$$

[10] In this chapter we use EM Gaussian units and atomic units, $e = \hbar = m_e = 1$.

On the other hand, as mentioned above, the interface terms $\nabla\widetilde{\omega}_p^2(\mathbf{r})$ and $\nabla\widetilde{\beta}^2(\mathbf{r})$ provide the boundary condition (BC) to obtain:

$$-\frac{1}{4\pi}\omega_p^2\frac{\partial}{\partial r}\int d\mathbf{r}'\frac{\rho(\mathbf{r}',\omega)}{\mid \mathbf{r}'-\mathbf{r}\mid}-\beta^2\frac{\partial}{\partial r}\rho(\mathbf{r},\omega)=\frac{1}{4\pi}\omega_p^2\frac{\partial}{\partial r}\int d\mathbf{r}'\frac{\rho^{\text{ext}}(\mathbf{r}',\omega)}{\mid \mathbf{r}'-\mathbf{r}\mid}, \tag{5.5}$$

to be satisfied at the interface $r = a$. This BC is the hydrodynamic condition of zero electron current normal to the surface [274,275], meaning that electrons moving in the radial direction cannot exit the hard boundary and must be reflected back towards its center.

Before addressing the calculation of the EEL probability, it is helpful to consider the dispersion of the plasmonic modes in the absence of an external perturbation. In such a situation, Helmholtz equation reduces to its homogeneous version,

$$[\nabla^2+\mu(\omega)^2]\rho(\mathbf{r},\omega)=0. \tag{5.6}$$

In spherical coordinates the charge density can be expressed in terms of spherical Bessel functions of the first kind, $j_l(x)$, and spherical harmonics, $Y_l^m(\Omega)$, as:

$$\rho(\mathbf{r},\omega)=\sum_{l=0}^{\infty}\sum_{m=-l}^{l}A_{lm}(\omega)j_l[\mu(\omega)r]Y_l^m(\Omega) \tag{5.7}$$

where the coefficients $A_{lm}(\omega)$ need to be obtained from the BC. The mode energies ω_{ln} (the meaning of the number n is explained in the following lines) are obtained from the solution of the BC [Eq. (5.5)] in absence of external perturbation, i.e., $\rho^{\text{ext}}(\mathbf{r},\omega)=0$ [268–270],

$$\frac{\omega_p^2}{2l+1}\frac{l+1}{\mu}j_{l+1}[\mu(\omega)a]-\beta^2\mu(\omega)j_l'[\mu(\omega)a]=0, \tag{5.8}$$

where we have used Laplace expansion,

$$\frac{1}{|\mathbf{r}-\mathbf{r}'|}=\sum_{l=0}^{\infty}\sum_{l=-m}^{m}\frac{4\pi}{2l+1}(-1)^m\frac{r_<^l}{r_>^{l+1}}Y_l^{-m}(\Omega)Y_l^m(\Omega'). \tag{5.9}$$

The condition given by Eq. (5.8) shows that the dispersion does not break the degeneration on the azimuthal number m present in the local dielectric approach [see Eq. (4.1)]. Nevertheless, it gives multiple energies for each l, related to the zeroes of the spherical Bessel function of the first kind and its derivatives, labelled as $n = 0, 1, 2, 3, ...$ The solutions of Eq. (5.8) can be obtained numerically, and provide all the possible plasma resonances excited at a NP of radius a and electron density parameter r_s. Nevertheless, it is instructive to distinguish two different regions in the frequency spectrum within the solutions: $\omega < \omega_p$ and $\omega > \omega_p$.

For $\omega < \omega_p$ (considering $\gamma = 0$) it is clear that $\mu(\omega)$ given by Eq. (5.4) is a purely imaginary number, as shown in Fig. 5.1(a) and the plasma oscillations are therefore

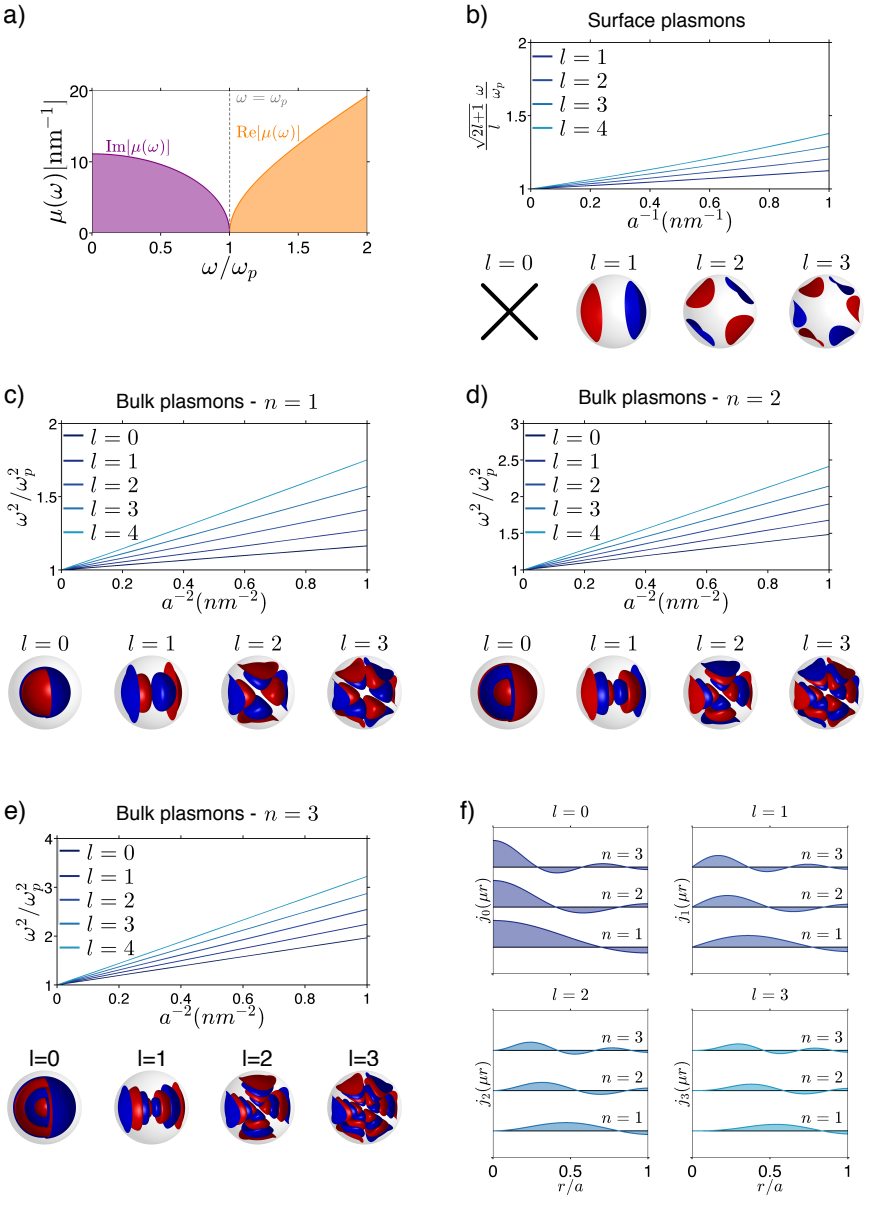

Figure 5.1: a) Real (orange) and imaginary (purple) parts of $\mu(\omega)$ for $\gamma = 0$, showing the region corresponding to surface plasmons at $\omega < \omega_p$ and the region corresponding to the bulk plasmons at $\omega > \omega_p$ (grey dashed line separates both regions). Size dependence of plasmonic modes in Na nanoparticles within the hydrodynamic model. b) Surface plasmons and c)-e) bulk plasmons associated with number (c) $n = 1$, (d) $n = 2$ and (e) $n = 3$. Bottom panels below b)-e) show isosurfaces for each mode, at isovalues equal to plus/minus (red/blue) b) ten times and c-e) twice the mean absolute value of the charge density in the sphere. The spherical NP outline is indicated in shaded gray. f) Spherical Bessel function plotted for $l = 0, 1, 2, 3$ and $n = 1, 2, 3$ showing the radial component of the charge density associated to the CBPs.

attenuated. Electron collective oscillations are confined to the surface $r = a$, as the spherical Bessel functions behave as exponentials for increasing imaginary arguments. In fact, using the large argument expansion of the spherical Bessel function, $x = \mu a \gg 1$,

$$j_l(x) \to \frac{1}{2}\frac{e^{|x|}}{|x|}, \tag{5.10}$$

it can be proved that

$$\xi_l(\omega) = \frac{l j_l(x)}{x j_l'(x)} \to 0, \tag{5.11}$$

and in the local limit ($\beta \to 0$, incompressible fluid) the well known energies of the LSP modes for spherical NPs are recovered:

$$\omega_l = \sqrt{\frac{l}{2l+1}}\omega_p. \tag{5.12}$$

In this regime below the plasma frequency. $\omega < \omega_p$, the EM field is screened and plasma oscillations are attenuated, i.e., there is no propagation of longitudinal plasma waves and the charge density is confined to the surface. In contrast, above the plasma frequency, $\omega > \omega_p$, $\mu(\omega)$ is real and the spherical Bessel functions are oscillatory functions describing longitudinal plasma oscillations that can propagate. In the case of finite geometries, such as a spherical nanoparticle, the longitudinal plasma oscillations are reflected back at the boundary providing stationary collective electron waves that we refer to as confined bulk plasmons (CBPs).

Figure 5.1(b-e) shows the mode dispersion for the lowest l and n CBPs (considering $\gamma = 0$). In principle, the $n = 0$ mode, the first eigenvalue obtained from Eq. (5.8) for each l (except for $l = 0$), corresponds to a surface plasmon, although for large l the energies can be larger than ω_p due to the dispersion, specially for small nanoparticles. Fig. 5.1(b) shows the dispersion relation for surface plasmons $l = 1 - 4$ which scale linearly with the inverse of the radius $\omega_{l,0} \sim a^{-1}$. The energy of the mode has been normalized to the local LSP energies, so that it can be clearly observed that for $a \gg 1$ the local LSP energies are recovered. Lower panels show the eigenmodes charge distributions corresponding to $m = l$ for each l. Note that there is no surface plasmon for $l = 0$, as it would violate charge conservation/neutrality.

The dispersion relations for the bulk plasmons ($n = 1 - 3$) in Figs. 5.1(c-e) show that for large nanoparticles $a \gg 1$ the energy of the modes tends to ω_p, as expected, and an inverse dispersion relation with NP size. It is helpful to consider Eq. (5.8) for $l = 0$, which, taking into account that $j_0'(x) = -j_1(x)$, yields $j_0'(\mu a) = 0$, and therefore,

$$\frac{\omega_{0,n}^2}{\omega_p^2} = 1 + x_{0,n}^2\left(\frac{\beta}{a}\right)^2, \tag{5.13}$$

where $x_{0,n}$ is the n^{th} positive root of $j_0'(x)$, the derivative of the 0^{th}-order spherical Bessel function. This is the signature of momentum quantization in the radial direction [99]. Indeed, Fig. 5.1(f) shows the radial component of the eigenmodes for $l = 0, 1, 2, 3$ and $n = 1, 2, 3$, showing the oscillation of the charge density. Christensen *et al.* [94] obtained a similar condition for all l's within a hydrodynamic model that includes retardation by neglecting the coupling of the pressure waves to light, i.e., by searching for radial standing wave solutions, thus neglecting the transverse components. Moreover, that work neglects $l = 0$ modes which do not couple to excitation sources that do not penetrate the nanoparticle, as they do not consider penetrating trajectories. In our expression all components are included for $l > 0$. While $l = 0$ bulk modes do not couple to light (plane waves), other bulk terms such as $l = 1$ do, albeit their intensity is orders of magnitude weaker than their surface counterparts.

5.2 Electron energy loss probability

We have introduced the hydrodynamic model for spherical nanoparticles and provided the main ingredients to understand the underlying plasmonic mode structure. Here we will apply this formalism to calculate the electron energy loss (EEL) probability in small spherical metallic nanoparticles. Although this problem has been tackled since long ago, the solutions for penetrating trajectories are limited in the literature to averages over impact parameters [268], momentum-dependent solutions [269], formal solutions without explicit expressions for the EEL probability [270], or direct local descriptions [257, 271, 272]. In this section we obtain an expression for the EEL probability within the hydrodynamic model that explicitly depends on the impact parameter of the electron probe and, as such, might be useful for interpretation of state-of-the-art experiments with narrow electron beams and high spatial precision, i.e., therefore precise impact parameter control.

The charge density for an external electron beam with a trajectory along the z-axis, impact parameter b and velocity v can be expressed in spherical coordinates (see schematics in Fig. 5.2) and in frequency domain as:

$$\rho^{\text{ext}}(\mathbf{r}, \omega) = -\frac{1}{v} \frac{\delta(r \sin\theta - b)\delta(\varphi)}{r \sin\theta} e^{i\omega r \cos\theta / v}. \tag{5.14}$$

The expansion into spherical harmonics gives:

$$\rho^{\text{ext}}(\mathbf{r}, \omega) = \sum_{l=0}^{\infty} \sum_{m=-l}^{l} \rho_{lm}^{\text{ext}}(r, \omega) Y_l^m(\Omega), \tag{5.15}$$

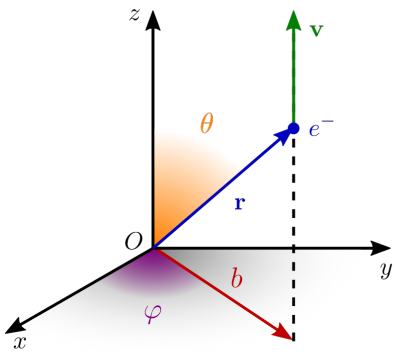

Figure 5.2: Sketch showing the electron (blue dot) at position $\mathbf{r} = (r, \theta, \varphi)$ (blue arrow, and shaded orange and purple angles) with a trajectory along the z-axis defined by impact parameter b (red arrow), and with velocity $\mathbf{v} = v\,\hat{\mathbf{z}}$ (green arrow).

where

$$\rho_{lm}^{\text{ext}}(r,\omega) = \frac{-2\alpha_{lm}}{v\sqrt{r^2-b^2}}\Pi_{lm}(r,b;\omega), \tag{5.16}$$

with

$$\alpha_{lm} = \sqrt{\frac{2l+1}{4\pi}\frac{(l-m)!}{(l+m)!}}, \tag{5.17}$$

and

$$\Pi_{lm}(r,b;\omega) = g_{lm}(\omega r/v)P_l^m(\sqrt{1-b^2/r^2}), \tag{5.18}$$

$$g_{lm}(x) = \begin{cases} \cos(x), & \text{if } l+m \text{ is even,} \\ i\sin(x), & \text{if } l+m \text{ is odd ,} \end{cases} \tag{5.19}$$

and $P_l^m(x)$ is the associated Legendre polynomial of degree l and order m.

Making use of the spherical symmetry of the problem we also expand $\rho(\mathbf{r},\omega)$ in terms of the spherical harmonics,

$$\rho(\mathbf{r},\omega) = \sum_{l=0}^{\infty}\sum_{m=0}^{l}\rho_{lm}(r,\omega)Y_l^m(\Omega). \tag{5.20}$$

This decomposition allows us to write the BC at $r = a$ [Eq. (5.5)] as,

$$\begin{aligned}\frac{\omega_p^2}{2l+1}\frac{l+1}{a^{l+2}}\int_0^a dr\, r^{l+2}\rho_{lm}(r,\omega) - \beta^2\frac{\partial\rho_{lm}(r,\omega)}{\partial r}\bigg|_{r=a} = \\ = \frac{\omega_p^2}{2l+1}\bigg\{-\frac{l+1}{a^{l+2}}\int_0^a dr\, r^{l+2}\rho_{lm}^{\text{ext}}(r,\omega) + l\,a^{l-1}\int_a^{\infty}\frac{dr}{r^{l-1}}\rho_{lm}^{\text{ext}}(r,\omega)\bigg\}.\end{aligned} \tag{5.21}$$

We tackle the general solution of the most complex case: penetrating trajectories. Our treatment requires separating the external potential into $r > a$ (the electron is outside the nanoparticle) and $r < a$ (the probing electron inside the nanoparticle). Moreover, penetrating trajectories require the solution of the inhomogeneous Helmholtz equation (5.3). This solution can be separated into an homogeneous solution that satisfies both the inhomogeneous BC and homogeneous Helmholtz equation (complementary solution), and a particular solution that satisfies the inhomogeneous Helmholtz equation and homogeneous BC. Herein we will omit any ω-dependence of the terms.

Below the particular solution is obtained by solving Helmholtz equation for the Green's function $\mathcal{G}(\mathbf{r}, \mathbf{r}')$:

$$\mathcal{G}(\mathbf{r}, \mathbf{r}') = \sum_{l=0}^{\infty} Y_l^m(\Omega')\, Y_l^m(\Omega) G_l(r, r') \tag{5.22}$$

which satisfies,

$$[\nabla^2 + \mu^2]\mathcal{G}(\mathbf{r}, \mathbf{r}') = \delta(\mathbf{r}, \mathbf{r}'). \tag{5.23}$$

The reduced Green's function introduced in Eq. (5.22), G_l, satisfies the spherical Bessel function,

$$\left[\frac{d^2}{dr^2} + \frac{2}{r}\frac{d}{dr} - \frac{l(l+1)}{r^2} + \mu^2\right] G_l(r, r') = \frac{1}{r^2}\delta(r - r'). \tag{5.24}$$

Moreover, G_l is continuous at $r = r'$ while its derivative has a discrete jump at $r = r'$ [276]. It also fulfills the homogeneous BC at $r = a$,

$$\frac{\omega_p^2}{2l+1}\frac{l+1}{a^{l+2}} \int_0^a dr\, r^{l+2} G_l(r, r') - \beta^2 \frac{\partial G_l(r, r')}{\partial r}\bigg|_{r=a} = 0. \tag{5.25}$$

This condition holds for all l, except for $l = 0$, which due to the divergence theorem, and in order to satisfy charge conservation/neutrality fulfills the following condition at the surface,

$$\frac{\partial G_0(r, r')}{\partial r}\bigg|_{r=a} = \frac{1}{a^2}. \tag{5.26}$$

Once the Green's function has been calculated, the particular solution is obtained as:

$$\rho_{lm}^{\mathrm{p}}(r) = \frac{\omega_p^2}{\beta^2} \int_0^a dr' r'^2 G_l(r, r') \rho_{lm}^{\mathrm{ext}}(r'). \tag{5.27}$$

By, adding the complementary solution, the full solution that satisfies both the BC

in Eq. (5.21) and the inhomogeneous Helmholtz equation (5.3) is:

$$\rho_{lm}(r) = \frac{2\omega_p^2}{v}\alpha_{lm}\Bigg\{ j_l(\mu r)\Bigg[\frac{l+1}{(2l+1)a^{l+2}M_l}\left(1+\frac{\omega_p^2}{\mu^2\beta^2}\right)\mathcal{E}^i_{lm} - \frac{l\,a^{l-1}}{(2l+1)M_l}\mathcal{E}^o_{lm} + \frac{N_l}{M_l}\frac{\mu}{\beta^2}\mathcal{I}^j_{lm}(b,a) - \frac{\mu}{\beta^2}\mathcal{I}^y_{lm}(b,a)\Bigg] - \frac{\mu}{\beta^2}\Theta\Big(\frac{r}{b}-1\Big)\Bigg[y_l(\mu r)\mathcal{I}^j_{lm}(b,r) - j_l(\mu r)\mathcal{I}^y_{lm}(b,r)\Bigg]\Bigg\}, \tag{5.28}$$

where, α_{lm} is defined by Eq. (5.17), $\Theta(x)$ is the Heaviside step-function, M_l is the mode's energy expression

$$M_l = \frac{\omega_p^2}{2l+1}\frac{l+1}{\mu}j_{l+1}(\mu a) - \beta^2\mu j_l'(\mu a), \tag{5.29}$$

and the following integrals are introduced:

$$\mathcal{E}^i_{lm} \equiv \frac{1}{a^{l+1}}\int_b^a dr\, r^l \frac{\Pi_{lm}(r,b)}{\sqrt{1-b^2/r^2}}, \tag{5.30}$$

$$\mathcal{E}^o_{lm} \equiv a^l \int_a^\infty \frac{dr}{r^{l+1}}\frac{\Pi_{lm}(r,b)}{\sqrt{1-b^2/r^2}}, \tag{5.31}$$

and

$$\mathcal{I}^f_{lm}(x_1,x_2) \equiv \int_{x_1}^{x_2} dx\, \frac{f_l(\mu x)\Pi_{lm}(x,b)}{\sqrt{1-b^2/x^2}}, \tag{5.32}$$

with $\Pi_{lm}(x,b) \equiv \Pi_{lm}(x,b;\omega)$ defined by Eq. (5.18). In the last integral f_l is a spherical Bessel function of either the first or second kind.

Once the induced charge density is known [Eqs. (5.20) and (5.28)], the induced potential at position $\mathbf{r}$ can be obtained by integration:

$$\begin{aligned}\phi(\mathbf{r}) &= \int_V \frac{\rho(\mathbf{r}')}{|\mathbf{r}-\mathbf{r}'|}d\mathbf{r}' \\ &= \sum_{l=0}^\infty \frac{4\pi}{2l+1}Y_l^m(\Omega)\int_0^a dr'\, r'^2 \frac{r_<^l}{r_>^{l+1}}\rho_{lm}(r') \\ &= \sum_{l=0}^\infty Y_l^m(\Omega)\phi_{lm}(r),\end{aligned} \tag{5.33}$$

where $\phi_{lm}(r)$ is the radial component of the induced potential

$$\phi_{lm}(r) = \frac{4\pi}{2l+1}\int_0^a dr'\, r'^2 \frac{r_<^l}{r_>^{l+1}}\rho_{lm}(r'). \tag{5.34}$$

Finally the energy loss experienced by the probing electron is obtained as usual:

$$W = \frac{1}{2\pi}\int_{-\infty}^{\infty} d\omega \int_{-\infty}^{\infty} dz' \frac{\partial \phi(\mathbf{r},\omega)}{\partial z}\bigg|_{z=z'} e^{-i\omega z'/v}. \tag{5.35}$$

This integral is calculated by parts, taking into account that, $\phi(x,y,\pm\infty) \to 0$, to obtain:

$$W = \frac{i}{2\pi v}\int_{-\infty}^{\infty} d\omega \int_{-\infty}^{\infty} dz' \omega\, \phi(\mathbf{r}',\omega) e^{-i\omega z'/v}. \tag{5.36}$$

Moreover, from the condition that both charge density and induced field are real variables, i.e., $\rho(\mathbf{r},\omega) = \rho^*(\mathbf{r},-\omega)$ and $\phi(\mathbf{r},\omega) = \phi^*(\mathbf{r},-\omega)$, we get to:

$$W = \frac{1}{\pi v}\int_{0}^{\infty} d\omega\, \omega \int_{-\infty}^{\infty} dz' \mathrm{Im}\Big\{ -\phi(\mathbf{r}',\omega) e^{-i\omega z'/v}\Big\}. \tag{5.37}$$

Thus, the electron energy loss probability is given by:

$$\Gamma_{\mathrm{EELS}}(\omega) = \frac{1}{\pi v}\int_{-\infty}^{\infty} dz' \mathrm{Im}\Big\{ -\phi(\mathbf{r}',\omega) e^{-i\omega z'/v}\Big\} \tag{5.38}$$

By taking into account the parity conditions $P_l^m(-x) = (-1)^{l+m} P_l^m(x)$ and $g_{lm}^*(x) = (-1)^{l+m} g_{lm}(x)$, Eq. (5.38) can be further recast as:

$$\Gamma_{\mathrm{EELS}}(\omega) = \frac{2}{\pi v}\sum_{l=0}^{\infty} \alpha_{lm}(-1)^{l+m+1}\int_{0}^{\infty} dz' \mathrm{Im}\Big\{ \phi_{lm}(r',\omega) P_l^m\Big(\frac{z'}{r'}\Big) g_{lm}(\omega z'/v)\Big\}. \tag{5.39}$$

In order to get furhter insight into this expression, the integral is separated into two regions, $z < \sqrt{a^2-b^2}$ and $z > \sqrt{a^2-b^2}$, inside and outside the nanoparticle respectively. This way the expressions obtained for the radial component of the induced potential [see Eqs. (E.2) and (E.3) in App. E], are introduced to obtain, after some algebra,

$$\begin{aligned}\Gamma_{\mathrm{EELS}}(\omega) = \frac{4a\omega_p^2}{\pi v^2}\sum_{l=0}^{\infty}\sum_{m=0}^{l}(-1)^{l+m}(2-\delta_{m0})\frac{(l-m)!}{(l+m)!}\mathrm{Im}\Big\{ &\Gamma_{lm}^{\mathrm{oo}} + \Gamma_{lm}^{\mathrm{io},1} + \Gamma_{lm}^{\mathrm{io},2} \\ &+ \Gamma_{lm}^{\mathrm{ii},1} + \Gamma_{lm}^{\mathrm{ii},2} + \Gamma_{lm}^{\mathrm{ii},3} + \Gamma_{lm}^{\mathrm{b}}\Big\},\end{aligned} \tag{5.40}$$

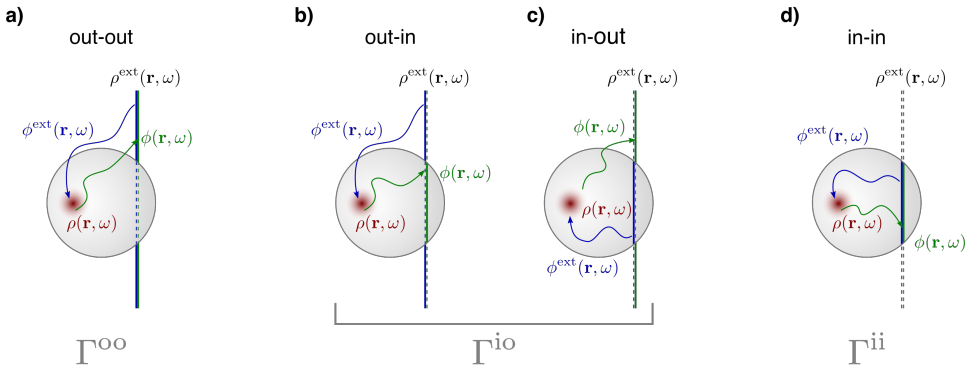

Figure 5.3: Contributions adding to the total electron energy loss probability. The external charge density $\rho^{\rm ext}(\mathbf{r},\omega)$ (blue solid line) creates an external potential $\phi^{\rm ext}(\mathbf{r},\omega)$ (blue arrow) inducing a charge density $\rho(\mathbf{r},\omega)$ (red area) in the nanoparticle, which in turn creates an induced potential $\phi(\mathbf{r},\omega)$ (green arrow) at the position of the external charge density $\rho^{\rm ext}(\mathbf{r},\omega)$ (green line). Different contributions to $\Gamma_{\rm EELS}$ are displayed in the different panels: a) $\Gamma^{\rm oo}$ (out-out), b) and c) $\Gamma^{\rm io}$ (out-in and in-out) and d) $\Gamma^{\rm ii}$ (in-in) are sketched.

where,

$$\Gamma^{\rm oo}_{lm} = \frac{l\, j_{l+1}(\mu a)}{(2l+1)\mu M_l}[\mathcal{E}^o_{lm}]^2 \tag{5.41}$$

$$\Gamma^{\rm io,1}_{lm} = -\frac{2\,l\, j_{l-1}(\mu a)}{(2l+1)\mu M_l}\mathcal{E}^i_{lm}\mathcal{E}^o_{lm} \tag{5.42}$$

$$\Gamma^{\rm io,2}_{lm} = \frac{2l}{a^2\mu^2 M_l}\mathcal{I}^j_{lm}(b,a)\mathcal{E}^o_{lm} \tag{5.43}$$

$$\Gamma^{\rm ii,1}_{lm} = \frac{(l+1)j_{l-1}(\mu a)}{(2l+1)\mu M_l}\left(1+\frac{\omega_p^2}{\mu^2\beta^2}\right)[\mathcal{E}^i_{lm}]^2 \tag{5.44}$$

$$\Gamma^{\rm ii,2}_{lm} = -\frac{2(l+1)}{a^2\mu^2 M_l}\left(1+\frac{\omega_p^2}{\mu^2\beta^2}\right)\mathcal{I}^j_{lm}(b,a)\mathcal{E}^i_{lm} \tag{5.45}$$

$$\Gamma^{\rm ii,3}_{lm} = -\frac{2l+1}{a\mu\beta^2}\left[\frac{N_l}{M_l}[\mathcal{I}^j_{lm}(b,a)]^2 - 2\int_b^a dr\,\frac{\Pi_{lm}(r,b;\omega)}{\sqrt{1-b^2/r^2}}y_l(\mu r)\mathcal{I}^j_{lm}(b,r)\right] \tag{5.46}$$

$$\Gamma^{\rm b}_{lm} = \frac{2}{a\mu^2\beta^2}\int_b^a dr\int_b^r dr'\,\frac{r'^l}{r^{l+1}}\frac{\Pi_{lm}(r,b;\omega)}{\sqrt{1-b^2/r^2}}\frac{\Pi_{lm}(r',b;\omega)}{\sqrt{1-b^2/r'^2}}, \tag{5.47}$$

where N_l is defined as,

$$N_l = \frac{\omega_p^2}{2l+1}\frac{l+1}{\mu}y_{l+1}(\mu a) - \beta^2\mu y_l'(\mu a). \tag{5.48}$$

The meaning of the subscripts labeling used in these definitions is explained below, and sketched in Fig. 5.3.

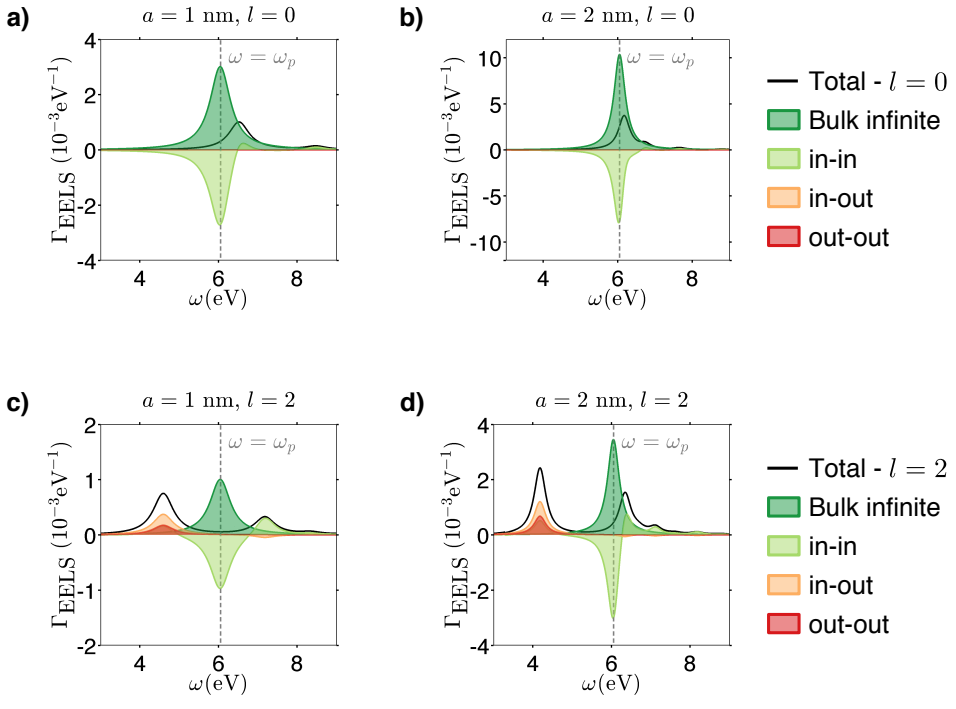

Figure 5.4: Decomposition of the EEL probability for impact parameter $b = 0$ with $l = 0$ for a) $a = 1$ nm and b) $a = 2$ nm, the total contribution (black line) and the pure bulk term (dark green), in-in (light green), in-out (orange) and out-out (red) terms. Similar decomposition with $l = 2$ for c) $a = 1$ nm and d) $a = 2$ nm. Dashed vertical grey line highlights the frequency $\omega = \omega_p$ corresponding to the pure bulk term.

oo (out-out): the electron is outside the nanoparticle when inducing a charge density in the NP, and the electron is also outside the nanoparticle when losing energy due to the induced potential [sketch in Fig. 5.3(a)].

io (in-out): the electron is inside (outside) the nanoparticle when inducing a charge density in the NP, and the electron is outside (inside) the nanoparticle when losing energy due to the induced potential [sketches in Fig. 5.3(b,c)].

ii (in-in): the electron is inside the nanoparticle when inducing a charge density in the NP, and the electron is also inside the nanoparticle when losing energy due to the induced potential [sketch in Fig. 5.3(d)].

Moreover, the last term, Γ^{b}_{lm}, corresponds to the direct bulk losses experienced by the electron in an infinite lossy material.

The plots of the calculated Γ_{EELS} in Fig. 5.4 support the interpretation of these terms and the total loss for each l (black line). We have calculated each term of the interaction, (in-in), (in-out/out-in) and (out-out), for nanoparticles of radii $a =$

1, 2 nm, axial trajectory $b = 0$, selecting the contributions with $l = 0$ and $l = 2$ to the total loss (due to azimuthal symmetry only even l and $m = 0$, are considered since the rest of the terms have small contributions). For $l = 0$ we observe in Fig. 5.4(a-b) that, apart from the direct bulk term Γ_{00}^{b} (dark green), only the in-in terms $\Gamma_{00}^{\mathrm{ii},1,2,3}$ (light green) contribute to the losses. This clearly suggests that $l = 0$ modes can only be excited for trajectories penetrating the nanoparticle, as they are radial oscillations that otherwise do not couple to outer electromagnetic fields. Moreover, we see that no LSPs are present for $l = 0$, and still a *begrenzung* or *boundary-effect* [61, 277] occurs for confined bulk plasmons, i.e., the in-in terms contain a correction (negative contribution) to the direct bulk term diminishing its intensity and instead exciting confined bulk plasmons. Another remarkable result is the blueshift of the peaks for $a = 1$ nm compared to $a = 2$ nm due to dispersion [278].

Opposite to the previous case, in Figs. 5.4(c-d) it is observed that all terms contribute to the excitation of the $l = 2$ contribution, including in-out (orange) and out-out (red) terms. In particular, the LSP shows the contribution of all terms except the direct bulk term. Actually $\Gamma_{20}^{\mathrm{ii},3}$ does not contribute to the LSP and can therefore be considered as a purely CBP term. It is therefore clear that the contribution to confined bulk plasmons mainly comes from the in-in terms, which only occurs in penetrating trajectories.

For external trajectories, i.e., probes outside the particle ($b > a$), the right-hand side of Helmholtz equation (5.3) is zero and the solution of the charge density is simply given by,

$$\rho(\mathbf{r}) = \sum_{l=0}^{\infty} \sum_{m=-l}^{l} A_{lm} j_l(\mu r) Y_l^m(\Omega), \tag{5.49}$$

where j_l is the l^{th} order spherical Bessel function of the first kind, and the coefficients A_{lm} are calculated from the BC, Eq. (5.5), which in this case reduces to:

$$A_{lm}\left[\frac{\omega_p^2}{2l+1}\frac{l+1}{\mu} j_{l+1}(\mu a) - \beta^2 \mu j_l'(\mu a)\right] = \frac{1}{4\pi}\omega_p^2 \phi_{lm}^{\mathrm{ext}}(r)|_{r=a}. \tag{5.50}$$

Following Ferrell *et al.* [259], the components of the potential due to the electron probe can be written as:

$$\phi_{lm}^{\mathrm{ext}}(r) = \frac{2\alpha_{lm}}{v(l-m)!}\left(\frac{i\omega}{|\omega|}\right)^{l+m}\left(\frac{|\omega| r}{v}\right)^{l} K_m\left(\frac{|\omega| b}{v}\right), \tag{5.51}$$

where $K_m(x)$ stands for the modified Bessel function of order m.

Once the induced charge density is obtained it is straightforward to calculate the induced potential and the energy loss probability:

$$\Gamma_{\mathrm{EELS}} = \frac{4}{\pi a^2 v^2} \sum_{l=0}^{\infty} \sum_{m=0}^{l} \frac{2-\delta_{m0}}{(l-m)!(l+m)!}\left(\frac{\omega}{v}\right)^{2l} K_m^2\left(\frac{\omega b}{v}\right) \mathrm{Im}\{\Xi_l(\omega)\}, \tag{5.52}$$

where $\Xi_l(\omega)$ is:

$$\Xi_l(\omega) \equiv a^3\omega_p^2 \frac{l j_{l+1}(\mu a)}{(2l+1)\mu M_l}, \tag{5.53}$$

which is the equivalent to the multipolar polarizability given in the literature to describe the interaction of light with NPs [83,94,279,280], but here using a momentum dependent $\varepsilon(k,\omega)$ dielectric framework, and integrals in momentum-space involving this function. This result can also be obtained by using Eq. (5.40) and taking into account that only Γ_{lm}^{oo} contributes in this case. The expression for external trajectories given by Eq. (5.52) was obtained in the literature [270], and we provide it for completeness. In the local limit $\beta \to 0$, Eq. (5.52) reduces to the expression given by Ferrell and Echenique [258] for a Drude-like dielectric function.

5.3 Impact parameter dependence

In the previous section we have introduced a hydrodynamic framework and given a semi-analytical expression of the EEL probability for penetrating electron trajectories in spherical nanoparticles. In this section we study the dependence of this EEL probability on the probing impact parameter b. As discussed in Chapter 4, this dependence is not properly described by the local dielectric approach. We consider a sodium nanoparticle ($r_s = 2.08$ Å, $\omega_p \sim 6.05$ eV) with radius $a = 1.5$ nm and damping term $\gamma = 0.1$ eV. The calculated Γ_{EELS} for both internal ($b/a < 1$) and external ($b/a > 1$) electron trajectories [see Fig. 5.5(a)] is represented in Fig. 5.5(b).

For external trajectories and large impact parameters ($b/a \sim 2$) the surface dipolar plasmon ($l = 1$, $n = 0$) dominates the spectra, as the external field created by the electron probe that reaches the nanoparticle is very similar to a plane wave. Nevertheless, as the impact parameter decreases, higher order modes are excited, specially at grazing trajectories ($b/a \sim 1$), as the external perturbing field that reaches the nanoparticle no longer resembles a plane wave. Compared to the local dielectric description, the higher order modes are more spread in energy, and they are not bounded by the surface plasmon energy $\omega_S = \omega_p/\sqrt{2}$ (see Fig. 5.5(b)). Moreover, no bulk plasmon excitation is observed at first sight for external trajectories.

The spectra for penetrating trajectories show greater dependence on the impact parameter. For instance, the surface dipolar mode ($l = 1$, $n = 0$) is the main mode excited for trajectories in the outer half of the NP ($0.5 < b/a < 1$), and it fades away for trajectories in the inner half ($b/a < 0.5$). As in the local description, this decrease in intensity for decreasing impact parameters is observed for all odd l modes, not only for the dipolar one. This is expected, as for central trajectories ($b/a = 0$), small nanoparticles, and fast electrons ($\omega a/v \ll \pi/2$) even l modes dominate the spectrum, as described in Chapter 4 and summarized in Fig. 4.2.

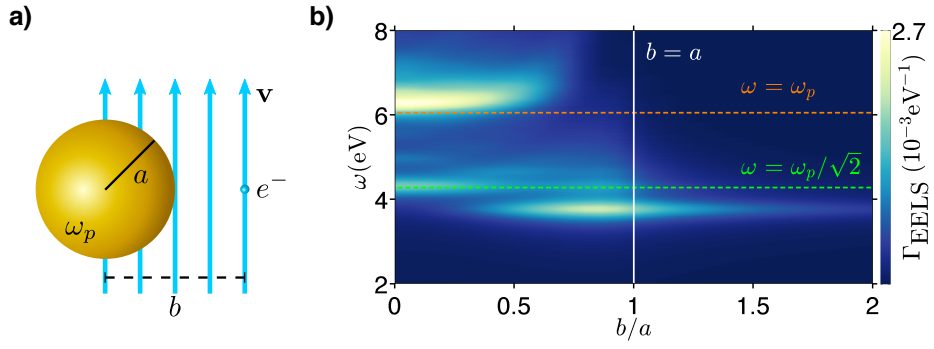

Figure 5.5: a) Spherical Na nanoparticle ($r_s = 2.08$ Å, $\omega_p \sim 6.05$ eV) with radius $a = 1.5$ nm targeted by electron beams with impact parameter b and velocity v ($E_k = 100$ keV). b) Electron energy loss probability, Γ_{EELS}, as a function of the normalized impact parameter b/a for such as nanoparticle calculated using the hydrodynamic model. Straight line highlights the grazing trajectories ($b = a$) and orange and green dashed lines the plasma frequency ω_p and the surface plasmon frequency $\omega_{sp} = \omega_p/\sqrt{2}$.

Regarding the bulk plasmon, close to 6 eV, there are two remarkable trends different to the EEL spectra obtained for the local model [Fig. 4.7(d)]. First, the bulk plasmon peak does not emerge immediately for $b = a$, but for impact parameters close to $b \sim 3a/4$. This is also observed in *ab initio* calculations for non-spherical particles and also with non-local models in planar interfaces [281]. Second, there is an apparent blueshift of the bulk peak for increasing impact parameters is observed. This behavior is further illustrated in the spectra of specific impact parameters ($b/a = 0, 1/5, 2/5, 3/5, 4/5, 1$) presented in Fig. 5.6, where the total EEL probability is plotted as a black line, and the contribution of the l multipoles in different colors. The domination of l even multipoles over the odd l multipoles for an axial trajectory is clear from Fig. 5.6(a) and the steady activation of the odd l modes as the impact parameter increases can be traced in Figs. 5.6(b-f), which happens both for surface and bulk modes. Moreover, these results show that the apparent blueshift of the bulk plasmon is due to the excitation of *several* confined bulk plasmons (CBPs) that are too close spectrally to be distinguished, and whose excitation depends on the impact parameter in a similar way as in the case of LSPs. Furthermore, the intensity of these CBP peaks also decreases for increasing impact parameters, becoming almost negligible for $b/a > 0.8$. This means that the bulk plasmon starts to be excited for impact parameters at a certain distance from the surface, contrary to the result in the local dielectric description, which could lead to an underestimation of the NPs size if the bulk plasmon loss is taken as a reference to measure the size of the NP. To highlight the impact parameter dependence of the activation of the bulk plasmon, in Fig. 5.7(a) we represent the intensity of the main CBP peak (blue line) as a function of impact parameter normalized to the maximum intensity (obtained for $b/a = 0$), together with the blue-shift of the peak energy. A similar behavior is observed for the full-width half maxima (FWHM) of the peak

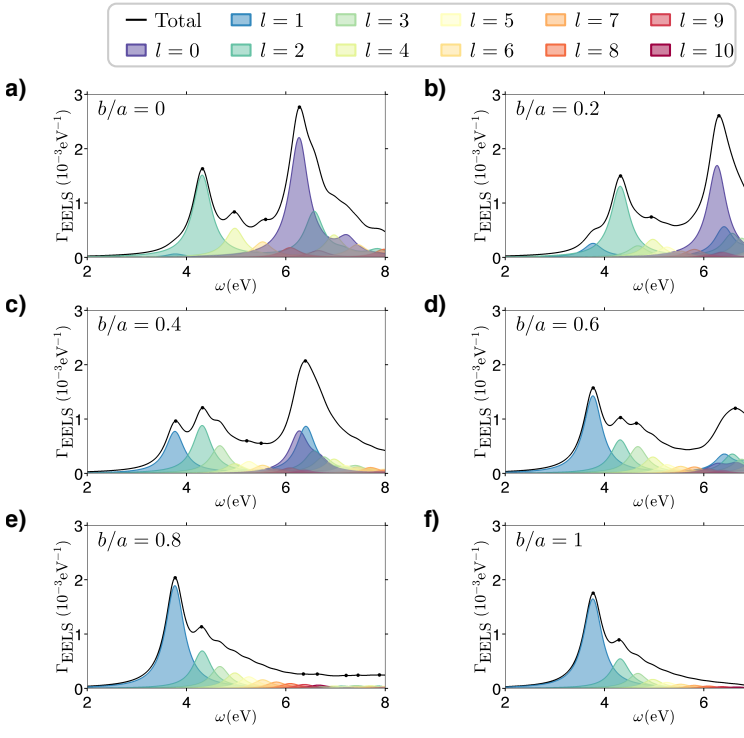

Figure 5.6: Electron energy loss probability (black line) and contribution of $l = 0 - 10$ term (all m are added for each l) to the total energy loss probability for normalized impact parameters $b/a = 0, 0.2, 0.4, 0.6, 0.8, 1$.

in Fig. 5.6(b), which increases for increasing impact parameters. Such behavior has been reported for Al disks in the literature [85].

To get further insight into the symmetry dependence of the CBP excitation, we direct our attention towards the induced charge distribution at the energy of the plasmonic resonance. The isosurfaces corresponding to such charge distributions are plotted in Fig. 5.8(a). In general we observe that the electron density (blue) is expelled from the trajectory of the electron beam (black line) and that positive charge density is localized around it. Moreover, there is some overlapping of the surface and the bulk modes, clearly observed for $b/a = 0.4$ and $b/a = 0.6$. The structure of the induced charge density inside the nanoparticle is better visualized by removing a hemisphere, as in Fig. 5.8(b), or by simply plotting the induced charge density in 2D maps such as in Figs. 5.8(c-d). The charge density for the central trajectory $b/a = 0$ shows perfect azimuthal symmetry, as the main excited mode is $l = 0, n = 1$, although there is some contribution from $l = 2, n = 1$ [see Fig. 5.6(a)]. This symmetry is broken as the impact parameter increases and odd l modes are excited, as observed for $b/a = 0.2$. For instance, $l = 1, n = 1$ has the largest contribution for $b/a = 0.4$

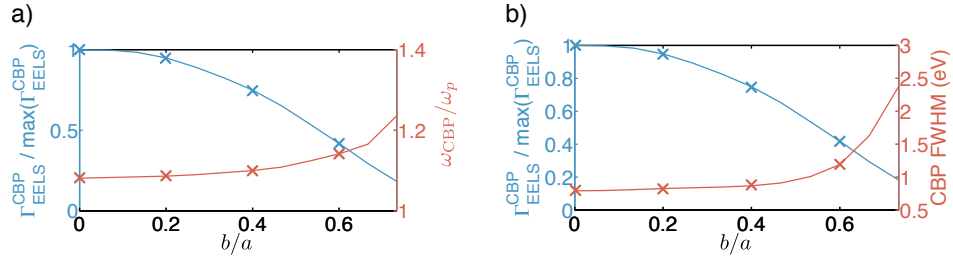

Figure 5.7: a) Normalized (to the maximum value of $b = 0$) CBP intensities and normalized energies plotted as a function of the position of the electron beam on a $a = 1.5$ nm Na sphere. b) Normalized CBP intensities and FWHM plotted as a function of the position of the electron beam for the same structure.

[see Fig. 5.6(c)], while for $b/a = 0.6$ many modes contribute with similar intensity [see Fig. 5.6(d)].

CBP modes should in principle be less sensitive to changes at the surface than LSPs. Nevertheless, spill-out effects, which are sensitive to the embedding media, can also affect the energy of the bulk modes. For instance, sodium nanostructures are known to sustain large electron spill-out effects, not included in our approach, which would increase the effective size of the nanoparticle, and as such, decrease the energy of the modes. Anyway, it is unclear if they would affect all modes equally, which could lead to larger energy differences between the different modes making them easier to detect individually. Certainly, NP size affects the dispersion of the modes with size and as such, for large nanoparticles the different modes should be difficult to distinguish as they would get closer in energy. Nevertheless, due to the interplay between the velocity of the electron beam and the size of the nanoparticle, one can expect the energy of the bulk plasmon to vary for increasing NP sizes depending on the dominance of odd or even l modes. We explore in the next section the role played by the electron probe velocity in the activation of CBPs.

5.4 Electron velocity dependence

It is known that within the local description the excitation of LSPs by external electrons depends on the $\omega a/v$ ratio [255], at least for central trajectories. In principle, the excitation of the CBPs should also depend on the velocity of the probe. Here we focus on the central trajectory $b = 0$ and check the influence of the probing electron's energy on the EEL spectrum.

Direct inspection of Eqs. (5.40) - (5.47) suggests that the excitation of the modes mainly depends on the integrals defined by Eqs. (5.30), (5.31) and (5.32), which define the coupling to the external source. In fact, for central trajectories, these

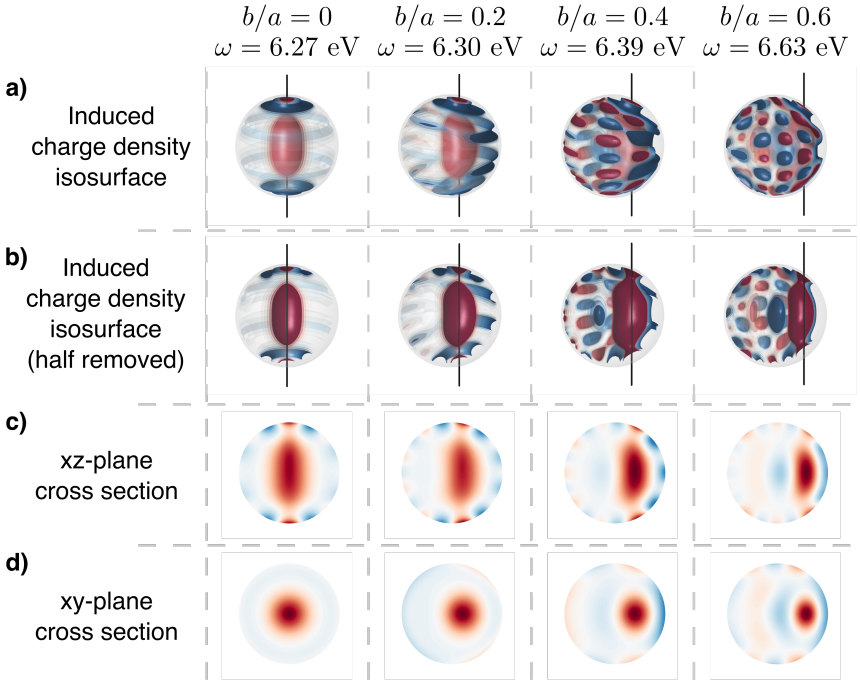

Figure 5.8: a) Isosurfaces calculated for the induced charge density (red positive, blue negative, isovalue taken as the mean value of the absolute value of the induced charge density) corresponding to the main CBPs excited for normalized impact parameters $b/a = 0, 0.2, 0.4, 0.6$. b) Half of the isosurface has been removed to visualize the induced charge density in the interior of the nanoparticle. c) and d) 2D induced charge density maps in the c) xz-plane and d) xy-plane for the corresponding normalized impact parameters. These cases are marked as crosses in Fig. 5.7.

integrals reduce to

$$\mathcal{E}^i_{l0} = \frac{1}{a^{l+1}} \int_0^a dr\, r^l g_{l0}(\omega r/v) \tag{5.54}$$

$$\mathcal{E}^o_{l0} = a^l \int_a^\infty \frac{dr}{r^{l+1}} g_{l0}(\omega r/v) \tag{5.55}$$

$$\mathcal{I}^j_{l0}(0,a) = \int_0^a dr\, j_l(\mu r) g_{l0}(\omega r/v), \tag{5.56}$$

for $m = 0$, and they are zero for $m \neq 0$. This gives us a hint about the relationship between $\omega a/v$ and the excitation of the modes: for $\omega a/v \sim 0$, i.e., for small nanoparticles ($a < 5$ nm) and fast electrons ($E_k \sim 100$keV), even-l's dominate the spectra as

$$\lim_{x\to 0} g_{l0}(x) \sim \begin{cases} \lim\limits_{x\to 0} \sin(x) \sim 0, & \text{if } l \text{ odd} \\ \lim\limits_{x\to 0} \cos(x) \sim 1, & \text{if } l \text{ even.} \end{cases} \tag{5.57}$$

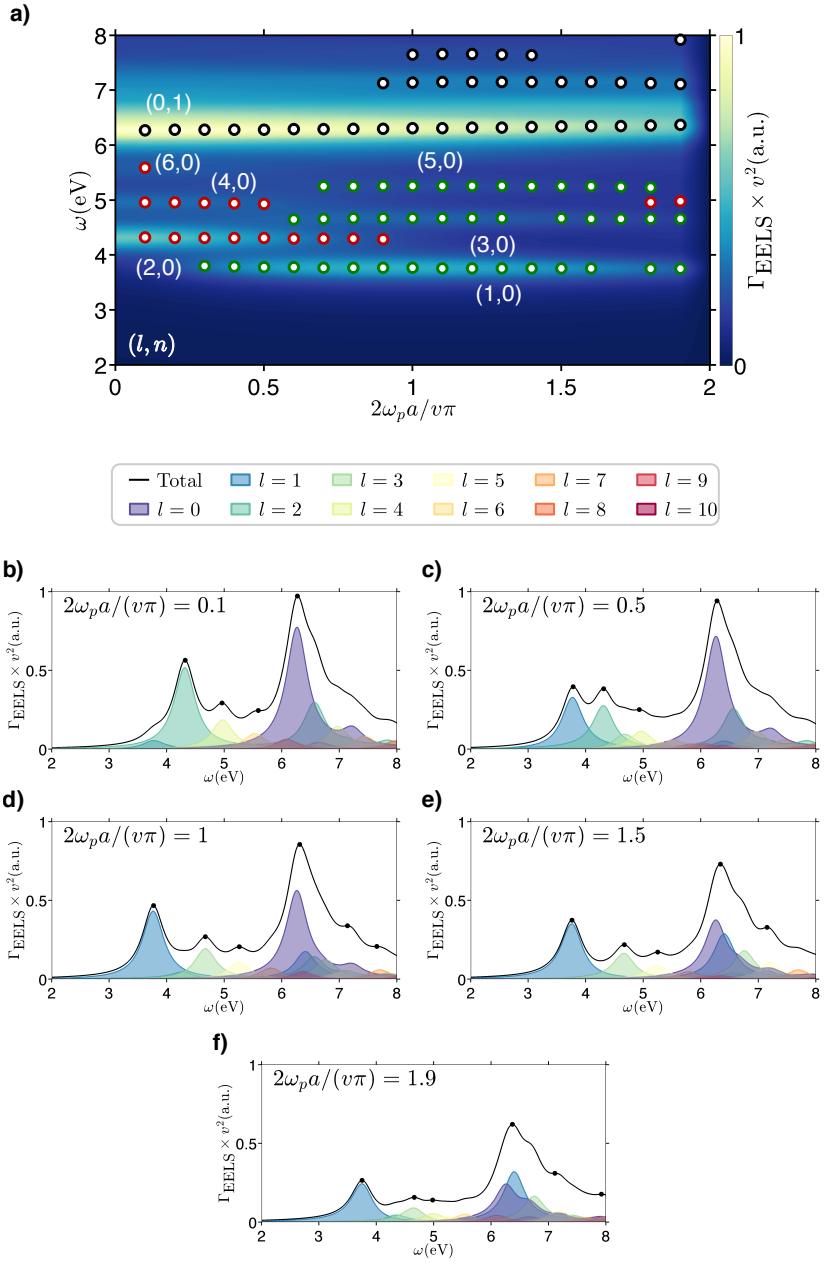

Figure 5.9: a) Normalized electron energy loss probability, $\Gamma_{\mathrm{EELS}} \times v^2$, as a function of reduced radius $a^{\mathrm{red}} = 2\omega_p a/v\pi$. Odd l modes (green circles), even l modes (red circles), and the main CBP peak (black circles) are highlighted. b)-f) Electron energy loss probability (black line) and contribution of $l = 0-10$ term (all m are added for each l) to the total energy loss probability for reduced radii $a^{\mathrm{red}} = 0.1, 0.5, 1, 1.5, 1.9$.

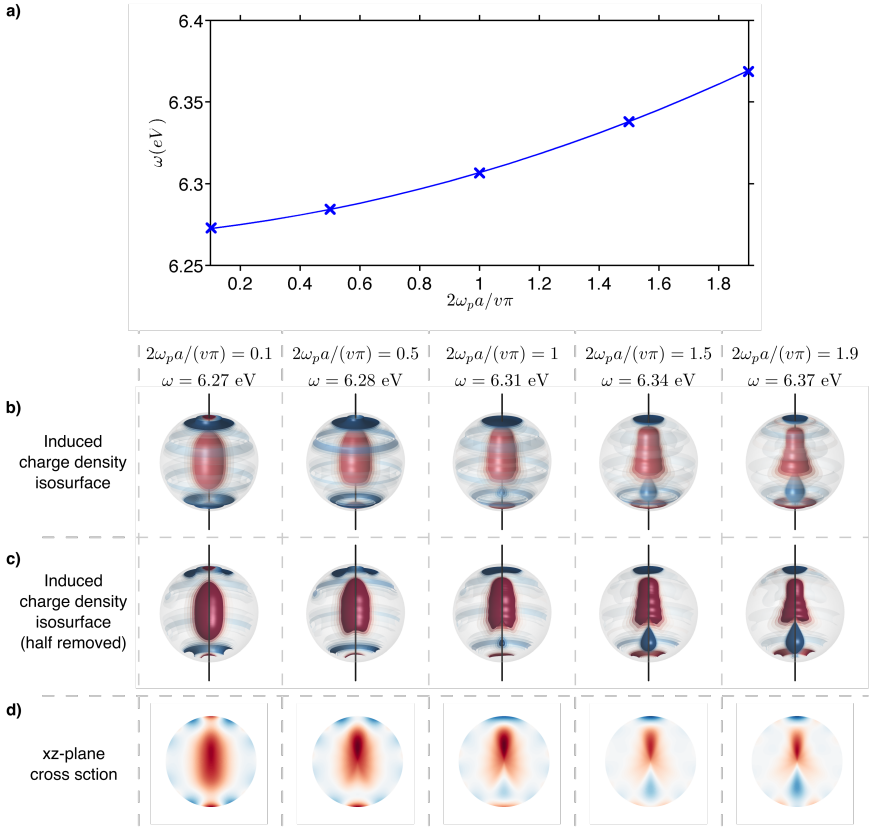

Figure 5.10: a) Energy of the main bulk plasmon peak showing a blueshift for increasing reduced radius $2\omega_p a/(v\pi)$ ofr a Na nanoparticle of radius $a = 1.5$ nm. b) Isosurfaces calculated for the induced charge density (red positive, blue negative) corresponding to the main CBPs excited for reduced radii $2\omega_p a/(v\pi) = 0.1, 0.5, 1, 1.5, 1.9$ marked as crosses in (a). c) Half of the isosurface has been removed to visualize the induced charge density inside the nanoparticle. d) 2D induced charge density maps in the xz-plane.

This means that the phase of the charge density is similar at the entry and exit points of the electron beam. We further analyze the dependence on the electron velocity v by keeping the size of the nanoparticle a untouched, so that the ratio between even and odd l modes changes due to dispersion effects without modifying their energy.

In Fig. 5.9(a) the EEL probability is plotted as a function of reduced radius $a^{\text{red}} = 2\omega_p a/v\pi$. The EEL probability has been multiplied by the square of the velocity in order to normalize the intensity, and the modes are labelled as (l, n). For small radii, $a^{\text{red}} \sim 0.1$ (large v, $E_k \sim$ keV) the LSP region of the spectra is dominated by even l modes (red circles), and the main CBP peak (black circles) corresponds to the $(0, 1)$ mode, as expected from the discussion in Sec. 5.3. For increasing a^{red} (decreasing v) well defined peaks emerge in the LSP region of the spectra due to the

activation of odd l modes (green circles). In this sense, the maximum intensity for each mode is approximately given by $2a\omega_l v^{-1} \simeq u\pi$ (u having the same parity as l). The frequency involved in this expression is the one corresponding to each mode ω_l, which due to dispersion can notably deviate from $\omega_{l,\mathrm{local}} = \sqrt{l/(2l+1)}\omega_p$ for LSPs, and therefore the velocity for which a maximum intensity can be achieved is different for each mode, i.e., different values of a^{red}, as shown in Fig. 5.9(a). This transition in the parity of the dominant modes is clearly observed for LSPs, with a complete domination of odd l modes for $a^{\mathrm{red}} = 1$. Additionally new peaks corresponding to CBPs emerge at higher energies, although the main bulk peak does not disappear. In fact one can observe a blueshift of ~ 0.1 eV for this peak from $a^{\mathrm{red}} = 0.1$ to $a^{\mathrm{red}} = 1.9$.

In order to understand this behavior and the underlying structure of the EEL spectra, Figs. 5.9(b-f) display the contributions of each l mode to the total energy loss probability for $a^{\mathrm{red}} = 0.1, 0.5, 1, 1.5, 1.9$. These plots show that for small a^{red} mainly even l CBP modes contribute to the spectra, as expected from the argument explained above, and that for increasing a^{red} odd l CBP modes are activated. Nevertheless, due to the large overlapping between the modes for $a^{\mathrm{red}} > 1$, the main peak is a mixture of modes (0,1) and (1,1), which results in an effective blueshift, as shown in Fig. 5.10(a).

The transition from the *pure* (0,1) mode to a mixture of (0,1) and (1,1) modes is further illustrated in Fig. 5.10(b-d), where we have plotted the induced charge density distributions corresponding to $a^{\mathrm{red}} = 0.1, 0.5, 1, 1.5, 1.9$.

The results presented in the previous section along with those presented in this section illustrate the possibility to address CBP excitations in small metallic NPs as probed by electron beams within a HDM. Interestingly, the high symmetry of the geometry allows for semi-analytical expressions that ease a straightforward characterization of the modes, and allows to gain insight of the interplay between different parameters, such as NP size, impact parameter and electron beam energy, on the EEL spectra. Thus, having such a tool at hand, in the next section we will make use of the HDM to gain insight of the CBPs observed for the *ab initio* atomistic simulations shown in Chapter 4.

5.5 CBPs within *ab initio* atomistic TDDFT

Taking advantage of the HDM analysis presented in this chapter for the interaction of fast electron beams with an electron gas confined to a sphere, we can get further insights into the nature of the CBPs by comparing these results with those from the *ab initio* atomistic simulations shown in Chapter 4. Such comparison is illustrated in Fig. 5.11. To observe the plasmonic excitations inside the NP, we remove a chunk (a quarter) of the isosurfaces corresponding to the modes of Fig. 4.8(a) for $b = 0$ nm

and $b = 0.5$ nm. In this way, the structure of the charge density inside the NP will be more clearly unveiled. The four CBP modes discussed in the previous chapter have a rich charge distribution. To analyze the CBP charge distributions we perform a parallel calculation of bulk modes within the HDM as described in Sec. 5.1 which serves now as a reference. The mode structure of the atomistic Na cluster is apparent in Fig. 5.11(a,b) for the nanocluster (TDDFT calculations) and in Figs. 5.11(c,d) for the spherical NP (HDM), where the cuts of the calculated charge distribution at the planes xy, xz and yz are shown to help for interpretation of the data.

As described in Secs. 5.2 and 5.3, the HDM provides semi-analytical expressions of the induced charge density for spherical nanoparticles expanded in spherical harmonics $Y_m^l(\Omega)$. The energy of the LSP (for $\omega < \omega_{\rm p}$) and CBP modes (for $\omega > \omega_{\rm p}$), is also addressed within the HDM, where $\omega_{\rm p}$ is the plasma frequency of the metal considered. This framework offers a clear and simple picture to identify the CBPs of the nanocluster studied in Chapter 4. The energies and charge distributions of the bulk modes of a spherical Na nanoparticle (radius a =1.85 nm) are obtained from Eqs. (5.7) and (5.8), and then compared with the TDDFT results for the nanocluster studied in Chapter 4. A bunch of modes is obtained for $\omega > \omega_{\rm p}$, for given (l, m) angular and azimuthal degrees of freedom of the charge distributions corresponding to radial oscillations of the charge density with different number of nodes. The HDM eigenmodes, labeled as (l, m, n) that best match the TDDFT results of Fig. 5.11(a,b) are displayed in Fig. 5.11(c,d). From this comparison we identify mode B1 as the HDM ($l = 0$, $m = 0$, $n = 1$) eigenmode, describing a breathing mode with an angular monopolar distribution and one radial node. Mode B2 is identified as the ($l = 1$, $m = 1$, $n = 1$) HDM eigenmode, i.e., a dipolar CBP mode with one radial node. Mode B3 corresponds to the ($l = 0$, $m = 0$, $n = 2$) HDM eigenmode, which is an angular monopolar CBP with two radial nodes. Last, mode B4 is identified as the ($l = 1$, $m = 1$, $n = 2$) HDM eigenmode, a dipolar CBP with two radial nodes.

Notice that for the atomistic cluster, shown in Fig. 5.11(a-c) the energy shown corresponds to the position of the spectral peak in Fig. 4.6(a), not to the energy of a particular mode (the charge density distributions are a superposition of different modes). In particular, the surface charge distribution of mode B3 represented in Fig. 4.8(a) shows a pattern closer to a quadrupolar distribution ($l = 2$, $m = 0$, $n = 1$), and thus contributions from that mode are probably present in the TDDFT results. In contrast, in the results of the HDM densities only the *actual* contributions of the pure individual modes are represented. Moreover, there is a general blueshift of the HDM modes with respect to the atomistic TDDFT resonances, which varies among different modes ($\omega_{010}^{\rm HDM} - \omega_{\rm B1}^{\rm TDDFT} = 0.59$ eV, $\omega_{111}^{\rm HDM} - \omega_{\rm B2}^{\rm TDDFT} = 0.38$ eV, $\omega_{020}^{\rm HDM} - \omega_{\rm B3}^{\rm TDDFT} = 0.11$ eV, $\omega_{121}^{\rm HDM} - \omega_{\rm B4}^{\rm TDDFT} = 0.11$ eV) and is more dramatic for the lowest B1 mode.

This large shift between CBP energies obtained for HDM and TDDFT is in part a consequence of the fundamental differences between both models: (i) on the one side, the HDM is a hard boundary closed box model for which the mode energies are systematically blueshift with decreasing NP size [83, 86, 95, 282, 283]; (ii) on the other hand, within TDDFT the plasmon modes are observed to redshift for alkali

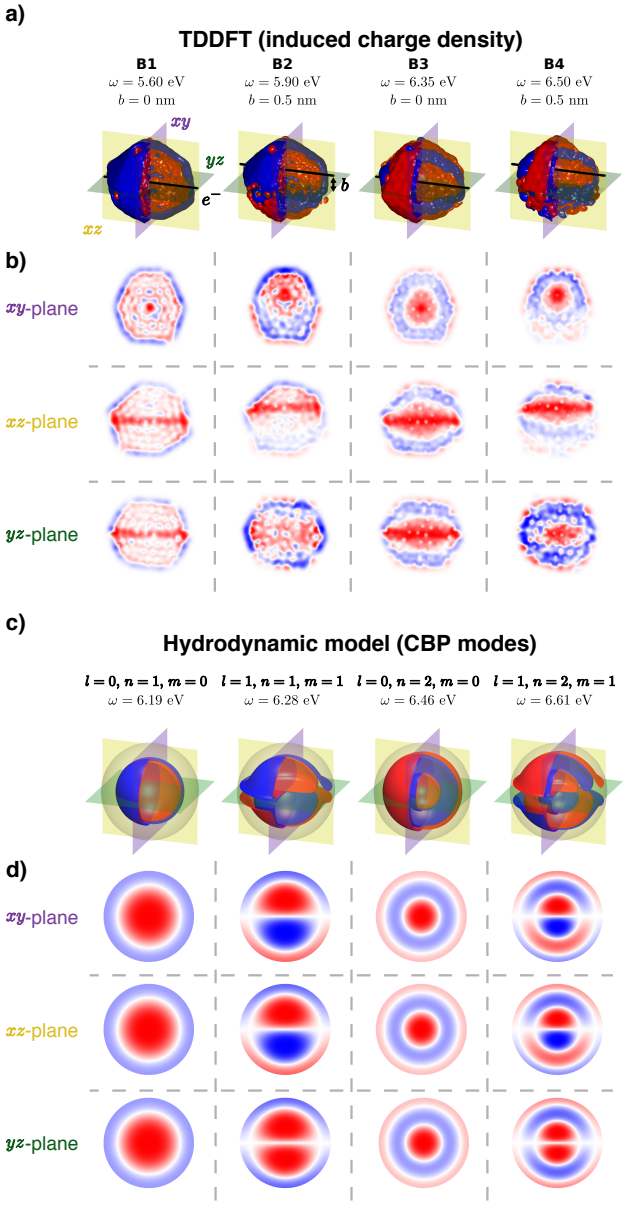

Figure 5.11: Comparison of bulk modes within TDDFT calculations and within the HDM. a) Isosurfaces of the charge density (with a quarter NP removed) for the different bulk modes excited for impact parameters $b = 0$ nm and $b = 0.5$ nm (EEL spectra in Fig. 4.6), and b) 2D charge density maps at the xy-, xz- and yz-planes. c) Isosurfaces of the eigenmodes in the absence of any perturbation, $l = 0$, $n = 1$, $m = 0$; $l = 0$, $n = 2$, $m = 0$; $l = 1$, $n = 1$, $m = 1$; and $l = 1$, $n = 2$, $m = 1$, obtained within the HDM for a spherical NP, and d) their corresponding charge distributions at the xy-, xz- and yz-planes.

metals such as Na for decreasing NP sizes due to the spill-out of electrons [31, 92], an effect not included in the HDM implemented here. Furthermore, although the HDM describes the confinement of the electron charge collective oscillations, both models consider different NP shapes, which may increase the energy mismatch of the plasmons, specially for the lowest order modes.

Moreover, the wake of the probing electron path through the nanoparticle is clearly observed in the TDDFT charge distribution maps, distorting the symmetry of the mode patterns with respect to those within the HDM. On the other hand, the excitation of the CBPs shows certain dependence on the orientation of the NP, although it is not as critical as for the LSPs. We have focused on a particular type of trajectory (facet) in this section, but similar results are obtained for different sets of trajectories (edge and vertex). Taking into account all these differences one can conclude that, albeit the HDM approach gives only qualitative values, it is a very useful tool to identify the symmetries of the CBPs obtained in the full quantum atomistic calculations.

5.6 Discussion and Summary

By using a hydrodynamic framework that neglects spill-out effects but incorporates dispersion effects, we have obtained an analytical expression for the mode dispersion in hard-bounded spherical nanoparticles, which showed two fundamental sets of modes: LSPs and CBPs. Using this approach we have derived an expression of the energy loss probability for both penetrating and external electron trajectories in spherical nanoparticles, and applied this approach to sodium nanoparticles.

We have calculated and analyzed the impact parameter dependence of the EEL probability spectra. The results show the sensitivity of CBPs to the impact parameter of the incoming electron beam trajectory, with an effective blueshift of the bulk peak for increasing impact parameters due to the excitation of higher order CBPs for penetrating trajectories close to the NP's surface, as experimentally observed in Al disks [85]. Moreover, we have studied the dependence of the EEL spectra on the electron beam velocity/energy, showing the relationship between the NP's size, mode energy and velocity. A comparison between the CBPs obtained within *ab initio* TDDFT and the HDM yields the characterization of the excited CBPs within TDDFT and their dependence on the impact parameter. Shifts already observed for different impact parameters in experiments [85, 102] are captured nicely within these models.

The BP peak in Al has recently been exploited to measure temperature in an active microelectronic device on the nanometer length scale [284] which emphasizes the importance of a full understanding of CBPs nature and excitation in nanostructures.

The HDM introduced in this chapter also provides a physical picture of the be-

grenzung effect for the CBPs. Moreover, the HDM can be extended to other metals such as silver, by including the d-band electrons as a background permittivity ε_∞, in a similar way to the local response approximation.

All in all, the HDM allows us to identify and analyze special CBPs in extremely small metallic nanoclusters, thus it serves as a very useful and adequate tool to explore atomic-scale nanoplasmonics.

Conclusions and outlook

The present thesis addresses theoretically the role of atomic-scale features in the plasmonic response of NPs as probed by light and swift electrons exploring the limits of light confinement. For this purpose, we have calculated the optical and electron energy loss spectra of such plasmonic nanostructures within atomistic *ab initio* and classical electrodynamics frameworks, in order to address the accuracy and limitations of the latter. After a brief introduction to the field of nanoplasmonics, and to the different theoretical approaches and numerical tools used in our calculations, we have addressed the optical response of plasmonic nanostructures in the first part (Chapters 2 and 3) and the signatures of atomistic features and electron confinement in Na nanoparticles in the second part (Chapters 3 and 4). We now summarize our results together with some of the possible future directions:

- In Chapter 2 we described the optical response of Na clusters composed by 380 atoms and nanogaps as canonical systems that contain atomic-scale features, with special focus on the extreme subnanometric localization of light associated with them, within three different models to describe the atomic-scale boundaries: *i*) an atomistic *ab initio* quantum model based on TDDFT, *ii*) an atomistic classical model based on the DDA, and *iii*) a continuous classical model based on the BEM. We observed that the presence of such atomistic fea-

tures allows for localizing and confining the near field down to subnanometric dimensions, well below the underlying plasmonic background, going therefore beyond nanocavities and thus reaching the realm of *picocavities*. The extra localization of the EM field is identified as a non-resonant atomic-scale lightning rod effect enhancing the plasmon-driven near field. Based on this study a simplified local model is proposed to address this effect. The good match as obtained from the full atomistic TDDFT results and the classical BEM results to address the optical response and light confinement on the nanogaps between two Na clusters in the non-tunnelling regime allows for the use of standard methods of electrodynamics approaches to address this challenging regime.

- In Chapter 3 we discussed the emergence of spectral flares in time-dependent molecular SERS experiments performed in Au NPoM plasmonic structures. We linked the appearance of these spectral flares to dynamical local changes in the metallic structure of the NP that temporarily produce larger field enhancements within the metal, producing a larger field in it and therefore a temporary increase in ERS emission, which would be observed as flares of the background signal in SERS. We propose an effective local plasma frequency model to address the influence of such structural inhomogeneities on the field penetration into the metal, and consequently on ERS emission. Moreover, this effective model provides us with a qualitative framework to understand the patterns experimentally observed for spectral flares, although further sophistication of theoretical methods might be needed to fully unveil the underlying microscopic origin of the inhomogeneities. Thus, this model could be considered as an initial stepping stone in the path to a more sophisticated theory that fully explains the spectral flares in SERS spectra.

The second part of this thesis is devoted to the plasmonic excitations induced by electron probes in nanoparticles using the same canonical Na cluster of Chapter 2.

- In Chapter 4 we explored the influence of atomistic features of nanometer-scale Na atomistic clusters on the EEL spectra within an atomistic *ab initio* framework TDDFT framework, which naturally includes the effects related to the quantum nature of electrons. We expose the different plasmonic response of these atomistic NPs as compared to perfect spherical NPs, and unveil the effects that the orientation and impact parameter of the electron beam have on the low energy EEL spectra associated to the different nature of LSP and CBP excitations in such atomistic NPs showing crystallographic facets. In order to gain insight into the influence of the NPs atomistic shape on the EEL spectra, we use two classical dielectric models of the NP, adapted to the icosahedral shape of the atomistic distribution and the electronic landscape of the nanocluster, showing that classical electrodynamics frameworks can accurately capture the influence of atomic-scale features in NPs on the LSP excitation by electron beams if an appropriate NP shape is considered. Nevertheless, we also conclude that classical continuous models are not able to reproduce at the same

level the spectral features associated to the CBP excitations provided by the TDDFT calculations for the electron trajectories penetrating the NPs.

- In order to gain insight into the physical description of these electron excitations we explored a non-local model of the electron gas participating in these collective excitations. Chapter 5 focused on a hydrodynamic model to describe the interaction of swift electrons and small spherical metallic NPs with abrupt boundaries. Within this framework we obtained a general semi-analytical expression for the EEL probability valid also for penetrating trajectories. Although non-local effects in the optical response of metallic NPs have been addressed in the literature, less attention has been paid to these effects in the interaction with electrons. We paid special attention to the role of confinement in such small NPs, which gives rise to longitudinal standing plasma waves along the radial direction of the NPs, appearing as additional peaks in the spectrum above the bulk plasmon energy. We characterized their dependence with the electron probe impact parameter, demonstrating that their excitation obeys similar symmetry arguments to those ruling the excitation of LSPs in spherical NPs. In this regard, we also explored the influence of the electron beam velocity on the excitation of CBPs, which supported the aforementioned symmetry arguments. The semi-analytical expression obtained for the EEL probability allowed us to characterize the CBPs excited within an atomistic *ab initio* TDDFT model used in Chapter 4, proving to be a useful tool to explore atomic-scale nanoplasmonics.

Nanoplasmonics at the atomic scale has plenty to offer, and opens a wide range of opportunities for future research and applications in extreme Nanophotonics. The topics discussed in this thesis and the results obtained might serve as milestones on the way to uncover novel physical and chemical phenomena as well as to apply those processes into the development of new devices.

Appendices

A Near field of an oblate spheroidal protrusion

The expression to address the atomic-scale lightning rod effect given in Chapter 2 is obtained by considering the atomic bump to be an oblate spheroid. Here we calculate the field enhancement proceeding in a similar fashion as in Ref. [285] where it is calculated for prolate spheroids. We employ the oblate spheroidal coordinates (ξ, η, φ), which are defined as,

$$x = d\sqrt{(1+\xi^2)(1-\eta^2)}\cos(\varphi) \tag{A.1}$$

$$y = d\sqrt{(1+\xi^2)(1-\eta^2)}\sin(\varphi) \tag{A.2}$$

$$z = d\,\xi\,\eta \tag{A.3}$$

where the coordinate η is restricted by $0 \leq \xi < \infty$, and η is restricted by $-1 \leq \eta < 1$, and $d = b^2 - a^2$ (a and b are the equatorial and polar radii, respectively, plotted in Figure 4(f)). Solving Poisson's equation, the potential is given by:

$$\begin{aligned}\phi &= \begin{cases} A\,P_1^0(\eta)P_1^0(i\xi), & \xi < \xi_0 \\ B\,P_1^0(\eta)Q_1^0(i\xi) - E_{\mathrm{bp}}d\,\xi\,\eta, & \xi > \xi_0 \end{cases} \\ &= \begin{cases} iA\,\eta\,\xi, & \xi < \xi_0 \\ B\,\eta\,Q_1^0(i\xi) - E_{\mathrm{bp}}d\,\xi\,\eta, & \xi > \xi_0 \end{cases} \end{aligned} \tag{A.4}$$

where,

$$A = iE_{\mathrm{bp}}d\left(1 - \frac{Q_1^0(i\xi_0)(\varepsilon-1)\xi_0}{\varepsilon Q_1^0(i\xi_0) - i\xi_0 Q_1^{0\prime}(i\xi_0)}\right),$$
$$B = \frac{E_{\mathrm{bp}}d(\varepsilon-1)\xi_0}{\varepsilon Q_1^0(i\xi_0) - i\xi_0 Q_1^{0\prime}(i\xi_0)}.$$

$P_1^0(x)$ and $Q_1^0(x)$ are the first- and second-kind Legendre functions, $\xi_0 = \frac{a}{\sqrt{a^2-b^2}}$, and ε is the dielectric function of the material inside the spheroid. The field along the z-axis, $x = 0$, $y = 0$, outside the spheroid is given by:

$$E = \left(1 - \frac{(\varepsilon-1)i\xi_0 Q_1^{0\prime}(i\xi)}{\varepsilon Q_1^0(i\xi_0) - i\xi_0 Q_1^{0\prime}(i\xi_0)}\right)E_{\mathrm{bp}}. \tag{A.5}$$

Considering the spheroidal bump to be metallic for the studied wavelengths, thus $\varepsilon << 1$, we can approximate the field enhancement at $z = a$ ($\xi = \xi_0$) to be:

$$\frac{E}{E_{\mathrm{bp}}} = 1 - \frac{i\xi_0 Q_1^{0\prime}(i\xi_0)}{Q_1^0(i\xi_0)}, \tag{A.6}$$

where the second-kind Legendre functions are defined as [286]:

$$Q_1^0(i\xi) = -1 + i\xi \mathrm{atanh}\left(\frac{1}{i\xi}\right), \tag{A.7}$$

$$Q_1^{0\prime}(i\xi) = \mathrm{atanh}\left(\frac{1}{i\xi}\right) + \frac{i\xi}{1+\xi^2} \tag{A.8}$$

Using these definitions, after some algebra, we reach the following expression:

$$\frac{E}{E_{\mathrm{bp}}} = \frac{-1}{(1+\xi_0^2)\left[-1 + i\xi_0 \,\mathrm{atanh}\left(\frac{1}{i\xi_0}\right)\right]}, \tag{A.9}$$

which can be simplified to the expression:

$$\frac{E}{E_{\mathrm{bp}}} = \frac{\sin^2 t}{1 - \frac{t}{\tan t}}, \tag{A.10}$$

using $\mathrm{atanh}(z) = \frac{1}{i}\mathrm{atan}(iz)$, and $a/b = \cos t$, [$\xi_0 = 1/\tan t$].

B Flares with laser + white light illumination

To investigate what happens during flares, in addition to laser excitation the system is simultaneously irradiated with broadband incoherent white-light and the ℓ_1 mode peak observed in real time from the elastic scattering (Fig. B.1). A typical flare event recorded in this way is shown in Fig. B.1(a). The higher-wavelength Raman modes of the BPT spacer molecule are visible as well as the tails of the flare events, giving the time of occurrence. The ℓ_1 mode (ℓ_1) is also observed, which matches the spectrum measured on the dark-field spectrometer at the start of the experiment (dashed red line). The ℓ_1 mode stays almost unperturbed before and after the flare (dashed grey line shows average value), however when a flare happens there is a small but instantaneous red-shift of the ℓ_1 mode and an overall increase in the intensity, before returning to the initial position and intensity of the mode. Red-shifts to the ℓ_1 at the exact time of the flare event evidence structural changes in the NPoM that, nevertheless, are reversible (opposed to processes that cause permanent damage), which suggest metastable changes, or that they are fleeting in the vicinity of the plasmonic hot-spot. Laser irradiation without white light shows no plasmonic ℓ_1 mode in Fig. B.1(b), as expected. On the other hand, illumination with white-light but no laser irradiation [Fig. B.1(c)] shows stable ℓ_1 modes and no flares.

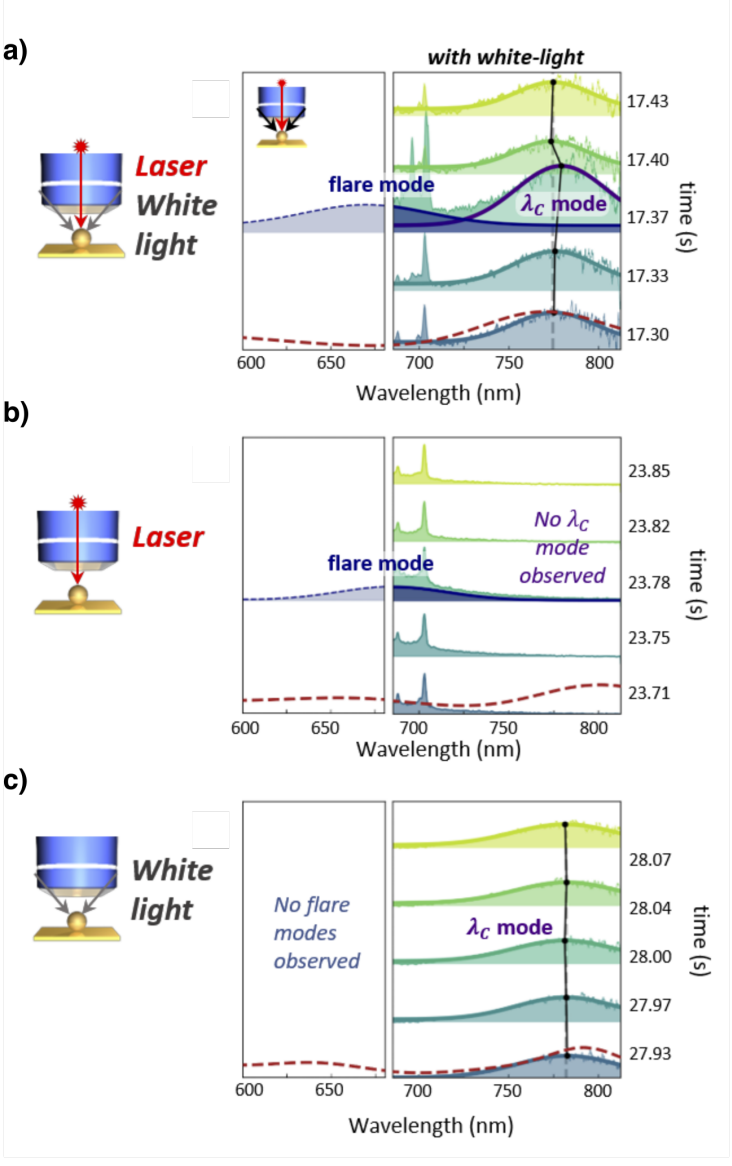

Figure B.1: a) When the system is illuminated with both incoherent white light and 633 nm laser, both ℓ_1 mode (ℓ_1) and flare modes can be observed. Left panel shows flare fit. b) Illumination with laser only enables observation of flare modes, but no coupled is visible (red dashed line shows ℓ_1 mode measured with dark- field spectrometer, measured prior to kinetic series). c) Conversely when illuminating solely with a white light, only the ℓ_1 mode is visible. Experimental measurements from Cloudy Carnegie at Cambridge University. Figure adapted from [218].

C Model for the increase in SERS background

For the nanogap without any change in plasma frequency ω_p, at the metal-insulator interface ($z = 0$) we have (omitting reference to the component $\perp$ in the notation),

$$\varepsilon_{\mathrm{m}}(\omega_p^0)E_{\mathrm{m}}^0 = \varepsilon_{\mathrm{g}}E_{\mathrm{g}} \Rightarrow \eta(\omega_p^0) = \left|\frac{E_{\mathrm{m}}^0}{E_{\mathrm{g}}}\right| = \left|\frac{\varepsilon_{\mathrm{g}}}{\varepsilon_{\mathrm{m}}(\omega_p^0)}\right| \tag{C.1}$$

The field inside the metal is thus given by,

$$E_{\mathrm{m}}^0(z) = E_{\mathrm{g}}\eta(\omega_p^0)e^{-z/\delta^0} \tag{C.2}$$

where δ^0 is the skin depth of the field within the metal. The ERS is proportional to the the 4th power of the field inside the metal. If we integrate the field for a cylinder of radius a, assuming the field to be invariant in the direction parallel to the gap

$$\begin{aligned} I_{\mathrm{fl}}^0 &\propto \int_0^{2\pi} d\varphi \int_0^a r\,dr \int_0^\infty dz |E_m^0(z)|^4 \\ &\propto \pi a^2 |E_{\mathrm{g}}|^4 [\eta(\omega_p^0)]^4 \int_0^\infty dz\, e^{-4z/\delta^0} \qquad \text{(C.3)} \\ &\propto \frac{\pi}{4} a^2 |E_{\mathrm{g}}|^4 [\eta(\omega_p^0)]^4 \delta^0. \qquad \text{(C.4)} \end{aligned}$$

Now, if we calculate the same for the patch, at the metal-insulator interface we have,

$$\varepsilon_{\rm m}(\omega_p)E_{\rm m}(0) = \varepsilon_{\rm g}E'_{\rm g} \Rightarrow \eta(\omega_p) = \left|\frac{E_{\rm m}(0)}{E'_{\rm g}}\right| = \left|\frac{\varepsilon_{\rm g}}{\varepsilon_{\rm m}(\omega_p)}\right| \tag{C.5}$$

The field inside the patch is therefore,

$$E_{\rm m}(z) = E'_{\rm g}\eta(\omega_p)e^{-z/\delta}. \tag{C.6}$$

At the metal-metal interface (ω_p - ω_p^0 interface), at $z = c$

$$\varepsilon_{\rm m}(\omega_p)E_{\rm m}(c) = \varepsilon_{\rm m}(\omega_p^0)E^0_{\rm m}(c) \Rightarrow \eta'(\omega_p) = \left|\frac{E^0_{\rm m}(c)}{E_{\rm m}(c)}\right| = \left|\frac{\varepsilon_{\rm m}(\omega_p)}{\varepsilon_{\rm m}(\omega_p^0)}\right| \tag{C.7}$$

and the field inside the metal is thus,

$$\begin{aligned} E^0_{\rm m}(z) = E_{\rm m}(c)\eta'(\omega_p)e^{-(z-c)/\delta^0} &= E'_{\rm g}\eta(\omega_p)\eta'(\omega_p)e^{-c/(\delta}e^{-(z-c)/\delta^0} \\ &= E'_{\rm g}\eta(\omega_p)\eta'(\omega_p)e^{c\frac{\delta-\delta^0}{\delta\delta^0}}e^{-z/\delta^0} \end{aligned} \tag{C.8}$$

Again, integrating over a cylinder of radius a we obtain,

$$\begin{aligned} I_{\rm fl} &\propto \frac{\pi}{4}a^2|E'_{\rm g}|^4[\eta(\omega_p)]^4\left\{\delta[1-e^{-4c/\delta}] + [\eta'(\omega_p)]^4e^{4c\frac{\delta-\delta^0}{\delta\delta^0}}\delta_0 e^{-4c/\delta^0}\right\} \\ &\propto \frac{\pi}{4}a^2|E'_{\rm g}|^4[\eta(\omega_p)]^4\delta\left\{[1-e^{-4c/\delta}] + [\eta'(\omega_p)]^5e^{-4c/\delta}\right\}. \end{aligned} \tag{C.9}$$

where we have used $\delta \propto 1/\varepsilon_{\rm m}$ in the last line. Considering that $\delta \sim 5$ nm for Au at optical frequencies, we can neglect the exponentials for $c \sim \delta/5 \sim 1$ nm, and finally,

$$I_{\rm fl} \propto \frac{\pi}{4}a^2\delta|E'_{\rm g}|^4[\eta(\omega_p)]^4.$$

If we assume that the Poynting is conserved for MIM plasmons propagating in the gap, $|E_{\rm g}|^2k_{\|}$ is conserved which leads to field enhancements within the dielectric material at the center of the facet of $E_{\rm g} \propto \sqrt{e}$. If we now consider the whole facet, the increase in the ERS background due to a defect of reduced $\omega_{\rm p}$ is given by,

$$\begin{aligned} \frac{I_{\rm fl}}{I_{\rm bgd}} &= \frac{a^2\frac{1}{e'}(e'\sqrt{e'})^4 + [(\frac{w}{2})^2 - a^2] + \frac{1}{e}(e\sqrt{e'})^4}{(\frac{w}{2})^2\frac{1}{e}(e\sqrt{e})^4} \\ &= \frac{a^2e'^5 + [(\frac{w}{2})^2 - a^2] + e^3e'^2}{(\frac{w}{2})^2e^5} \end{aligned} \tag{C.10}$$

where $e \equiv e(\omega_p)$ and $e' \equiv e(\omega_p - \Delta\omega_p)$. Taking into account that $e'^3 \gg e^3$ we can neglect the second term and only take into account the ERS coming from the region with reduced ω_p, which leaves,

$$\frac{I_{\rm fl}}{I_{\rm bgd}} = \left(\frac{2a}{w}\right)^2\frac{e}{e'}\left(\frac{e'\sqrt{e'}}{e\sqrt{e}}\right)^4. \tag{C.11}$$

D Effective plasma model for antenna mode shift

Here we adopt quantum mechanical notation to calculate the first-order correction given by a perturbation method for a $\hat{H} = \hat{H}_0 + \lambda\hat{V}$, where $\hat{V}$ is the perturbation and λ a small parameter. The unperturbed Hamiltonian gives,

$$\hat{H}_0 \left|n^{(0)}\right\rangle = E_n^{(0)} \left|n^{(0)}\right\rangle \tag{D.1}$$

The first-order correction to the energy is given by

$$E_n^{(1)} = \langle n^{(0)}|\hat{V}|n^{(0)}\rangle \,. \tag{D.2}$$

The MIM dispersion relation tells us that this energy is proportional to the plasma frequency ω_p for fixed facet widths w. We will assume that for a finite MIM structure the energy of the lowest mode is given by

$$E_1^{(0)} = \omega_{\mathrm{C}} \tag{D.3}$$

We will also consider the potential that holds the modes confined to the cavity is proportional to the *local* plasma frequency $V(r) \propto \omega_p(r)$, which for the unperturbed cavity is $\omega_p(r) = \omega_p^0$, and for the perturbed cavity $\omega_p(r) = \omega_p^0 - \Theta(a - r)\Delta\omega_p$

Therefore, the frequency shift of the perturbation is given by,

$$-\frac{\delta\lambda}{\lambda_C} = \frac{\delta\omega}{\omega_C} = \frac{E_1^{(1)}}{E_1^{(0)}} = \frac{1}{2}\frac{\int_0^{w/2} r\,dr|\psi(r)|^2[-\Theta(a-r)\Delta\omega_p]}{\int_0^{w/2} r\,dr|\psi(r)|^2\omega_p^0}$$
$$= -\frac{1}{2}\frac{\Delta\omega_p}{\omega_p^0}\frac{\int_0^a r\,drI(r)}{\int_0^{w/2} r\,drI(r)} \tag{D.4}$$

where the prefactor of a half comes from our placement of the perturbed patch on only one metal surface of the MIM cavity. We now can use the Gaussian intensity distribution of the lowest mode, with a full width at half maximum (FWHM):

$$\Delta x = \sqrt{2Rd/\varepsilon_g}. \tag{D.5}$$

Therefore, if $\Delta x = \text{FWHM}$, we have

$$I(r) \sim e^{-4\ln 2\frac{r^2}{(\Delta x)^2}}. \tag{D.6}$$

Therefore

$$\frac{\delta\lambda}{\lambda_C} = \frac{1}{2}\frac{\Delta\omega_p}{\omega_p^0}\frac{\int_0^a r\,dr\exp\left\{-4\ln 2\frac{r^2}{(\Delta x)^2}\right\}}{\int_0^{w/2} r\,dr\exp\left\{-4\ln 2\frac{r^2}{(\Delta x)^2}\right\}} \tag{D.7}$$

$$= \frac{1}{2}\frac{\Delta\omega_p}{\omega_p^0}\frac{1-\exp\left\{-4\ln 2\frac{a^2\varepsilon_g}{2Rd}\right\}}{1-\exp\left\{-4\ln 2\frac{w^2\varepsilon_g}{8Rd}\right\}} \tag{D.8}$$

$$\sim \frac{1}{2}\frac{\Delta\omega_p}{\omega_p^0}\left\{1-\exp\left(-4\ln 2\frac{a^2\varepsilon_g}{2Rd}\right)\right\} \tag{D.9}$$

E Induced potential within the Hydrodynamic Model

The calculation of EEL probability in Chapter 5 requires the calculation of the induced potential at the position of the electron. One has $z = \sqrt{r^2 - b^2}$ for $z > 0$ and $z = -\sqrt{r^2 - b^2}$ for $z < 0$, i.e. $z = \frac{z}{|z|} r$, which allows to express the induced potential as,

$$\phi(\mathbf{r}) = \sum_{l=0}^{\infty} \sum_{m=-l}^{l} \alpha_{lm} \left(\frac{z}{|z|} \right)^{l+m} P_l^m(\sqrt{1 - b^2/r^2}) e^{im\varphi} \phi_{lm}(r) \tag{E.1}$$

taking into account that $Y_l^m(\Omega) = \alpha_{lm} P_l^m(z/r) e^{im\varphi}$ and $P_l^m(-x) = (-1)^{l+m} P_l^m(x)$, where α_{lm} is defined by Eq. (5.17), $P_l^m(x)$ is the associated Legendre polynomial of degree l and order m, and $\phi_{lm}(r)$ is the radial component of the induced potential defined by Eq. (5.34). Furthermore, separating the cases $r < a$ and $r > a$, for $r < a$

yields,

$$\begin{aligned}\phi^i_{lm}(r) = \frac{4\pi}{2l+1}\frac{2\omega_p^2}{v}\alpha_{lm}\Bigg\{\Bigg[\frac{l+1}{a^{l+2}\mu}\left(1+\frac{\omega_p^2}{\mu^2\beta^2}\right)\mathcal{E}^i_{lm} - \frac{l\,a^{l-1}}{\mu}\mathcal{E}^o_{lm} \\ + \frac{2l+1}{\beta^2}\Big(N_l\mathcal{I}^j_{lm}(b,a) - M_l\mathcal{I}^y_{lm}(b,a)\Big)\Bigg]\frac{j_l(\mu r)}{\mu M_l} \\ + \Bigg[-\frac{(l+1)j_{l-1}(\mu a)}{(2l+1)a^{2l+1}\mu M_l}\left(1+\frac{\omega_p^2}{\mu^2\beta^2}\right)\mathcal{E}^i_{lm} + \frac{l j_{l-1}(\mu a)}{(2l+1)\mu M_l}\mathcal{E}^o_{lm} \\ + \frac{l+1}{a^{l+2}\mu^2 M_l}\left(1+\frac{\omega_p^2}{\beta^2\mu^2}\right)\mathcal{I}^j_{lm}(b,a) - \frac{1}{\mu^2\beta^2}\mathcal{E}^i_{lm}\Bigg]r^l \\ - \frac{1}{\beta^2}\Theta\Big(\frac{r}{b}-1\Big)\Bigg[\frac{2l+1}{\mu}y_l(\mu r)\mathcal{I}^j_{lm}(b,r) - \frac{2l+1}{\mu}j_l(\mu r)\mathcal{I}^y_{lm}(b,r) \\ + \frac{1}{r^{l+1}\mu^2}\int_b^r dr' r'^l\frac{\Pi_{lm}(r',b;\omega)}{\sqrt{1-b^2/r'^2}} - \frac{r^l}{\mu^2}\int_b^r\frac{dr'}{r'^{l+1}}\frac{\Pi_{lm}(r',b;\omega)}{\sqrt{1-b^2/r'^2}}\Bigg]\Bigg\} \qquad \text{(E.2)}\end{aligned}$$

and for $r > a$,

$$\begin{aligned}\phi^o_{lm}(r) = \frac{4\pi}{2l+1}\frac{2\omega_p^2\alpha_{lm}}{v}\frac{1}{r^{l+1}}\Bigg\{\frac{l}{(2l+1)}\frac{j_{l-1}(\mu a)}{\mu M_l}\mathcal{E}^i_{lm} \\ - \frac{l\,a^{2l+1}j_{l+1}(\mu a)}{(2l+1)\mu M_l}\mathcal{E}^o_{lm} - \frac{l\,a^{l-1}}{\mu^2 M_l}\mathcal{I}^j_{lm}(b,a)\Bigg\}. \qquad \text{(E.3)}\end{aligned}$$

where $\mathcal{E}^i_{lm}(x)$ and $\mathcal{E}^o_{lm}(x)$ are defined by Eqs. (5.30) and (5.31) respectively, $\mathcal{I}^j_{lm}(x_1,x_2)$ and $\mathcal{I}^y_{lm}(x_1,x_2)$ are defined by Eq. (5.32), $\Pi_{lm}(x)$ is defined by Eq. (5.18), and M_l and N_l are defined by Eqs. (5.29) and (5.48) respectively.

Laburpena

Antzinako istorio batek dioenez, K.a. 214-212 urteen arteko egun eguzkitsu batean, alegia, erromatarren eta kartagoarren arteko Bigarren Gerra Puniko betean, Sirakusa erasotzen ari ziren erromatarren ontziei su eman zien Arkimedesek. Izan ere, ispiluekin berak sortutako tramankulu batez baliatuz eguzki-argia islatu eta ontziei su eman omen zien. Tamalez, Arkimedesen bizitzari buruz informazio gutxi iritsi zaigu gaur egundaino, eta gertaera hauen egiazkotasuna askotan jarri izan da zalantzan [287]. Fikziozko ipuina izan, ala antzinako historiaren pasartea izan, argia lokalizatzearen ideiak historian zehar onuragarri izan diren hainbat gailu eta tresna sortzea eragin du, horren dramatikoak ez diren aplikazioetarako izan bada ere. Aipatzekoa da argiaren lokalizazioaren erabilera bestela bereizezin liratekeen objektu urrunak edo txikiak bistaratzeko. Izan ere, gure ikusmen-gaitasuna hobetzea hobekuntza teknologiko eta aurkikuntza zientifiko askoren oinarria da. Adibidez, luparen, eta bereziki, lehen mikroskopio optikoen agerpenak, XVI. eta XVII. mendeetan bultzada nabarmena eman zien biologiari eta medikuntzari, gaur egundaino gizartearen bizi-kalitatea hobetuz.

Argi ikusgaia eta infragorria oso erabiliak dira irudiak sortzeko eta mikroskopia optikoko beste hainbat teknikarako, nahiz eta argiaren uhin-luzeraren tamaina bera edo handiagoa duten xehetasunak soilik bereiz daitezkeen modu honetan, alegia,

difrakzio-muga deritzona pairatzen dute ohiko sistema optikoek tradizionalek [2]. Argiaren uhin-luzera baino txikiagoak diren objektuak behatu ahal izateko, argia bere uhin-luzera baino txikiagoa den espazioan konfinatu dezaketen tekniken beharra dugu. Hain zuzen ere, nanoeskalan argiaren eta materiaren arteko elkarrekintzaren ondorioz, argiaren lokalizazioa lor daiteke eskala honetan. Elkarrekintza berezi hori aztertzeaz eta deskribatzeaz arduratzen den Fisikaren arloari *Nanofotonika* deritzo [3].

Argiaren uhin-luzera azpiko konfinamendua gainazaleko plasmoi polaritoien (ingelesez *surface plasmon polariton*, SPP) bidez erdietsi daiteke, hots, metal/dielektriko-gainazaletan kitzikatzen diren elektroi-dentsitatearen uhin erresonanteen bidez. SPPak metaleko banda eroaleko elektroien oszilazioen, alegia, gainazaleko plasmoien (ingelesez *surface plasmon*), eta maiztasun ikusgai eta infragorriko uhin elektromagnetiko (EM) erasotzaileen arteko hibridazioaren ondorio dira. Metaleko elektroiek kanpoko eremu elektromagnetikoen aurrean duten portaera konplexutasun maila ezberdinekin aztertzen dira *Nanoplasmonika* arloan. Adibidez, Drude-ren eredua deritzonean, metalaren eroapen-banda elektroien erantzuna elektroi askeen gas baten gisa deskribatzen da. Bere sinpletasuna gorabehera, hurbilketa hau oso erabilia da nanofotonikan, zehaztasun handiz deskribatzen baitu elektroien erantzuna d-bandako kitzikapen-energia baino baxuagoak diren energietan, metalen espektroskopia optikoan behatzen diren ezaugarri nagusiak ulertzeko aukera emanez.

Metal/dielektriko-gainazal lauetan hedatzen diren SPPek nanometro gutxi batzuetan konfinatu dezakete eremu elektrikoa gainazalarekiko normala den norabidean. Nahiz eta SPPak geometria lau guztiz perfektuan ez zaizkion argiari akoplatzen SPPen eta argiaren momentuak bat ez datozela eta [5, 6], estrategia ezberdinak proposatu izan dira arazo honi aurre egiteko. Besteak beste, ekorketako hurbileko eremuko mikroskopia optikoan (ingelesez *scanning near-field optical microscopy*, SNOM) punta metaliko zorrotz bat jartzen da gainazal metalikoaren gainean [7]. Molekula fluoreszenteak gainazal metalikotik gertu kokatzean datza beste teknika bat [8, 9]. Hauez gain, momentuen arteko tartea gainditzeko eta SPPak kitzikatzeko ohiko irtenbidea ohi da gainazal metalikoan patroi-sareak sortzea teknika litografikoen bidez [10, 11].

SPPak metal/dielektriko-gainazal batean hedatzen diren bitartean, gainazaleko plasmoi lokalizatuak (ingelesez *localized surface plasmon*, LSP) nanopartikula txikietan konfinatuta daude eta zuzenean argiztatuta kitzika daitezke. Kasu honetan SPP eta argiaren arteko momentuaren tartea gainditzeko behar den momentu gehigarria nanopartikularen geometria finituak ematen du. Argipean, nanopartikula esferiko txikiek erresonantzia plasmoniko bat erakusten dute, NP esferikoen plasmoi dipolarrari (ingelesez *dipolar plasmon*, DP) dagokiona. Argiztapenaren maiztasunarekin erresonantzian dagoen elektroi-hodeiak denboran oszilatzen du, patroi dipolarrari segiz, eta kitzikapen-eremu elektromagnetikoarekiko $\pi/2$-ko desfasearekin. Honek eremuaren handitze nabarmena dakar eta eremu hurbilaren lokalizazioa eragiten du nanopartikularen inguruan. Fenomeno hau oso interesgarria da, argiztapenaren uhin-luzera baino askoz txikiagoa den eskualde

batean lokalizatzen baita eremua. Gainera, plasmoi-erresonantzien maiztasuna NPren tamaina, eitea, material eta ingurunearen araberakoa da [12–15], eta honek oso erabilgarri bihurtzen ditu nanopartikulak erantzun optiko zehatza duten nanogailu sentikorrak diseinatzeko. Horrez gain, SPPek eta LSPek sorturiko eremu hain lokalizatuak argiaren eta nanoegitura metalikoen inguruko materiaren arteko elkarrekintza areagotzeko erabil daitezke [16, 17], bestela ezinezkoa gertatuko litzatekeena.

Nanopartikula plasmonikoek, argia eremu hurbilean lokalizatzeko duten gaitasunaz gain, argia eremu urrunera sakabanatzeko duten gaitasuna dela eta, nanoantena optikotzat jotzen dira. Nanoantena hauen tamaina nanometro gutxi batzuetatik ehunka nanometrorainokoa izan daiteke. Azken urteotan, Plasmonikaren erronka ugarietako bat nanopartikulen fabrikazioaren kontrol zehatza izan da, honek ezartzen baititu nanopartikularen eitea, konposaketa eta substratu gaineko posizioa. Izan ere, fabrikazio-teknika berrien hobekuntzak eta esplorazioak ahalegin eta arreta handia jaso dute azken hamarkadetan, punta-puntako zehaztasuna emanez goitik beherako fabrikazio metodoei (ingelesez *top-down fabrication*) [19–21], eta moldakortasun handia behetik gorako fabrikazio metodoei (ingelesez *bottom-up fabrication*) [22–24].

Nanoegitura plasmonikoen kontrola nanofotonikaren muina da, hein handi batean eremu hurbilak metal/dielektriko-gainazalaren geometriarekiko duen menpekotasun handiagatik. Izan ere, argiztapena plasmoiarekiko erresonantziaz kanpo egonik ere, nanoegitura batek eremuaren handitze ez-erresonantea erakutsi dezake metalezko punta zorrotzetan edo nanopartikulek izan ditzaketen erpinetan. Fenomeno hau, tximistorratz efektu (ingelesez *lightning rod effect*, LRE) izenez ezaguna elektrostatikan, metalezko ertz zorrotzetan pilatzen den karga dela eta gertatzen da. Hau da, lerro ekipotentzialak elkarrengandik gertuago daude geometria zorrotzetan, eta horrek eremu elektromagnetiko handiagoak inplikatzen ditu halako eskualdeetan [2]. Adibidez, tximistorratz efektua, erresonantzia plasmonikoek sorturiko eremuaren konfinamenduarekin batera, sakabanatze-motako ekorketako hurbileko eremuko mikroskopio optikoan (ingelesez *scattering-type scanning near-field optical microscope*, s-SNOM) baliatzen da.

Bestalde, elkarrengandik gertu dauden nanoegitura metalikoetan kitzikatutako plasmoien akoplamendua baliatuz, Coulomb elkarrekintza dela eta, eremu elektromagnetikoaren handitze eta lokalizazio are handiagoak lor daitezke nanoegituren arteko hutsarteetan. Izan ere, ~ 1 nm edo txikiagoak diren hutsarteek "puntu-bero" (ingelesez *hot-spot*) deritzenak azaltzen dituzte, alegia, alboko nanoegituretan kitzikatutako plasmoien akoplamenduak are gehiago handitzen du eremua nanoegituren arteko hutsarteetan. Halako egituren (tartean *dimero* deritzen bi nanopartikulez osatutako egiturak) erantzun optikoak menpekotasun handia du hutsartearen luzera eta morfologiarekiko, espektro-sentikortasun handiko plataforma bat eskainiz. Zentzu horretan, nanohutsarte horietan, *nanobarrunbe* (ingelesez *nanocavity*) ere deitutakoetan, konfinatutako eremuaren intentsitate handiek prozesu optikoak bultzatu ditzakete.

Nanobarrunbea elkarrengandik oso gertu kokaturiko bi nanopartikulak osatu

ohi dute. Gertutasun horren ondorioz, partikula bien LSP moduen arteko hibridazioa sortzen da Coulomb elkarrekintza dela eta, molekula bat osatzean atomoetako orbitalak hibridatzen diren gisan. Nanopartikulen kasuan dimeroen lotura-plasmoia (ingelesez *bonding dimer plasmon*, BDP) deritzona eratzen da [26–28]. Karga hutsartearen albo banako metalezko gainazaletan pilatzen da, nanopartikula isolatuen aldean eremuaren handitze eta lokalizazio nabarmenak sortuz hutsartean [29, 30]. Horrez gain, karga hauen arteko Coulomb elkarrekintza oso indartsua denez, espektroan BDP erresonantziek duten posizioa oso sentikorra da hutsartearen luzerarekiko, hau da, bi partikulen gainazal metalikoen arteko distantziarekiko [30, 31], hutsarte-nanoantenak erregela plasmoniko oso sentikorrak bihurtuz. Partikulen arteko ukipena dagoenean, karga elektrikoa partikula batetik bestera pasa daiteke eta beraz, karga-transferentziaren plasmoiak (ingelesez *Charge Transfer Plasmon*, CTP) kitzika daitezke. Horrez gain, CTPak ukipen zuzenik gabeko nanopartikuletan ere kitzika daitezke, elektroiak nanopartikula batetik bestera beste mekanismo baten bidez lekualdatzen badira, adibidez, elektroien tunel-efektu kuantikoaren bidez [32, 33].

Dimeroez gain, argiaren nanometro-eskalako konfinamendua erdiesteko beste aukera bat *ispilu gaineko nanopartikula* (ingelesez *NanoParticle-on-Mirror*, NPoM) deritzon egituran aurki daiteke. Egitura hau substratu metaliko batez eta bere gainean jarritako nanopartikula metaliko batez osatuta dago, elkarrengandik film-bereizgailuaz bereizita daudenak, horrela nanopartikula eta substratuaren artean hutsart bat sortuz. NPoM egiturek egonkortasun handia erakusten dute eta plataforma oso egokia eskaintzen dute nanobarrunbean jarritako molekulekin espektroskopia molekularreko esperimentuak egiteko.

Gaur egun gehien erabiltzen den molekula-espektroskopia tekniketako bat Raman sakabanaketan oinarritua dago, arkeologian [34], medikuntzan [35], drogen detekzioan [36] eta konposatu kimikoen detekzioan [37] oso erabilia dena. Raman sakabanaketa C. V. Raman-ek aurkitu zuen 1920. hamarkadan [38] eta argiaren sakabanaketa prozesu inelastiko bat deskribatzen du. Prozesu honetan fotoi batek (argia) molekula bat egoera birtual batera kitzikatzen du, eta ondoren beste egoera ezberdin batera erlaxatu daiteke molekula, energia txikiagoko fotoi bat igorriz eta bibrazio bat sortuz (Stokes prozesua), edo bestela, beste egoera batera erlaxatu daiteke energia altuagoko fotoi bat igorriz eta bibrazio bat xurgatuz (anti-Stokes prozesua). Raman sakabanaketa Lord Rayleigh-en sakabanaketaren teoriaren osagarria da, azken honek argiaren prozesu elastiko bat deskribatzen baitu.

Raman sakabanaketan, sakabanatutako argiaren eta argiztatzeko erabilitako argiaren energien arteko aldeari dagokion energia molekularen bibrazio-egoeraren energia-tarteari dagokio. Molekula batek bibrazio-modu anitz izan ditzakeenez, sakabanatutako argiak ere uhin-luzera ezberdinak izan ditzake, uhin-luzera bakoitza bibrazio-modu jakin baten sakabanaketa prozesuari dagokiolarik. Ondorioz lortutako espektroa, beraz, oso baliagarria da molekula baten bibrazio-moduak eta talde funtzionalak identifikatzeko, molekularen egitura kimikoa berreraikitzeko tresna bat eskainiz. Hori dela eta, molekula baten Raman sakabanatze-espektroa molekula horren *bibrazioen hatz-marka* (*vibrational fingerprint* ingelesez) modura hartzen da.

Anti-Stokes sakabanaketa gertatzeko molekulak kitzikatutako egoera batean egon behar du. Zero tenperaturan, $T = 0$ K, molekula guztiak oinarrizko egoeran daudela jotzen da, eta beraz, egoera horretan ezin daiteke anti-Stokes sakabanaketarik behatu. Giro-tenperaturan eginiko esperimentuetan Stokes sakabanaketa gailentzen da molekula gehienak oinarrizko egoeran baitaude. Gainera, Stokes/anti-Stokes proportzioa molekularen tenperatura neurtzeko erabil daiteke bibrazio-egoeren banaketak Bose-Eistein banaketa betetzen duela suposatuz gero.

Hala ere, Raman sakabanaketak eragozpen handia du: bere sekzio-eragilea oso txikia da, ohiko balioak $\ll 10^{-28}\mathrm{m}^2$ direlarik. Raman sakabanaketaren erabilera, espektroskopiarako teknika gisa, nabarmen hobetzen da nanoantena plasmonikoek eremua handitzeko duten gaitasuna probestuz gero. Izan ere, nanoantenen erresonantziak sorturiko eremu hurbilean kokatutako molekulen Raman sakabanaketa nabarmen handitzen da. Hau gertatzen da, adibidez, molekulak nanobarrunbe bateko eremu hurbilean kokatzen direnean, molekuletatik argiaren igorpena erraztuz, Gainazalez Handitutako Raman Sakabanaketa (ingelesez *Surface Enhanced Raman Scattering*, SERS). Honen oinarri fisikoa ondokoa da: Raman sakabanaketa eremu elektromagnetiko lokalaren 4. berredurarekiko menpekotasun lineala duenez, eremu plasmonikoak $\sim 10^{10}$ handitze-faktoreak eragin ditzake SERSen.

Nanobarrunbeetako eremu hurbila are gehiago handitu eta lokalizatu daiteke irtengune atomikoen presentzia dela eta, zeinak tximistorratz efektua eragin dezakeen eskala atomikoan, argiaren lokalizazio azpinanometrikoa ahalbidetuz *pikobarrunbe* (ingelesez *picocavity*) deritzenetan, 2. kapituluan azalduko dugun bezala. Pikobarrunbeek fotoien eta fotoi-bakarreko igorleen trantsizio elektronikoen akoplamendua areagotu dezakete [42], edo fotoien eta molekuletako bibrazioen arteko elkarrekintza optomekanikoak [43]. Horrez gain, pikobarrunbeetako eremuen gradiente handiek molekuletako bibrazioen simetria-arauak hautsi ditzakete, debekatutako trantsizio molekularrak aztertzeko bidea irekiz SERSen. Trantsizio hauek gailur zorrotz gehigarri gisa agertzen diren SERS espektroetan [43].

Nanobarrunbeetan sortutako pikobarrunbeek eragindako gailur gehigarriez gain, SERS espektroan beste zenbait xehetasun ageri ohi dira maiz. Zehazki, ms-ko denbora-eskalan hondoko seinale zabalaren handitzea behatu da hainbat ikerketa lanetan [44–48]. SERS espektroko hondoko seinalearen jatorria metaleko Raman elektroi-sakabanaketa (ingelesez *electronic Raman scattering process*, ERS) deritzon prozesuaren ondorioz sortzen den argiaren sakabanaketa inelastikoarekin erlazionatu izan da. Prozesu hau molekuletan gertatzen den Raman sakabanaketaren parekoa da, baina kasu honetan metaleko Fermiren itsasoko elektroien trantsizioetarako izango litzateke. Prozesu honen inguruan xehetasun gehiago ematen ditugu 3. kapituluan.

Nanoeskalan *ikusteko* beste aukera bat, atomoak behatzera iristeraino, elektroi-sorta azkarrak erabiliz materian kitzikapenak sortzea da. 1931. urtean Ernst Ruskak eta Max Knoll-ek transmisioko mikroskopia elektronikoan (ingelesez *Transmission Electron Microscopy*, TEM) erabilitako lehen prototipoa frogatu zutenetik [49, 50], TEMak zientzia modernoko tresnarik garrantzitsuenetako bat bihurtu dira eta funtsezko izan dira fisikan, kimikan eta biologian XX. mendean zehar egindako

aurkikuntza ugaritan [51, 52].

Elektronikan izandako hobekuntzei esker laginak abiadura handian eskaneatzen dituzten elektroi sorta oso enfokatuak sortu dira, bereizmen atomikoa duten irudiak lortzea ahalbidetuz. Aberrazio-zuzenketak dituzten gaur egungo punta-puntako ekorketa eta transmisioko mikroskopio elektronikoekin (ingelesez *Scanning Transmission Electron Microscope*, STEM) gaur egun posible da Ångstrom-azpiko bereizmena lortzea [53, 54]. Are gehiago, mikroskopiari erantsitako neugailu ezberdinei esker elektroi azkarren eta materiaren arteko elkarrekintzatik sorturiko seinale anitzak (adibidez, erradiazio elektromagnetikoa, Auger elektroien eta elektroi sekundarioen igorpena) neur ditzakete elektroi sortaren posizioarekin zehaztasun handiz korrelazionatuta. Beraz, STEMak materialak espazio-bereizmenarekin eskala atomikoan aztertzeko teknika oso malgua eskaintzen du.

Lagin bat zeharkatzen duten edo laginetik gertu igarotzen diren elektroi sortek hasierako energiaren (eta momentuaren) zati txiki bat gal dezakete laginarekin duten elkarrekintzaren ondorioz. Elektroiek energia zehatz bat galtzeko probabilitatea laginean sortzen duten kitzikapenaren izaerarekin zuzenean erlazionatua dago. Elektroien energia-galera (ingelesez *electron energy loss*, EEL) probabilitatearen espektro-analisiak materiaren kitzikapenak energia-tarte zabal batean identifikatzeko balio du, elektroien energia-galera espektroskopia (ingelesez *electron energy loss probability*, EELS) STEMen teknika analitiko garrantzitsua bihurtuz. Adibidez, atomoen barne-geruzetako elektroien kitzikapenetatik datozen energia altuko galerak (gutxi gorabehera 50 eV-tik keV-ra) detektatzeko erabil daiteke EELS [55, 56], horrela, eskala atomikoko irudiekin korrelazionatuta, egitura kimikoari buruzko informazioa emanez [57–59]. Bestalde, energia baxuetan (normalean 50 eV-tik beherakoak) balentzia-bandako elektroien kitzikapenarekin, banda-arteko trantsizio elektronikoekin, eta kristal-sarearen edo molekulen bibrazioeki erlazionatutako energia-galerak ager daitezke EEL espektroan.

Elektroi azkarrek sorturiko eremu desgerkorra dela eta modu eraginkorrean akopla daitezke plasmoiekin eV gutxi batzutako energia-tartean. Izan ere, elektroi azkarrek sorturiko eremu elektromagnetikoaren izaera desagerkorrak argi-espektroskopia konbentzionalean kitzika ezin daitezkeen plasmoi "ilunak" kitzikatzea ahalbidetzen du STEM-EELS teknikan. Egitura plasmonikoen portaera eta funtzionalitatea ulertzeko ezinbestekoa izaten da maiz eremu hurbila karakterizatzea, eta hauxe era naturalean azter daiteke elektroi sorta azkarren bidez [64].

Kitzikapen plasmonikoak eta egitura nanoplasmonikoak aztertzeko EELSen erabilera oso hedatua dago gaur egun. Aipagarria da bolumeneko plasmoien identifikazioa [65, 66] eta SSPen aurkikuntza XX. mendeko 50.-60. hamarkadetan [61] zuzenean erlazionatuta daudela xafla eta gainazal metalikoekin egindako EELS esperimentuekin [67, 68]. Garai hartako ikerketak orokorrean elektroi sorta zabalekin (fokatu gabeak) egin ohi ziren, eta momentu-espazioan aztertzen zen EELS espektroa, neurketa hauek kitzikatutako modoen dispertsioarekin erlazionatu baitaitezke.

Azken bi hamarkadetan bereizmen azpinanometrikoa [53, 72] eta eV-az azpiko energia-sentikortasuna [73] ahalbidetu duten hainbat hobekuntza teknikoren lekuko

izan da STEM-EELS [69–71]. Aurrerapen horiek bideak ireki dituzte material eta nanoegitura berriak ezaugarritzeko [54, 74], fonoien bereizmen nanometrikoarekin espektroskopia bibrazionala egiteko [56, 75–78], edo energia baxuko elektroi sortekin eta erradiazio-kalte murritzarekin biomaterialak ezaugarritzeko [56, 79, 80]. Horrez gain, aipatutako hobekuntzek 10 nm baino txikiagoak diren nanopartikula isolatuetan EELS esperimentuak egitea ahalbidetu dute [81–86] Å-azpiko bereizmenarekin.

Azken urteotan, LSPen erresonantzia-energien gorriranzko eta urdineranzko lerrakuntzek NP txikien tamainarekiko duten menpekotasunak arreta nabarmena bereganatu du literaturan [82–84, 87–89]. Gainera, tresneria esperimentalean lorturiko bereizmenaren hobekuntzak LSP erresonantzietan eragina duten efektu kuantikoak agerian utzi ditu. Horrek eredu teorikoen garapena bultzatu du efektu desberdinak deskribatzeko, hala nola, elektroien konfinamendua [90], elektroien isurpena (ingelesez *spill-out*) gainazaletan [31, 91–93], ez-lokaltasun efektuak funtzio dielektrikoan [94,95], aldaketak ingurune lokalean [86], edo tunel-efektu kuantikoaren aktibazioa partikulen arteko hutsarte azpinanometrikoetan [33, 87, 96]. Hala ere, NP txikien eite poliedrikoa eta ezaugarri atomistikoek EEL espektroan duten eragina arbuiatu egin izan da gehienetan, NPren eitea esferikoa dela suposatuz.

Nanopartikula metalikoen gainazalean konfinatuta dauden LSPak kitzikatzeaz gain, elektroi sortek elektroi-dentsitatearen luzetarako presio-uhinak kitzika ditzakete bolumenean, hots, konfinatutako bolumeneko plasmoiak (ingelesez *confined bulk plasmons*, CBP) [94]. CBPak 1971. urtean behatu ziren esperimentalki lehen aldiz, zilarrezko [97] eta potasiozko, [98] xafla finetan espektroskopia optikoa erabiliz. EELSen, CBPak egitura eta material anitzentzat behatu dira esperimentalki, besteak beste, germaniozko nanoharietan [100], bismutozko nanoharietan [101], bismutozko nanopartikuletan [90, 102], eta aluminiozko nanodiskoetan [85]. Teorikoki, CBPak naturalki agertzen dira elektroi-dentsitatearen erantzunaren eredu hidrodinamikoen baitan, elektroi-dentsitatearen konpresibilitate finitua kontuan hartzen baitute. Gutxienez dimentsio finitu bat duten nanoegituretan, karga-dentsitatearen bolumeneko oszilazioak konfina daitezke dimentsio horretan, uhin geldikorrak sortuz. Adibidez, zilindroearen kasuan eginiko azterketa teorikoek CBPen kitzikapena erakusten dute elektroien ibilbideak lagina zeharkatzen duenean [103–105]. Tesi honetan, eskala nanometrikoa duen materiaren eta uhin-elektromagnetikoen arteko elkarrekintza aztertuko dugu, hala nola, argiak edo elektroi sortak kitzikatzen dituzten nanopartikula metaliko txikietan eta nanobarrunbeetan ageri diren ezaugarri atomistikoen eraginean arreta berezia jarriz.

Egitura plasmonikoen erantzun optikoa eta kitzikapen-iturriak deskribatzeko erabili ditugun metodo numerikoak azaldu ditugu 1. kapituluan: (i) mugako elementuen metodoa (ingelesez *Boundary Element Method*, BEM), ingurune jarraituak eta homogeneoak eta hauen arteko muga definituak onartzen dituen erantzun lokalaren metodoa, (ii) dipolo diskretuen hurbilketa (ingelesez *Discrete Dipole Approximation*, DDA), zeinean nanoegiturak osatzen dituzten atomoak dipolo gisa deskribatzen diren, eta (iii) denboraren menpeko dentsitatearen funtzionalaren teoria (ingelesez *Time Dependent Density Functional Theory*, TDDFT) *ab initio* metodo atomistikoa, zeinak nanoegitura plasmonikoaren egitura atomistikoa eta

efektu kuantikoak kontuan hartzen dituen.

Aipaturiko metodoak erabiliz, 2. kapituluan ezaugarri atomistikoak, hala nola, erpin, ertz eta aurpegiak dituzten nanometro gutxi batzutako sodiozko NPen (380 atomo) erantzun optikoa eta eremu hurbila aztertu ditugu. Ezaugarri atomistiko horiek eremu hurbila dimentsio azpinanometrikoetan lokalizatzea eta konfinatzea ahalbidetzen dute [106], hondoko eremu plasmonikoa baino gehiago, induzitutako eremu hurbilen ezaugarri espazialak nanobarrunbeek inposaturiko muga espazialetatik harago bultzatuz, eta beraz, *pikobarrunbeen* erreinura iritsiz. Nanoegitura plasmoniko jakin bateko egitura atomistikoari dagokion kargadentsitatearen profilaren antza duen gainazal jarraitua eta leuna aukeratuz, NP hauen gainazalean induzitzen den eremu hurbilaren ezaugarriak fideltasunez erreproduzitu ditzakete hurbilketa klasikoek. Plasmoiek sorturiko eremu hurbila handitzen duen eskala atomiko tximistorratz efektu ez-erresonantea identifikatu dugu lokalizazio gehigarriaren arrazoi gisa, eta eredu lokal sinple bat proposatu dugu hura azaltzeko. Horrez gain, kontzeptu hau nanohutsarteetan pikobarrunbeek duten eraginaren azterketara hedatu dugu, muturreko egoera honetan eredu kuantiko eta klasikoek ematen duten erantzunean adostasuna lortuz. Maila atomistikoan eginiko pikobarrunbe optikoen deskribapen kuantikoak agerian uzten du eskala atomikoko ezaugarrien garrantzia, nahiz eta halako deskribapenak eskakizun konputazionalek mugatzen dituzten, nanoegitura handietarako simulazioak egitea ezinezko bihurtuz. Tesi honetan proposatutako eredu klasiko sinpleagoak pikobarrunbeen presentzia nanoegitura handietan kontuan izatea ahalbidetzen du, egitura hauen erantzun optikoa kalkulatzeko erronka ohiko metodo elektrodinamikoen bidez egitea ahalbidetuz [107].

3. kapituluan nanohutsartean molekulak dituzten NPoM egituretan lorturiko SERS espektroetan agertzen diren hondoko seinalearen handitze aldakorra eztabaidatu dugu. Argiaren sakabanaketa inelastikoaren gertaera hauei *distira* deritzegu, eta esparru kontzeptual bat ematen dugu beraien ezaugarri optikoak aintzat hartzeko. Cambridge-ko Unibertsitateko Jeremy J. Baumberg irakaslearen taldean esperimentalki lortutako SERS espektroetan atzemandako distirak aztertu ditugu. Defektu aldakorretako, hala nola makla-planoetako eta ale-ertzetako, atomoen berregituraketa dinamikoaren eraginez sortzen diren distirak azaltzeko eredu bat proposatu dugu. Eredu honen arabera, atomoen berregituraketak plasma-maiztasunaren aldaketa lokalizatuak eragiten ditu metalean, eta horren ondorioz eremu elektriko indartsuagoak induzitzen ditu NP metalikoaren baitan, horrela hondoko ERS seinalea handituz.

Espektroskopia optikoan bezala, 2. kapituluan eztabaidatua, TDDFT *ab initio* metodoak esparru egokia eskaintzen du EELSen efektu kuantikoen eta egitura atomistikoaren eragina kontuan izateko. Ezaugarri atomistikoek sodiozko nanopartikulen EEL espektroan duten eragina aztertu dugu 4. kapituluan, TDDFT erabiliz. Lortutako emaitzak, nanopartikularen itxura atomistikoa kontuan hartzen duten eredu klasikoekin lortutako emaitzekin alderatu ditugu, ezaugarri azpinanometrikoek EELSen duten eragina aztertzeko. Horrela, ezaugarri atomistikoak EEL espektroan agerian gelditzen direla frogatu dugu, elektroi sorten

ibilbidearekiko eta nanopartikularen orientazioarekiko duen sentikortasuna ageriko jarriz, ohiko nanopartikula esferikoen hurbilketak deskribatzen ez duena. Gainera, EEL espektroan LSP eta CBP moduen kitzikapenak identifikatu ditugu, azkenak nanopartikula zeharkatzen duten elektroien ibilbideentzat soilik kitzikatzen direlarik. Bestalde, espektroek elektroi sortaren talka-parametroarekiko menpekotasuna duten aztertu dugu.

Bukatzeko, 4. kapituluan aurkeztutako TDDFT espektroetan behatutako CBPen aztarnak 5. kapituluan aztertu ditugu xehetasun gehiagoz, materialaren erantzuna ez-lokaltasuna kontuan hartuz deskribatzen duen Eredu Hidrodinamiko lineal bat erabiliz. Formalismo honen baitan nanopartikula esferikoen EEL probabilitatearen adierazpen semi-analitikoa lortu dugu, talka-parametroaren menpekotasuna deskribatzen duena, zeinak egitura zeharkatzen duten ibilbideentzat ere balio duen. Horrez gain, eredu honek CBPek hainbat parametrorekiko duten menpekotasuna aztertzeko aukera ematen digu, hala nola, nanopartikularen tamaina edo elektroi sorten abiadura. Guk sodiozko partikula esferikoen EEL espektroak aztertzeko baliatu badugu ere, gure ereduak aluminiozko diskoetan esperimentalki behatu diren CBPen portaera azaltzen du [85], besteak beste.

Ezaugarri atomistikoak dituzten nanoantena eta nanobarrunbe plasmonikoen erantzun optikoa eredu kuantiko eta klasikoen bidez deskribatu dugu tesi honetan, agerian utziz egitura hauetan fenomeno optiko berriak aztertzeko eredu hauek duten baliagarritasuna. Tesi honek, beraz, espektroskopia optikoaren eta elektroi-espektrokopiaren esparruetan pikofotonika aztertzeko lehen pauso bat eskaintzen du.

List of Publications

This thesis is supported on the following publications:

Chapter 2: Optical response of metallic picocavities

1. M. Urbieta, M. Barbry, Y. Zhang, P. Koval, D. Sánchez, N. Zabala, J. Aizpurua
Atomic-Scale Lightning Rod Effect in Plasmonic Picocavities: A Classical View to a Quantum Effect,
ACS Nano **12**, 585-595 (2018).

Chapter 3: Addressing structural inhomogeneities in metallic nanocavities as probed by optical spectroscopy

2. C. Carnegie, M. Urbieta, R. Chikkaraddy, B. de Nijs, J. Griffiths, W. M. Deacon, M. Kamp, N. Zabala, J. Aizpurua, J. J. Baumberg
Flickering nanometre-scale disorder in a crystal lattice tracked by plasmonic flare light emission,
Nature Communications **11** 682 (2020)

Chapter 4: Atomic-scale structural features as probed by swift electrons

3. M. Urbieta, M. Barbry, P. Koval, A. Rivacoba, D. Sánchez, N. Zabala, J. Aizpurua
Unveiling atomic-scale features in plasmonic nanoparticles probed by electron beams,
In preparation (2021)

Chapter 5: Hydrodynamic model to address EELS of plasmonic nanoparticles

4. M. Urbieta, E. Ogando, A. Rivacoba, N. Zabala, J. Aizpurua
Confined bulk plasmon excitation in EELS within a hydrodynamic model,
In preparation (2021)

Other publications not included in this thesis:

5. Y. Zhang, R. Esteban, R. A. Boto, M. Urbieta, X. Arrieta, C. Shan, S. Li, J. J. Baumberg, J. Aizpurua
Addressing molecular optomechanical effects in nanocavity-enhanced Raman scattering beyond the single plasmonic mode,
Nanoscale **13**, 1938-1954 (2020)

Bibliography

I only know one story. But oftentimes small pieces seem to be stories themselves.
-Patrick Rothfuss, The Name of the Wind

[1] J. Wesley, *"A Compendium of Natural Philosophy (1810) Chapter XII, Burning Glasses"*, 1810. https://web.archive.org/web/20071012154432/http://wesley.nnu.edu/john{_}wesley/wesley{_}natural{_}philosophy/duten12.htm.

[2] L. Novotny and B. Hecht, *Principles of Nano-Optics*. Cambridge University Press, Cambridge, 2012.

[3] P. N. Prasad, *Nanophotonics*. John Wiley & Sons, Inc., Hoboken, NJ, USA, 2004.

[4] S. A. Maier, *Plasmonics: Fundamentals and Applications*. Springer US, New York, NY, 2007.

[5] A. Otto, *"Excitation of nonradiative surface plasma waves in silver by the method of frustrated total reflection"*, Zeitschrift für Physik A Hadrons and nuclei **216**, 398–410 (1968).

[6] E. Kretschmann and H. Raether, *"Radiative Decay of Non Radiative Surface Plasmons Excited by Light"*, Zeitschrift fur Naturforschung - Section A Journal of Physical Sciences **23**, 2135–2136 (1968).

[7] B. Hecht, H. Bielefeldt, L. Novotny, Y. Inouye, and D. W. Pohl, *"Local Excitation, Scattering, and Interference of Surface Plasmons"*, Physical Review Letters **77**, 1889–1892 (1996).

[8] J. R. Lakowicz, *"Radiative decay engineering 3. Surface plasmon-coupled directional emission"*, Analytical Biochemistry **324**, 153–169 (2004).

[9] H. Ditlbacher, J. R. Krenn, N. Felidj, B. Lamprecht, G. Schider, M. Salerno, A. Leitner, and F. R. Aussenegg, *"Fluorescence imaging of surface plasmon fields"*, Applied Physics Letters **80**, 404–406 (2002).

[10] Y.-Y. Teng and E. A. Stern, *"Plasma Radiation from Metal Grating Surfaces"*, Physical Review Letters **19**, 511–514 (1967).

[11] W. L. Barnes, A. Dereux, and T. W. Ebbesen, *"Surface plasmon subwavelength optics"*, Nature **424**, 824–830 (2003).

[12] J. J. Mock, M. Barbic, D. R. Smith, D. A. Schultz, and S. Schultz, *"Shape effects in plasmon resonance of individual colloidal silver nanoparticles"*, The Journal of Chemical Physics **116**, 6755–6759 (2002).

[13] M. Pelton, J. Aizpurua, and G. Bryant, *"MetalâĂŘnanoparticle plasmonics"*, Laser & Photonics Review **2**, 136–159 (2008).

[14] R. Vogelgesang and A. Dmitriev, *"Real-space imaging of nanoplasmonic resonances"*, The Analyst **135**, 1175 (2010).

[15] B. Sharma, R. R. Frontiera, A.-I. Henry, E. Ringe, and R. P. Van Duyne, *"SERS: Materials, applications, and the future"*, Materials Today **15**, 16–25 (2012).

[16] H. Xu, E. J. Bjerneld, M. Käll, and L. Börjesson, *"Spectroscopy of single hemoglobin molecules by surface enhanced raman scattering"*, Physical Review Letters **83**, 4357–4360 (1999).

[17] J. Aizpurua, G. W. Bryant, L. J. Richter, F. J. García de Abajo, B. K. Kelley, and T. Mallouk, *"Optical properties of coupled metallic nanorods for field-enhanced spectroscopy"*, Physical Review B **71**, 235420 (2005).

[18] P. B. Johnson and R. W. Christy, *"Optical Constants of the Noble Metals"*, Physical Review B **6**, 4370–4379 (1972).

[19] A. Sundaramurthy, K. B. Crozier, G. S. Kino, D. P. Fromm, P. J. Schuck, and W. E. Moerner, *"Field enhancement and gap-dependent resonance in a system of two opposing tip-to-tip Au nanotriangles"*, Physical Review B **72**, 165409 (2005).

[20] J. Alegret, T. Rindzevicius, T. Pakizeh, Y. Alaverdyan, L. Gunnarsson, and M. Käll, *"Plasmonic Properties of Silver Trimers with Trigonal Symmetry Fabricated by Electron-Beam Lithography"*, The Journal of Physical Chemistry C **112**, 14313–14317 (2008).

[21] S. S. Aćimović, M. P. Kreuzer, M. U. González, and R. Quidant, *"Plasmon Near-Field Coupling in Metal Dimers as a Step toward Single-Molecule Sensing"*, ACS Nano **3**, 1231–1237 (2009).

[22] L. M. Liz-Marzán, *"Tailoring Surface Plasmons through the Morphology and Assembly of Metal Nanoparticles"*, Langmuir **22**, 32–41 (2006).

[23] M. Grzelczak, J. Vermant, E. M. Furst, and L. M. Liz-Marzán, *"Directed Self-Assembly of Nanoparticles"*, ACS Nano **4**, 3591–3605 (2010).

[24] G. González-Rubio, P. Díaz-Núñez, A. Rivera, A. Prada, G. Tardajos, J. González-Izquierdo, L. Bañares, P. Llombart, L. G. Macdowell, M. Alcolea Palafox, L. M. Liz-Marzán, O. Peña-Rodríguez, and A. Guerrero-Martínez, *"Femtosecond laser reshaping yields gold nanorods with ultranarrow surface plasmon resonances"*, Science **358**, 640–644 (2017).

[25] F. Keilmann and R. Hillenbrand, *"Near-field microscopy by elastic light scattering from a tip"*, Philosophical Transactions of the Royal Society of London. Series A: Mathematical, Physical and Engineering Sciences **362**, 787–805 (2004).

[26] E. Prodan, C. Radloff, N. J. Halas, and P. Nordlander, *"A Hybridization Model for the Plasmon Response of Complex Nanostructures"*, Science **302**, 419–422 (2003).

[27] E. Prodan and P. Nordlander, *"Plasmon hybridization in spherical nanoparticles"*, Journal of Chemical Physics **120**, 5444–5454 (2004).

[28] P. Nordlander, C. Oubre, E. Prodan, K. Li, and M. I. Stockman, *"Plasmon Hybridization in Nanoparticle Dimers"*, Nano Letters **4**, 899–903 (2004).

[29] P. Mühlschlegel, H. J. Eisler, O. J. Martin, B. Hecht, and D. W. Pohl, *"Applied physics: Resonant optical antennas"*, Science **308**, 1607–1609 (2005).

[30] I. Romero, J. Aizpurua, G. W. Bryant, and F. J. García De Abajo, *"Plasmons in nearly touching metallic nanoparticles: singular response in the limit of touching dimers"*, Optics Express **14**, 9988 (2006).

[31] T. V. Teperik, P. Nordlander, J. Aizpurua, and A. G. Borisov, *"Robust Subnanometric Plasmon Ruler by Rescaling of the Nonlocal Optical Response"*, Physical Review Letters **110**, 263901 (2013).

[32] K. J. Savage, M. M. Hawkeye, R. Esteban, A. G. Borisov, J. Aizpurua, and J. J. Baumberg, *"Revealing the quantum regime in tunnelling plasmonics"*, Nature **491**, 574–577 (2012).

[33] J. A. Scholl, A. Garcia-Etxarri, G. Aguirregabiria, R. Esteban, T. C. Narayan, A. L. Koh, J. Aizpurua, and J. A. Dionne, *"Evolution of Plasmonic Metamolecule Modes in the Quantum Tunneling Regime"*, ACS Nano **10**, 1346–1354 (2016).

[34] P. Vandenabeele, H. G. M. Edwards, and L. Moens, *"A Decade of Raman Spectroscopy in Art and Archaeology"*, Chemical Reviews **107**, 675–686 (2007).

[35] L.-P. Choo-Smith, H. G. M. Edwards, H. P. Endtz, J. M. Kros, F. Heule, H. Barr, J. S. Robinson, H. A. Bruining, and G. J. Puppels, *"Medical applications of Raman spectroscopy: From proof of principle to clinical implementation"*, Biopolymers **67**, 1–9 (2002).

[36] B. de Nijs, C. Carnegie, I. Szabó, D.-B. Grys, R. Chikkaraddy, M. Kamp, S. J. Barrow, C. A. Readman, M.-E. Kleemann, O. A. Scherman, E. Rosta, and J. J.

Baumberg, *"Inhibiting Analyte Theft in Surface-Enhanced Raman Spectroscopy Substrates: Subnanomolar Quantitative Drug Detection"*, ACS Sensors **4**, 2988–2996 (2019).

[37] B. de Nijs, F. Benz, S. J. Barrow, D. O. Sigle, R. Chikkaraddy, A. Palma, C. Carnegie, M. Kamp, R. Sundararaman, P. Narang, O. A. Scherman, and J. J. Baumberg, *"Plasmonic tunnel junctions for single-molecule redox chemistry"*, Nature Communications **8**, 994 (2017).

[38] C. V. Raman and K. S. Krishnan, *"A New Type of Secondary Radiation"*, Nature **121**, 501–502 (1928).

[39] E. C. Le Ru and P. G. Etchegoin, *Principles of Surface-Enhanced Raman Spectroscopy*. Elsevier, 2009.

[40] J. Mertens, M.-E. Kleemann, R. Chikkaraddy, P. Narang, and J. J. Baumberg, *"How Light Is Emitted by Plasmonic Metals"*, Nano Letters **17**, 2568–2574 (2017).

[41] A. J. McQuillan, *"The discovery of surface-enhanced Raman scattering"*, Notes and Records of the Royal Society **63**, 105–109 (2009).

[42] Y. Zhang, Q. S. Meng, L. Zhang, Y. Luo, Y. J. Yu, B. Yang, Y. Zhang, R. Esteban, J. Aizpurua, Y. Luo, J. L. Yang, Z. C. Dong, and J. G. Hou, *"Sub-nanometre control of the coherent interaction between a single molecule and a plasmonic nanocavity"*, Nature Communications **8**, 1–7 (2017).

[43] F. Benz, M. K. Schmidt, A. Dreismann, R. Chikkaraddy, Y. Zhang, A. Demetriadou, C. Carnegie, H. Ohadi, B. De Nijs, R. Esteban, J. Aizpurua, and J. J. Baumberg, *"Single-molecule optomechanics in "picocavities""*, Science **354**, 726–729 (2016).

[44] S. Nie, *"Probing Single Molecules and Single Nanoparticles by Surface-Enhanced Raman Scattering"*, Science **275**, 1102–1106 (1997).

[45] K. Kneipp, Y. Wang, H. Kneipp, L. T. Perelman, I. Itzkan, R. R. Dasari, and M. S. Feld, *"Single Molecule Detection Using Surface-Enhanced Raman Scattering (SERS)"*, Physical Review Letters **78**, 1667–1670 (1997).

[46] H.-H. Shin, G. J. Yeon, H.-K. Choi, S.-M. Park, K. S. Lee, and Z. H. Kim, *"Frequency-Domain Proof of the Existence of Atomic-Scale SERS Hot-Spots"*, Nano Letters **18**, 262–271 (2018).

[47] A. Weiss and G. Haran, *"Time-dependent single-molecule Raman scattering as a probe of surface dynamics"*, Journal of Physical Chemistry B **105**, 12348–12354 (2001).

[48] Y. Cheng, J. Zhao, T. Wen, G. Li, J. Xu, A. Hu, Q. Gong, and G. Lu, *"Enhanced Light Emission from Plasmonic Nanostructures by Molecules"*, Journal of Physical Chemistry C **121**, 23626–23632 (2017).

[49] M. Knoll and E. Ruska, *"Das Elektronenmikroskop"*, Zeitschrift für Physik **78**, 318–339 (1932).

[50] E. Ruska, *"The development of the electron microscope and of electron microscopy"*, Reviews of Modern Physics **59**, 627–638 (1987).

[51] D. Shechtman, I. Blech, D. Gratias, and J. W. Cahn, *"Metallic Phase with Long-Range Orientational Order and No Translational Symmetry"*, Physical Review Letters **53**, 1951–1953 (1984).

[52] R. Henderson and P. N. T. Unwin, *"Three-dimensional model of purple membrane obtained by electron microscopy"*, Nature **257**, 28–32 (1975).

[53] P. E. Batson, N. Dellby, and O. L. Krivanek, *"Sub-ångstrom resolution using aberration corrected electron optics"*, Nature **418**, 617–620 (2002).

[54] O. L. Krivanek, M. F. Chisholm, V. Nicolosi, T. J. Pennycook, G. J. Corbin, N. Dellby, M. F. Murfitt, C. S. Own, Z. S. Szilagyi, M. P. Oxley, S. T. Pantelides, and S. J. Pennycook, *"Atom-by-atom structural and chemical analysis by annular dark-field electron microscopy"*, Nature **464**, 571–574 (2010).

[55] R. Egerton, *Electron Energy-Loss Spectroscopy in the Electron Microscope*. Springer US, Boston, MA, 2011.

[56] O. L. Krivanek, T. C. Lovejoy, N. Dellby, T. Aoki, R. W. Carpenter, P. Rez, E. Soignard, J. Zhu, P. E. Batson, M. J. Lagos, R. F. Egerton, and P. A. Crozier, *"Vibrational spectroscopy in the electron microscope"*, Nature **514**, 209–212 (2014).

[57] N. D. Browning, M. F. Chisholm, and S. J. Pennycook, *"Atomic-resolution chemical analysis using a scanning transmission electron microscope"*, Nature **366**, 143–146 (1993).

[58] P. E. Batson, *"Simultaneous STEM imaging and electron energy-loss spectroscopy with atomic-column sensitivity"*, Nature **366**, 727–728 (1993).

[59] D. Kepaptsoglou, T. P. Hardcastle, C. R. Seabourne, U. Bangert, R. Zan, J. A. Amani, H. Hofsäss, R. J. Nicholls, R. M. Brydson, A. J. Scott, and Q. M. Ramasse, *"Electronic Structure Modification of Ion Implanted Graphene: The Spectroscopic Signatures of p- and n-Type Doping"*, ACS Nano **9**, 11398–11407 (2015).

[60] H. Lüth, *Surfaces and Interfaces of Solid Materials*. Springer Berlin Heidelberg, Berlin, Heidelberg, 1995.

[61] R. H. Ritchie, *"Plasma Losses by Fast Electrons in Thin Films"*, Physical Review **106**, 874–881 (1957).

[62] E. Fermi, *"The Ionization Loss of Energy in Gases and in Condensed Materials"*, Physical Review **57**, 485–493 (1940).

[63] R. H. Ritchie, *"Quantal aspects of the spatial resolution of energy-loss measurements in electron microscopy I. Broad-beam geometry"*, Philosophical Magazine A **44**, 931–942 (1981).

[64] F. J. García De Abajo, *"Optical excitations in electron microscopy"*, Reviews of Modern Physics **82**, 209–275 (2010).

[65] D. Bohm and D. Pines, *"A collective description of electron interactions: III. Coulomb interactions in a degenerate electron gas"*, Physical Review **92**, 609–625 (1953).

[66] D. Pines, *"Collective Energy Losses in Solids"*, Reviews of Modern Physics **28**, 184–198 (1956).

[67] C. J. Powell and J. B. Swan, *"Origin of the Characteristic Electron Energy Losses in Magnesium"*, Physical Review **116**, 81–83 (1959).

[68] C. J. Powell and J. B. Swan, *"Origin of the Characteristic Electron Energy Losses in Aluminum"*, Physical Review **115**, 869–875 (1959).

[69] P. Hawkes, *"The correction of electron lens aberrations"*, Ultramicroscopy **156**, A1–A64 (2015).

[70] Q. M. Ramasse, *"Twenty years after: How âĂIJAberration correction in the STEMâĂİ truly placed a âĂIJA synchrotron in a MicroscopeâĂİ"*, Ultramicroscopy **180**, 41–51 (2017).

[71] S. J. Pennycook, *"A Scan Through the History of STEM"*, in *Scanning Transmission Electron Microscopy*, S. J. Pennycook and P. D. Nellist, eds., pp. 1–90. Springer New York, New York, NY, 2011.

[72] P. D. Nellist, *"Direct Sub-Angstrom Imaging of a Crystal Lattice"*, Science **305**, 1741–1741 (2004).

[73] J. L. Hart, A. C. Lang, A. C. Leff, P. Longo, C. Trevor, R. D. Twesten, and M. L. Taheri, *"Direct Detection Electron Energy-Loss Spectroscopy: A Method to Push the Limits of Resolution and Sensitivity"*, Scientific Reports **7**, 8243 (2017).

[74] X. Ke, C. Bittencourt, and G. Van Tendeloo, *"Possibilities and limitations of advanced transmission electron microscopy for carbon-based nanomaterials"*, Beilstein Journal of Nanotechnology **6**, 1541–1557 (2015).

[75] M. J. Lagos, A. Trügler, U. Hohenester, and P. E. Batson, *"Mapping vibrational surface and bulk modes in a single nanocube"*, Nature **543**, 529–532 (2017).

[76] A. A. Govyadinov, A. Konečná, A. Chuvilin, S. Vélez, I. Dolado, A. Y. Nikitin, S. Lopatin, F. Casanova, L. E. Hueso, J. Aizpurua, and R. Hillenbrand, *"Probing low-energy hyperbolic polaritons in van der Waals crystals with an electron microscope"*, Nature Communications **8**, (2017).

[77] P. M. Zeiger and J. Rusz, *"Efficient and Versatile Model for Vibrational STEM-EELS"*, Physical Review Letters **124**, 25501 (2020).

[78] H. Lourenço-Martins and M. Kociak, *"Vibrational surface electron-energy-loss spectroscopy probes confined surface-phonon modes"*, Physical Review X **7**, 1–11 (2017).

[79] P. Rez, T. Aoki, K. March, D. Gur, O. L. Krivanek, N. Dellby, T. C. Lovejoy, S. G. Wolf, and H. Cohen, *"Damage-free vibrational spectroscopy of biological materials in the electron microscope"*, Nature Communications **7**, 10945 (2016).

[80] J. A. Hachtel, J. Huang, I. Popovs, S. Jansone-Popova, J. K. Keum, J. Jakowski, T. C. Lovejoy, N. Dellby, O. L. Krivanek, and J. C. Idrobo, *"Identification of site-specific isotopic labels by vibrational spectroscopy in the electron microscope"*, Science **363**, 525–528 (2019).

[81] N. Jiang, D. Su, J. C. Spence, S. Zhou, and J. Qiu, *"Volume plasmon of bismuth nanoparticles"*, Solid State Communications **149**, 111–114 (2009).

[82] J. A. Scholl, A. L. Koh, and J. A. Dionne, *"Quantum plasmon resonances of individual metallic nanoparticles"*, Nature **483**, 421–427 (2012).

[83] S. Raza, N. Stenger, S. Kadkhodazadeh, S. V. Fischer, N. Kostesha, A. P. Jauho, A. Burrows, M. Wubs, and N. A. Mortensen, *"Blueshift of the surface plasmon resonance in silver nanoparticles studied with EELS"*, Nanophotonics **2**, 131–138 (2013).

[84] S. Raza, S. Kadkhodazadeh, T. Christensen, M. Di Vece, M. Wubs, N. A. Mortensen, and N. Stenger, *"Multipole plasmons and their disappearance in few-nanometre silver nanoparticles"*, Nature Communications **6**, 1–30 (2015).

[85] R. G. Hobbs, V. R. Manfrinato, Y. Yang, S. A. Goodman, L. Zhang, E. A. Stach, and K. K. Berggren, *"High-Energy Surface and Volume Plasmons in Nanopatterned Sub-10 nm Aluminum Nanostructures"*, Nano Letters **16**, 4149–4157 (2016).

[86] A. Campos, N. Troc, E. Cottancin, M. Pellarin, H.-C. Weissker, J. Lermé, M. Kociak, and M. Hillenkamp, *"Plasmonic quantum size effects in silver nanoparticles are dominated by interfaces and local environments"*, Nature Physics **15**, 275–280 (2019).

[87] J. A. Scholl, A. García-Etxarri, A. L. Koh, and J. A. Dionne, *"Observation of quantum tunneling between two plasmonic nanoparticles"*, Nano Letters **13**, 564–569 (2013).

[88] S. Kadkhodazadeh, J. B. Wagner, H. Kneipp, and K. Kneipp, *"Coexistence of classical and quantum plasmonics in large plasmonic structures with subnanometer gaps"*, Applied Physics Letters **103**, 83103 (2013).

[89] T. Lünskens, P. Heister, M. Thämer, C. A. Walenta, A. Kartouzian, and U. Heiz, *"Plasmons in supported size-selected silver nanoclusters"*, Physical Chemistry Chemical Physics **17**, 17541–17544 (2015).

[90] Y. W. Wang, J. S. Kim, G. H. Kim, and K. S. Kim, *"Quantum size effects in the volume plasmon excitation of bismuth nanoparticles investigated by electron energy loss spectroscopy"*, Applied Physics Letters **88**, 3–6 (2006).

[91] N. D. Lang and W. Kohn, *"Theory of Metal Surfaces: Charge Density and Surface Energy"*, Physical Review B **1**, 4555–4568 (1970).

[92] A. Liebsch, *"Surface-plasmon dispersion and size dependence of Mie resonance: Silver versus simple metals"*, Physical Review B **48**, 11317–11328 (1993).

[93] A. Rivacoba, *"Electron spill-out effects in plasmon excitations by fast electrons"*, Ultramicroscopy **207**, 112835 (2019).

[94] T. Christensen, W. Yan, S. Raza, A.-P. Jauho, N. A. Mortensen, and M. Wubs, *"Nonlocal Response of Metallic Nanospheres Probed by Light, Electrons, and Atoms"*, ACS Nano **8**, 1745–1758 (2014).

[95] N. A. Mortensen, S. Raza, M. Wubs, T. Søndergaard, and S. I. Bozhevolnyi, *"A generalized non-local optical response theory for plasmonic nanostructures"*, Nature Communications **5**, (2014).

[96] R. Esteban, A. G. Borisov, P. Nordlander, and J. Aizpurua, *"Bridging quantum and classical plasmonics with a quantum-corrected model"*, Nature Communications **3**, 1–9 (2012).

[97] I. Lindau and P. O. Nilsson, *"Experimental Verification of Optically Excited Longitudinal Plasmons"*, Physica Scripta **3**, 87–92 (1971).

[98] M. Anderegg, B. Feuerbacher, and B. Fitton, *"Optically Excited Longitudinal Plasmons in Potassium"*, Physical Review Letters **27**, 1565–1568 (1971).

[99] M. M. Özer, E. J. Moon, A. G. Eguiluz, and H. H. Weitering, *"Plasmon response of a quantum-confined electron gas probed by core-level photoemission"*, Physical Review Letters **106**, 1–4 (2011).

[100] T. Hanrath and B. A. Korgel, *"A comprehensive study of electron energy losses in Ge nanowires"*, Nano Letters **4**, 1455–1461 (2004).

[101] M. S. Sander, R. Gronsky, Y. M. Lin, and M. S. Dresselhaus, *"Plasmon excitation modes in nanowire arrays"*, Journal of Applied Physics **89**, 2733–2736 (2001).

[102] R. Borja-Urby, S. P. Paredes-Carrera, H. Viltres-Cobas, P. Santiago-Jacinto, F. Paraguay-Delgado, G. Herrera-Pérez, L. Rendón-Vázquez, J. C. Sánchez-Ochoa, and D. Morales-Cruz, *"Confined volume plasmon spatial distribution by low-loss EELS on self-assemble bismuth nanoparticles"*, Journal of Electron Spectroscopy and Related Phenomena **237**, 146891 (2019).

[103] J. L. Gervasoni and N. R. Arista, *"Plasmon excitations in cylindrical wires by external charged particles"*, Physical Review B **68**, 235302 (2003).

[104] S. Segui, J. Gervasoni, and N. Arista, *"Impact parameter dependence of plasmon excitations in cylindrical nanostructures"*, Nuclear Instruments and Methods in Physics Research Section B: Beam Interactions with Materials and Atoms **233**, 227–231 (2005).

[105] J. Aizpurua and A. Rivacoba, *"Nonlocal effects in the plasmons of nanowires and nanocavities excited by fast electron beams"*, Physical Review B **78**, 035404 (2008).

[106] M. Barbry, P. Koval, F. Marchesin, R. Esteban, A. G. Borisov, J. Aizpurua, and D. Sánchez-Portal, *"Atomistic near-field nanoplasmonics: Reaching atomic-scale resolution in nanooptics"*, Nano Letters **15**, 3410–3419 (2015).

[107] S. Trautmann, J. Aizpurua, I. Götz, A. Undisz, J. Dellith, H. Schneidewind, M. Rettenmayr, and V. Deckert, *"A classical description of subnanometer resolution by atomic features in metallic structures"*, Nanoscale **9**, 391–401 (2017).

[108] F. J. García de Abajo and A. Howie, *"Retarded field calculation of electron energy loss in inhomogeneous dielectrics"*, Physical Review B **65**, 115418 (2002).

[109] U. Hohenester and A. Trügler, *"MNPBEM - A Matlab toolbox for the simulation of plasmonic nanoparticles"*, Computer Physics Communications **183**, 370–381 (2012).

[110] U. Hohenester, *"Simulating electron energy loss spectroscopy with the MNPBEM toolbox"*, Computer Physics Communications **185**, 1177–1187 (2014).

[111] J. Waxenegger, A. Trügler, and U. Hohenester, *"Plasmonics simulations with the MNPBEM toolbox: Consideration of substrates and layer structures"*, Computer Physics Communications **193**, 138–150 (2015).

[112] A. Trügler, *Optical Properties of Metallic Nanoparticles*, volume 232 of *Springer Series in Materials Science*. Springer International Publishing, Cham, 2016.

[113] J. D. Jackson, *"Classical Electrodynamics"*, in *Classical Electrodynamics*. WIley, New York, NY, 3rd ed., 1999.

[114] F. García de Abajo and J. Aizpurua, *"Numerical simulation of electron energy loss near inhomogeneous dielectrics"*, Physical Review B - Condensed Matter and Materials Physics **56**, 15873–15884 (1997).

[115] C. Weng Cho, *Waves and Fields in Inhomogenous Media*. Wiley-IEEE Press, 1999.

[116] M. Paulus, P. Gay-Balmaz, and O. J. F. Martin, *"Accurate and efficient computation of the Green's tensor for stratified media"*, Physical Review E **62**, 5797–5807 (2000).

[117] X. Chen, J. E. Moore, M. Zekarias, and L. Jensen, *"Atomistic electrodynamics simulations of bare and ligand-coated nanoparticles in the quantum size regime"*, Nature Communications **6**, 8921 (2015).

[118] L. Silberstein, *"L. Molecular refractivity and atomic interaction . II"*, The London, Edinburgh, and Dublin Philosophical Magazine and Journal of Science **33**, 521–533 (1917).

[119] J. Applequist, J. R. Carl, and K.-K. Fung, *"Atom dipole interaction model for molecular polarizability. Application to polyatomic molecules and determination of atom polarizabilities"*, Journal of the American Chemical Society **94**, 2952–2960 (1972).

[120] J. Applequist, *"An atom dipole interaction model for molecular optical properties"*, Accounts of Chemical Research **10**, 79–85 (1977).

[121] L. Jensen, P. O. Åstrand, and K. V. Mikkelsen, *"An atomic capacitance-polarizability model for the calculation of molecular dipole moments and polarizabilities"*, International Journal of Quantum Chemistry **84**, 513–522 (2001).

[122] R. R. Birge, *"Calculation of molecular polarizabilities using an anisotropic atom point dipole interaction model which includes the effect of electron repulsion"*, The Journal of Chemical Physics **72**, 5312–5319 (1980).

[123] B. T. Thole, *"Molecular polarizabilities calculated with a modified dipole interaction"*, Chemical Physics **59**, 341–350 (1981).

[124] R. R. Birge, G. A. Schick, and D. F. Bocian, *"Calculation of molecular polarizabilities using a semiclassical SlaterâĂŘtype orbitalâĂŘpoint dipole interaction (STOPDI) model"*, The Journal of Chemical Physics **79**, 2256–2264 (1983).

[125] S. W. Rick, S. J. Stuart, and B. J. Berne, *"Dynamical fluctuating charge force fields: Application to liquid water"*, The Journal of Chemical Physics **101**, 6141–6156 (1994).

[126] D. M. York and W. Yang, *"A chemical potential equalization method for molecular simulations"*, The Journal of Chemical Physics **104**, 159–172 (1996).

[127] L. Jensen, P.-O. Åstrand, K. O. Sylvester-Hvid, and K. V. Mikkelsen, *"Frequency-Dependent Molecular Polarizability Calculated within an Interaction Model"*, The Journal of Physical Chemistry A **104**, 1563–1569 (2000).

[128] L. Jensen, P.-O. Åstrand, A. Osted, J. Kongsted, and K. V. Mikkelsen, *"Polarizability of molecular clusters as calculated by a dipole interaction model"*, The Journal of Chemical Physics **116**, 4001–4010 (2002).

[129] M. L. Olson and K. R. Sundberg, *"An atom monopoleâĂŞdipole interaction model with charge transfer for the treatment of polarizabilities of πâĂŘbonded molecules."*, The Journal of Chemical Physics **69**, 5400–5404 (1978).

[130] J. Applequist, *"Atom charge transfer in molecular polarizabilities: application of the Olson-Sundberg model to aliphatic and aromatic hydrocarbons"*, The Journal of Physical Chemistry **97**, 6016–6023 (1993).

[131] H. A. Stern, F. Rittner, B. J. Berne, and R. A. Friesner, *"Combined fluctuating charge and polarizable dipole models: Application to a five-site water potential function"*, The Journal of Chemical Physics **115**, 2237–2251 (2001).

[132] A. Mayer, *"Formulation in terms of normalized propagators of a charge-dipole model enabling the calculation of the polarization properties of fullerenes and carbon nanotubes"*, Physical Review B **75**, 045407 (2007).

[133] A. Mayer and P.-O. Åstrand, *"A ChargeâĹŠDipole Model for the Static Polarizability of Nanostructures Including Aliphatic, Olephinic, and Aromatic Systems"*, The Journal of Physical Chemistry A **112**, 1277–1285 (2008).

[134] L. L. Jensen and L. Jensen, *"Electrostatic Interaction Model for the Calculation of the Polarizability of Large Noble Metal Nanoclusters"*, The Journal of Physical Chemistry C **112**, 15697–15703 (2008).

[135] L. L. Jensen and L. Jensen, *"Atomistic Electrodynamics Model for Optical Properties of Silver Nanoclusters"*, The Journal of Physical Chemistry C **113**, 15182–15190 (2009).

[136] E. M. Purcell and C. R. Pennypacker, *"Scattering and Absorption of Light by Nonspherical Dielectric Grains"*, The Astrophysical Journal **186**, 705 (1973).

[137] B. T. Draine and P. J. Flatau, *"Discrete-Dipole Approximation For Scattering Calculations"*, Journal of the Optical Society of America A **11**, 1491 (1994).

[138] C. Cohen-Tannoudji, B. Diu, F. LaloÌĹ, and B. Crasemann, *Quantum Mechanics*. 1979.

[139] R. M. Dreizler and E. K. U. Gross, *Density Functional Theory: An Approach to the Quantum Many-Body Problem*. 1990.

[140] R. O. Jones and O. Gunnarsson, *"The density functional formalism, its applications and prospects"*, Reviews of Modern Physics **61**, 689–746 (1989).

[141] P. Hohenberg and W. Kohn, *"Inhomogeneous Electron Gas"*, Physical Review **136**, B864–B871 (1964).

[142] W. Kohn and L. J. Sham, *"Self-Consistent Equations Including Exchange and Correlation Effects"*, Physical Review **140**, A1133–A1138 (1965).

[143] J. P. Perdew and A. Zunger, *"Self-interaction correction to density-functional approximations for many-electron systems"*, Physical Review B **23**, 5048–5079 (1981).

[144] J. P. Perdew, K. Burke, and M. Ernzerhof, *"Generalized Gradient Approximation Made Simple"*, Physical Review Letters **77**, 3865–3868 (1996).

[145] Z. Wu and R. E. Cohen, *"More accurate generalized gradient approximation for solids"*, Physical Review B - Condensed Matter and Materials Physics **73**, 235116 (2006).

[146] E. Runge and E. K. Gross, *"Density-functional theory for time-dependent systems"*, Physical Review Letters **52**, 997–1000 (1984).

[147] K. Yabana and G. F. Bertsch, *"Time-dependent local-density approximation in real time"*, Physical Review B **54**, 4484–4487 (1996).

[148] A. Tsolakidis, D. Sánchez-Portal, and R. M. Martin, *"Calculation of the optical response of atomic clusters using time-dependent density functional theory and local orbitals"*, Physical Review B - Condensed Matter and Materials Physics **66**, 1–9 (2002).

[149] M. Petersilka, U. J. Gossmann, and E. K. Gross, *"Excitation energies from time-dependent density-functional theory"*, Physical Review Letters **76**, 1212–1215 (1996).

[150] P. Koval, F. Marchesin, D. Foerster, and D. Sánchez-Portal, *"Optical response of silver clusters and their hollow shells from linear-response TDDFT"*, Journal of Physics: Condensed Matter **28**, 214001 (2016).

[151] P. Koval, M. Barbry, and D. Sánchez-Portal, *"PySCF-NAO: An efficient and flexible implementation of linear response time-dependent density functional theory with numerical atomic orbitals"*, Computer Physics Communications **236**, 188–204 (2019).

[152] N. H. F. Beebe and J. Linderberg, *"Simplifications in the generation and transformation of two-electron integrals in molecular calculations"*, International Journal of Quantum Chemistry **12**, 683–705 (1977).

[153] C.-K. Skylaris, L. Gagliardi, N. Handy, A. Ioannou, S. Spencer, and A. Willetts, *"On the resolution of identity Coulomb energy approximation in density functional theory"*, Journal of Molecular Structure: THEOCHEM **501-502**, 229–239 (2000).

[154] E. Baerends, D. Ellis, and P. Ros, *"Self-consistent molecular Hartree-Fock-Slater calculations I. The computational procedure"*, Chemical Physics **2**, 41–51 (1973).

[155] D. Foerster, *"On an "interaction by moments" property of four center integrals"*,.

[156] D. Foerster, *"Elimination, in electronic structure calculations, of redundant orbital products"*, Journal of Chemical Physics **128**, 034108 (2008).

[157] M. Barbry, *Plasmons in Nanoparticles: Atomistic Ab Initio Theory for Large Systems*. PhD thesis, University of the Basque Country, UPV-EHU, San Sebastian, 2018. `http://hdl.handle.net/10261/180261`.

[158] P. Bharadwaj, B. Deutsch, and L. Novotny, *"Optical Antennas"*, Advances in Optics and Photonics **1**, 438 (2009).

[159] V. Giannini, A. I. Fernández-Domínguez, S. C. Heck, and S. A. Maier, *"Plasmonic Nanoantennas: Fundamentals and Their Use in Controlling the Radiative Properties of Nanoemitters"*, Chemical Reviews **111**, 3888–3912 (2011).

[160] P. Biagioni, J.-S. Huang, and B. Hecht, *"Nanoantennas for visible and infrared radiation"*, Reports on Progress in Physics **75**, 024402 (2012).

[161] S. A. Maier, P. G. Kik, H. A. Atwater, S. Meltzer, E. Harel, B. E. Koel, and A. A. Requicha, *"Local detection of electromagnetic energy transport below the diffraction limit in metal nanoparticle plasmon waveguides"*, Nature Materials **2**, 229–232 (2003).

[162] S. Link and M. A. El-Sayed, *"Spectral Properties and Relaxation Dynamics of Surface Plasmon Electronic Oscillations in Gold and Silver Nanodots and Nanorods"*, Journal of Physical Chemistry B **103**, 8410–8426 (1999).

[163] R. Jin, Y. Cao, C. A. Mirkin, K. L. Kelly, G. C. Schatz, and J. G. Zheng, *"Photoinduced conversion of silver nanospheres to nanoprisms"*, Science **294**, 1901–1903 (2001).

[164] R. D. Averitt, D. Sarkar, and N. J. Halas, *"Plasmon resonance shifts of au-coated Au2S nanoshells: Insight into multicomponent nanoparticle growth"*, Physical Review Letters **78**, 4217–4220 (1997).

[165] F. J. Recio, N. Zabala, A. Rivacoba, P. Crespo, A. Ayuela, P. M. Echenique, and A. Hernando, *"Optical resonances of colloidal gold nanorods: From seeds to chemically thiolated long nanorods"*, Journal of Physical Chemistry C **119**, 7856–7864 (2015).

[166] V. Myroshnychenko, J. Rodríguez-Fernández, I. Pastoriza-Santos, A. M. Funston, C. Novo, P. Mulvaney, L. M. Liz-Marzán, and F. J. García de Abajo, *"Modelling the optical response of gold nanoparticles"*, Chemical Society Reviews **37**, 1792 (2008).

[167] J. Aizpurua, P. Hanarp, D. S. Sutherland, M. Käll, G. W. Bryant, and F. J. García de Abajo, *"Optical Properties of Gold Nanorings"*, Physical Review Letters **90**, 4 (2003).

[168] A. M. Funston, C. Novo, T. J. Davis, and P. Mulvaney, *"Plasmon coupling of gold nanorods at short distances and in different geometries"*, Nano Letters **9**, 1651–1658 (2009).

[169] F. Hao, C. L. Nehl, J. H. Hafner, and P. Nordlander, *"Plasmon resonances of a gold nanostar"*, Nano Letters **7**, 729–732 (2007).

[170] S. M. Novikov, A. Sánchez-Iglesias, M. K. Schmidt, A. Chuvilin, J. Aizpurua, M. Grzelczak, and L. M. Liz-Marzán, *"Gold Spiky Nanodumbbells: Anisotropy in Gold Nanostars"*, Particle & Particle Systems Characterization **31**, 77–80 (2014).

[171] O. Pérez-González, N. Zabala, A. G. Borisov, N. J. Halas, P. Nordlander, and J. Aizpurua, *"Optical spectroscopy of conductive junctions in plasmonic cavities"*, Nano Letters **10**, 3090–3095 (2010).

[172] E. Townsend and G. W. Bryant, *"Plasmonic Properties of Metallic Nanoparticles: The Effects of Size Quantization"*, Nano Letters **12**, 429–434 (2012).

[173] R. Carmina Monreal, T. J. Antosiewicz, and S. P. Apell, *"Competition between surface screening and size quantization for surface plasmons in nanoparticles"*, New Journal of Physics **15**, 083044 (2013).

[174] C. F. A. Negre, E. M. Perassi, E. A. Coronado, and C. G. Sánchez, *"Quantum dynamical simulations of local field enhancement in metal nanoparticles"*, J. Phys.: Condens. Matter **25**, 125304–125313 (2013).

[175] K. Iida, M. Noda, K. Ishimura, and K. Nobusada, *"First-principles computational visualization of localized surface plasmon resonance in gold nanoclusters"*, Journal of Physical Chemistry A **118**, 11317–11322 (2014).

[176] P. J. Feibelman, *"Microscopic calculation of electromagnetic fields in refraction at a jellium-vacuum interface"*, Physical Review B **12**, 1319–1336 (1975).

[177] A. Liebsch and W. L. Schaich, *"Influence of a polarizable medium on the nonlocal optical response of a metal surface"*, Physical Review B **52**, 14219–14234 (1995).

[178] P. Zhang, J. Feist, A. Rubio, P. García-González, and F. J. García-Vidal, *"Ab initio nanoplasmonics: The impact of atomic structure"*, Physical Review B - Condensed Matter and Materials Physics **90**, 161407 (2014).

[179] J. Zuloaga, E. Prodan, and P. Nordlander, *"Quantum Description of the Plasmon Resonances of a Nanoparticle Dimer"*, Nano Letters **9**, 887–891 (2009).

[180] D. C. Marinica, A. K. Kazansky, P. Nordlander, J. Aizpurua, and A. G. Borisov, *"Quantum plasmonics: Nonlinear effects in the field enhancement of a plasmonic nanoparticle dimer"*, Nano Letters **12**, 1333–1339 (2012).

[181] C. Ciracì, J. B. Pendry, and D. R. Smith, *"Hydrodynamic Model for Plasmonics: A Macroscopic Approach to a Microscopic Problem"*, ChemPhysChem **14**, 1109–1116 (2013).

[182] R. Esteban, A. Zugarramurdi, P. Zhang, P. Nordlander, F. J. García-Vidal, A. G. Borisov, and J. Aizpurua, *"A classical treatment of optical tunneling in plasmonic gaps: Extending the quantum corrected model to practical situations"*, Faraday Discussions **178**, 151–183 (2015).

[183] L. Jensen, J. Autschbach, and G. C. Schatz, *"Finite lifetime effects on the polarizability within time-dependent density-functional theory"*, Journal of Chemical Physics **122**, 224115 (2005).

[184] L. Zhao, L. Jensen, and G. C. Schatz, *"Pyridine-Ag20 cluster: A model system for studying surface-enhanced Raman scattering"*, Journal of the American Chemical Society **128**, 2911–2919 (2006).

[185] C. M. Aikens, S. Li, and G. C. Schatz, *"From discrete electronic states to plasmons: TDDFT optical absorption properties of Agn (n = 10, 20, 35, 56, 84, 120) tetrahedral clusters"*, Journal of Physical Chemistry C **112**, 11272–11279 (2008).

[186] S. Malola, L. Lehtovaara, J. Enkovaara, and H. Häkkinen, *"Birth of the localized surface plasmon resonance in monolayer-protected gold nanoclusters"*, ACS Nano **7**, 10263–10270 (2013).

[187] M. Kuisma, A. Sakko, T. P. Rossi, A. H. Larsen, J. Enkovaara, L. Lehtovaara, and T. T. Rantala, *"Localized surface plasmon resonance in silver nanoparticles: Atomistic first-principles time-dependent density-functional theory calculations"*, Physical Review B **91**, 115431 (2015).

[188] F. Marchesin, P. Koval, M. Barbry, J. Aizpurua, and D. Sánchez-Portal, *"Plasmonic Response of Metallic Nanojunctions Driven by Single Atom Motion: Quantum Transport Revealed in Optics"*, ACS Photonics **3**, 269–277 (2016).

[189] R. G. Parr and W. Yang, *Density-Functional Theory of Atoms and Molecules*. Oxford University Press, 1989.

[190] J. N. Murrell and R. E. Mottram, *"Potential energy functions for atomic solids"*, Molecular Physics **69**, 571–585 (1990).

[191] E. G. Noya, J. P. Doye, D. J. Wales, and A. Aguado, *"Geometric magic numbers of sodium clusters: Interpretation of the melting behaviour"*, The European Physical Journal D **43**, 57–60 (2007).

[192] D. Sánchez-Portal, P. Ordejón, E. Artacho, and J. M. Soler, *"Density-functional method for very large systems with LCAO basis sets"*, International Journal of Quantum Chemistry **65**, 453–461 (1997).

[193] J. M. Soler, E. Artacho, J. D. Gale, A. García, J. Junquera, P. Ordejón, and D. Sánchez-Portal, *"The SIESTA method for ab initio order- N materials simulation"*, Journal of Physics: Condensed Matter **14**, 2745–2779 (2002).

[194] A. Manjavacas, F. Marchesin, S. Thongrattanasiri, P. Koval, P. Nordlander, D. Sánchez-Portal, and F. J. García de Abajo, *"Tunable Molecular Plasmons in Polycyclic Aromatic Hydrocarbons"*, ACS Nano **7**, 3635–3643 (2013).

[195] A. Moroz, *"Electron Mean Free Path in a Spherical Shell Geometry"*, The Journal of Physical Chemistry C **112**, 10641–10652 (2008).

[196] U. Kreibig and C. v. Fragstein, *"The limitation of electron mean free path in small silver particles"*, Zeitschrift für Physik **224**, 307–323 (1969).

[197] C. Dellago and H. A. Posch, *"Lyapunov Instability of the Boundary-Driven ChernovâĂŞLebowitz Model for Stationary Shear Flow"*, Journal of Statistical Physics **88**, 825–842 (1997).

[198] N. W. Ashcroft and N. D. Mermin, *Solid state physics*. Saunders College, Philadelphia Pa., 1976.

[199] M. G. Blaber, M. D. Arnold, and M. J. Ford, *"Search for the Ideal Plasmonic Nanoshell: The Effects of Surface Scattering and Alternatives to Gold and Silver"*, The Journal of Physical Chemistry C **113**, 3041–3045 (2009).

[200] D. R. Ward, N. K. Grady, C. S. Levin, N. J. Halas, Y. Wu, P. Nordlander, and D. Natelson, *"Electromigrated Nanoscale Gaps for Surface-Enhanced Raman Spectroscopy"*, Nano Letters **7**, 1396–1400 (2007).

[201] K. A. Willets and R. P. Van Duyne, *"Localized Surface Plasmon Resonance Spectroscopy and Sensing"*, Annual Review of Physical Chemistry **58**, 267–297 (2007).

[202] D.-K. Lim, K.-S. Jeon, H. M. Kim, J.-M. Nam, and Y. D. Suh, *"Nanogap-engineerable Raman-active nanodumbbells for single-molecule detection"*, Nature Materials **9**, 60–67 (2010).

[203] G. Haran, *"Single-Molecule Raman Spectroscopy: A Probe of Surface Dynamics and Plasmonic Fields"*, Accounts of Chemical Research **43**, 1135–1143 (2010).

[204] P. T. Kristensen and S. Hughes, *"Modes and Mode Volumes of Leaky Optical Cavities and Plasmonic Nanoresonators"*, ACS Photonics **1**, 2–10 (2014).

[205] P. Lalanne, W. Yan, K. Vynck, C. Sauvan, and J.-P. Hugonin, *"Light Interaction with Photonic and Plasmonic Resonances"*, Laser & Photonics Reviews **12**, 1700113 (2018).

[206] P. T. Kristensen, C. Van Vlack, and S. Hughes, *"Generalized effective mode volume for leaky optical cavities"*, Optics Letters **37**, 1649 (2012).

[207] M. Moskovits, *"Surface-enhanced spectroscopy"*, Reviews of Modern Physics **57**, 783–826 (1985).

[208] J. J. Baumberg, J. Aizpurua, M. H. Mikkelsen, and D. R. Smith, *"Extreme nanophotonics from ultrathin metallic gaps"*, Nature Materials **18**, 668–678 (2019).

[209] C. Ciracì, R. T. Hill, J. J. Mock, Y. Urzhumov, A. I. Fernández-Domínguez, S. A. Maier, J. B. Pendry, A. Chilkoti, and D. R. Smith, *"Probing the ultimate limits of plasmonic enhancement"*, Science **337**, 1072–1074 (2012).

[210] J. Mertens, A. L. Eiden, D. O. Sigle, F. Huang, A. Lombardo, Z. Sun, R. S. Sundaram, A. Colli, C. Tserkezis, J. Aizpurua, S. Milana, A. C. Ferrari, and J. J. Baumberg, *"Controlling subnanometer gaps in plasmonic dimers using graphene"*, Nano Letters **13**, 5033–5038 (2013).

[211] N. Yamamoto, S. Ohtani, and F. J. García De Abajo, *"Gap and mie plasmons in individual silver nanospheres near a silver surface"*, Nano Letters **11**, 91–95 (2011).

[212] C. Carnegie, J. Griffiths, B. De Nijs, C. Readman, R. Chikkaraddy, W. M. Deacon, Y. Zhang, I. Szabó, E. Rosta, J. Aizpurua, and J. J. Baumberg, *"Room-Temperature Optical Picocavities below 1 nm 3 Accessing Single-Atom Geometries"*, Journal of Physical Chemistry Letters **9**, 7146–7151 (2018).

[213] S. I. Bozhevolnyi and T. Søndergaard, *"General properties of slow-plasmon resonant nanostructures: nano-antennas and resonators"*, Optics Express **15**, 10869 (2007).

[214] M. Kuttge, W. Cai, F. J. García de Abajo, and A. Polman, *"Dispersion of metal-insulator-metal plasmon polaritons probed by cathodoluminescence imaging spectroscopy"*, Physical Review B **80**, 033409 (2009).

[215] R. Filter, J. Qi, C. Rockstuhl, and F. Lederer, *"Circular optical nanoantennas: an analytical theory"*, Physical Review B **85**, 125429 (2012).

[216] C. Tserkezis, R. Esteban, D. O. Sigle, J. Mertens, L. O. Herrmann, J. J. Baumberg, and J. Aizpurua, *"Hybridization of plasmonic antenna and cavity modes: Extreme optics of nanoparticle-on-mirror nanogaps"*, Physical Review A - Atomic, Molecular, and Optical Physics **92**, 1–6 (2015).

[217] R. Gordon, *"Light in a subwavelength slit in a metal: Propagation and reflection"*, Physical Review B - Condensed Matter and Materials Physics **73**, 153405 (2006).

[218] C. Carnegie, M. Urbieta, R. Chikkaraddy, B. de Nijs, J. Griffiths, W. M. Deacon, M. Kamp, N. Zabala, J. Aizpurua, and J. J. Baumberg, *"Flickering nanometre-scale disorder in a crystal lattice tracked by plasmonic flare light emission"*, Nature Communications **11**, 682 (2020).

[219] C. Carnegie, *Plasmonic Sensing via Surface-Enhanced Spectroscopies*. PhD thesis, University of Cambridge, 2019. https://www.repository.cam.ac.uk/handle/1810/298860.

[220] S. Alekseeva, A. B. D. S. Fanta, B. Iandolo, T. J. Antosiewicz, F. A. A. Nugroho, J. B. Wagner, A. Burrows, V. P. Zhdanov, and C. Langhammer, *"Grain boundary mediated hydriding phase transformations in individual polycrystalline metal nanoparticles"*, Nature Communications **8**, 1–9 (2017).

[221] O. Hunderi, *"Influence of Grain Boundaries and Lattice Defects on the Optical Properties of Some Metals"*, Physical Review B **7**, 3419–3429 (1973).

[222] L. D. Marks, *"Surface structure and energetics of multiply twinned particles"*, Philosophical Magazine A **49**, 81–93 (1984).

[223] L. D. Marks, *"Experimental studies of small particle structures"*, Reports on Progress in Physics **57**, 603–649 (1994).

[224] P. M. Ajayan and L. D. Marks, *"Quasimelting and phases of small particles"*, Physical Review Letters **60**, 585–587 (1988).

[225] J. Mertens, A. Demetriadou, R. W. Bowman, F. Benz, M. E. Kleemann, C. Tserkezis, Y. Shi, H. Y. Yang, O. Hess, J. Aizpurua, and J. J. Baumberg, *"Tracking Optical Welding through Groove Modes in Plasmonic Nanocavities"*, Nano Letters **16**, 5605–5611 (2016).

[226] F. Benz, C. Tserkezis, L. O. Herrmann, B. De Nijs, A. Sanders, D. O. Sigle, L. Pukenas, S. D. Evans, J. Aizpurua, and J. J. Baumberg, *"Nanooptics of molecular-shunted plasmonic nanojunctions"*, Nano Letters **15**, 669–674 (2015).

[227] R. Chikkaraddy, B. de Nijs, F. Benz, S. J. Barrow, O. A. Scherman, E. Rosta, A. Demetriadou, P. Fox, O. Hess, and J. J. Baumberg, *"Single-molecule strong coupling at room temperature in plasmonic nanocavities"*, Nature **535**, 127–130 (2016).

[228] J. T. Hugall and J. J. Baumberg, *"Demonstrating Photoluminescence from Au is Electronic Inelastic Light Scattering of a Plasmonic Metal: The Origin of SERS Backgrounds"*, Nano Letters **15**, 2600–2604 (2015).

[229] M. Fox, *Optical Properties of Solids*. Oxford University Press, New York, 2001.

[230] F. Benz, B. de Nijs, C. Tserkezis, R. Chikkaraddy, D. O. Sigle, L. Pukenas, S. D. Evans, J. Aizpurua, and J. J. Baumberg, *"Generalized circuit model for coupled plasmonic systems"*, Optics Express **23**, 33255 (2015).

[231] K. Lu, *"Stabilizing nanostructures in metals using grain and twin boundary architectures"*, Nature Reviews Materials **1**, 16019 (2016).

[232] M. A. Tschopp and D. L. Mcdowell, *"Asymmetric tilt grain boundary structure and energy in copper and aluminium"*, Philosophical Magazine **87**, 3871–3892 (2007).

[233] J. Miao, P. Ercius, and S. J. L. Billinge, *"Atomic electron tomography: 3D structures without crystals"*, Science **353**, aaf2157–aaf2157 (2016).

[234] Z. Pei, X. Zhang, T. Hickel, M. Friák, S. Sandlöbes, B. Dutta, and J. Neugebauer, *"Atomic structures of twin boundaries in hexagonal close-packed metallic crystals with particular focus on Mg"*, npj Computational Materials **3**, 6 (2017).

[235] B. Goris, J. De Beenhouwer, A. De Backer, D. Zanaga, K. J. Batenburg, A. Sánchez-Iglesias, L. M. Liz-Marzán, S. Van Aert, S. Bals, J. Sijbers, and G. Van Tendeloo, *"Measuring Lattice Strain in Three Dimensions through Electron Microscopy"*, Nano Letters **15**, 6996–7001 (2015).

[236] D. Holec, P. Dumitraschkewitz, F. D. Fischer, and D. Vollath, *"Size-dependent surface energies of Au nanoparticles"*, arXiv (2014).

[237] M.-E. Kleemann, R. Chikkaraddy, E. M. Alexeev, D. Kos, C. Carnegie, W. Deacon, A. C. de Pury, C. Große, B. de Nijs, J. Mertens, A. I. Tartakovskii, and J. J. Baumberg, *"Strong-coupling of WSe2 in ultra-compact plasmonic nanocavities at room temperature"*, Nature Communications **8**, 1296 (2017).

[238] A. Surrey, D. Pohl, L. Schultz, and B. Rellinghaus, *"Quantitative Measurement of the Surface Self-Diffusion on Au Nanoparticles by Aberration-Corrected Transmission Electron Microscopy"*, Nano Letters **12**, 6071–6077 (2012).

[239] B. Song, J. Jansen, F. Tichelaar, H. Zandbergen, G. Gajewski, C. Pao, and D. Srolovitz, *"In-situ transmission electron microscopy and first-principles study of Au (100) surface dislocation dynamics"*, Surface Science **608**, 154–164 (2013).

[240] A. Owyoung and E. D. Jones, *"Stimulated Raman spectroscopy using low-power cw lasers"*, Optics Letters **1**, 152 (1977).

[241] J. Wu, A. K. Gupta, H. R. Gutierrez, and P. C. Eklund, *"Cavity-Enhanced Stimulated Raman Scattering from Short GaP Nanowires"*, Nano Letters **9**, 3252–3257 (2009).

[242] C.-R. Hu, M. N. Slipchenko, P. Wang, P. Wang, J. D. Lin, G. Simpson, B. Hu, and J.-X. Cheng, *"Stimulated Raman scattering imaging by continuous-wave laser excitation"*, Optics Letters **38**, 1479 (2013).

[243] C. L. D. Lee and K. C. Hewitt, *"First demonstration of surface enhanced-stimulated Raman spectroscopy (SE-SRS) using low-power CW sources"*, Faraday Discussions **205**, 227–232 (2017).

[244] N. Grillet, D. Manchon, F. Bertorelle, C. Bonnet, M. Broyer, E. Cottancin, J. Lermé, M. Hillenkamp, and M. Pellarin, *"Plasmon coupling in silver nanocube dimers: Resonance splitting induced by edge rounding"*, ACS Nano **5**, 9450–9462 (2011).

[245] D. O. Sigle, J. Mertens, L. O. Herrmann, R. W. Bowman, S. Ithurria, B. Dubertret, Y. Shi, H. Y. Yang, C. Tserkezis, J. Aizpurua, and J. J. Baumberg, *"Monitoring morphological changes in 2D monolayer semiconductors using atom-thick plasmonic nanocavities"*, ACS Nano **9**, 825–830 (2015).

[246] P. E. Batson, *"Surface Plasmon Coupling in Clusters of Small Spheres"*, Physical Review Letters **49**, 936–940 (1982).

[247] P. E. Batson, *"A new surface plasmon resonance in clusters of small aluminum spheres"*, Ultramicroscopy **9**, 277–282 (1982).

[248] A. L. Koh, A. I. FernaÌĄndez-DomiÌĄnguez, D. W. McComb, S. A. Maier, and J. K. W. Yang, *"High-Resolution Mapping of Electron-Beam-Excited Plasmon Modes in Lithographically Defined Gold Nanostructures"*, Nano Letters **11**, 1323–1330 (2011).

[249] H. Duan, A. I. Fernández-Domínguez, M. Bosman, S. A. Maier, and J. K. W. Yang, *"Nanoplasmonics: Classical down to the Nanometer Scale"*, Nano Letters **12**, 1683–1689 (2012).

[250] S. F. Tan, L. Wu, J. K. Yang, P. Bai, M. Bosman, and C. A. Nijhuis, *"Quantum plasmon resonances controlled by molecular tunnel junctions"*, Science **343**, 1496–1499 (2014).

[251] O. Nicoletti, F. De La Peña, R. K. Leary, D. J. Holland, C. Ducati, and P. A. Midgley, *"Three-dimensional imaging of localized surface plasmon resonances of metal nanoparticles"*, Nature **502**, 80–84 (2013).

[252] A. Hörl, G. Haberfehlner, A. Trügler, F.-P. Schmidt, U. Hohenester, and G. Kothleitner, *"Tomographic imaging of the photonic environment of plasmonic nanoparticles"*, Nature Communications **8**, 37 (2017).

[253] A. Rivacoba, N. Zabala, and P. M. Echenique, *"Theory of energy loss in scanning transmission electron microscopy of supported small particles"*, Physical Review Letters **69**, 3362–3365 (1992).

[254] N. Zabala, A. Rivacoba, and P. M. Echenique, *"Coupling effects in the excitations by an external electron beam near close particles"*, Physical Review B **56**, 7623–7635 (1997).

[255] A. Rivacoba, N. Zabala, and J. Aizpurua, *"Image potential in scanning transmission electron microscopy"*, Progress in Surface Science **65**, 1–64 (2000).

[256] Y. Cao, A. Manjavacas, N. Large, and P. Nordlander, *"Electron Energy-Loss Spectroscopy Calculation in Finite-Difference Time-Domain Package"*, ACS Photonics **2**, 369–375 (2015).

[257] A. Rivacoba and P. M. Echenique, *"Surface corrections to bulk energy losses in scanning transmission electron microscopy of spheres"*, Scanning Microscopy **4**, 73–78 (1990).

[258] T. L. Ferrell and P. M. Echenique, *"Generation of surface excitations on dielectric spheres by an external electron beam"*, Physical Review Letters **55**, 1526–1529 (1985).

[259] T. L. Ferrell, R. J. Warmack, V. E. Anderson, and P. M. Echenique, *"Analytical calculation of stopping power for isolated small spheres"*, Physical Review B **35**, 7365–7371 (1987).

[260] C. Noguez, *"Surface plasmons on metal nanoparticles: The influence of shape and physical environment"*, Journal of Physical Chemistry C **111**, 3606–3619 (2007).

[261] G. Toscano, J. Straubel, A. Kwiatkowski, C. Rockstuhl, F. Evers, H. Xu, N. Asger Mortensen, and M. Wubs, *"Resonance shifts and spill-out effects in self-consistent hydrodynamic nanoplasmonics"*, Nature Communications **6**, 1–11 (2015).

[262] S. A. Mezzasalma, S. A. Mezzasalma, M. Grzelczak, and J. Sancho-Parramon, *"The Crystal Field Plasmon Splitting"*, ACS Photonics **7**, 1551–1559 (2020).

[263] M. Urbieta, M. Barbry, Y. Zhang, P. Koval, D. Sánchez-Portal, N. Zabala, and J. Aizpurua, *"Atomic-Scale Lightning Rod Effect in Plasmonic Picocavities: A Classical View to a Quantum Effect"*, ACS Nano **12**, 585–595 (2018).

[264] S. Raza, S. I. Bozhevolnyi, M. Wubs, and N. Asger Mortensen, *"Nonlocal optical response in metallic nanostructures"*, Journal of Physics Condensed Matter **27**, (2015).

[265] S. M. Collins, *"Dispersion characteristics of face modes in ionic-crystal and plasmonic-metal nanoparticles"*, Physical Review B **97**, 1–8 (2018).

[266] H. Haberland, *"Looking from both sides"*, Nature **494**, 6–7 (2013).

[267] A. Konečná, T. Neuman, J. Aizpurua, and R. Hillenbrand, *"Surface-Enhanced Molecular Electron Energy Loss Spectroscopy"*, ACS Nano **12**, 4775–4786 (2018).

[268] F. Fujimoto and K.-i. Komaki, *"Plasma Oscillations Excited by a Fast Electron in a Metallic Particle"*, Journal of the Physical Society of Japan **25**, 1679–1687 (1968).

[269] R. v. Baltz, M. Mensch, and H. Zohm, *"Longitudinal electric response and loss-function of metallic microspheres and voids"*, Zeitschrift für Physik B Condensed Matter **98**, 151–161 (1995).

[270] D. B. Tran Thoai, *"Surface Excitations on Small Metal Particles by Fast Electrons"*, physica status solidi (b) **136**, 291–298 (1986).

[271] J. Bausells, A. Rivacoba, and P. M. Echenique, *"Energy loss in spheres by penetrating electrons"*, Surface Science **189-190**, 1015–1022 (1987).

[272] D. B. Tran Thoai and E. Zeitler, *"Inelastic scattering of fast electrons by small metal particles"*, Physica Status Solidi (a) **107**, 791–797 (1988).

[273] R. Ritchie and A. Marusak, *"The surface plasmon dispersion relation for an electron gas"*, Surface Science **4**, 234–240 (1966).

[274] J. Crowell and R. H. Ritchie, *"Radiative Decay of Coulomb-Stimulated Plasmons in Spheres"*, Physical Review **172**, 436–440 (1968).

[275] I. Villó-Pérez and N. R. Arista, *"Hydrodynamical model for bulk and surface plasmons in cylindrical wires"*, Surface Science **603**, 1–13 (2009).

[276] K. F. Riley, M. P. Hobson, and S. J. Bence, *Mathematical Methods for Physics and Engineering*. Cambridge University Press, Cambridge, 2006.

[277] M. Schmeits, *"Inelastic scattering of fast electrons by spherical surfaces"*, Journal of Physics C: Solid State Physics **14**, 1203–1216 (1981).

[278] S. B. Ogale, V. N. Bhoraskar, and P. V. Panat, *"Surface plasmon dispersion relation for spherical metal particles"*, Pramana **11**, 135–144 (1978).

[279] R. Fuchs and F. Claro, *"Multipolar response of small metallic spheres: Nonlocal theory"*, Physical Review B **35**, 3722–3727 (1987).

[280] F. J. García de Abajo, *"Nonlocal Effects in the Plasmons of Strongly Interacting Nanoparticles, Dimers, and Waveguides"*, The Journal of Physical Chemistry C **112**, 17983–17987 (2008).

[281] N. Zabala and P. Echenique, *"Energy loss of fast electrons moving near plane boundaries with dispersive media"*, Ultramicroscopy **32**, 327–335 (1990).

[282] R. Ruppin, *"Optical properties of a plasma sphere"*, Physical Review Letters **31**, 1434–1437 (1973).

[283] G. Toscano, S. Raza, W. Yan, C. Jeppesen, S. Xiao, M. Wubs, A.-P. Jauho, S. I. Bozhevolnyi, and N. A. Mortensen, *"Nonlocal response in plasmonic waveguiding with extreme light confinement"*, Nanophotonics **2**, 161–166 (2013).

[284] M. Mecklenburg, W. A. Hubbard, E. R. White, R. Dhall, S. B. Cronin, S. Aloni, and B. C. Regan, *"Nanoscale temperature mapping in operating microelectronic devices"*, Science **347**, 629–632 (2015).

[285] J. I. Gersten and A. Nitzan, *"Electromagnetic Theory: A Spheroidal Model"*, in *Surface Enhanced Raman Scattering*, pp. 89–107. Springer US, Boston, MA, 1982.

[286] S. Abramowitz and I. Stegun, *Handbook of Mathematical Functions with Formulas, Graphs, and Mathematical Tables*. Dover, New York, 10th ed., 1972.

[287] J. Wesley, *A Compendium of Natural Philosophy*. Thomas Tegg and Son, London, 1810.